Improving Remote Sensing Evapotranspiration Estimates to Constrain Groundwater Contributions to Catchment Water Balances in Western Victoria, Australia.

Submitted by
Rakhshan Roohi
Ph.D.

A thesis submitted in total fulfilment
of the requirements for the degree of
Doctor of Philosophy

Department of Ecology, Environment and Evolution
School of Life Sciences
College of Science, Health and Engineering

Latrobe University
Victoria, Australia

November 2019

Table of Contents

List of Figures

List of Tables

List of Symbol & Acronyms

Symbols

Symbol	Description	**Units**
$Cos\theta$	Cosine of the solar incidence angle	
C_p	Air specific Heat	J/Kg/K
$C_{p\_cold/hot}$	Air specific heat of the hot or cold pixels.	
d_{e-s}	Relative Earth Sun Distance	AU
d_r	Inverse Squared Relative Earth Sun Distance	AU
dT	The temperature difference between the two heights	°K
$ESUN_\lambda$	Mean solar exo-atmospheric irradiance for each band	W/m^2
ET	Evapotranspiration	mm/time unit
ET_{24}	Cumulative daily ET of satellite pass day	mm/day
ET_{inst}	the image pass time ET of each pixel (mm/hr)	mm/hr
ET_o	Reference evapotranspiration for grass	mm/hr
ET_r	Reference evapotranspiration for alfalfa	mm/hr
ET_rf	Reference ET Fraction	
g	Gravitational constant = 9.81	m/s^2
G	Soil Heat Flux	W/m^2
G_{sc}	Solar Constant = 1367	W/m^2
h	plank's constant = 6.626 * 10^-34	Js
H	Sensible Heat Flux	W/m^2
$H_{cold/hot}$	Sensible Heat of the cold or hot pixels	
k	von Karman's constant	0.41
K_1	Band-specific thermal conversion constant	
K_2	Band-specific thermal conversion constant	
K_c	Crop Coefficients	
L	Monin-Obukhov length	m
L_{max}	The maximum L value for the respective band	
L_{min}	The minimum value for the respective band	
Lv (λ)	Latent heat of vaporization of water	kJ/Kg
L_λ	Spectral radiance of each band	(Watts/(m2 * srad * µm))
M_L	Band-specific multiplicative rescaling factor	
Q_{cal}	Quantized and calibrated standard product pixel values (DN)	
r_{ah}	Aerodynamic resistance to heat transport	s/m
$r_{ah\_cold/hot}$	Aerodynamic resistance to heat transport of the hot or cold pixels.	
R_c	Corrected thermal radiance from the surface	(Watts/(m2 * srad * µm))
$R_L\uparrow$	Outgoing Longwave Radiation	W/m^2
$R_L\downarrow$	Incoming Longwave Radiation	W/m^2
$R_{L\downarrow net}$	Net incoming longwave radiation	W/m^2

R_n	Net Radiation Flux	W/m^2
$R_s \uparrow$	Outgoing Shortwave Radiation	W/m^2
$R_s \downarrow$	Incoming Shortwave Radiation	W/m^2
$R_s\downarrow_{net}$	Net incoming shortwave radiation	W/m^2
s	Boltzmann constant = 1.38 * 10^-23	J/K
T_a	Near-surface air temperature	°K
T_b	At-satellite brightness Temperature	°K
Z	Height	m
Z_1	Height just above the zero-plane displacement for the surface or the crop canopy	m
Z_2	Some distance above the Z_1 but less than the surface boundary layer	m
Zom	A measure of the drag and skin friction for the air layer that interacts with the surface.	m
Zom_{pix}	Momentum roughness length for each pixel	
Z_x	Height of the weather station's wind instrument (anemometer)	m
α	Albedo	
$\alpha_{path\_radiance}$	the values range between 0.025 and 0.04 (Bastiaanssen, 2002 and Allan et al. 2000)	
α_{toa}	Albedo at the top of the atmosphere	
β	Bowen ratio	
θ	Solar Incidence angle	Degrees
θ_{SE}	Local sun elevation angle	
θ_{SZ}	Local solar zenith angle	
λ	Latent heat of vaporization	J/Kg
λET	Latent Heat Flux	W/m^2
μ^*_{200}	Friction velocity (m/s) at blending height (200m)	m/s
μ^*_{pix}	Friction velocity of each pixel	m/s
μ^*_{ws}	Friction velocity at the weather station	m/s
μ_{200}	Wind speed at 200m	m/s
μ_x	Wind speed at a height Zx	m/s
π	Pi = 3.14	
ρ	Air density	Kg/m^3
$\rho_{cold/hot}$	Air density of the hot or cold pixels.	
$\rho\lambda$	Reflectance	
σ	Stefan–Boltzmann constant = 5.671×10^{-8}	$W{\cdot}m^{-2}.K^{-4}$
Ψ_h	Stability correction for heat transport between two layers Z1 (0.1m) and Z2 (2m)	
$\Psi_{m\ (200m)}$	Stability correction for momentum transport at 200 meters	
$\dot{\omega}\lambda$	Weighting coefficient for each band λ	
ε_a	Atmospheric emissivity	

Acronyms

ASTER	Advanced Spaceborne Thermal Emission and Reflection Radiometer
CATHY	Catchment hydrology (CATHY) distributed model
DBNS	Depth Below Natural Surface (meters)
DEPI	Department of Primary Industries
DOY	DOY Julian Day Number (JDN)
FAO	Food and Agriculture Organization
GloVis	Global Visualization Viewer
LAI	Leaf Area Index
LST	Land Surface Temperature (°K or °C)
LWI	Longwave Infrared
MODIS	Moderate Resolution Imaging Spectroradiometer
NASA	National Aeronautics and Space Administration
NCGRT	National Center for Ground Research and Training
NDVI	Normalized Difference Vegetation Index
NIR	Near-Infrared Radiation
NIR	Near Infra-Red
SAVI	Soil Adjusted Vegetation Index
SEB	Surface Energy Balance
SEBAL	Surface Energy Balance Algorithms for Land
SEBARA	Surface Energy Balance Algorithms for Rainfed Agriculture
SRB	Surface Radiation Balance
SRTM	Shuttle Radar Topography Mission
S-SEBI	Simplified Surface Energy Balance Index
SVAT	Soil-Vegetation-Atmosphere Transfer Model
SWIR	Shortwave radiation
SWIR	Shortwave Infrared
TIR	Thermal Infrared Radiation
T_s	Surface Temperature (°K or °C)
USGS	United States Geological Survey
VIS	Visible
VIs	Visible
VIs	Vegetation Indices

List of Appendices

Summary

Evapotranspiration, the sum of evaporation from land and transpiration by plants, is a significant component of the hydrological cycle, constituting on average more than 80% of continental precipitation in SE Australia. However, this component of the energy balance equation is the most difficult to estimate as it is influenced by many factors, especially in rainfed ecosystems. Under this research project, following the principals of Surface Energy Balance Algorithms for Land (SEBAL), an approach is developed to estimate the evapotranspiration (ET) of rainfed agrosystems using medium spatial resolution Landsat data as an input for Surface Energy Balance Algorithms for Rainfed Agriculture (SEBARA). ET calculated using climatic data which includes solar radiation, humidity, vapour pressure deficit and wind speed, as well as soil heat flux. The model was used to estimate ET of two adjacent catchments with similar climatic conditions but contrasting landuse (tree plantation and pasture), located at Mirranatwa, western Victoria, south-eastern Australia. After comparison with measured values at flux tower for pasture and sapflow meters for plantations, SEBARA applied to another pair of catchments located in the same region at Gatum with similar climate and landuse.

The spatial ET estimates derived from SEBARA for Mirranatwa were within 95% of measurements obtained from a flux tower and sapflow data. The pasture catchment, in general, has a higher surface albedo and emissivity, resulting in higher energy loss in terms of outgoing longwave radiation and higher surface temperature, leading to a higher soil heat flux. Due to limited access to soil moisture of the shallow root system of pasture species, especially in elevated areas with deep groundwater, the ET of the pasture catchment is low. However, a cultivated oats crop in this catchment has higher ET due to a better vegetation cover and low elevation resulting

in higher moisture availability. An old tree plantation in the pasture catchment has an extensive, deep root system and a farm dam, also resulting in higher ET. The tree plantation catchment mirrored the response of the pasture catchment in general. However, the young plantations at elevated areas with deep groundwater could not exceed the ET rates of pasture. In contrast, the plantations at lower elevations with better soil moisture consistently showed higher ET (15-20% higher than pastures).

The groundwater depth surface, generated using borehole data, helped in understanding the spatial variability of ET, especially in plantations, and its role in the hydrological lift and groundwater redistribution by the trees. In young plantations, ET limited by either shallow saline groundwater or a groundwater depth of > 15 m.

In winter, at both sites, although the spatial distribution was similar to summer except for sensible heat flux, the energy fluxes were lower, resulting in an average winter ET that is 22% of summer ET.

This study has shown that SEBARA can be successfully used in hydrological modelling to estimate evapotranspiration for each landuse within a catchment and to derive a realistic estimate of water loss at the catchment scale. This approach can be used to monitor the impact of any shift in land use on hydrological resources.

Statement of Authorship

Except where reference made in the text of the thesis, this thesis contains no material published elsewhere or extracted in whole or in part from a thesis submitted for the award of any other degree or diploma.

No other person's work used without due acknowledgement in the main text of the thesis.

The thesis not submitted for the award of any degree or diploma in any other tertiary institution.

This work was partially supported by:

- La Trobe University Postgraduate Research Scholarship
- The research project funded by the National Centre for Groundwater Research and Training and
- Project No. LP140100871 entitled Catchment water balance and CO_2 fluxes.

Rakhshan Roohi

Submitted:11-11-2019

Acknowledgements

Foremost, I would like to express my sincere gratitude to my supervisor Prof. John A. Webb for his continuous support, patience, and guidance which helped me complete this research project and the writing of the thesis. I highly value his help in arranging financial support through the following sources:

- LaTrobe University PhD scholarship (through John A. Webb)
- Partial financial support through the research project funded by National Centre for Groundwater Research and Training under Program 4: Vegetation – Atmosphere – Groundwater Interaction; Influence of land-use change on groundwater resources in western Victoria and
- Partial financial support through project No. LP140100871 entitled Catchment water balance and CO2 fluxes: a comparison between productive landuse. I am also thankful to all the PIs of the project including Edorado Daly, Christoph Rüdiger, John A. Webb, Jason Beringer, Jeffrey Walker, Evan Dresel, Elizabeth Morse-McNabb, Matteo Camporese for this support.

I would like to extend my sincere thanks to my committee members Caixian Tang, Peter Sale and Simon Jones for their guidance and valuable comments and suggestions.

I would like to extend thanks to the following people for their help and contributions throughout my study period:

- Team of Department of Environment and Primary Industries based at Bendigo, especially Evan Dresel, Elizabeth Morse-McNabb, Malcolm McCaskill, Michael Adelana, Phill Cook and Peter Hekmeijer for valuable comments and providing the field data.

- Edorado Daly, Christoph Rudiger, Bertrand Teodosio from Monash University, Victoria, Australia for setting up the Flux tower, providing data and critical review of the research outcome.

- The landowners of the catchments at Mirranatwa (Marcia and Ivan) for allowing me to visit their property.

- Joshua F. Dean for sharing the flux tower and sapflow data for both the catchments at Mirranatwa.

- All the postgraduate students of my supervisor, John Webb, especially Michael Sephton, Tim Robson, Fahmida Perveen, Matej Lipar, Sarah Hagerty, Fiona Glover, Sanjeeva Manamperi, Emre Sayar, Julia Kirschbaum, Shannon Burnett, Farah Ali, Wendy Stanford and staff of the EEE for their prompt support whenever asked for.

- Dr. Mubeen-ud Din Ahmad (CSIRO), Bushra Minhas (NUST) and Mirza Muhammad Waqar (IRSDE) for sharing SEBAL algorithms and their support.

I would like to extend my most profound respect and gratitude to my parents and my siblings – my parents for their ever-lasting support of my educational and professional pursuits and my siblings for providing moral support whenever it was required the most.

Lastly (probably for good reasons) I would like to thank my family for remembering to breathe while I worked on this project. Beyond base survival, I genuinely believe that my family far exceeded my expectations – albeit very low ones. My husband of all people helped me understand

some of the complex mathematics behind the thesis. I guess it truly does not matter how many engineers it takes to screw a light bulb as long as they can understand the Monin-Obukhov length equations. My kids (Zunaira, Ammar, Kanza and Osama) provided amazing emotional support throughout the project. In reality, I was hoping for more than just “emotional support”, an iPad or two would have been nice.

Chapter 1. Introduction

The processes of evaporation and transpiration are large components of the hydrological cycle, constituting 60% of the precipitation worldwide (Brutsaert, 1986) and often greater than 90% in SE Australia (Thorburn *et al*., 1993a & 1993b). These two components of the energy balance equation are the most difficult ones to estimate, especially in rainfed conditions, as they are influenced by factors such as spatial variability in temperature, soil moisture, vegetation type and growth stage and atmospheric advection (McMahon *et al*., 2013). Transpiration, which is the principal component of ET over most of the land surfaces (Calder, 1998), is strongly coupled with the rate of carbon assimilation and thus, with primary productivity (Monteith, 1973). Any structural change in vegetation, particularly alteration between the tree and grass-dominated covers, often modifies evaporative water losses because of plant-mediated shifts in moisture access and demand (Horton, 1919; Bosch and Hewlett, 1982; Zheng *et al*., 2001).

To understand the behaviour of terrestrial ecosystems and their response to landuse change, evapotranspiration is the key element of the energy balance equation to be considered and monitored (Kelliher *et al*., 1993; André *et al*., 1986 & 1988). It has been recognized that land surface processes affect atmospheric circulations at all temporal and spatial scales, ranging from multi-annual-climatic scales (Charney, I975; Shukla and Mintz, I982; Yeh *et al*., I984) to local mesoscale circulations (Anthes, I984; Andre *et al.*, 1986). Any shift in land surface processes results in a higher ET because of lower albedo, enhanced roughness, and large minimal stomatal resistance of forested area as compared to croplands or pastures (André *et al.*, 1988).

Advection and radiation control the atmospheric demand of water vapour which, in turn, limit the rate of ET. Under dry conditions, the availability of soil moisture becomes the primary control of ET, besides the differences in the capacity of plants to access water, often dictated by rooting depth, (Calder, 1998; Schenk and Jackson, 2002). Trees tend to have deeper roots than herbaceous plants (Canadell *et al*., 1996; Schenk and Jackson, 2002), and hence can maintain higher ET than grasslands when the water supply declines (Calder *et al*., 1993; Calder *et al*., 1997; Sapanov, 2000). Further, the higher aerodynamic roughness of forests leads to a higher exchange rate of heat and water vapour between the canopy surface and the air. Under wet conditions, it can be up to 10 times more than that possible for short vegetation, and ET is coupled to the supply of radiant energy (Kelliher *et al*., 1993; Calder, 1998).

The contrasting water loss between tree plantations and grasslands through ET has been evidenced by a diverse array of approaches such as plot studies, paired catchments, and hydrological modeling. Relationships between vegetation type and catchment ET, and runoff are determined primarily through paired catchment studies. Research into the role of catchment vegetation within the hydrologic cycle has a long history in hydrologic literature (Peel, 2009; Brown *et al*., 2005). In a review of catchment experiments carried out by Bosch and Hewlett (1982), the general conclusion was that the water yield following forest operations could be predicted with fair accuracy. In another detailed review (Best *et al.*, 2003) on the use of paired catchment studies for determining the changes in water yield at various time scales resulting from permanent changes in vegetation. The review considered long-term annual changes, adjustment time scales, the seasonal pattern of flows and changes in both yearly and seasonal flow duration curves. These studies concluded that the seasonal changes in water yield highlight the proportionally more significant impact on low flows. However, these studies focused mainly on regrowth experiments. Further, these studies also emphasized that generally drier soils and vadose zones in paired watershed experiments decreased streamflow when grassland watersheds are afforested (Calder *et al*., 1993; 1997; Sahin and Hall, 1996;

Scott and Lesch, 1997; Dean *et al.*, 2014b; Camporese *et al.*, 2013). The groundwater observations revealed the onset of phreatic water discharge under afforested plots within herbaceous landscapes (Heuperman, 1999; Sapanov, 2000; Dean *et al.*, 2014b; Jobbágy and Jackson, 2004).

Soil as a predominant media for water storage and transport has a strong influence on ET (Noy-Meir, 1973; Hillel, 1998). The study concludes that under humid and sub-humid conditions, medium-textured soils present the highest available water for plants.

The methods classically used to measure evapotranspiration (ET) at the field scale (Bowen ratio, eddy correlation system, soil water balance) do not allow estimation at large spatial scales (Courault *et al.*, 2005). With advances in space technology and the availability of high spatial and spectral resolution satellite data, different methods have been developed to use this data for estimation of various components of the energy balance equation including the spatial variability of the ET. These methods range from simplified empirical approaches to sophisticated processes based on remote sensing data assimilation (Courault, *et al.*, 2005; Singh and Senay, 2016), and can be classified into ***residual energy budget methods*** that combine empirical relationships with physical modules, e.g. SEBAL (Allen *et al.*, 2005a; 2011 & 2013; Bastiaanssen *et al.*, 1998a & b; Allen *et al.*, 2002a; Gowda *et al.*, 2007; Gurney and Camillo, 1984; Jaber, *et al.*, 2016), SEBS (Su, 2002), and S-SEBI (Roerink, *et al.*, 2000); ***empirical direct methods*** (Courault *et al.*, 2005) using remote sensing data (thermal infrared, shortwave infrared and visible spectra), ***two-source approach*** for computing turbulent fluxes (Kustas and Norman,1997) and meteorological data as inputs in ***semi-empirical models***; ***deterministic methods*** (Courault *et al.*, 2005) based on more complex relationships such as the Soil-Vegetation-Atmosphere-Transfer (SVAT) model and the Vegetation Index method; and ***inference methods*** based on the use of remote sensing to compute a reduction factor (such as K_c

or Priestley Taylor-alpha parameters) for the estimation of the actual evapotranspiration. Among the residual energy budget methods, SEBAL is an intermediate approach using both empirical relationships and physical parameterizations (Morse *et al.,* 2000; Bastiaanssen *et al.,* 1998a & b; Allen *et al.,* 2002a; Jacob *et al.,* 2002a & b) designed to calculate the surface energy budget at the regional scale with minimum ground data. Though this graphic approach requires the identification of ‘hot’ and ‘cold’ pixels and the air temperature (T_a), it has advantages over other methods in being operational, widely used, and low cost (Courault *et al.,* 2005). However, it is most suitable for irrigated crops with uniform crop cover having no limitation of moisture availability and is challenging to apply to rainfed agriculture.

Remotely sensed data is now available at a variety of costs and resolutions. McCabe and Wood (2006 & 2008) compared estimates of ET using higher and lower resolution satellite products (Landsat/ASTER and MODIS respectively), and found that although the ET estimates were consistent, the MODIS-based assessment is unable to discriminate the influence of land surface heterogeneity at the field scale. Landsat data has considerable advantages in this regard; it has a moderate spatial resolution, high spectral resolution, and the thermal bands, and it is free. It is suitable for the estimation procedures based on remote sensing data that use different spectral domains to retrieve input parameters (Valor and Caselles, 1996) such as albedo, emissivity, Vegetation Indices like Normalized Difference Vegetation Index (NDVI), Leaf Area Index (LAI) and Soil Adjusted Vegetation Index (SAVI), and land surface temperature.

In Australia, the early settlers attempted to create a 'little England' in the colony, and the impacts of their activities on many Australian landscapes varied in their extent and severity (Powell, 1996). Alterations were made to vegetative cover, producing a change from native forest to degraded land in many localities. The sophisticated series of interactions between various environmental components were fundamentally associated with the changes in the hydrological cycle, and the outcomes differ in nature, extent, and severity between landscapes.

The cattle farming introduced to the High Plains in the1830s and there was a rapid pastoral occupation of land in both south-eastern and south-western Australia around this time. The cattle and sheep industry boosted and touched it's highest in the 1970s. Later, reoccurring droughts and changing international trade resulted in a shift in landuse. The pasture lands converted into plantations, predominantly *Eucalyptus spp*., which resulted in a shift in the hydrological cycle. Compared to pastures, having a higher ET, *Eucalyptus* plantations impacted the groundwater quality and quantity. In Australia, massive afforestation of native grasslands/pasturelands may have strong yet poorly quantified effects on the hydrological cycle.

The research questions addressed in this research project include:

- Can spatial variability of ET be estimated accurately using satellite data?
- Is *Eucalyptus* plantation or forest have a higher ET compared to pastures and can?
- Is there any correlation between ET and groundwater?

To answer these research questions, following hypotheses formulated and tested:

- The spatial pattern of ET of different landcover in the rainfed environment can be estimated using multispectral and thermal bands of satellite images, and climatic data.
- Trees have higher ET than pastures in rainfed environments
- Higher ET of plantations can impact the groundwater.

The overall research objective is to estimate the evapotranspiration of a mixed landcover, at a catchment scale, using satellite data, and to see the relationship between ET and groundwater, if any.

This research is funded by the National Centre for Groundwater Research and Training (NCGRT) and coordinated with Monash University, Melbourne and the Department of Environment and Primary Industries, Victoria, Australia. Under this Ph.D. research, a conceptual model for ET estimation is developed, using Landsat data, that applies to all landuses, not just irrigated fields. It is based on the existing SEBAL (Surface Energy Balance Algorithms for Land) model (Allen *et al.*, 2002a & 2011, Bastiaanssen *et al.*, 2005, Teixeira *et al.*, 2009), modified for rainfed agrosystems at a catchment scale. It is here called Surface Energy Balance Algorithms for Rainfed Agriculture (SEBARA).

The thesis is divided into six more chapters. Chapter 2 describes the Mirranatwa study site, used for model development and comparison with the field measurement of ET, climate, and groundwater. Chapter 3 covers the theoretical background of the ET, energy balance equation and controlling factors, available satellite data sets and model requirements. The first section of Chapter 4 includes the details of computation of Surface radiation budget, data acquisition and modelling. In contrast, the second section elaborates the computation of surface energy budget and evapotranspiration. Chapter 5, results and discussion, covers catchment scale ET estimation and comparison of pasture and plantation at catchments scale, the response of major landcover in both the catchments, comparison of SEBARA output with field measurements, RefET model output, Catchment hydrology (CATHY) distributed model output, Bowen ratio and evaporative fraction. Chapter 6 focuses on groundwater and ET interaction both at catchment scale as well for dominant landcover. Chapter 7 focuses on the application of SEBARA to Gatum site having a pair of catchments along with Mirranatwa site. Finally, Chapter 8 covers the main conclusions of this research project including key outcomes, research highlights, way forward and recommendations.

Chapter 2. Study Site

The SEBARA model developed and tested using a study site located near Mirranatwa, about 230 km west of Melbourne, south-eastern Australia (Figure 2.1). Sandstone ridges of the Grampian Ranges surround it. The study site consists of a pair of small, adjacent catchments; one with an area of 0.813 km^2, predominantly covered with plantations of *Eucalyptus globulus* (Blue Gum) planted in 2008, and the other is 0.514 km^2 in size and is managed predominantly as pasture for sheep. In both the catchments, there are small patches of natural vegetation, including *Eucalyptus regnans* (Figure 2.2). There are four small farm dams in each, primarily used for stock watering (Figure. 2.1); the area of the largest dams in the pasture and plantation catchments is 1,019 m^2 and 347 m^2 respectively. An unsealed single lane road passes through the catchments, although the road is less permeable than the normal ground surface, only limited runoff generated due to its small area (Dean *et al.,* 2014a & 2014b).

The elevation ranges from 259 to 307 meters above sea level (Figure 2.3). There is about 50m relief in the plantation catchment, which slopes predominantly west, and 30m in the farm catchment, which slopes mainly south (Roohi and Webb, 2016b). The highest elevation in both the catchments is on the north and north-eastern side. The plantation catchment drains towards the west, whereas the pasture catchment drains towards the south.

The climate is Mediterranean or maritime/temperate region (Cfb in the Köppen classification), with an average annual rainfall of 672 mm (±125σ) and pan evaporation of 1350 mm which exceeds precipitation for the majority of the year, except for the months from May through September (Dean *et al.*, 2014a and b). Based on the stream hydrograph record, the runoff ratios for the farm and plantation catchments are 3.4% and 4.3% respectively.

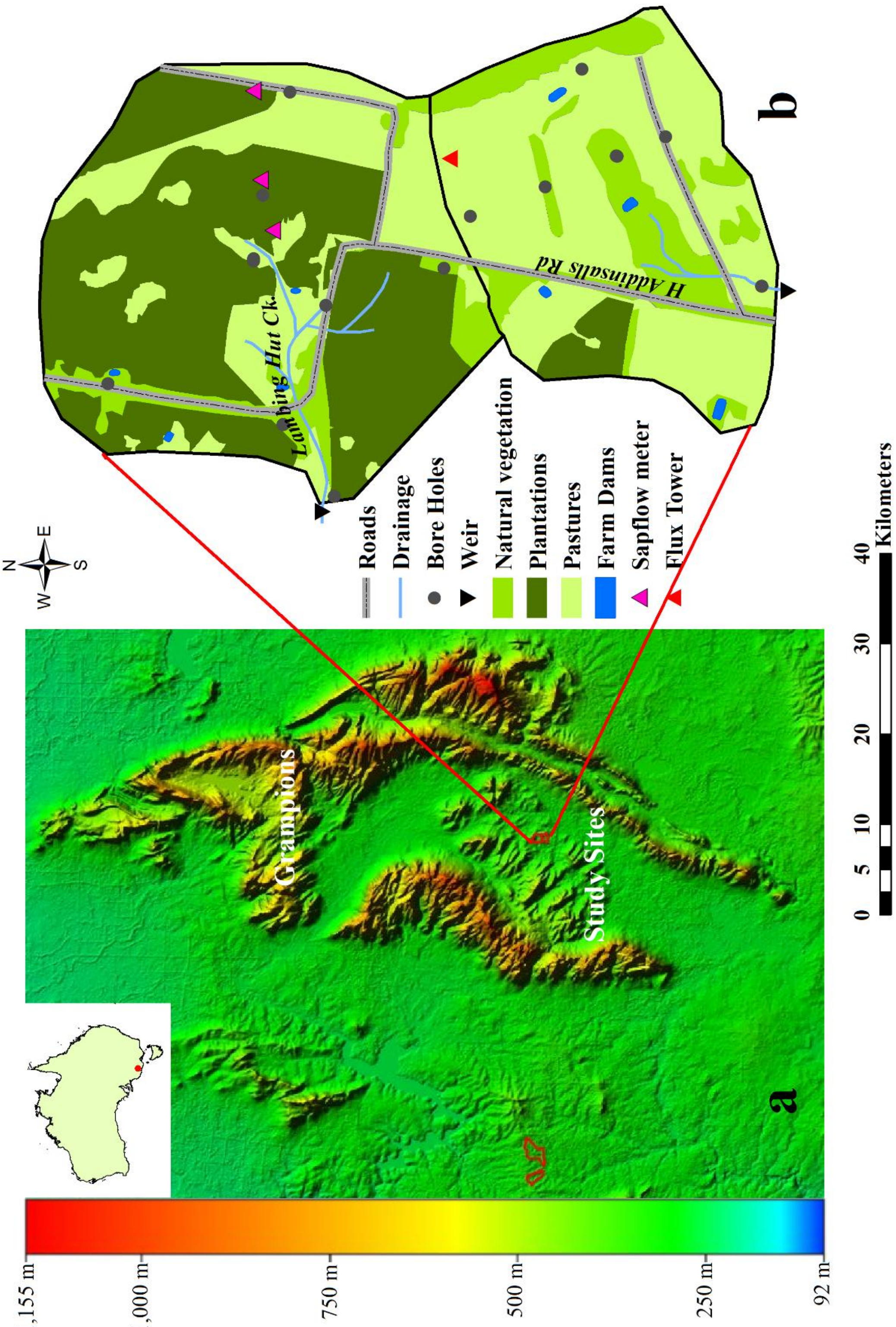

Figure 2.1 Location of paired catchments at Mirranatwa in western Victoria, Australia (a) and the catchments with Landover types and location of eddy covariance tower (Flux tower), sapflow meters, weir and borehole (b).

Figure 2.2. Panoramic view of the study site at Mirranatwa: (a) plantation catchments and (b) pasture catchments (with the courtesy of Dr. John Webb).

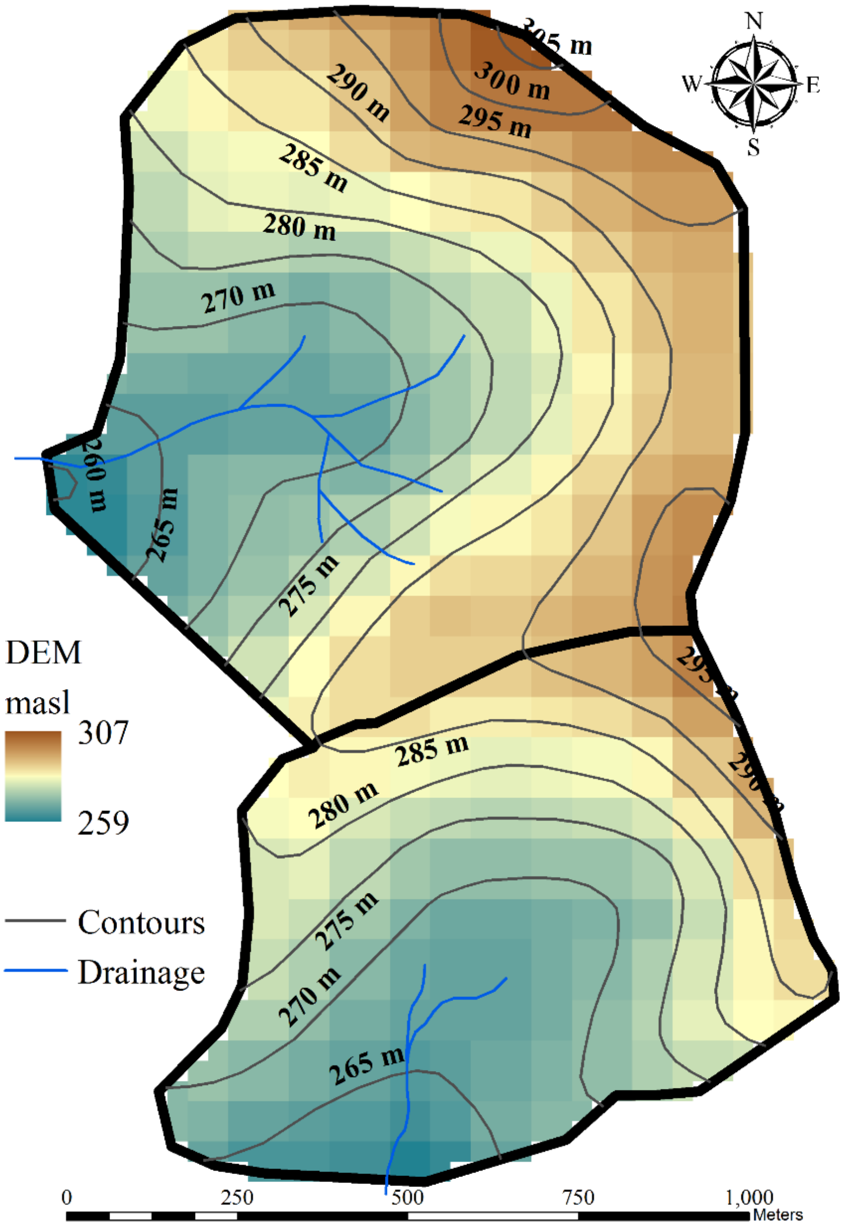

Figure 2.3. The topography of Mirranatwa study site.

The vegetation of the area before European settlement was mostly open eucalypt woodland (Dean *et al.*, 2014b). There was an extensive land clearance following the European settlement, , and the catchments entirely converted to pasture by 1869 (White *et al.*, 2003).

In the plantation catchment, 62% of the area was converted to *E. globulus* plantation in July 2008 with a tree density of 1,010 stems per ha (2.2m between trees along a row, and 4.5m between rows). Before the establishment of the plantation, the predominant landuse was grazing, and the area was identical to the existing pasture catchment (Dean et al. 2014b). In both the catchments there are three land cover types, namely plantations (LC1), pasture (LC2), and native forest (LC3). In the plantation catchment, consolidated plantation blocks (LC1) cover 62% of the catchment, 29 % is pasture (LC2), and about 10% of the area covered by native forest (LC3) (Figure 2.1). Seventy-five percent of the pasture catchment categorized as LC2 and 22% as LC3 and only 3% as tree plantations (LC1) (Figure 2.1).

For monitoring groundwater and surface hydrology and measuring climatic parameters and ET, a network of instruments was put in place. The pasture catchment has eight bores, and the plantation catchment has ten bores, drilled to variable depths. Every bore in the plantation catchment is equipped with a groundwater logger, measuring groundwater elevation at a minimum 4-hour time interval. Each catchment is equipped with a weir at the outlet point, with one bore adjacent to the weir in the plantation catchment and two next to the weir in the pasture catchment. At the weirs, the surface water level is measured using a standard V-notch construction (Dresel *et al.*, 2012). Sapflow meters were installed to measure ET of the plantation, while an Eddy Covariance flux tower was in operation in the farm catchment from March 2012, recording evapotranspiration. The monitoring network also included a complete weather station measuring rainfall, humidity, solar radiation, wind speed and direction. The data from the weather stations was collected and corrected by DEPI and Monash University. The groundwater level from the loggers for the image pass day was used to develop a raster layer of corresponding pixel size as of Landsat, representing the spatial variability of groundwater at the catchment scale (Figure 2.4).

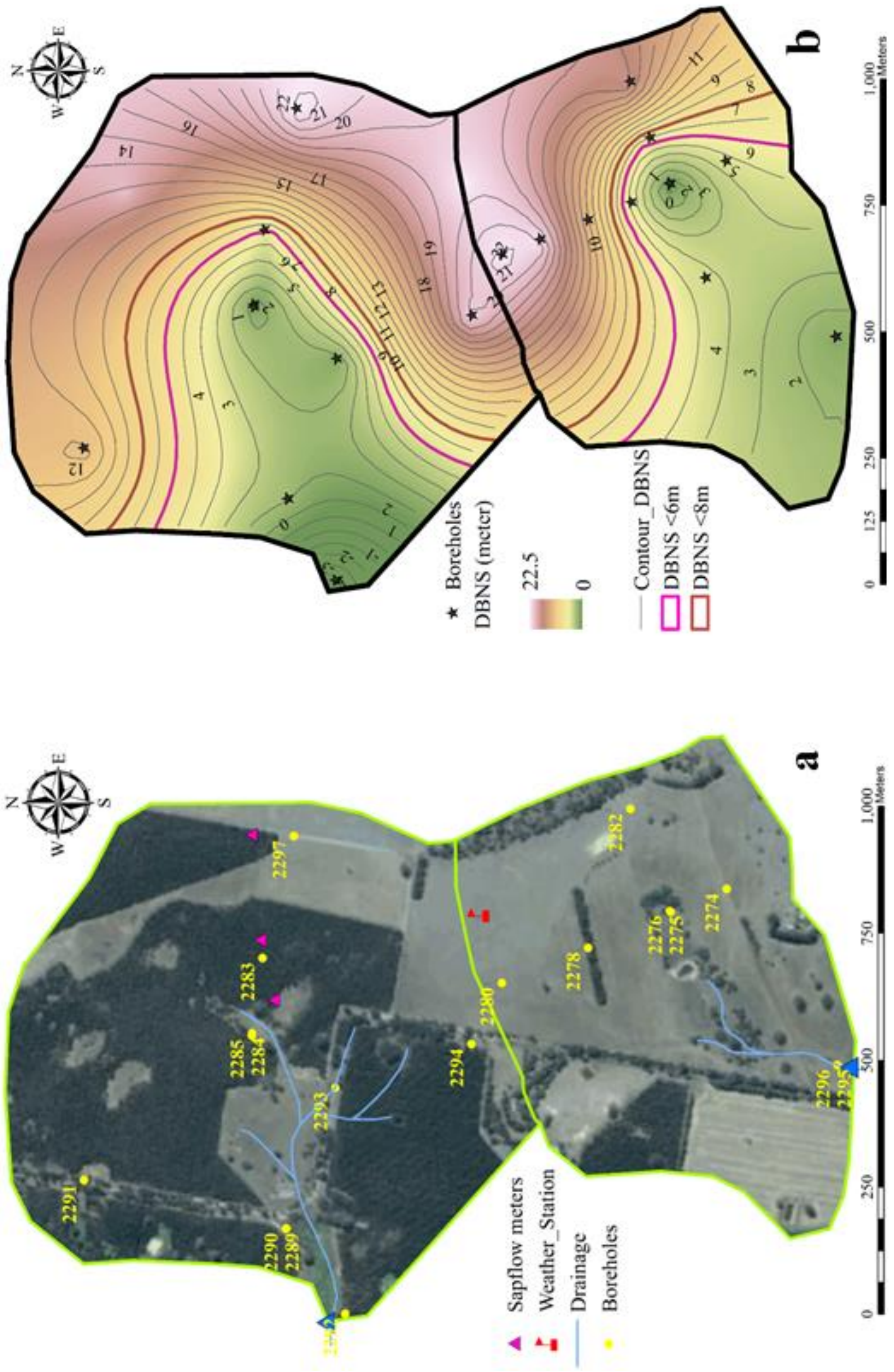

Figure 2.4. Location of sapflow meters installed in plantation catchment, weather station and boreholes (a) and groundwater Depth Below Natural Surface (DBNS) highlighting the variability in both the catchments at Mirranatwa site.

Chapter 3. Conceptual and Theoretical Background

Global natural and agricultural production systems are the products of complex interactions between energy, available water resources and prevailing climate. Any change in weather or production system can determine the outcome. Water is the primary component which is highly sensitive to climate change. Recent decades witnessed the shifting precipitation patterns in terms of droughts or extreme precipitations events, increasing temperature and CO_2.

Evaporation and transpiration (ET) drive the hydrological cycle. They are especially crucial in the rainfed agroecosystems, which are the essential components of the world's food production system, accounting up to 65 - 95% of total agriculture. The surface energy balance equation (Figure 3.1 & eq. 3.1) governs ET and needs to be understood to interpret spatial relationships between an agroecosystem and available surface and groundwater resources (Thorburn, 1999; Thorburn *et al.,* 1992, 1993a & 1993b; Thorburn and Walker, 1993; Cramer, 1999; Kelliher *et al.*, 1993; Andre *et al.,* 1986 & 1988). Both the processes of evaporation and transpiration are significant components of the hydrological cycle constituting 60% of the continental precipitation (Brutsaert, 1986). However, these two components of the energy balance equation are the most difficult ones to estimate as they are influenced by many factors such as spatial variability in temperature; soil moisture; vegetation type and growth stage; and atmospheric advection (Kutal *et al.,* 2012; McMahon *et al.,* 2013). The importance of climatic variability has been a topic of much debate over centuries (Herschel, 1801; Koppen, 1873; Labitzke and Loon, 1992; Gray *et al.,* 2010 & 2011; Fritschen, 1982) and there have been continuous improvements in modelling various components of the surface energy budget.

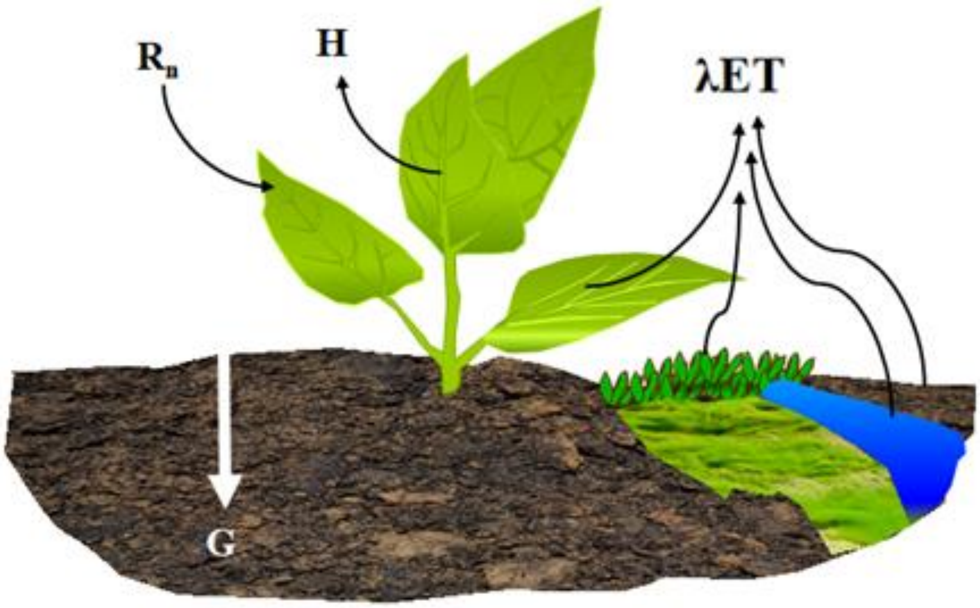

Figure 3.1. Components of Surface Energy Balance: Latent Heat Flux (λET), Net Radiation (Rn), Sensible Heat Flux (H), and Soil Heat Flux (G).

$$R_n = \lambda ET + H + G \qquad \text{(eq. 3.1)}$$

where:

R_n	Net Radiation
λET	Latent Heat Flux
H	Sensible Heat Flux
G	Soil Heat Flux

ET can be measured directly by eddy correlation (Burba, 2013) weighing lysimeters (Fisher, 2012) and the Bowen ratio technique (Tomlinson, 1997; Allen and Tasumi, 2005; Bowen,1926; Holland *et al.*, 2013). However, these methods generate point data, which is hard to extrapolate, especially in the complicated relationship that frequently exists in the landscape (Courault *et al.*, 2005).

The advancement of space technology, computing platforms and available algorithms has made it possible to compute ET from satellite imagery, to obtain measurements across the landscape and at variable time scales, to understand the ET patterns caused by rainfall distribution, soil characteristics, vegetation types and density, topography, groundwater depth, etc. The input for these models is the remote sensing data. Since 1972, under the joint United States Geological Survey (USGS)/ National Aeronautics and Space Administration (NASA) as well as the European Space Agency, the satellites of Earth Observation programmes are continuously acquiring space-based images of the Earth's land surface.

For calculation of net radiation, two components (emissivity and albedo) are essential, especially for rainfed agroecosystems with heterogeneous landcover. All object surfaces emit thermal radiation at temperatures above absolute zero. At a given temperature and wavelength, the emitted thermal radiation depends upon the emissivity characteristics of the surface of the object. The surface emissivity is defined as a ratio of the energy radiated from a material's surface to that radiated from a blackbody (a perfect emitter) at the same temperature and wavelength and under the same viewing conditions. The surface emissivity in net radiation estimation is not only crucial for accurate non-contact temperature measurement but also heat transfer calculations.

The second term, albedo, is the fraction of the incoming solar energy which is scattered by earth back to space, is a fundamental component of the Earth's energy balance, and the processes that govern its magnitude, distribution and variability shape the earth's climate and climate change (Stephen *et al.*, 2015; Liang *et al.*, 1998 & 1999; Cess, 1978; Dickinson, 1983; Dickinson *et al.*, 1990; Liang *et al.*, 1998, 1999, 2002 & 2012; Sofia and Li, 2001). Light-coloured surfaces or thin vegetative cover return a large part of the solar energy to the atmosphere, which means they have a higher albedo. In contrast, dark surfaces or thick forest cover absorb more solar energy, resulting in a lower albedo which in turn leads to higher energy uptake, hence, more ET (Chapter 4, section 4.1 includes the details).

There are several reasons for understanding the variability of albedo while modelling surface energy balance, include:

i. Models of the climate system are unstable to small changes in the amount of reflected energy. In these simple models with an albedo overly can be sensitive to surface temperature, relatively small changes in the absorbed solar energy can lead to under or overestimation.

ii. These models can swing from a near ice-free Earth to a fully ice-covered state (Budyko, 1969; Cahalan and North, 1979).

iii. Regulation of the system albedo through biotic adaptation towards differing albedos might buffer the system from the instabilities inherent to some energy balance models (Lovelock, 1983; Watson and Lovelock, 1983).

iv. More locally, the Earth's albedo appears to be resilient to other internal changes that might otherwise alter the system albedo (Stephen *et al.*, 2015). Aerosol present on clouds can impact albedo through the effects of buffering mechanism of compensating processes (Stevens and Feingold, 2009) that restrict local albedo changes to changing aerosol influences (Christensen and Stephens, 2011; Chen *et al.*, 2012). The implications of the local compensations to the concepts proposed to mitigate climate change are through geo-engineering-cloud albedo (Latham, 2002).

v. Regulation of the Earth's albedo is also central to other essential climate feedbacks, including the snow/ice surface albedo feedback as well as cloud feedbacks.

vi. It has also been thought that the energy transport mechanism from low to high latitudes is insensitive to the structure and dynamics of the atmosphere-ocean system. Instead, it is determined primarily by external controls such as the solar constant, the size of the Earth, the tilt of the Earth's axis, and the mean hemispheric albedo (Stone, 1978; Enterton and Marshall, 2010). The results of Donohoe and Battisti (2012) are further consistent with this notion. They show that the maximum in annual mean meridional heat transport differs by approximately 20% among coupled climate models due to model differences in equator to pole planetary albedo.

The energy consumers in the surface energy balance equation are Soil Heat Flux (G) and Sensible Heat Flux (H). Soil heat flux is the amount of thermal energy that moves through an area of soil in a unit of time (Sauer and Horton, 2005). Properties of the surface soil layer including colour, water content, texture, and density, along with the vegetative cover, determine the partitioning of incident radiation to the energy required to evaporate water, warm the air above the ground, or warm the soil. The ability of soil to conduct heat determines how fast its temperature changes during a day or between seasons.

Soil temperature is a crucial factor affecting the rate of chemical and biological processes in the soil, essential to plant growth. Soil heat flux is vital in micrometeorology because it effectively couples energy transfer processes at the surface (surface energy balance) with energy transfer processes in the soil (soil thermal regime). This interaction between surface and subsurface energy transfer processes has led to detailed investigations of soil heat flux for a wide variety of agricultural systems. An empirical equation was developed by Bastiaanssen (2000) to compute G/R_n ratio using surface albedo and Normalized Difference Vegetation Index (NDVI). Following this approach, G is calculated by multiplying the ratio with G (details are given in Chapter 4, section 4.2).

The last parameter required to complete the energy balance equation is the Sensible Heat Flux (H). This parameter is the turbulent or conductive flux of heat from the Earth's surface to the atmosphere due to the temperature difference, which is not associated with changes in the phase of water. It is a function of the temperature gradient, surface roughness and wind speed. It is a complex process due to two unknown parameters: aerodynamic resistance to heat transport (rah) and the temperature difference between two heights (dT) to account for a vertical profile. Friction velocity is required to compute aerodynamic resistance to heat transport for the temperature gradient (dT) which is achieved through an iterative process until near stable condition is achieved (details are given in Chapter 4, section 4.2).

Finally, the Latent Heat Flux (λET), which is the heat flux from the Earth's surface to the atmosphere associated with evaporation, transpiration or condensation of water vapour at the surface, is computed using the three parameters of the energy balance equation discussed above.

Chapter 4. Surface Energy Balance Algorithm

Following the SEBAL concept, the Surface Energy Balance Algorithm for Rainfed Agriculture (SEBARA) was developed to compute the ET of a mixed landuse including plantation, natural vegetation and pastures in a rainfed environment. The differences and similarities between the two approaches are included in table 4.1. Satellite data (visible, NIR, SWIR and thermal bands) and weather data are the input for the models of various components of the surface radiation balance and the surface energy balance.

Table 4-1. Differences between SEBAL and SEBARA algorithm.

Parameters		**SEBAL**	**SEBARA**
Application		SEBAL is used predominantly for agricultural areas for estimation of evapotranspiration, biomass growth, crop water requirement and irrigation scheduling.	SEBARA focuses on the evapotranspiration estimation of plantation, pastures, or mixed vegetation in the rainfed environment.
Image preprocessing	Image extent	Probably the algorithm applied for the entire image.	A subset of the image is used including the interest area to minimize the processing time; however, the entire image or a mosaic of the same date can be used depending upon the extent of the target area.
Image preprocessing	Radiance & Reflectance	Followed the same approach for Landsat 5 image for SEBARA algorithm; however, for Landsat 8, the procedure is modified for SEBARA following USGS (2019a, b & c).	
Albedo (α)	Atmospheric transmissivity (τ_{sw})	τ_{sw} computed using FAO56 elevation base relationship = 0.75+ 2 x 10-5 $*$ z (assuming clear sky and relatively dry conditions) using the elevation of the relevant weather station. It is considered that additive factor (0.75) is site-specific and may vary under variable situations.	τ_{sw} depends upon several atmospheric conditions (cloud cover and it's optical thickness and absorption by water vapours, gases and aerosols). These conditions may have spatial and temporal variability. SEBARA uses the geographical coordinates, date and time of the specific satellite as input for USGS-NASA online calculator. The calculator output is based on the site-specific interpolated atmospheric profile for the relevant date and time.

			For SEBAL, there is a need to adjust the multiplier according to the landcover and location., It is difficult to define a multiplier for a mixed ecosystem in the rainfed environment.
Incoming shortwave radiation	**$R_s\downarrow$**	The same approach, however, different sources for τ_{sw}.	
VIs	NDVI	The same approach but for Landsat 8 reflectance calculation are different.	
	SAVI	L= 0.1	Due to different soil conditions and vegetation cover at the study site, a range of L values plotted against the corresponding maximum and standard deviation of SAVI values. The L value where the decline in the trend line starts, the corresponding L value was used.
	LAI	The same approach, however, SAVI with the respective L value.	
Emissivity	$\mathcal{E}_o$ & $\mathcal{E}_{nb}$	Based on LAI. Emissivity for narrowband ($\mathcal{E}_{nb}$) and broadband ($\mathcal{E}_o$) calculated separately.	Computes $\mathcal{E}_o$ using NDVI. Conditions set for water and bare soil following Gieske and Timmerman, 2002
Atmospheric correction		The same approach followed, however, for Landsat 8 it is not required.	
Land surface temperature	**T_s**	$T_{s.}$ computed with $\mathcal{E}_{nb}$.	The same approach followed, however, $\mathcal{E}_o$ based on NDVI was used. This emissivity may be a better representation of temperature as the difference between measured and estimate is very low.
Outgoing longwave radiation	**$R_L\uparrow$**	$\mathcal{E}_o$ based on LAI	$\mathcal{E}_o$ based on NDVI.
Incoming longwave radiation	**$R_L\downarrow$**	The same approach, however, different sources of τ_{sw} value.	
Net radiation	**R_n**	The same approach adopted, however, since albedo and emissivity have greater control over net available radiation, the τ_{sw} value from the online calculator and NDVI based emissivity used for SEBARA. The value of the corresponding pixel is comparable with the flux tower estimates**.**	
Soil heat flux	G	The same approach adopted.	
Friction velocity at the weather station	**μ***	The same approach adopted.	
Wind speed at blending height	**μ_{200}**	The same approach adopted.	
Friction velocity of each pixel	**$\mu *_{pix}$**	SEBAL suggests both the NDVI and LAI approaches, however, the LAI approach used for SEBARA due to young plantation with canopy opening, different pastures species and variable moisture availability.	

Aerodynamic resistance to heat transport	r_{ah}	0.1m for Z_1 and 2m for Z_2	SEBAL approach followed, however, Z_2 adjusted according to landcover/vegetation type. Used Momentum roughness length of respective landcover/vegetation type (plantation and pasture).
Near-surface temperature difference	**dT**	The same approach adopted. However, to compute dT for plantation and pasture, the respective coefficients used to adjust RefET required to get 'a' and 'b' coefficients. To get K_c, one-year climatic data used to compute reference ET using RefET model. The model output compared with ET recorded at the flux tower for pasture, and sapflow readings (adjusted for surface evaporation) for the plantations and respective K_c s were calculated.	
Air temperature	T_a	The same approach followed; however, the model uses dT for pasture and plantations separately.	
Sensible heat flux	**H**	The same approach followed; however, H for pasture and plantation computed using respective r_{ah} and dT.	
Latent heat flux	λET	The same approach used; however, adjusted reference ET used for plantation and pasture to compute latent heat flux (λET).	
Instantaneous Evapotranspiration	ET_{inst}	The same approach, however, two-steps for dominant landcover using adjusted λET for each landcover.	
Reference ET Fraction	ETrf	SEBAL uses reference ET.	Crop coefficients are used for dominant landcover to adjust the reference ET.
Daily ET	ET_{24}	SEBAL uses daily reference ET.	SEBARA uses daily adjusted reference daily ET.
Model environment		ERDAS imagine.	ArcGIS model builder was used to develop the models which can be used as such or exported as a Python file for further modelling.

4.1. Surface Radiation Balance (SRB)

Some of the incoming solar radiation directly penetrates through the atmosphere to the Earth's surface. In contrast, gases scatter some in the atmosphere, and these weak rays reach the Earth surface as a diffused radiation (Figure 4.1). Together direct and diffuse shortwave radiation accounts for the total incoming shortwave radiation (Ritter, 2003). On the contrary, the outgoing longwave radiation is the energy radiating from the Earth as infrared, thermal, or terrestrial radiation to space. This flux comes to the surface from different atmospheric heights where an ensemble of gases has different infrared emissivity properties. Out of these gases, some are good absorbers, e.g., CO_2 and water vapour. In contrast, the others are good emitters like greenhouse gases and aerosols, which finally determines the amount of incoming longwave radiations. Both the shortwave and longwave radiations measured in W/m^2. The surface absorbs a portion of the Rs, and a part reflected away. The reflected portion from the surface is the Albedo (α), which ranges from 0 (no reflection) to 1 (a complete reflection of light striking the surface) (Appendix 1a and b).

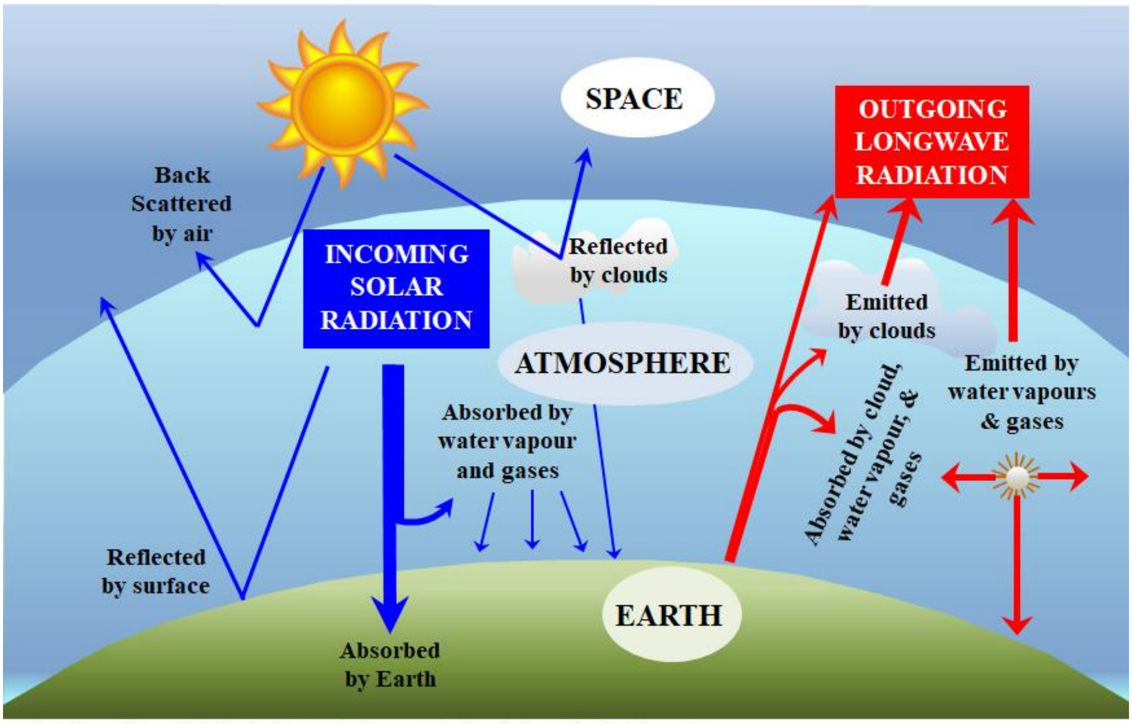

Adopted from: Ritter, M. (2003) The Physical Environment: An Introduction to Physical Geography. *https://www.earthonlinemedia.com/ebooks/tpe_3e/energy/outline.html date visited March 03, 2019.*

Figure 4.1. Pathways of incoming and outgoing solar radiation.

The first component required for estimation of ET using satellite data is to compute the net surface radiative flux (eq. 4.1.1) which is a composite of net shortwave radiation (eq. 4.1.2), and net longwave radiation (eq. 4.1.3) received at the Earth surface.

$$R_n = ((1-\alpha)_*R_s\downarrow) + R_L\downarrow - R_L\uparrow - ((1-\varepsilon_o)_*R_L\downarrow) \qquad \text{eq. 4.1.1}$$

Where:

$RS\downarrow$	Incoming shortwave radiation (W/m2)
α	Surface albedo (dimensionless)
$RL\downarrow$	Incoming longwave radiation (W/m2)
$RL\uparrow$	Outgoing longwave radiation (W/m2)
εo	Surface emissivity (dimensionless)

$$R_s\downarrow_{net} = (R_s\downarrow - R_s\uparrow) \qquad \text{eq.4.1.2}$$

Where:

$R_s\downarrow$ Incoming shortwave radiation

$R_s\uparrow$ Outgoing shortwave radiation

$$R_L\downarrow_{net} = (R_L\downarrow - R_L\uparrow) \qquad \text{eq. 4.1.3}$$

Where:

$R_L\downarrow$ Incoming longwave radiation

$R_L\uparrow$ Outgoing longwave radiation

The absorbed energy by the Earth's surface radiated as terrestrial longwave radiation ($R_L\uparrow$). The amount and wavelength of the energy emitted are primarily dependent on the temperature of the surface (Ritter, 2003). The hotter the surface, the more radiant energy of shorter wavelength it will emit. The gases of the atmosphere are relatively good absorber of longwave radiation and thus absorb the energy emitted by the surface. The absorbed radiation emitted in all directions with the downward directed portion being longwave atmospheric counter-radiation ($R_L\downarrow$). The amount of thermal radiation emitted depends on the emissivity properties of the object. In most situations, net longwave radiation is a negative value, as the Earth emits more longwave radiation than it gains from the atmosphere (Ritter, 2003; Diak *et al.*, 2000). Some of the emitted radiation is a loss from the Earth to space; however, under other circumstances, net longwave radiation can be zero or a positive number depending upon the emissivity characteristics of the surfaces (Appendix 2). The workflow for the computation of net radiation is shown in Figure 4.2.

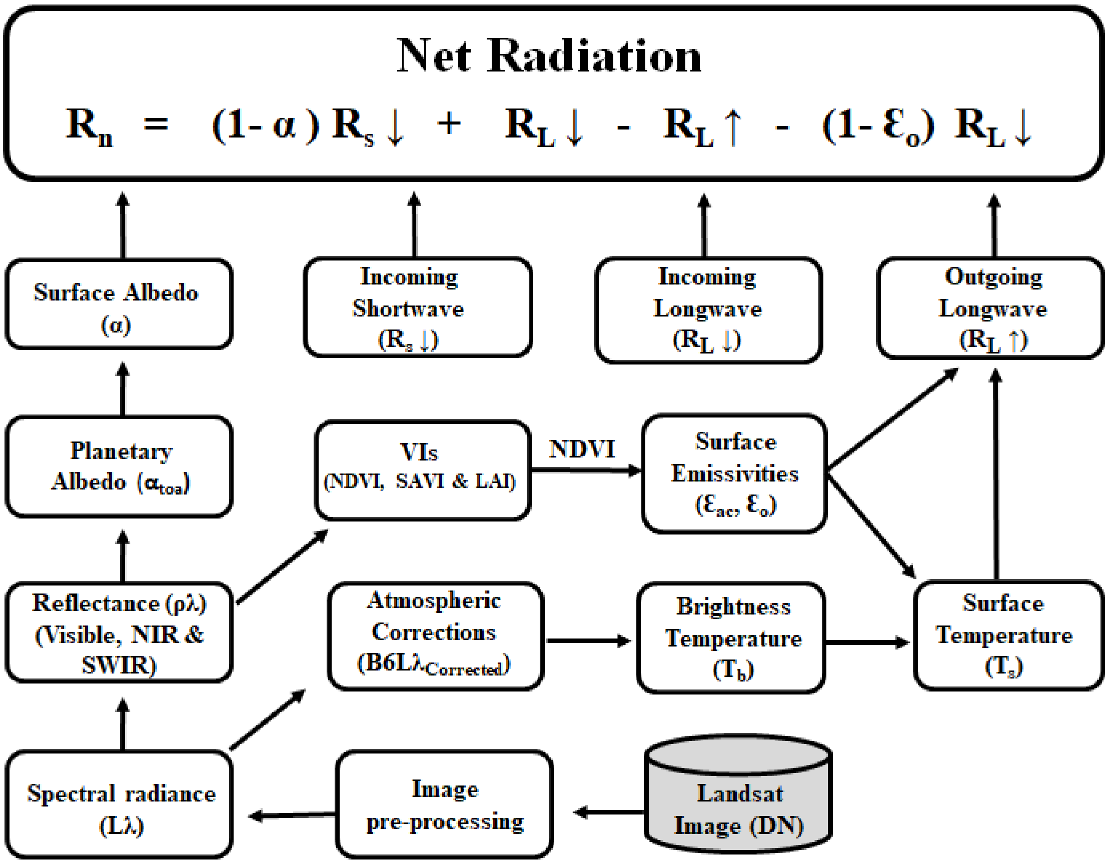

Figure 4.2. Workflow for Surface radiation budget.

4.1.1. Model Data Requirements

SEBARA requires a satellite image and weather data, preferably at a finer spatial and temporal resolution. Good knowledge of the area (topography, vegetation composition and height, and land-use) is also helpful.

4.1.1.1. Satellite Data

Among various satellites in space, Landsat is an excellent candidate to study Earth surface energy balance because it is freely available and has a medium spatial resolution, with the thermal band. The Earth images recorded as emitted or reflected radiation by the object or surrounding areas in different parts of the electromagnetic spectrum including Visible (VIS), Near-Infrared (NIR), Shortwave Infrared (SWIR) and Longwave Infrared (IR). The outgoing longwave radiation is the radiation in the wavelengths range of 3.0 and 100 µm emitted from Earth and atmosphere to space in the form of thermal radiation. It also referred to as up-welling longwave radiation or terrestrial longwave flux.

SEBARA algorithm is suitable for Landsat 5, 7 and 8 images and uses the Visible, NIR and Thermal bands. The wavelength and spatial resolution of various bands of Landsat missions are included in table 4.1. The Sentinel 2 mission lacks the thermal band, and despite it's a high temporal and spatial resolution, it is not a right candidate for surface energy balance algorithm. However, Sentinel 3 will be suitable for energy balance algorithms provided if the thermal bands and calibration constants are available. The pixel size for the thermal bands of Landsat varies (120m for TM, 60 for ETM+ and 100m for Landsat 8-OLI_TIRS) however, all are rescaled to 30m. Despite the excellent data quality of Landsat ETM+, serious hardware failure was responsible for scan lines on either side of the image after May 31, 2003. The Landsat dataset from March 1984 to date provides an ample opportunity to study the evaporative loss from different land covers using this algorithm.

The satellite images are preferred to be cloud-free, cloud cover interferes with the solar radiation and the intensity of the thermal band, which is critical for the estimation of Sensible Heat Flux. The incoming and outgoing radiation through low and high cloud cover is shown in Figure 4.3. High cirrus clouds are generally visible in the image, especially in OLI_TIRS Band 9 images, but at times the low clouds are not detectable and impact the model output. It is necessary to have a look for the extreme values in the image to rule out the cloud cover. If cloud-free images are not available, it is better to mask the cloud cover area for better model output.

Table 4-2. Satellite images from the sensors suitable for SEBARA algorithm.

Bands	Wavelength (µm)	Resolution (m)
a. Landsat 5: Thematic Mapper ™		
Band 1 – Blue (VIS)	0.45-0.52	30
Band 3 – Red (VIS)	0.63-0.69	30
Band 4 – Near Infrared (NIR)	0.76-0.90	30
Band 5 – Shortwave Infrared (SWIR) 1	1.55-1.75	30
Band 6 – Thermal	10.40-12.50	120* (30)
Band 7 – Shortwave Infrared (SWIR) 2	2.08-2.35	30
b. Landsat 7: Enhanced Thematic Mapper Plus (ETM+)		
Band 1 – Blue (VIS)	0.45-0.52	30
Band 2 – Green (VIS)	0.52-0.60	30
Band 3 – Red (VIS)	0.63-0.69	30
Band 4 – Near Infrared (NIR)	0.77-0.90	30
Band 5 – Shortwave Infrared (SWIR) 1	1.55-1.75	30
Band 6 – Thermal	10.40-12.50	60 * (30)
Band 7 – Shortwave Infrared (SWIR) 2	2.09-2.35	30
Band 8 – Panchromatic	0.52-0.90	15
c. Landsat 8: Operational Land Imager (OLI)and Thermal Infrared Sensor (TIRS)		
Band 1 – Ultra Blue (coastal/aerosol)	0.435 – 0.451	30
Band 2 – Blue (VIS)	0.452 – 0.512	30
Band 3 – Green (VIS)	0.533 – 0.590	30
Band 4 – Red (VIS)	0.636 – 0.673	30
Band 5 – Near Infrared (NIR)	0.851 – 0.879	30
Band 6 – Shortwave Infrared (SWIR) 1	1.566 – 1.651	30
Band 7 – Shortwave Infrared (SWIR) 2	2.107 – 2.294	30
Band 8 – Panchromatic	0.503 – 0.676	15
Band 9 – Cirrus	1.363 – 1.384	30
Band 10 – Thermal Infrared (TIRS) 1	10.60 – 11.19	100 * (30)
Band 11 – Thermal Infrared (TIRS) 2	11.50 – 12.51	100 * (30)

* Thermal band rescaled to 30m

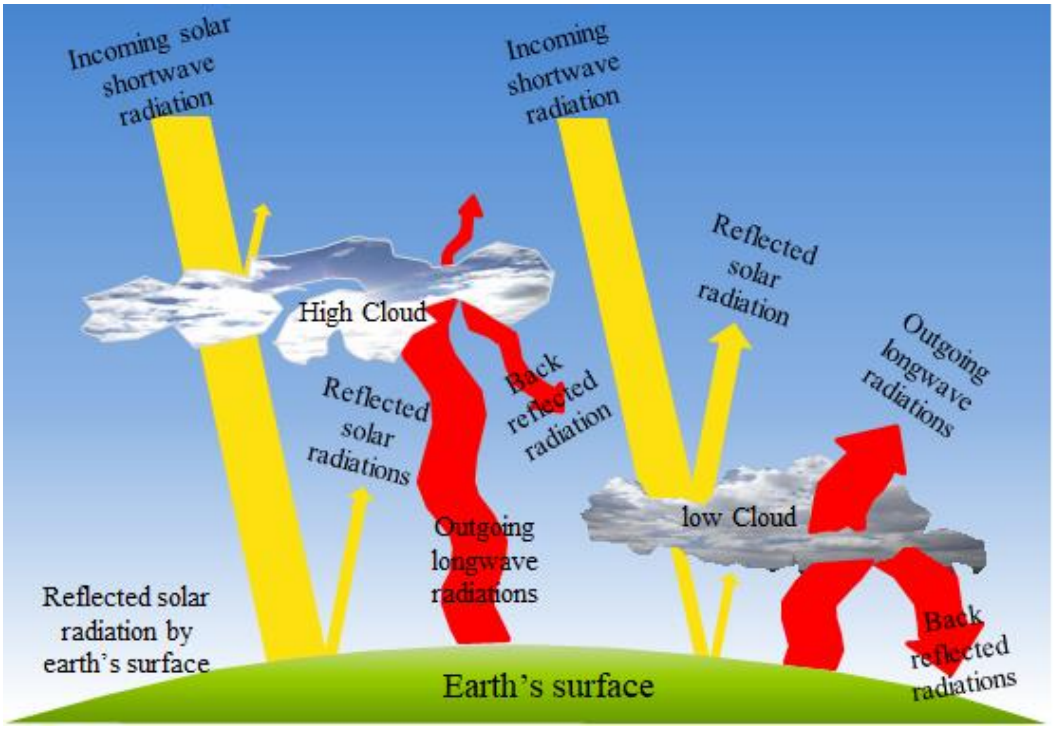

Figure 4.3. Impact of low and high cloud cover on incoming shortwave and outgoing longwave radiations. (*Adopted from NASA catalogue of images and animations*).

The Landsat 5 TM image of summer (3.10.2011 @ 11:03:59am) was used for model development for Mirranatwa site at the start of the project. However, for SEBARA testing at Mirranatwa and Gatum sites, Landsat 8 image of June 26, 2016, acquired at 10:15:03 am was used because of the following reasons:

- Landsat 5 decommissioned, and there were delays in the launch and calibration of LC8.
- Further, there were delays in approval of the flux tower at Gatum plantation catchment.
- The only available image with minimum cloud was available for 26.06.2016.

Each satellite image has an associated metadata file containing all the related information saved as a text document. Out of this information, the following parameters required for SEBARA:

- *Image acquisition date and time:* The image pass date converted into Julian Day of the Year and time in GTM converted into local time considering daylight saving, if applicable.

- Sun elevation angle (β), Earth-Sun Distance (d_{es}) and Sun Azimuth.

- *Gain and Bias* values for each band. In the raw image, the values given as digital numbers which need to be converted into radiance and reflectance using gain and bias values.

4.1.1.2. Climatic Data

Climatic data collected at the nearest weather station is preferred. From this data, the following variables are required:

- *Wind speed* (m/s) at the time of image acquisition to compute sensible heat flux

- *Precipitation* for 7-10 days before the image acquisition date to assess the wetness of the area and interpret the model output.

- *Land surface temperature* (°C) to compare the surface temperature raster layer, which in turn used for computing soil heat flux.

- *To compute Reference ET (RefET).* To calculate the reference ET of a well-watered alfalfa crop using RefET model, (Allen, 2011), the following variables are required:

  - Precipitation,
  - Wind speed,
  - Relative humidity,

- Air temperature (minimum and maximum temperature),
- Net radiation,
- Ambient water vapour partial pressure,
- Ambient specific humidity on a mass basis,
- Ambient dew point temperature.

It is recommended that the data for at least ten days before the image pass day, at hourly or 30 minutes interval, should be used for model output validation. However, if the ET estimation for a targeted length of time is planned, the climatic data for that specific period should be considered for the RefET model. The RefET model input data structure is included in section 4.2.2.2.

4.1.1.3. Weather Station Information

- Coordinates
- Elevation of the weather station
- Instrument height (m)
- Grass height (m) maintained at the weather station.

4.1.1.4. Site Information

To account for the variability; detailed topographic information about the study site is required along with the data on vegetation types and vegetation height; water bodies like farm dams, creeks, standing water; infrastructure, etc. If the primary interest is obtaining ET from agricultural fields, the weather data should be obtained from a weather station located nearby in a similar agrarian area. If the study area encompasses widely varying terrain or land-use, data should be obtained from two or more nearby weather stations representing the terrain and landuses under investigation. A land-use map is not essential; however, it is useful in estimating the surface roughness parameter. The land surfaces have different ground cover and canopy properties which can influence ET due to varied aerodynamic resistance, the bulk leaf boundary layer within the canopy, roughness and sub-layer-resistance (Miller, 1981; Schuepp, 1993, Allen *et al.*, 1998a; Fisch *et al.*, 2004). The knowledge of landuse can help to interpret the model output and use the appropriate crop coefficients (K_c).

4.1.2. Data Acquisition

4.1.2.1. Satellite Data Download

Landsat satellite data is freely downloadable from USGS websites like Earth Explorer (*https://earthexplorer.usgs.gov/*), USGS LandsatLook (*https://landsatlook.usgs.gov/viewer.html*) and GloVis (*https://glovis.usgs.gov/*). An account needs to be created, and login required for data download. For the model development and comparison of the model output with field measurements, Landsat 5 TM image, acquired on October 3 2011, @ 11:03:59am was used. However, for SEBARA testing at Mirranatwa and Gatum sites, Landsat 8 image of June 26, 2016, acquired at 10:15:03 am was used. The highlighted information in the respective header files (Appendix 3a for Landsat 5 TM and Appendix 3b for Landsat 8 OLI) is required for image processing.

4.1.2.2. Digital Elevation Model (DEM)

Shuttle Radar Topography Mission (SRTM) Digital Elevation Model (DEM) with a 30m resolution can assist the interpretation of the SEBARA model output, especially in the topographically variable terrain. For Mirranatwa study site GPS data was used to develop a DEM, however, for model validation for Gatum site, freely available SRTM DEM was downloaded from Earth Explorer website under the Digital Elevation data category.

4.1.2.3. Meteorological Data

For both the study sites, the weather data was acquired from the Department of Primary Industries (DEPI). Further, SILO data for Mirranatwa and Gatum was also collected from the Bureau of Meteorology. Flux Tower data from

Monash University, Melbourne, Victoria and sapflow meter adjusted ET data (Dean, 2013) were also acquired.

4.1.3. Model Development for Surface Radiative Flux

Following the principals of SEBAL, a modified approach, Surface Energy Balance for Rainfed Agriculture (SEBARA), is developed. The details of the algorithms used are given in the following sections:

4.1.3.1. A Subset for the Area of Interest

Using the full scene of the satellite for analysis is not recommended unless the entire image covers the area of interest. There are several reasons for taking a subset, including the study site: ***i.*** it takes a long time to process the entire image, ***ii.*** sometimes parts of the image have a cloud cover that interacts with the analysis and ***iii.*** high topographic variability in the area covered in the entire scene can impact the computation of aerodynamic resistance and turbulent fluxes. On the contrary, if two scenes cover the target area, it is required to make a mosaic first, and then the subset should be clipped for the study site.

After the analysis, using a vector layer of the study site/catchments, images of various components of the radiation budget were clipped and used for the final assessment and comparison.

All the spatial analysis was done in ArcGIS using the model builder. The various equations were used in the raster calculator in the model builder to automate the process. Few parameters computed in Excel sheet.

Raster clip tool used to develop Model 001 (Appendix 4) for the subset of all the bands of the Landsat raw image (digital number). The model inputs were raster layers of the Visible, NIR, SWIR and Thermal bands (details given in table 4.2) and a shapefile of the study area.

4.1.3.2. Radiance (Lλ)

The data presented in the Landsat image is in digital numbers (DN) which need to be converted first in spectral radiance using L_{max} and L_{min} values (Table 4.2 for Landsat 5 TM and Table 4.3 and 4.4 for Landsat 7 ETM+) whereas for Landsat 8, the rescaling factors are given in metadata file. The DN of Landsat 5 TM and Landsat 8 OLI were converted into radiance values using a general relationship, equation 4.1.4 and 4.1.5 for Landsat 5 TM and equation 4.1.6 for Landsat 8 OLI (Chander *et al.*, 2003, 2007 & 2009; USGS, 2019a, 2019b & 2019c) and the respective coefficients. Values of calibration constants (L_{min} and L_{max}) given in Table 4.3 - 4.5 used for Landsat 5 or 7. Multiplicative and additive rescaling factors for Landsat 8 OLI included in the metadata are used (Appendix 3b: highlighted values of RADIANCE_MULT_BAND_x and RADIANCE_ADD_BAND_x where x is the band number). For Landsat 8 OLI, only the DN of thermal bands were converted into radiance, whereas for Landsat 5 TM for all the band's radiance was calculated.

$$\mathbf{L_{\lambda} = \text{“gain”} * QCAL + \text{“bias”}} \qquad \text{eq. 4.1.4}$$

which can be expressed as:

$$\mathbf{L_{\lambda} = \left[\frac{L_{max} - L_{min}}{255}\right] * DN + L_{min}} \qquad \text{eq. 4.1.5}$$

Where

L_{λ}	Spectral radiance (Watts/ (m^2 * srad * μm))
L_{max}	Maximum L value for the respective band
L_{min}	Minimum value for the respective band
DN	Digital numbers

$$L_\lambda = M_L * Q_{cal} + A_L$$ eq. 4.1.6

Where

L_λ Spectral radiance (Watts/ (m^2 * srad * µm))

M_L Band-specific multiplicative rescaling factor from the metadata (RADIANCE_MULT_BAND_x, where x is the band number)

A_L Band-specific additive rescaling factor from the metadata (RADIANCE_ADD_BAND_x, where x is the band number)

Q_{cal} Quantized and calibrated standard product pixel values (DN)

Model 002 and Model 003 were used to compute the radiance of Landsat 5 TM and Landsat 8 OLI bands (Appendix 5 and 6) respectively. The model input parameters are raw digital images and rescaling coefficients for the respective bands.

*Table 4-3. Landsat 5 TM Data L_{min} and L_{max} (Watts/ (m^2 * srad * µm)).*

Processing date: From April 2, 2007			
Band	Band wavelength (µm)	L_{min}	L_{max}
B1	Blue (0.45 – 0.52)	-1.52	193.0
B2	Green (0.52 – 0.60)	-2.84	365.0
B3	Red (0.63 – 0.69)	-1.17	264.0
B4	Near-Infrared (0.76 – 0.90)	-1.51	221.0
B5	Near-Infrared (1.55 – 1.75)	-0.37	30.2
B6	Thermal (10.40 – 12.50)	1.2378	15.303
B7	Mid-Infrared (2.08 – 2.35)	-0.15	16.5

Source: https://landsat.usgs.gov/sites/default/files/documents/L5TM_postcal.pdf

*Table 4-4. Landsat 7 ETM+ Lmin and L_{max} Range (Watts/ (m^2 * srad * µm)).*

Processed Before July 1, 2000					
Bands	Band wavelength (µm)	Low Gain		High Gain	
		L_{min}	L_{max}	L_{min}	L_{max}
B1	Blue (0.45 – 0.52)	6.2	297.5	6.2	194.3
B2	Green (0.52 – 0.60)	6.0	303.4	6.0	202.4
B3	Red (0.63 – 0.69)	4.5	235.5	4.5	158.6
B4	Near-Infrared (0.77 – 0.90)	4.5	235.0	4.5	157.5
B5	Near-Infrared (1.55 – 1.75)	1.0	47.70	1.0	31.76
B6	Thermal (10.40 – 12.50)	0.0	17.04	3.2	12.65
B7	Mid-Infrared (2.08 – 2.35)	0.35	16.60	0.35	10.932
B8	Panchromatic (PAN)	5.0	244.00	5.0	158.40

Source: https://landsat.usgs.gov/landsat-7-data-users-handbook-section-5

*Table 4-5. Landsat 7 ETM+ Lmin and L_{max} Range (Watts/ (m^2 * srad * μm)).*

Processed After July 1, 2000					
		Low Gain		High Gain	
Bands	Band wavelength (μm)	L_{min}	L_{max}	L_{min}	L_{max}
B1	Blue (0.45 – 0.52)	6.2	293.7	6.2	191.6
B2	Green (0.52 – 0.60)	6.4	300.9	6.4	169.5
B3	Red (0.63 – 0.69)	5.0	234.4	5.0	152.9
B4	Near-Infrared (0.77 – 0.90)	5.1	241.1	5.1	157.4
B5	Near-Infrared (1.55 – 1.75)	1.0	47.57	1.0	31.06
B6	Thermal (10.40 – 12.50)	0.0	17.04	3.2	12.65
B7	Mid-Infrared (2.08 – 2.35)	0.35	16.54	0.35	10.80
B8	Panchromatic (PAN)	4.7	243.1	4.7	158.3

Source: https://landsat.usgs.gov/landsat-7-data-users-handbook-section-5

4.1.3.3. Reflectance (ρλ)

The reflectance is the ratio of incoming radiation to the outgoing radiation. Equations 4.1.7 to 4.1.9 used to compute the reflectance of each band, for Landsat 5 TM and equation 4.1.10 and 4.1.11 for Landsat 8 OLI (Chander *et al.*, 2003, 2007 & 2009; USGS, 2019a, 2019b & 2019c).

$$\rho\lambda = (\pi * L_\lambda * d^2) / (ESUN_\lambda * Cos\theta_s) \qquad \text{eq. 4.1.7}$$

Where

$\rho\lambda$	Reflectance
π	Pi = 3.14
L_λ	Spectral radiance (Watts/ (m^2 * srad * μm)) of each band
$ESUN_\lambda$	Mean solar exo-atmospheric irradiance for each band of respective Landsat missions (table 4.6 & 4.7)
θ_s	Solar zenith angle in degrees (eq. 4.1.8)
d	Earth-sun distance in astronomical units (eq. 4.1.9)

Table 4-6. ESUN Values of Landsat 5 TM and 7 EMT+ bands (W/m^2).

Bands	Blue	Green	Red	NIR	SWIR1	SWIR2	Σ_{ESUN}
Landsat 5	1958	1827	1551	1036	215	80.65	6667.67
Landsat 7	1970	1842	1545	1044	225.7	82.07	6712.77

A dummy value of 1 is used for Thermal band. Source: https://www.usgs.gov/land-resources/nli/landsat/using-usgs-landsat-level-1-data-product

Table 4-7. ESUN Values of Landsat 8 OLI bands (W/m²).

Blue	Green	Red	NIR	SWIR1	SWIR2
2004.57	1820.75	1549.49	951.76	247.55	85.46

http://bleutner.github.io/RStoolbox/r/2016/01/26/estimating-landsat-8-esun-values

$$\mathbf{Cos\theta = Cos\ (Radians\ (90 - \beta))} \qquad \text{eq. 4.1.8}$$

To compute Cosθ, the value of sun elevation angle (β) available in the header file (Appendix 3a and 3b) was used as an input in equation 4.1.8.

The last component of equation 4.1.7 is $\mathbf{d_r}$, defined as 1/de-s^2 where de-s is the relative earth-sun distance in astronomical units. equation 4.1.9 was used to computed it.

$$\mathbf{d_r = 1 + 0.033\ cos\ (DOY * 2\ \pi\ /\ 365)} \qquad \text{eq. 4.1.9}$$

Where

d_r Relative earth-sun distance
(Note: d_r values range from 0.97 to 1.03 and are dimensionless)

DOY Julian Day Number (JDN) – convert the image acquisition date into JDN (Appendix 7)

Angle (DOY * 2 π / 365) in radians

For Landsat 8 (equation 4.1.10), the digital numbers are input to compute the Top of the atmosphere (TOA) reflectance and then was corrected for the sun angle using (equation 4.1.11).

$$\mathbf{\rho\lambda' = M_\rho * Q_{cal} + A_\rho} \qquad \text{eq. 4.1.10}$$

Where

ρλ' Top of the Atmosphere (TOA) planetary reflectance (without correction of solar angle).

Note that ρλ' does not contain a correction for the sun angle

M_ρ Band-specific multiplicative rescaling factor from the metadata (REFLECTANCE_MULT_BAND_x, where x is the band number)

A_ρ Band-specific additive rescaling factor from the metadata (REFLECTANCE_ADD_BAND_x, where x is the band number)

Q_{cal} Quantized and calibrated standard product pixel values (DN)

$$\rho\lambda = \frac{\rho\lambda'}{\cos(\theta_{SZ})} \quad = \quad \rho\lambda = \frac{\rho\lambda'}{\sin(\theta_{SE})} \qquad \text{eq. 4.1.11}$$

Where

$\rho\lambda$ Corrected TOA planetary reflectance

θ_{SE} Local sun elevation angle (degrees) of the centre of the scene provided in the metadata (SUN_ELEVATION)

θ_{SZ} Local solar zenith angle; $\theta_{SZ} = 90° - \theta_{SE}$

Two models (Model 004 and Model 005) were developed to compute reflectance of Landsat 5 TM and Landsat 8 OLI products, respectively (Appendix 8 and 9). The model input parameters for Landsat 5TM are spectral radiance and mean solar exo-atmospheric irradiance for each band, the cosine of the solar incidence angle from the nadir and inverse squared relative earth-sun distance. The model inputs for Landsat 8 OLI are the band-specific multiplicative rescaling and additive rescaling factors, DN, local sun elevation angle and zenith angle in degrees.

4.1.3.4. Top of the Atmosphere (TOA) Albedo (α_{toa}) and Surface Albedo (α_{surf})

Several algorithms are developed and used for the retrieval of surface albedo from remote sensing data. Despite difficulties in albedo retrieval algorithms, the recent remote sensing algorithms are beginning to meet accuracy requirements (Stroeve *et al.*, 2002; Liang *et al.*, 2005; Bastiaanssen *et al.*, 1998a & b; 1995 & 2005; Ahmad and Lockwood, 1979). The relationship for retrieval of albedo used by Bastiaanssen (2005) was followed here.

Albedo at the top of the atmosphere was computed using reflectance of each band along with its weighting coefficient (equation 4.1.12).

$$\boldsymbol{\alpha_{toa} = \Sigma\, (\dot{\omega}_{\lambda} * \rho_{\lambda})} \qquad \text{eq. 4.1.12}$$

Where

α_{toa}	Albedo at the top of the atmosphere
$\dot{\omega}\lambda$	Weighting coefficient for each band
$\rho\lambda$	Reflectivity of each band

The weighting coefficient for each band was computed using equation 4.1.13.

$$\boldsymbol{\dot{\omega}_{\lambda} = ESUN_{\lambda} / \Sigma\, (ESUN_{\lambda})} \qquad \text{eq. 4.1.13}$$

Where

$ESUN_{\lambda}$ is the respective band's exo-atmospheric spectral irradiance value (ESUN) given in Table 4.6 for Landsat 5TM and 7 ETM+ and Table 4.7 for Landsat 8 OLI.

The equation 4.1.14. was used to compute surface albedo.

$$\boldsymbol{\alpha = (\alpha_{toa} - \alpha_{path\_radiance}) / \tau_{s\omega})} \qquad \text{eq. 4.1.14}$$

Where

α_{toa}	Albedo at the top of the atmosphere
$\alpha_{path\_radiance}$	the values range between 0.025 and 0.04, however, as recommended by Bastiaanssen (2002) and Allan *et al*., (2000) a value of 0.03 was used for this analysis.
$\tau_{s\omega}$	Shortwave transmissivity of air. Using the information of the image pass day and weather station, the atmospheric transmissivity was computed using NASA online atmospheric correction calculator (*https://atmcorr.gsfc.nasa.gov/*) (Appendix 10).

Figure 4.4 highlights the input requirement of the calculator. The output of this calculator includes band average atmospheric transmission and effective bandpass upwelling irradiance and downwelling radiance in $W/m^2.sr.\mu m$. The atmospheric transmission computed was in line with the values measured by Austin *et al.* (2013).

Two models (Model 006 and Model 007) used to compute surface albedo of Landsat 5 TM and Landsat 8 OLI products, respectively (Appendix 11 and 12). The model input parameters are reflectance of VIS, NIR and SWIR bands, respective ESUN values and alpha path radiance.

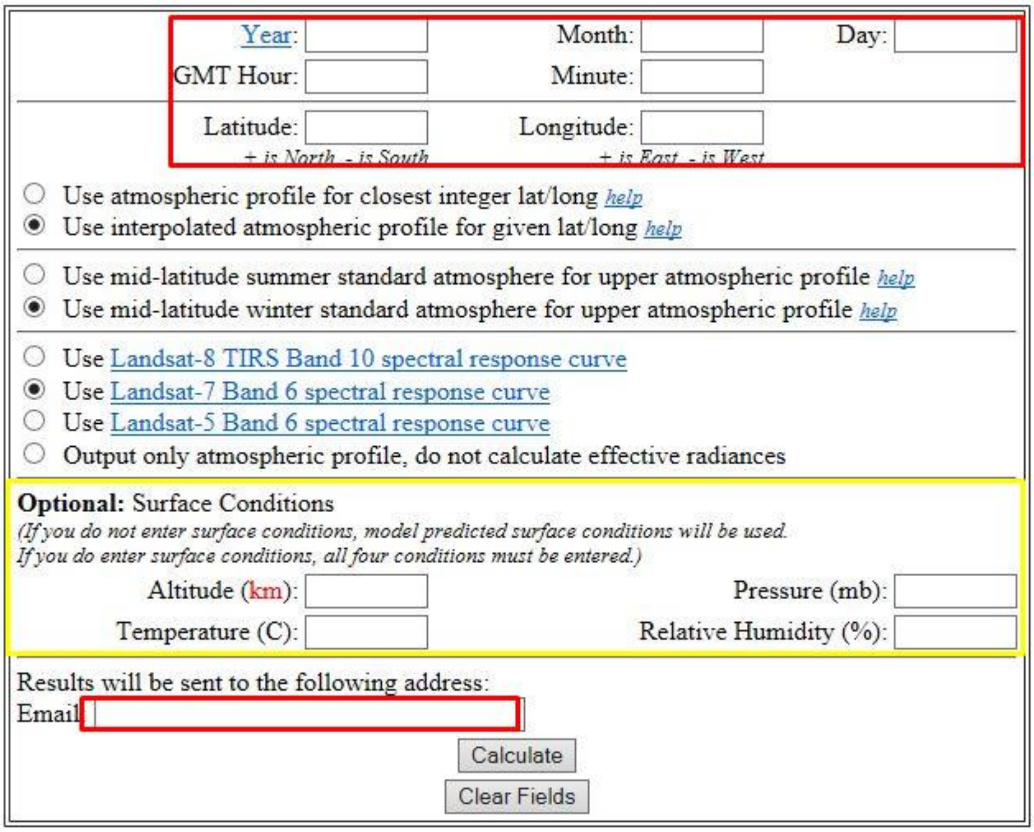

Figure 4.4. NASA online atmospheric correction calculator. Red highlighted are the minimum required parameters.

4.1.3.5. Incoming Shortwave Radiation ($R_s\downarrow$)

Generally, about 70% of the available solar radiation at the top of the atmosphere reaches the ground (Ritter, 2003, Gupta *et al.*, 1999; Kiehl and Trenberth, 1997). The gases absorb only about 20% of what is available at the outer edge of the atmosphere. The remaining about 50% of solar radiation reaches the Earth surface as $R_s\downarrow$. $R_s\downarrow$ flux (W/m^2) includes both the direct and diffuse solar radiation that reaches the Earth surface and is computed using the following relationship (eq. 4.1.15). The assumption was a clear sky at the image pass time.

$$\mathbf{R_s\downarrow = G_{sc} * \cos(\theta_{SZ}) * dr * \tau_{s\omega}} \qquad \text{eq. 4.1.15}$$

Where

$R_s\downarrow$	Incoming shortwave radiation (W/m^2)
G_{sc}	Solar Constant
$\cos(\theta)$	Cosine of the solar incidence angle
d_r	Inversed squared relative earth-sun distance
$\tau_{s\omega}$	Atmospheric transmissivity

The solar constant value (1365.4 ± 1.3 W/m^2), established in the 1990s, was predominantly used for surface energy balance calculations. However, Kopp and Lean (2010) indicated the accurate solar constant value of 1360.8 ± 0.5 for the solar minimum period in 2008 measured by NASA using the Total Irradiance Monitor (TIM). Both the values tested, and there was only 1-2 W/m^2 difference in total incoming radiation; therefore, for summer, the solar constant value of 1365 W/m^2 was used. $R_s\downarrow$ was calculated in an Excel sheet using the values of G_{sc}, $\cos(\theta)$, d_r from the header file and atmospheric transmissivity ($\tau_{s\omega}$) calculated in the previous step.

4.1.3.6. Outgoing Longwave Radiation ($R_L\uparrow$)

Earth emits energy constantly in terms of longwave terrestrial radiation ($R_L\uparrow$), like the Sun that emits shortwave radiation (Kiehl and Trenberth, 1997; Trenberth *et al.*, 2009). After emission, most of longwave radiation absorbed by H_2O, CO_2, and other greenhouse gases in the troposphere. In turn, greenhouse gases and water vapours emit longwave at different temperatures. The amount of energy emitted is primarily dependent on the temperature of the surface. The hotter the surface, the more radiant energy it will emit. The absorbed radiation emitted in all directions with the downward directed portion being longwave atmospheric counter-radiation ($R_L\downarrow$). On an annual average basis, the energy of the longwave radiation that escapes from the top of the atmosphere equals the energy of the shortwave radiation received from Sun; any significant deviation from the balance may result in global climate change (Kiehl and Trenberth, 1997).

The difference between incoming and outgoing longwave radiation is net longwave radiation ($R_L\downarrow_{net}$) expressed in equation 4.1.3. Knowing that heat is transferred from warmer to cooler bodies, this means the surface usually is hotter than the air above. The outgoing thermal radiation reflux emitted from the surface of the Earth depends upon the emissivity properties of the earth surface. The vegetation indices were computed, which are required to calculate surface emissivity and temperature (Allen *et al.*, 2002a & 2011; Bastiaanssen *et al.*, 2005).

4.1.3.7. Vegetation Indices

Vegetation index (Normalized Difference Vegetation Index - NDVI or Leaf Area Index-LAI) was used to compute the surface emissivity. To compute LAI index, Soil Adjusted Vegetation Index (SAVI) is required to account for the soil cover. Equations 4.1.16 to 4.1.18 were used to computed these indices as follows:

- ***Normalized Vegetation Index (NDVI)*** is a numerical indicator that uses the visible and near-infrared bands to assess the greenness or health of vegetation (equation 4.1.16).

$$\mathbf{NDVI} = \frac{(\rho\lambda_{NIR} - \rho\lambda_{Red})}{(\rho\lambda_{NIR} + \rho\lambda_{Red})} \qquad \text{eq. 4.1.16}$$

Where

$\rho\lambda_{NIR}$ Reflectance of the near-infrared band

$\rho\lambda_{Red}$ Reflectance of the red band

The value of NDVI ranges between -1 and +1. Generally, green surfaces have NDVI values between 0 and 1, whereas clouds and water are usually less than zero. Model 008 was used to compute this index with the input of the reflectance images of Red and NIR bands (Appendix 13).

- ***Soil Adjusted Vegetation Index (SAVI)*** is like NDVI, but it normalizes the variations in the soils and does not influence measurements of the vegetation canopy (Huete, 1988). It uses a constant value (L) such that if L = 0, it becomes NDVI. Generally, in the literature value of 0.5 is used for L; however, based on the different values tested for the project site, 0.3 or 0.2 are suitable depending upon the weather and season. SAVI was computed following equation 4.1.17.

$$\mathbf{SAVI} = \frac{(1 + L) * (\rho\lambda_{NIR} - \rho\lambda_{Red})}{(L + \rho\lambda_{NIR} + \rho\lambda_{Red})} \qquad \text{eq. 4.1.17}$$

Where

$P\lambda_{NIR}$ Reflectance of the near-infrared band

$\rho\lambda_{Red}$ Reflectance of the red band

L Constant for SAVI

Model 009 (Appendix 14) was used to compute SAVI with the reflectance images of red and near infra-red bands, and the value range of 0.2 to 0.5 for L was used. The image with an L value where SAVI values were high, and the standard deviation started to decline was used. The best L value for the October image was 0.2.

- ***Leaf Area Index (LAI)*** characterizes the plant canopies, which is defined as the one-sided green leaf area per unit ground surface area and indicates the plant biomass and canopy resistance (equation 4.1.18).

$$LAI = -\frac{\ln\left(\frac{0.7 - SAVI}{0.59}\right)}{0.91} \qquad \text{eq. 4.1.18}$$

The vegetation indices have differential relationship depending upon the climatic variables and vegetation cover (Carlson and Ripley, 1997). Bastiaanssen *et al.* (2005) reported that the maximum value of LAI is 6.0, which corresponds to maximum SAVI of 0.687. Beyond this value, the SAVI value saturates with increasing LAI and does not change significantly; however, it varies depending upon the location, landuse and season (Baret and Guyot, 1991). Model 010 was used to compute LAI (Appendix 15) with an input of SAVI raster file.

4.1.3.8. Emissivity

Emissivity is a ratio of the energy radiated from a material's surface to that emitted from a blackbody (a perfect emitter) at the same temperature and wavelength and under the same viewing conditions. It is a dimensionless number between 0 (for an ideal reflector) and 1 (for a perfect emitter). All objects at temperatures above absolute zero emit thermal radiation. However, for any particular wavelength and temperature, the amount of thermal radiation emitted depends on the emissivity of the object's surface (Nemani *et* *al.*, 1993). The emissivity of a surface depends not only on the material but also on the nature of the surface.

Knowledge of surface emissivity is essential both for accurate non-contact temperature measurement and for heat transfer calculations. Unfortunately, because the emissivity of a material surface depends on many chemical and physical properties, it is often difficult to estimate. Since emissivity is essential for modelling the Earth's surface energy balance, it can be computed using either NDVI or LAI. The research shows a strong correlation between emissivity and vegetation indices especially NDVI (French *et al.*, 2005; French and Inamdar, 2010; Bastiaanssen *et al.*, 2005; Allen *et al.*, 1998b; Van de Griend and Owe, 1993). Allen *et al.* (2002a) and Bastiaanssen *et al.* (2005) suggested the relationship between LAI and emissivity for both narrowband (ε_{NB}) and broadband (ε_0). The surface behaviour for thermal emission in a relatively narrow band (10.4 to 12.5 μm) is represented by ε_{NB} whereas in the broad thermal spectrum (6 to 14 μm) is represented by ε_0 (equation 4.1.19 and 4.1.20).

$$\boldsymbol{\varepsilon_{NB} = 0.97 + 0.0033 * LAI \quad \text{for } LAI < 3} \qquad \text{eq. 4.1.19}$$

$$\boldsymbol{\varepsilon_{0} = 0.95 + 0.01 * LAI \quad \text{for } LAI < 3} \qquad \text{eq. 4.1.20}$$

ε_{NB} and $\varepsilon_0 = 0.98$ if the $LAI \geq 3$

Similarly, for NDVI the following conditions were proposed for water and snow by (Bastiaanssen *et al.*, 2005):

For water NDVI < 0 and $\alpha < 0.47$ $\quad$ $\varepsilon_{NB} = 0.99$ and $\varepsilon_0 = 0.985$

For snow NDVI < 0 and $\alpha \geq 0.47$ $\quad$ $\varepsilon_{NB} = 0.99$ and $\varepsilon_0 = 0.985$

Based on simultaneous field measurements of surface emissivity (ε_0) and radiometer measurements for NDVI, a simple empirical correlation (equation 4.1.21) is suggested by Van de Griend and Owe (1993 and 1994).

$$\varepsilon_{0\,(x,y)} = 1.009 + 0.047 \ln NDVI_{(x,y)} \qquad \text{eq. 4.1.21}$$

Both the approaches were tested, and the results were comparable, having a difference of 0.001 (higher for NDVI approach); therefore, this relationship was used. Model 011 was used to compute surface emissivity (Appendix 16), with NDVI raster layer as an input parameter.

4.1.3.9. Land Surface Temperature (LST)

LST is an important variable to estimate the actual and potential ET, understand ecological processes and compute various indices like stress degree-days and crop water stress and crop water requirement as well as air temperature modelling (Ulivieri *et al.*, 1994; Teixeira *et al.*, 2009; Kite and Droogers, 2000; Kalma *et al.*, 2008; Anderson *et al.*, 2012; Cristóbal *et al.*, 2009; Jiménez-Muñoz *et al.*, 2008 & 2014; Bastiaanssen *et al.*, 2012 & 1998a; Diak *et al.*, 2004; Dash *et al.*, 2002; Sobrino *et al.*, 2004; Li *et al.*, 2004; Kustas *et al.*, 2003; Quattrochi and Luvall, 2004 & 2009). Over the time there have been significant improvements in the accuracy of remotely sensed LST estimation algorithms (Qin *et al.*, 2001; Cristóbal *et al.*, 2009; Coll *et al.*, 2010). Several algorithms are available to retrieve the LST like Split-Window, Dual-Angle and Single-Channel (Qin *et al.*, 2001, Jiménez-Muñoz and Sobrino, 2003).

The flow diagrams for land surface temperature estimation using Landsat 5TM and Landsat 8 OLI are shown in Figure 4.5 and Figure 4.6, respectively. First, the brightness temperature at the satellite (T_b) was computed using equation 4.1.22 (Bastiaanssen *et al.* 2005; Rajeshwari and Mani, 2014). The second step was to compute land surface temperature: for Landsat 5TM using equation 4.1.23 (Jiménez-Muñoz and Sobrino 2003; Qin *et al.*, 2001) and Landsat 8 OLI using equation 4.1.24 (de Jesus and Santana, 2017; USGS, 2019c; Meng *et al.*, 2019; Rozenstein *et al.*, 2014; Kamila *et al.* 2018).

$$\mathbf{T_b = K_2 / Ln \{(K1 / L\lambda) + 1\}} \qquad \text{eq. 4.1.22}$$

Where

T_b At-satellite brightness temperature (°K)

L_λ Spectral radiance (Watts/ (m^2 * srad * µm))

K_1 Band-specific thermal conversion constant

K_2 Band-specific thermal conversion constant

$$\mathbf{T_s = T_b / (\varepsilon_0)^{0.25}} \qquad \text{eq. 4.1.23}$$

Where

T_s Land Surface Temperature (°K)

T_b At-satellite brightness temperature (°K)

ε_0 Surface emissivity

$$\mathbf{LST = T_b / 1 + Q_{cal} * (T_b / p) * ln (\varepsilon_o)} \qquad \text{eq. 4.1.24}$$

Where

T_b At-Satellite Brightness Temperature

Q_{cal} Quantized and calibrated standard product pixel values (DN) of Thermal band B10 or B11

$p = h * c/s$

where

h Plank's constant ($6.626 * 10^{-34}$ Js)

c velocity of light ($2.998 * 10^{8}$ m/s)

s Boltzmann constant ($1.38 * 10^{-23}$ J/K)

Therefore, p = 14380

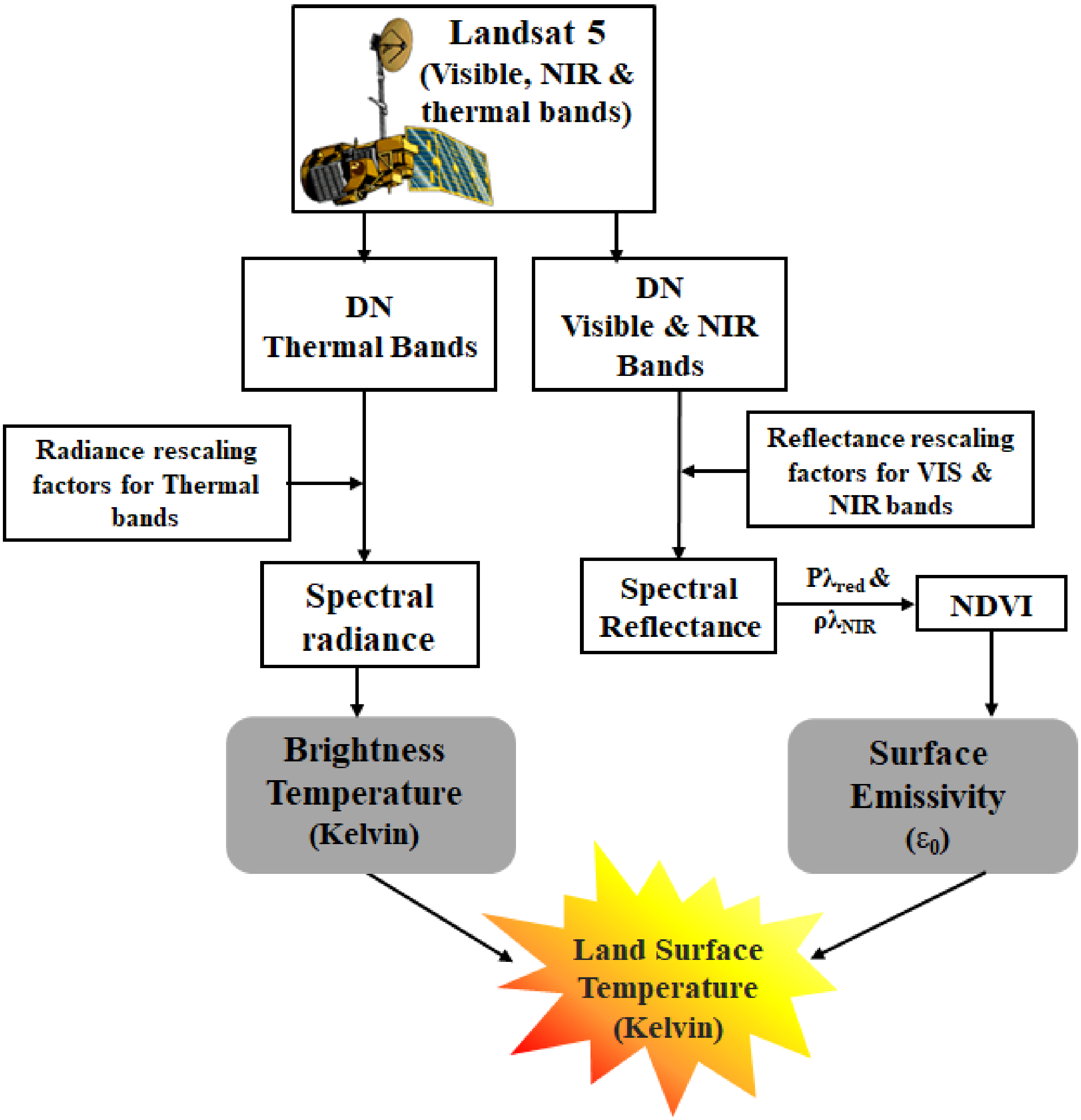

Figure 4.5. The workflow of land surface temperature retrieval using Landsat 5 TM and 7 ETM+.

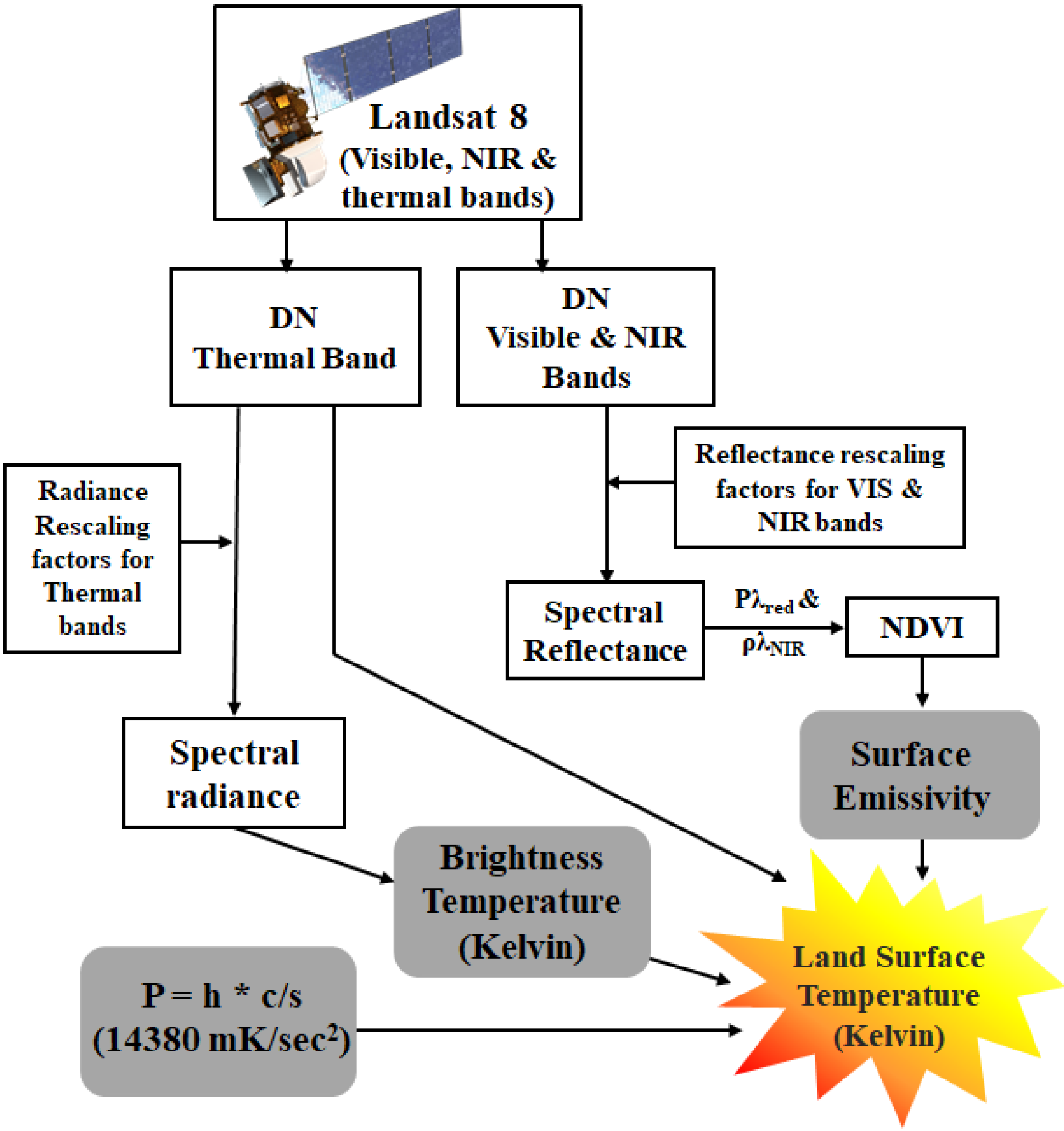

Figure 4.6. The workflow of land surface temperature retrieval using Landsat 8 OLI data.

The band-specific thermal conversion constants (K_1 and K_2) are required to compute the brightness temperature. The rescaling factors for Landsat 5 TM and Landsat 7 ETM+ are given in table 4.8 (Coll *et al.*, 2009). In contrast, the rescaling factors for Band 10 and band 11 of Landsat 8 OLI are included in the metadata file of the image of as K1_CONSTANT_BAND_x, and K2_CONSTANT_BAND_x, where x is the respective band number for band 10 or 11 (highlighted in Appendix 3b).

Table 4-8. Thermal band calibration Constants (K1 and K2).

Satellite	K_1 ($W/m^2 * Sr * m^2$)	K_2 (T °K)
Landsat 5 TM[A]	607.76	1260.56
Landsat 7 ETM+ [B]	666.09	1282.71

[A] Chander and Markham, 2003: https://landsat.usgs.gov/sites/default/files/documents/L5_TM_Cal_2003.pdf
[B] NASA Landsat 7 Science Data Users Handbook:
https://landsat.gsfc.nasa.gov/wp-content/uploads/2016/08/Landsat7_Handbook.pdf

The spectral radiance of thermal band 6 for Landsat 5TM and band 10 for Landsat 8 OLI, computed earlier, was used. Model 012 used for Landsat 5 TM (Appendix 17) and Model 013 for Landsat 8 OLI (Appendix 18). The model inputs were the radiance image of thermal bands, calibration constants (K_1 and K_2) and surface emissivity raster image. The Model 012 first computes the brightness temperature of Landsat 5 TM and then using surface emissivity, computes the surface temperature in °C and °K. For Landsat 8, the model inputs are the radiance of thermal bands (B10), surface emissivity raster image, quantized and calibrated DN of the thermal band, Boltzmann constant, plank's constant and velocity of light. To compute LST in °C and °K, first, the brightness temperature was calculated.

Once all the components required for the computation of outgoing longwave radiations are available, equation 4.1.25 was used to compute the low energy electromagnetic radiation emitted from Earth and its atmosphere out to space in the form of thermal radiation (W/m^2).

$$R_L\uparrow = \varepsilon_o * \sigma * LST^4 \qquad \text{eq. 4.1.25}$$

Where:

ε_o	Surface emissivity
σ	Stefan–Boltzmann constant (5.6704×10^{-8} W.m^2 K^4)
LST^4	Land Surface Temperature (°K)

Model 014 (Appendix 19) was used to compute the outgoing longwave radiation with the input of the images (emissivity and land surface temperature) and the value of Stefan-Boltzmann constant. Values for $R_L\uparrow$ can vary depending upon the location and time of the image.

4.1.3.10. Incoming Longwave Radiation ($R_L\downarrow$)

The clear-sky surface downward longwave radiation depends on the vertical profiles of atmospheric temperature, moisture, and presence of other gases (Ellingson, 1995; Lee and Ellingson, 2002; Miller, 1981; Ellingson *et al.*, 1989). Generally, this flux is contributed by shallow layers of the atmosphere close to the Earth surface, e.g., lower 10% of the atmosphere accounts for 32-36%. In contrast, above 500 meters from the surface, the contribution is only about 16–20% of the total $R_L\downarrow$ (Schmetz, 1989). The longwave radiation entering an ecosystem is usually augmented downward by emission from the upper leaves. Previous studies have indicated that the atmospheric temperature and moisture profiles are the essential parameters for estimation of the clear-sky surface downward longwave radiation. Under cloudy conditions, the cloud base height, cover, temperature, and emissivity are important parameters to impact the $R_L\downarrow$, it is, therefore, suggested to avoid using an image with cloud cover. There are several approaches suggested to compute $R_L\downarrow$ including profile-based (physical), hybrid, and meteorological parameter-based methods (Niemela¨*et al.*, 2001; Diak *et al.*, 2000; Ellingson, 1995; Schmetz, 1989). However, an empirical relationship between the atmospheric emissivity, Stefen Boltzmann Constant, and the near-surface air temperature (Allen *et al.*, 2011) was used to compute $R_L\downarrow$ (eq. 4.1.26).

$$\mathbf{R_L\downarrow = \varepsilon_a * \sigma * T_a^4} \qquad \text{eq. 4.1.26}$$

Where

ε_a	Atmospheric emissivity(dimensionless),
σ	Stefan-Boltzmann constant
T_a	Near-surface air temperature (°K).

The atmospheric emissivity computed by an empirical relationship suggested by Bastiaanssen (1995) as in equation 4.1.27:

$$\mathbf{\varepsilon_a = 0.85 * (-\ln\tau_{s\omega})^{0.09}} \qquad \text{eq. 4.1.27}$$

Where

$\tau_{s\omega}$ Atmospheric transmissivity

(the value of atmospheric transmissivity from the output of NASA online atmospheric correction calculator output (https://atmcorr.gsfc.nasa.gov/) was used).

As an example, the parameters of the Landsat image of 03-10-2011 were used to compute the $\boldsymbol{\tau_{s\omega}}$, upwelling and downwelling radiance using online atmospheric correction calculator following Barsi *et al.* (2003) (Figure 4.7a and 4.7b).

To calculate $R_L\downarrow$ (equation 4.1.26), the air temperature (T_a) is also required. To derive T_a, two clusters of “anchor” pixels representing “cold” and “hot” spots in the image were identified (Figure 4.8). Bastiaanssen *et al.* (2005) and Allan *et al.* (2002) suggested the size of these spots should be more than a pixel of the thermal band. For SEBARA the “cold” cluster of pixels represents a spot with a good vegetation cover with a relatively less “water-stressed” situation under rainfed conditions. For this cluster, the near-surface temperature and air temperature assumed to be similar. The "hot" cluster, on the other extreme, represented a dry spot with no or sparse vegetation and low soil moisture and assumed to have negligible or no evapotranspiration.

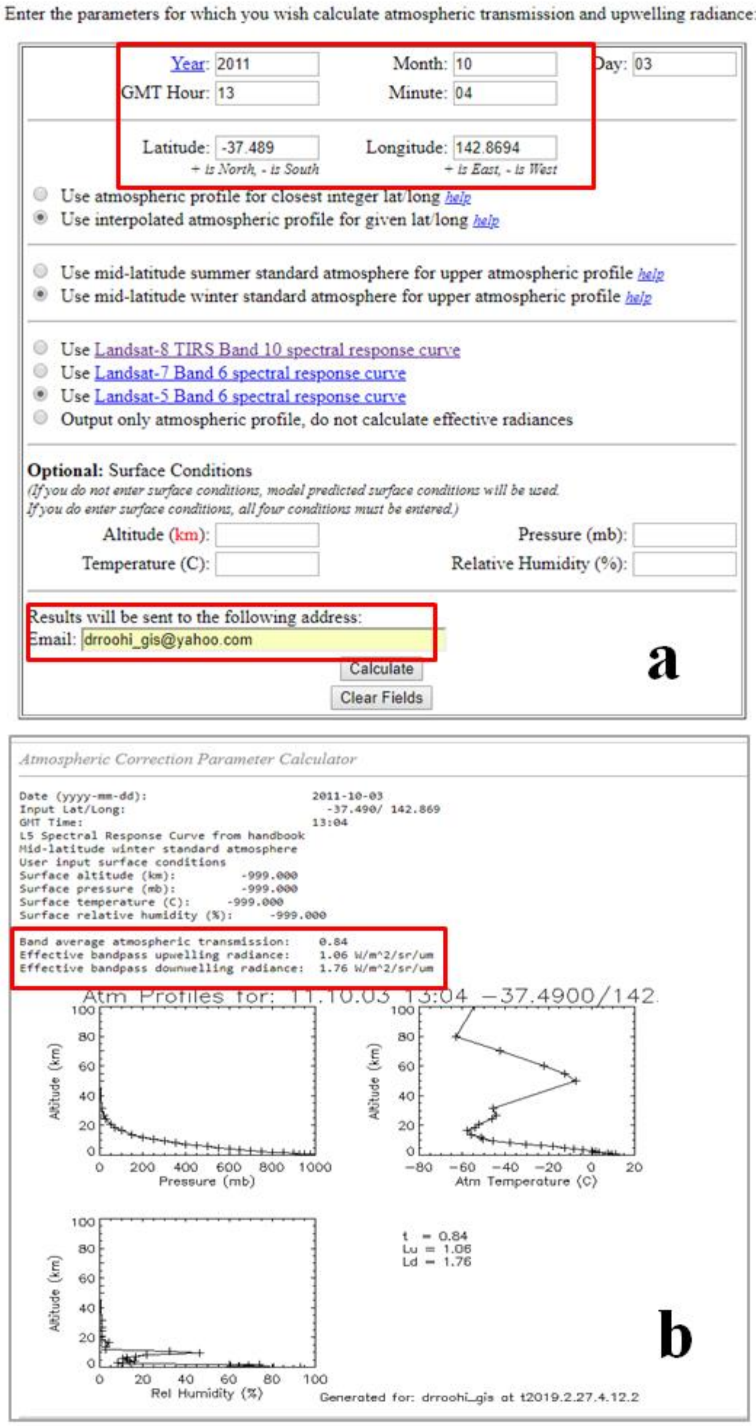

Output summary

Band average atmospheric transmission: 0.84
Effective bandpass upwelling radiance: 1.06 W/m^2.sard.µm
Effective bandpass downwelling radiance: 1.76 W/m^2.sard.µm

Figure 4.7. Atmospheric transmissivity using NASA online atmospheric calculator (*a.* input parameters and *b.* output of the model)

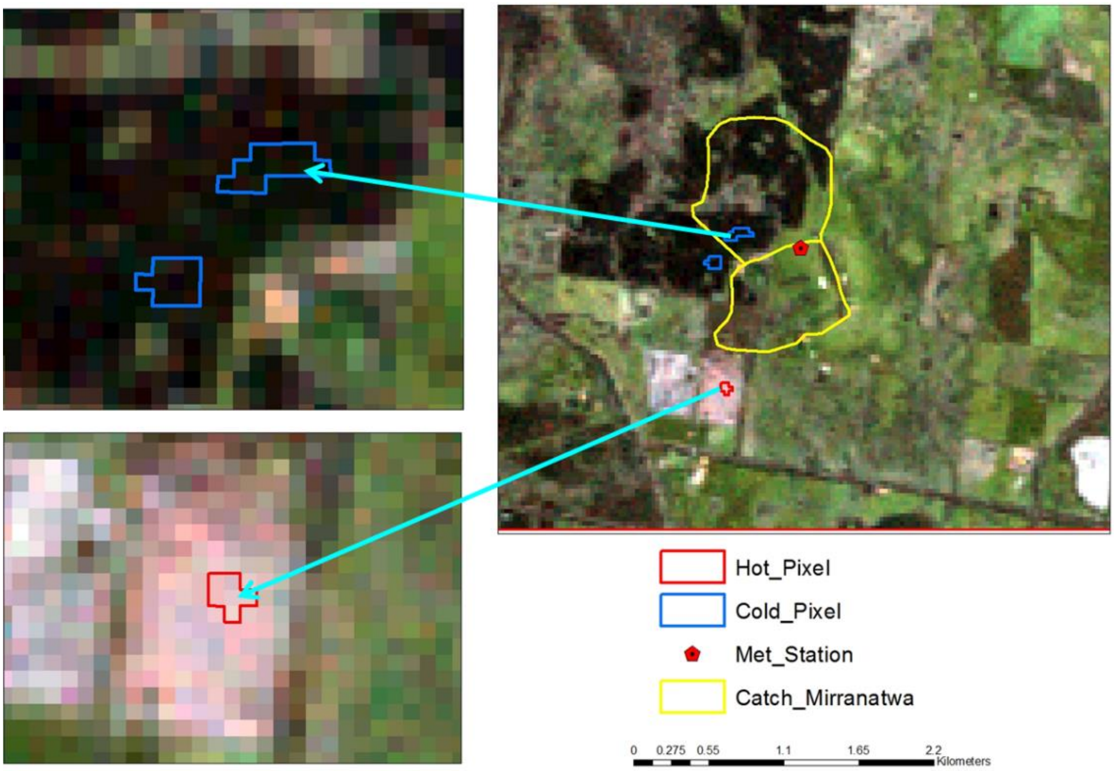

Figure 4.8. Selection of “Hot” and “Cold” pixels.

For identification of “anchor” pixels, the following images were considered:

i. A true colour image showing landuse of the study area so that the area of maximum vegetation cover and bare ground can be identified.

ii. Classified surface temperature image showing the minimum and maximum temperature values.

iii. LAI image with maximum and minimum LAI.

iv. The surface albedo: full vegetation cover represents lower values, while higher values represent “hot pixels”.

Once the average temperature of ‘cold’ pixels was retrieved, equation 4.1.26 was used to compute $R_L\downarrow$ in an Excel sheet.

4.1.3.11. Closure of Net Radiative Flux (R_n)

Net radiation is the difference between the total incoming and out outgoing radiations (eq. 4.1.1). To compute the net radiation (Model 015 - Appendix 20) the input parameters used were the raster layers of $R_L\uparrow$, surface albedo and emissivity and the total $R_s\downarrow$ and $R_L\downarrow$ on the satellite pass day and time.

4.2. Surface Energy Balance (SEB)

The Surface Energy Balance of the Earth can be defined as the partitioning of energy fluxes towards and away from the surface or the sum of all fluxes of energy passing each second through a horizontal surface of unit area (Van den Broeke *et al.,* 2011; Mareschal and Jaupart, 2011). The local SEB determines the surface temperature of the Earth (T_s) and the associated exchange of energy between the surface and the atmosphere on the one hand, and between the surface and the subsurface layers (whether it be soil, rock, water, snow, or ice) on the other. The fluxes are positive when they are directed toward the surface, i.e., when they represent an energy gain for the surface, or negative when the direction is reversed. In this section, the available net radiation (R_n) will be partitioned for three surface processes: soil heat flux, sensible heat flux and latent heat flux (eq. 4.2.1).

$$\mathbf{R_n = + G + H + \lambda ET} \qquad \text{eq. 4.2.1}$$

Where:

G	Soil Heat Flux (W/m^2)
H	Sensible Heat Flux (W/m^2)
λET	Latent Heat Flux (W/m^2)

At a sufficiently small distance above the Earth's surface, sensible heat flux and latent heat flux occur between the surface and air predominantly by molecular conduction. The sensible heat flux (H) is the rate of heat loss to the air by convection and conduction due to a temperature difference. In contrast, the latent heat flux (λET) is the heat loss from the surface due to evapotranspiration without changes in temperature (Bastiaanssen *et al.*, 2005). Higher above the surface, due to atmospheric turbulence, there is vertical mixing of heat and moisture. The turbulence is a more effective transporting mechanism than molecular diffusion (Stull, 2012), and therefore, H and λET are dominated by the turbulent exchange. Below the surface, the vertical heat flux is the Soil Heat Flux (G) due to molecular conduction of heat in the soil profile.

The available net radiation (R_n) computed is an outcome of the Surface Radiation Balance (eq. 4.1.1). By rearranging equation 4.1.1, λET is computed as a residual of net surface energy (eq. 4.2.2).

$$\boldsymbol{\lambda ET = R_n - G - H} \qquad \text{eq.4.2.2}$$

The workflow for the computation of variables of the Surface Energy Budget is presented in Figure 4.9.

In the past few decades, improvements in measurement techniques and data handling capabilities led to the development of better instruments for accurate measurements of environmental variables (Fritschen and Gay, 1979; Diak *et al.*, 2004), particularly through global atmospheric and space research programmes. In this section, the methodology used to estimate the consumers of the available energy in terms of Soil Heat Flux (G), Sensible Heat Flux to the air (H) and Latent Heat Flux (λET) are discussed, and computational details are given.

4.2.1. Soil Heat Flux (G)

Soil Heat Flux (G) is the portion of the solar energy available at the surface that is absorbed or released by the soil in a given time. The factors like soil microclimatology, hydrology, ET, surface energy system closure, thermal capacity, microbiology, chemistry, etc. determine the value of G (Yang *et al.*, 2013; Rouse, 1984; Harte *et al.*, 1995; Rosenberg *et al.*, 1983; Harper *et al.*, 1976; Payero *et al.*, 2005; Oladosu *et al.*, 2007; Cobos and Baker 2003). Vegetation growth is exposed, and thus the vegetation performance is highly dependent upon this flux.

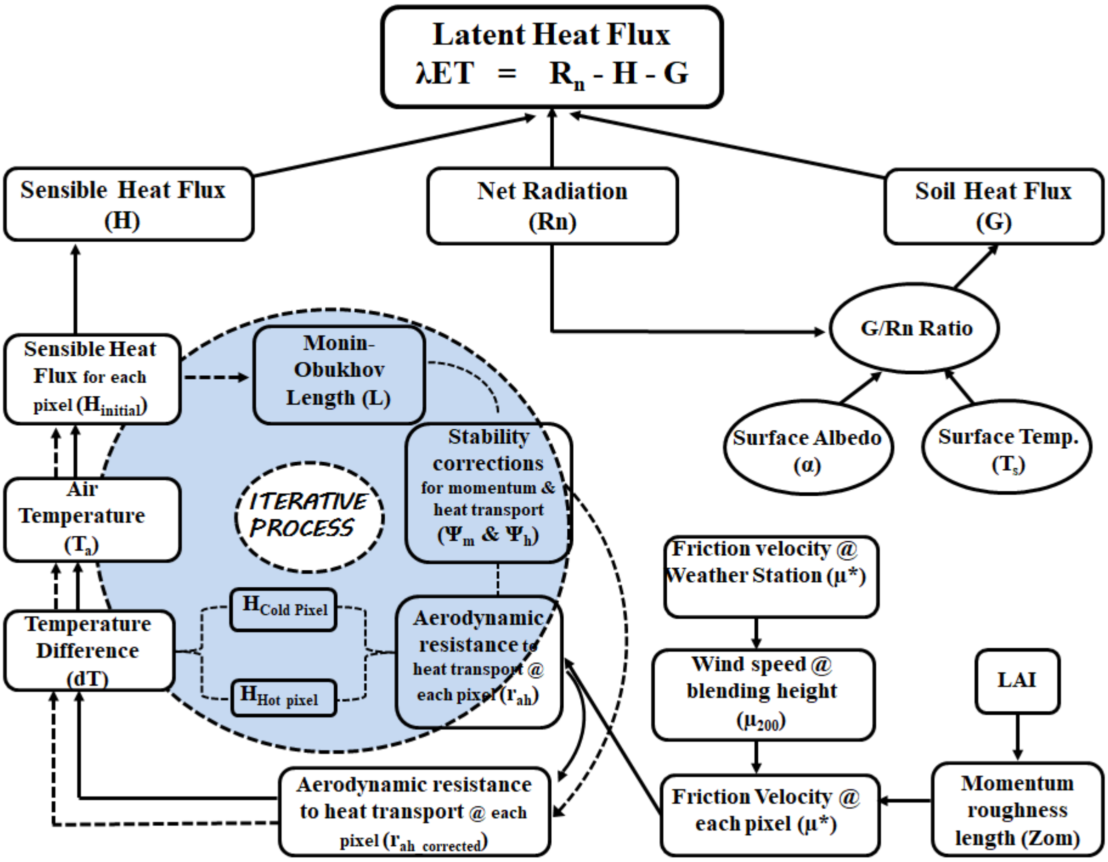

Figure 4.9. Workflow for Surface Energy Balance.

In the field, G is measured by soil heat sensors like net radiometers, pyranometers, and pyrometers as well as heat flux sensors and ultra-high accuracy soil temperature profile sensors. These instruments measure the rate of energy transfer through a surface, and the recorded data is the function of time at a location. Because soil is complex heterogeneous medium, point data cannot represent G over an extensive area. Methods have been developed to use remote sensing data for estimating soil heat flux for a range of canopy conditions applicable to local and regional surface energy balance estimations to overcome the limitations associated with the extrapolation of field measurements, (Kustas and Daughtry, 1990; Daughtry *et al.*, 1990; Su, 2002; Heusinkveld, 2004; Allen *et al.*, 2007; Bastiaanssen, 2000). The relationship between R_n and G was derived using field measurements under variable land cover conditions including bare ground, of reflectance factor with a multi-band radiometer (Kustas and Daughtry, 1990; Gausman *et al.*, 1975). Midday values of G/R_n ratio were linearly related to the NIR/R ratio and NDVI. Relative to measurement errors, the estimates of G/R_n for cotton were found to be practically insensitive to changes in the value of the vegetative indices caused by spectral data collected at the significantly different solar zenith and azimuth angles (Kustas and Daughtry, 1990; Choudhury *et al.*, 1987; Clothier *et al.*, 1986; Huete, 1987 & 1988; Huete *et al.*, 1985; Fuchs and Tanner, 1967 & 1968). Although most literature describes this ratio as a function only of the leaf area index (Kustas *et al.*, 1993 &1990, Clothier *et al.*, 1986; and Choudhury, 1987), the role of surface temperature and albedo in the physical description of heat diffusion is recognized, and an empirical equation (eq. 4.2.3) was integrated by Bastiaanssen (2000) which was used to estimate G in SEBARA.

Since different landcovers have a range of input parameters, especially in a rainfed situation, the output ratio can be quite variable.

$$\mathbf{G/Rn = (T_s{}^\circ c/\alpha) * (0.0038*\alpha + 0.0074\,\alpha^2) * (1\text{-}0.98 \times NDVI^4)} \qquad \text{eq. 4.2.3}$$

Where:

G Soil Heat Flux (W/m^2)

R_n Net Solar Radiation (W/m^2)

T_s Surface temperature in ˚C

α Surface albedo

NDVI Normalized Difference Vegetation Index

Soil heat flux computed by multiplying the G/R_n ratio by the R_n derived from the satellite image (eq. 4.2.4).

$$\mathbf{G = (G/Rn) * Rn} \qquad \text{eq. 4.2.4}$$

Where

G Soil Heat Flux (W/m^2)

R_n Net solar radiation (W/m^2)

Appendix 21 (Model 016) shows the computation of the G/N ratio and G. The input parameters are raster files of NDVI, surface albedo, and surface temperature. The typical G/R_n ratios for various land covers are calculated (Table 4.9); however, these values may vary depending upon the local conditions (Allen *et al.,* 2002a). Further, for areas having snow, low surface temperatures during winter or water bodies, the conditions need to be set for NDVI and T_s (Allen *et al.,* 2002a).

Table 4-9. Estimates of G/Rn ratio.

Surface Type	G/R_n
Deep clear water	0.5
Snow	0.5
Desert	0.2 – 0.4
Agriculture	0.05 – 0.15
Bare soil	0.2 – 0.4
Full cover alfalfa	0.04
Rock	0.2 – 0.6

Source: Bastiaanssen et al., 2005.

4.2.2. Sensible Heat Flux (H)

Sensible Heat Flux (H) describes the heat exchange between the surface and the air above it, resulting in a change in the system's/body's temperature and some macroscopic variables; however, other variables remain unchanged, e.g., volume or pressure (Partington, 1949; Adkins, 1975; Landsberg, 1978). The measurement and prediction of turbulent heat fluxes near the Earth's surface are subject to intrinsic errors. Realizing the issue, after the first International Satellite Land Surface Climatology Project, based on field experiments it was concluded that the daily uncertainty in the flux values was at least 10 to 20% or up to 20-30 W/m^2 (Brutsaert, 1982, 1993,1998 & 2013; Brutsaert and Sugita, 1996; Jimenez *et al.*, 2011; Sellers *et al.*, 1992; Hall and Sellers 1995). This high variability attributed to the inherent dynamics of the turbulent transport mechanisms and the heterogeneity of natural land surface conditions (Figure 4.10).

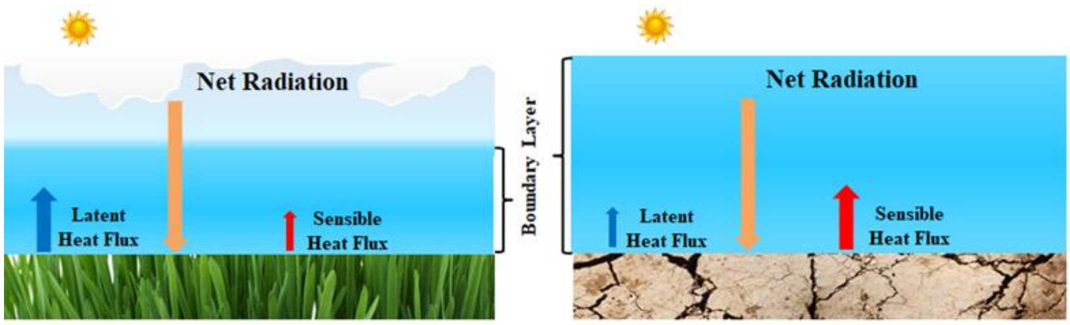

Source: Alexander, L., 2011. Climate science: Extreme heat rooted in dry soils. Nature Geoscience, 4(1), p.12.

Figure 4.10. The response of turbulent fluxes under variable conditions.

Typically, H in the surface layer can be directly measured using sonic anemometers which measures rapid (turbulent) fluctuations in temperature and vertical velocity (Schotanus *et al.*, 1983; Mahrt and Vickers, 2002; Mahart and Khelif, 2010; Mahrt *et al.*, 2012; Van den and Bange, 2007). However, these instruments are relatively vulnerable and expensive and therefore, H is often calculated based on measured profiles of wind and temperature, in combination with surface-layer similarity theory (Stull, 2012; Högström, 1988; Paulson, 1970; Castellví and Snyder, 2009).

The air stability conditions stable, unstable, or neutral (Figure 4.11), impact the aerodynamic resistance to heat transport (Allen *et al.*, 2002; Liu *et al.*, 2007; van de Griend and Owe 1994; McNaughton, 1998). The surrounding air temperature determines the response and direction of this force. The air temperature drop per 100 m elevational gain under neutral stability conditions is 0.65°C (Beljaars and Holtslag, 1991; Bastiaanssen, 2000). Generally, stable conditions occur at night; however, such response can occur in the afternoon in irrigated areas surrounded by desert.

Sensible heat flux (H) is negative when directed away from the ground surface because the surface is warm compared to the air and often referred to as convection. This negative flux cools the Earth's surface as well as the associated atmospheric boundary layer, resulting in a surface-based temperature inversion, in which the temperature increases with height. The cold near-surface air is denser than the air in the free atmosphere at the same elevation, which sets up a horizontal pressure gradient over a sloping surface, forcing katabatic or downslope winds (Renfrew, 2004; Barry, 1992; Garratt, 1992). The Sensible Heat Flux computed using following equation 4.2.5:

$$\mathbf{H = (\rho * C_p * dT) / r_{ah}} \qquad \text{eq. 4.2.5}$$

Where:

H	Sensible Heat Flux (W/m^2)
ρ	Air density (Kg/m^3)
C_p	Air specific heat (it varies with temperature). *Allen et al. (2005) suggested 1004J/Kg/K for a temperature range of 20-40 °C.*
dT	Temperature difference (T_1-T_2) between two heights (Z_1 and Z_2) for anchor pixels ('hot' and 'cold')
r_{ah}	Aerodynamic resistance to heat transport (s/m)

To compute Sensible Heat Flux (H), a gradient of temperature, surface roughness, and wind speed needs to be considered. It is difficult to calculate because of two unknown variables (r_{ah} and dT) in equation 4.2.5. To overcome the issue, two anchor points (clusters of pixels selected in the image) and the wind speed at a given height were used. Figure 4.9 shows the iterative process of computing Sensible Heat Flux.

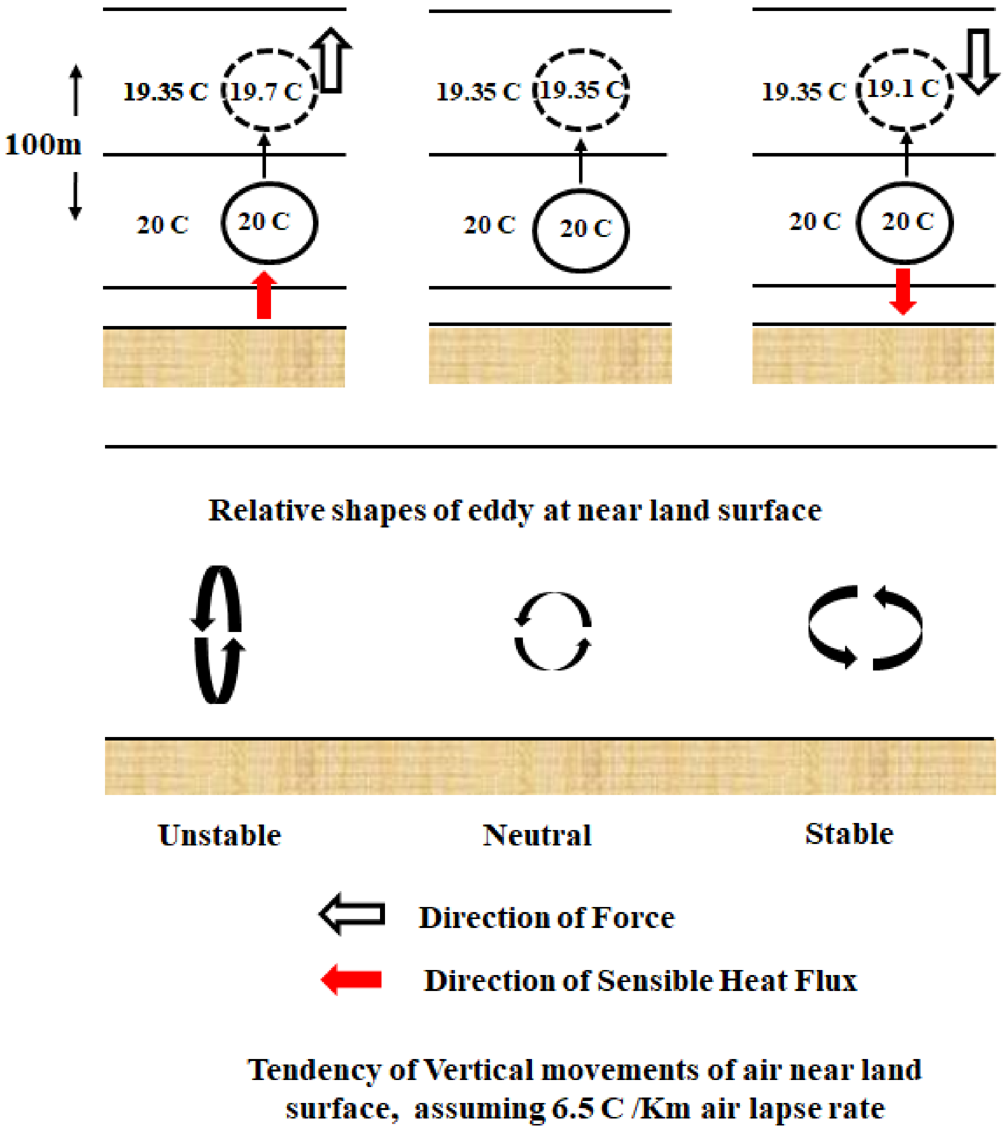

Figure 4.11. Atmospheric stability conditions
(adopted from Allen et al., 2002a).

4.2.2.1. Aerodynamic resistance to heat transport (r_{ah})

First, the r_{ah} computed for the neutral stability conditions using equation 4.2.6.

$$\mathbf{r_{ah}} = \frac{\ln\left(\frac{Z_2}{Z_1}\right)}{\mu^*_{pix} * K} \qquad \text{eq. 4.2.6}$$

Where

r_{ah} Aerodynamic resistance to heat transport

Z_1 Height just above the zero-plane displacement for the surface of the crop canopy (d ~ 0.67 * vegetation height)

Z_2 Some distance above the Z_1 but less than the surface boundary layer. *Generally, 0.1m used for Z_1 and 2.0m for Z_2*

μ^*_{pix} Friction velocity (m/s) of each pixel which quantifies the turbulent velocity fluctuations in the air. To compute the friction velocity of each pixel, first, the μ* at the weather station and blending height was computed.

k von Karman's constant

Initially, the logarithmic wind law for neutral atmospheric conditions was used to compute μ^*_{pix} in the above equation (eq. 4.2.6). It is shown that the von Karman's universal constant (0.41) is applicable only in a particular asymptotic sense and in typical atmospheric conditions, its value is probably about 10% larger than the asymptotic one (Tennekes, 1973; Tseng *et al.*, 1992; Monin and Obukhov, 1954). Pending the development of a second-order theory, the value of 0.35 ± 0.02 is recommended for micrometeorological applications over smooth terrain, however, for SEBARA, following the SEBAL approach (Allen et al., 2002), a value of 0.41 was used for von Karman's constant.

- First, the friction velocity at the weather station was computed using equation 4.2.7.

$$\mu^*_{ws} = \frac{k\ \mu_x}{\ln\left(\frac{Z_x}{Zom}\right)}$$

eq. 4.2.7

Where

μ^*_{ws}	Friction velocity (m/s) at the weather station
k	von Karman's constant = 0.41
μ_x	Wind speed (m/s) at a height Z_x
Zom	A measure of the drag and skin friction for the air layer that interacts with the surface. Used an empirical relationship between the vegetation height at the weather station (Zom_{ws} = 0.12 * h, where h is the vegetation height at the weather station).
Z_x	Height of weather station's wind instrument (anemometer)

It is computed in an excel spreadsheet using the values of the variables of above equation assuming neutral conditions.

- The second step is to compute the friction velocity at blending height, a height where it is assumed that there is no impact of surface roughness using equation 4.2.8.

$$\mu^*_{200} = \mu^*_{ws}\ \frac{\ln\left(\frac{200}{Zom}\right)}{k}$$

eq. 4.2.8

Where

μ^*_{200}	Friction velocity (m/s) at blending height (200m)
μ^*_{ws}	Friction velocity (m/s) at weather station
Zom	Momentum roughness length = (0.12 * h)
k	von Karman's constant = 0.41
200	Blending height

It is computed in an excel spreadsheet using the values of the variables of the above equation assuming neutral conditions.

- Finally, computed the friction velocity for each pixel using equation 4.2.9:

$$\mu^*_{pix} = \frac{k\,\mu^*_{200}}{\ln\left(\dfrac{200}{Zom_{pix}}\right)} \qquad \text{eq. 4.2.9}$$

Where

μ^*_{pix}	Friction velocity (m/s) at each pixel
k	von Karman's constant = 0.41
μ^*_{200}	Friction velocity (m/s) at blending height (200m)
Zom_{pix}	Momentum roughness length for each pixel

The momentum roughness length of each pixel needs to be computed by either of the following methods:

- **Leaf Area Index**: when LAI image is available, equation 4.2.10 can be used to compute Zom_{pix} (Bastiaanssen, 2000 and Allen *et al.*, 2002a):

$$Zom_{pix} = 0.018 * LAI \qquad \text{eq. 4.2.10}$$

where LAI is the Leaf Area Index, computed earlier in section 4.1.3.7.

For non-vegetative surfaces, used the Zom values given in table 4.10, and for vegetative surfaces, the values computed using LAI.

When the target area has a complex mix of landcover, the momentum roughness length computed using NDVI and surface albedo layers (Equation 4.2.11) following Bastiaanssen (2000) can be used.

$$Zom_{pix} = \exp\left[(a * NDVI/\alpha) + b\right] \qquad \text{eq. 4.2.11}$$

Where

a & b are correlation constants derived from a plot of ln(Zom) vs NDVI/α ratio for a cluster of pixels representing specific vegetation.

(Note: since it is an empirical relationship, attention must be given to the local conditions.)

The role of α is the above equation is to account for the vegetation height by modifying NDVI (Bastiaanssen *et al.*, 2005), e.g. trees have lower albedo as compared to crops or grassland.

Table 4-10. Zom values for non- agricultural landcover.

Landcover/Landuse	Zom value
Water	0.0005
Cities	0.2
Forest	0.5
Grassland	0.02
Desert with vegetation	0.1
Snow	0.005

Considering the heterogeneous landcover in the study catchments (Figure 4.12), for the current analysis, correlation constants were used (eq. 4.2.11). First, using the raster layers of the NDVI and surface albedo, a ratio was computed (Appendix 22). Later, the average ratio values for the pixels representing forest, grass/pasture, water, and infrastructure were obtained from the image. For each landcover, a characteristic vegetation height (h) is assigned, and the value of Zom is computed (Zom = 0.12 * h). The multiplier in the equation varied depending upon the type of vegetation, e.g. 0.12 for crops, 0.2 for open forest and < 0.2 for the thick forest as suggested by Allen et al. (2002a). In addition to these values, 0.05 was used for pasture. Later the natural log of the Zom values of different vegetation types was plotted against the NDVI/α ratio values. The ‘a’ and ‘b’ values from the correlation equation of this graph were used for the calculation of Zom_{pix} (eq. 4.2.11) using Model 017b (Appendix 22).

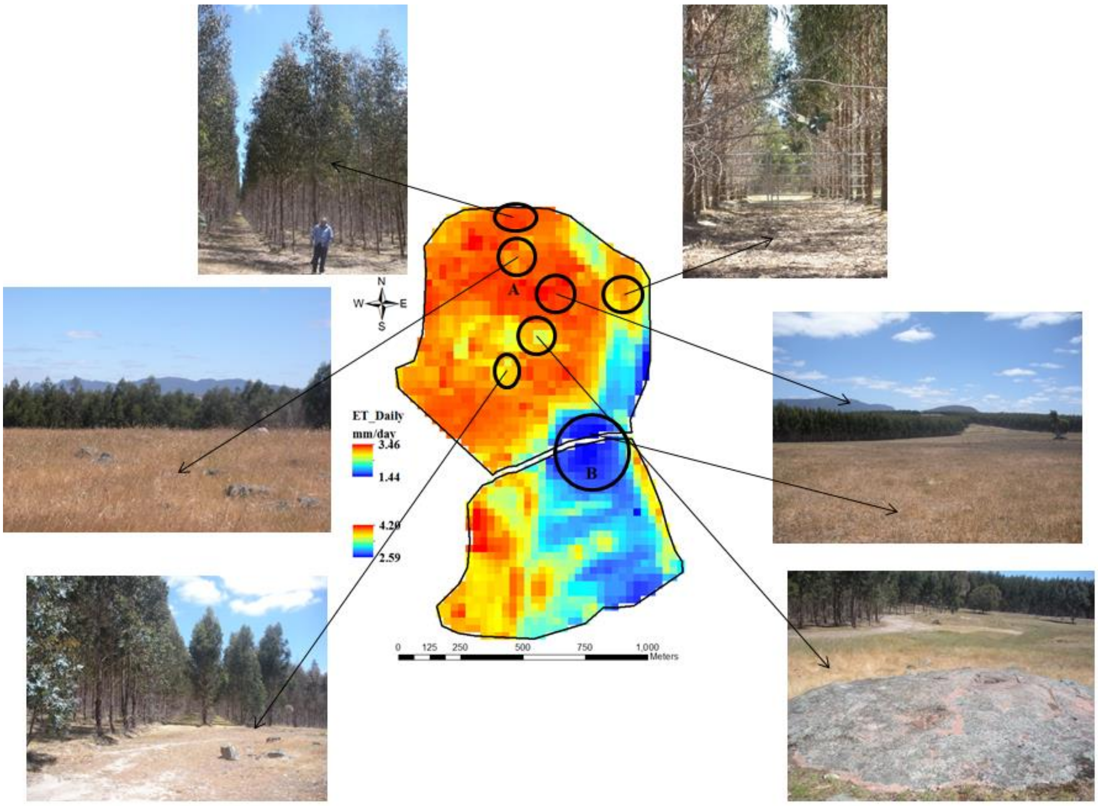

Figure 4.12. Landcover variability in study site at Mirranatwa.

The friction velocity raster file along with von Karman's constant and friction velocity at blending height (μ^*_{200}) was used as an input for Model 017c (Appendix 22) to compute aerodynamic resistance to heat transport for each pixel (eq. 4.2.9).

4.2.2.2. dT (near-surface temperature difference between two heights)

The second essential component required for the sensible heat flux equation (eq. 4.2.5) is dT, which is the near-surface temperature difference for each pixel. The temperature difference (T_1-T_2) between two heights (Z_1 and Z_2) for each pixel is challenging to know. Therefore, the assumption of linearity between dT and surface temperature (T_s) of two heights as proposed by Bastiaanssen (1995) and also used by Allen et, al. (2002a) was followed (eq. 4.1.12).

$$\mathbf{dT = b + a * T_s} \quad \text{eq. 4.2.12}$$

Where

dT	Near-surface temperature difference between two heights Z_1 and Z_2
a & b	Correlation constants
T_s	Land surface temperature

The linearity between dT and T_s is a big assumption of the SEBAL model. However, it is followed for SEBARA since it is based on extensive research which found it's applicability in varied conditions (Bastiaanssen, 1998a & b; Allen, 2002a & b, 2002, 2011 and 2013; Mohamed *et al.,* 2004; Farah and Bastiaanssen, 2001).

To define the coefficients of equation 4.2.12, two anchor pixels, namely 'Cold' and 'Hot', are required. The selection process of these pixels is already explained in the section 4.1.3.9. The corresponding location of 'Hot' or 'Cold' sites marked in the image and used for dT calculations. The average values of surface radiation and energy balance variables for 'Cold' and 'Hot' pixels, already computed, were retrieved. The relative humidity for the image pass date and time extracted from the weather station data.

The calculations of dT_{cold} and dT_{hot} were done in a spreadsheet (eq. 4.2.13 and eq. 4.2.14) using average values of clusters of 'Hot' and 'Cold' pixels for the required parameters.

$$\mathbf{dT_{cold} = (H_{cold} * rah_{cold}) / (\rho_{cold} * Cp_{cold})} \quad \text{eq.4.2.13}$$

$$\mathbf{dT_{hot} = (H_{hot} * rah_{hot}) / (\rho_{hot} * Cp_{hot})} \quad \text{eq.4.2.14}$$

Where

$H_{cold/hot}$	Sensible Heat Flux for the respective'cold' and 'hot' pixels
$r_{ah\_cold/hot}$	Aerodynamic resistance to heat transport of the respective 'hot' and 'cold' pixels.

$\rho_{cold/hot}$	Air density
$C_{p\_cold/hot}$	Air specific heat

The aerodynamic resistance to heat transport computed earlier for the study area (eq. 4.2.6), and the averages for 'hot' and 'cold' clusters of pixels (Figure 4.8) were used. Using the average surface temperature of the respective 'hot' and 'cold' pixels and the respective air density and specific heat values retrieved from the tables (Appendix 23 and 24).

In the equations, 4.2.13 and 4.2.14, the unsolved variables left are H_{cold} and $H_{hot,}$ which was computed by re-arranging the surface energy balance equation (eq. 4.2.13 and 4.2.14). Bastiaanssen (1995) and Allen et al. (2011) proposed equations 4.2.15 and 4.2.16 for the calculation of λET for 'cold' and 'hot' pixel assuming λET_{hot} is equal to zero. However, if there is some λET due to absence of a dry patch without vegetation cover or rain prior to the satellite pass date and time, equation 4.2.17 can be used to compute H_{hot}:

$$\mathbf{H_{cold} = R_{n\text{-}cold} - G_{cold} - \lambda ET_{cold}} \quad \text{eq. 4.2.15}$$

$$\mathbf{H_{hot} = R_{n\_hot} - G_{hot}} \quad \text{eq. 4.2.16}$$

$$\mathbf{H_{hot} = R_{n\text{-}hot} - G_{hot} - \lambda ET_{hot}} \quad \text{eq. 4.2.17}$$

Where:

$R_{n\_cold/hot}$	Average net radiation of respective 'cold' and 'hot' pixels
$G_{\_cold/hot}$	Average soil heat flux for respective 'cold' and 'hot' pixels
$\lambda ET_{\_cold/hot}$	Latent Heat flux of 'cold' and 'hot' pixels.

The only one variable (λET), for both the clusters of pixels, is required to compute the above equations. The latent heat of condensation of water (λ) for 'cold' and 'hot' pixel calculated using respective temperatures for the empirical cubic function as described in eq. 4.2.18 (Yau, 1996; Gallant, 2012):

$$L_{water}(\lambda) = [2500.8 - (2.3642 * T) + (1.5893x\ 10^{-3} * T^2) - (6.1434x10^{-5} * T^3)]$$

eq. 4.2.18

Where:

L_{water} (λ)	Latent heat of vaporization of water (kJ/Kg) as a function of temperature between - 40 and +40 °C
T	Temperature in °C

The values of temperature (°C and °K), ET_r, R_n, G, r_{ah}, air density and air specific heat were retrieved for the respective clusters of 'cold' and 'hot' pixels. First, the λ_{cold} and λ_{hot} using temperatures (°C) for equation 4.2.18 were computed. Depending upon the availability, hourly or 30 min weather data, using RefET model ET_r and ET_o were calculated. The reference ET values were used to compute ET_rf (section 4.2.4.2). RefET software developed by the University of Idaho (https://www.uidaho.edu/cals/kimberly-research-and-extension-center/research/water-resources/ref-et-software) (Allen, 2011) was used to compute reference ET of alfalfa and grass. The RefET program provides standardized calculations of reference evapotranspiration (ET_r or ET_o) by fifteen of the more commonly used methods. To run the model, weather station information, as well as data of maximum available meteorological parameters (Appendix 25), are required.

An ASCII (.csv) data file was created for the corrected weather data collected at the study sites for one year, including the satellite pass day. Consideration was given to add the data for at least 15 days before the image pass day. The file contained data for time (year, day, hh:min), air temperature (°C), relative humidity (%), wind speed (km/hr), precipitation (mm) and solar radiation (W/m^2). Preference was given to the data at the 30-minute interval, where available, due to better proximity to the satellite pass time. The description of the weather station entered in the model is presented in Figure 4.13 and equations used in Figure 4.14.

The output of RefET model for different methods was compared to the recorded ET (flux tower and adjusted sapflow meter readings). There was not a significant difference in the output of different methods. Therefore, a widely used approach (FAO 56) was used. If the satellite pass time falls towards the end of the time step, the average value was used for the analysis. Similarly, the total daily ET_r for the image pass day were computed.

Crop coefficients (K_c) are required for the adjustment of the RefET output considering the season, health, and vegetation type/cover under the local conditions. For irrigated areas, it is a general observation that 'Cold' or wet agricultural fields have 5% higher ET rates than reference ET (ET_r); therefore, ET_{cold} and ET_{hot} were adjusted. The crop coefficients (K_c) are widely used for adjusting the ET_r or ET_o for different crops (Allen et al., 1998b). The factors that can affect the K_c may include climate, soil moisture, groundwater, irrigation, cultural practices, etc. (Doorenbos and Pruitt, 1977; Steduto et al., 2012).

For Mirranatwa site the annual reference ET for alfalfa (ET_r) was considered for the *Eucalyptus* plantation. Various coefficients were tested, and a K_c value of 0.75 for long term data has a better match to the measured ET of a young plantation block at Mirranatwa site (Dean, 2013). However, local conditions, plantation age, management practices, tree species, soil nutrient, groundwater depth, time of the year and canopy must be considered, and the K_c value should be adjusted accordingly. The K_c value of 0.7 for the early season to 0.82 for the midseason is recommended for drip-irrigated *Eucalyptus* (Alves *et al.,* 2013).

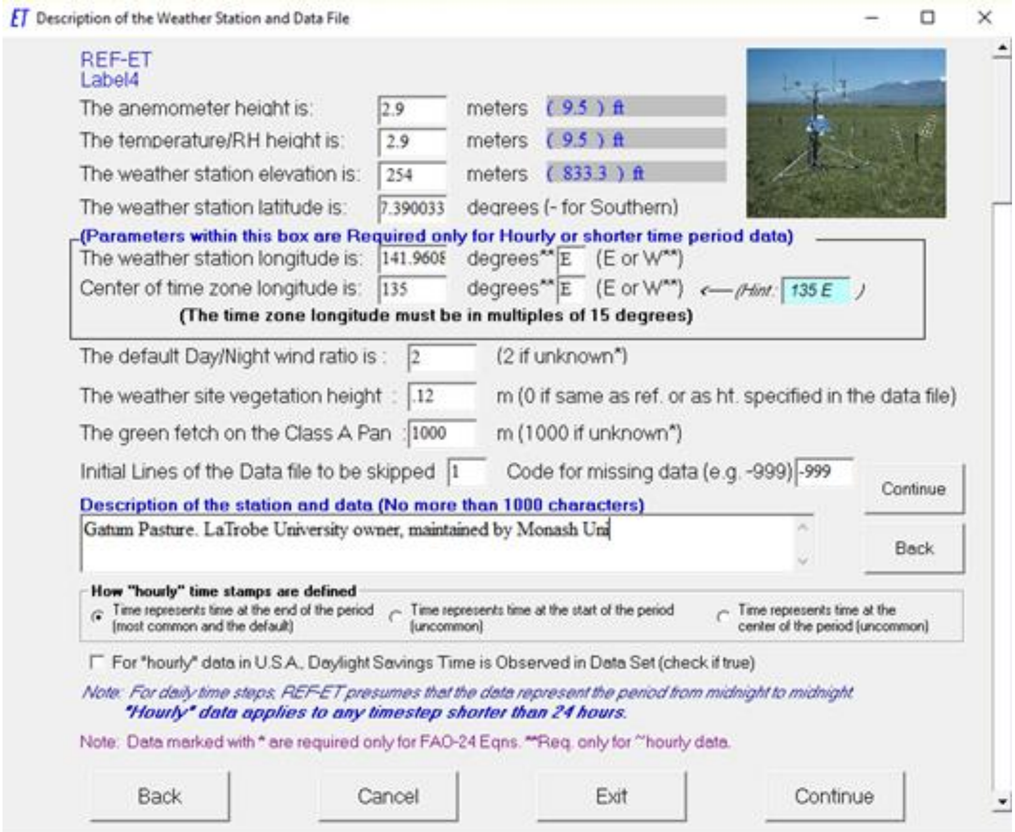

Figure 4.13. Description of the weather station for RefET model.

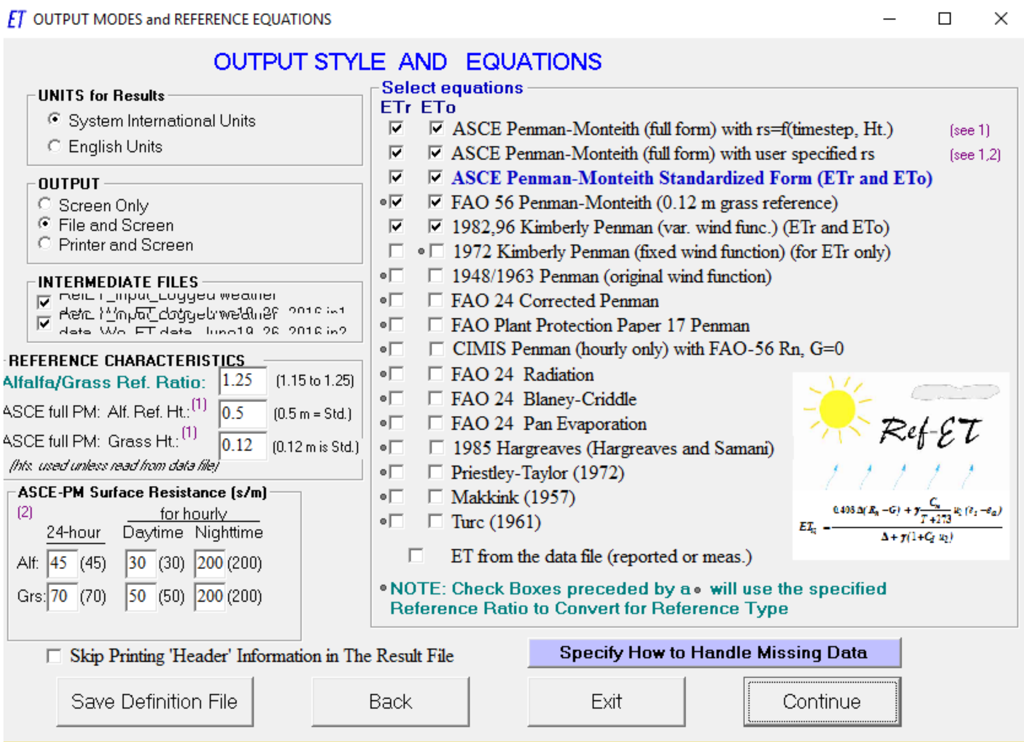

Figure 4.14. Output mode and reference equations selected for the ET_o and ET_r.

Compared to the annual measured *Eucalyptus* transpiration and soil evaporation of the plantation block at Mirranatwa site (Dean, 2013), reference ET (ET_r) with a K_c value of 0.7 was only 2% higher. For pastures, a K_c value of 0.5 was the more appropriate to adjust reference ET_o at Mirranatwa and was only 4% less than measured ET at flux tower. These coefficients for reference ET (ET_r and ET_o) are for early October; however, for the dry season, these may be lower than the K_c used.

Once the values of λ_{cold} and λ_{hot} and ET_r were available, λET was computed by simply multiplying the values and used for eq. 4.2.15 and 4.2.16 or 2.4.17 to compute the sensible heat flux of respective pixels. For the plantation and pasture catchments, the value of ET_r and ET_o was used with respective K_c (*Note: since λ is in kJ/Kg and ET_r is in mm/hr there is a need to equate the units*).

All the required variables for equations 4.2.15 & 4.2.16 or 4.2.17 have already been computed, and after calculating dT for both cold and hot pixels, the respective dT values were plotted against the corresponding surface temperature (°K). From this plot, the coefficients 'a' and 'b' were used to compute the dT between two heights (eq. 4.2.12). The coefficient values and surface temperature raster layer were used to generate a near-surface temperature difference (dT) layer (Appendix 26).

Assuming the linearity between dT and T_s, an approximate air temperature (T_a) layer was developed (4.2.19).

$$\mathbf{T_a = T_s - dT} \qquad \text{eq. 4.2.19}$$

Where

T_s Land surface temperature

dT Near-surface temperature difference between two heights Z_1 and Z_2

An initial Sensible Heat Flux (H) calculated (eq. 4.2.5, Appendix 27) assuming the neutral conditions.

The atmospheric stability conditions impact the aerodynamic resistance (r_{ah}), which filters down to sensible heat flux (H), as illustrated in figure 4.9, especially under dry conditions (Allen *et al.*, 2002a). The Monin-Obukhov theory was applied to accommodate the buoyancy effects generated by surface heating, and the Monin-Obukhov Length (L) was computed using equation 4.2.20 (Appendix 28) as:

$$L = \frac{(\rho * C_p * \mu^{*3} * T_s)}{k * g * H} \qquad \text{eq. 4.2.20}$$

Where

L	Monin-Obukhov length
ρ	Air density (Kg/m^3)
C_p	Air specific heat
μ^*	Friction velocity (m/sec)
T_s	Land surface temperature (°K)
k	von Karman’s constant (0.41)
g	Gravitational constant ($9.81 m/s^2$)
H	Sensible Heat Flux (W/m^2)

The three stability conditions are: stable ($L > 0$); neutral ($L = 0$) or unstable (< 0). The Monin-Obukhov Length (L) was computed (Appendix 28) to understand the stability conditions at the study site at satellite pass time. As suggested in the earlier research (Allen et al., 2011; Koloskov et al., 2007; Webb, 1970), if the L value reflects unstable or stable conditions, there is a need for stability corrections for momentum and heat transport (Ψ_m and Ψ_h) in an iterative process. The iterative process can be continued with the new value of $\mu^*$and updated r_{ah} and H until the impact of any further stability correction on H becomes negligible.

If the conditions are unstable ($L < 0$), equations 4.2.21 to 4.2.26 are used to compute the stability corrections:

$$\Psi_{m\,(200m)} = 2\ln\left[\frac{1 + X_{(200m)}}{2}\right] + \ln\left[\frac{1 + X_{(200m)}{}^{2}}{2}\right] - 2\,\mathrm{ARCTAN}\,(x_{200m}) + 0.5\pi$$
eq. 4.2.21

$$\Psi_{h\,(2m)} = 2\ln\left[\frac{1 + X_{(2m)}{}^{2}}{2}\right]$$
eq. 4.2.22

$$\Psi_{h\,(0.1m)} = 2\ln\left[\frac{1 + X_{(0.1m)}{}^{2}}{2}\right]$$
eq. 4.2.23

Ψ_m and Ψ_h are the stability corrections for momentum and heat transport.

Where:

$$X_{(200m)} = \left[1 - 16\,\frac{200}{L}\right]^{0.25}$$
eq. 4.2.24

$$X_{(2m)} = \left[1 - 16\,\frac{2}{L}\right]^{0.25}$$
eq. 4.2.25

$$X_{(0.1m)} = \left[1 - 16\,\frac{0.1}{L}\right]^{0.25}$$
eq. 4.2.26

In the situation where the boundary conditions are stable ($L \geq 0$), a value of 1 is assigned to X_{200m}, X_{2m} and $X_{0.1}$, however, for $L > 0$ (stable conditions), the stability corrections for momentum and heat transport are computed (eq. 4.2.27 to 4.2.29).

$$\Psi_{m\,(200m)} = \left[-5\,\frac{2}{L}\right]$$
eq. 4.2.27

$$\Psi_{h\,(2m)} = \left[5\ \frac{2}{L}\right]$$
eq. 4.2.28

$$\Psi_{h\,(0.1m)} = \left[-5\ \frac{0.1}{L}\right]$$
eq. 4.2.29

Where:

$\Psi_{m\,(200m)}$	Stability correction for momentum transport at 200 meters
Ψ_h	Stability correction for heat transport between two layers Z_1 (0.1m) and Z_2 (2m)

In equation 4.2.27 a value of 2 is used instead of 200 for z because under stable conditions it is assumed that the boundary layer height is just a few meters and using larger value can cause a numerical instability (Allen, et al., 2011). Considering this, with a value of 2 in equation 4.2.27 a neutral condition is achieved at the boundary height (200m).

In each iteration, revised values for friction velocity ($\mu^*_{revised}$) and aerodynamic resistance to heat transport ($r_{ah\_revised}$) were computed (eq. 4.2.30 & 4.2.31) followed by a revised dT and T_a values leading to a revised H and L values.

$$\mu^*_{revised} = \frac{\mu_{200} * k}{\ln\left(\frac{200}{Zom}\right) \Psi_{m\,(200m)}}$$

eq. 4.2.30

Where:

μ_{200}	Wind speed at 200m (m/s)
k	von Karman's constant (0.41)
Zom	Roughness length for each pixel (m)
$\Psi_{m\,(200m)}$	Stability correction

$$r_{ah\_revised} = \frac{\ln\,[Z_2/Z_1] - \Psi_{h\,(Z2)} + \Psi_{h\,(Z1)}}{\mu^*_{revised} * k}$$

eq. 4.2.31

Where:

$r_{ah\_revised}$	Revised aerodynamic resistance to heat transport
Z_2	2.0 m
Z_1	0.1 m

$\Psi_{h\,(Z2)}$ and $\Psi_{h\,(Z1)}$	Stability correction for heat transport at 2m and 0.1 m
$\mu^*_{revised}$	Revised friction velocity
k	von Karman's constant (0.41)

The L value for 3rd October 2013, was close to 0 (0.05 - 0.1); therefore, the prevailing conditions were considered as neutral conditions as recommended by Bastiaanssen et al., 2002 and Allen et al., 2011. However, for the June 2016 image, the conditions were unstable (L< 0); therefore, stability corrections process followed for winter (Model 021a, Appendix 29a). Under stable conditions, Model 021b (Appendix 29b) can be used for stability correction. The model input includes Monin Obukhov length, Zom_{pix}, dT and T_s raster files along with the air specific heat and air density values which depend upon the season of the image, as both these values are a function of the temperature gradient, surface roughness, and wind speed. The model also computes the revised values of friction velocity ($\mu^*_{revised}$) following equation 4.2.30, which can then be used to calculate a revised aerodynamic resistance to heat transport (r_{ah}) following equation 4.2.31. The iterative process continued until the impact of any further stability corrections on H became negligible, and finally, sensible heat flux (H) was computed.

4.2.3. Latent Heat Flux (λET)

Latent heat flux was computed by Surface Energy Balance equation (eq. 4.2.2). For this equation, all the required variables were computed in the previous sections. To compute the ET for the image pass time and the day, first instantaneous ET was computed.

4.2.4. Evapotranspiration

4.2.4.1. Instantaneous ET

Equation 4.2.32 used to compute the instant ET (ET_{inst}) mm/hr at satellite pass time.

$$\mathbf{ET_{inst} = 3600 * (\lambda ET / \lambda \rho w)} \qquad \text{eq. 4.2.32}$$

Where

λET	Latent Heat Flux
3600	Time conversion from seconds to hours
ρw	Density of water (Kg/m^3)
λ	Latent heat of vaporization (J/Kg)

$$\mathbf{\lambda = [2.501 - 0.00236\,(T_s - 273.15)] \times 10^6}$$

4.2.4.2. Reference ET fraction (ET_rf)

ET_rf is a ratio of the instant ET (ET_{inst}) of each pixel to the reference ET (ET_r) at the image pass time. The adjusted RefET model output (ET_r) for the time closest to the image pass time was used to compute ET_rf using equation 4.2.33:

$$\mathbf{ET_rf = ET_{inst} / ET_r} \qquad \text{eq. 4.2.33}$$

Where

ET_{inst}	Image pass time ET of each pixel (mm/hr).
ET_r	Reference ET (RefET model output).

The ET_rf for a pixel representing dry soil can be close to zero, and for a wet pixel with full vegetation cover, it may have a value of ≥ 1. Since several assumptions were made for the computation of various variables, especially sensible heat flux, negative values can be expected.

4.2.4.3. Daily Evapotranspiration (ET_{24})

While computing ET_{24}, an assumption is made that the ET_rf is the same for the entire day. Daily ET (ET_{24}) was computed using ET_rf and cumulative ET_r for satellite pass day (eq. 4.2.34).

$$\mathbf{ET_{24} = ET_rf * ET_{r\_24}} \qquad \text{eq. 4.2.34}$$

ET_{inst}, ET_rf and daily ET were computed using the input parameters including net radiation (R_n), soil heat flux (G) and sensible heat flux (H) raster files and reference ET values for the image pass time and day Model 022 (Appendix 30).

4.2.5. Comparison of Model Output

The following sources of data were used for comparison of model output:

- Climatic data
- Flux tower data for pasture and adjusted sapflow meter data for plantations
- Catchment hydrology distributed model (CATHY) output

At the Mirranatwa study site, in the pasture catchment, there is a flux tower in the northern part of the catchment (Figure 4.15a). In the plantation catchment, there are three sapflow meters (Figure 4.15b) installed in three plots with variable water table depth, including 1, 5 and 12m below the surface (Dean, 2013). At the Gatum study site, the pasture catchment has a flux tower installed in the middle of the catchment; however, the proposed location for a flux tower in the plantation catchment is marked (Figure 4.15b).

The weather station data of the Mirranatwa catchments as well as RefET model output (for ET_r and ET_o) were used. Any environmental or biological limitation like soil fertility, waterlogging, pest, diseases, aridity, deep groundwater, etc. can hamper the targeted potential ET (Allen *et al.*, 1998b; Gentine *et al.*, Dean, 2013). Further, in a natural ecosystem with a mix of plant species, especially in arid environments, standard ET cannot be achieved. Under the unfavourable environmental conditions, stress coefficients or crop coefficients (K_c) are used.

The third comparison source is the catchment hydrology (CATHY) distributed numerical model (Camporese *et al.*, 2013). A particular feature of CATHY is that it controls the switching between atmosphere-controlled and soil-limited evapotranspiration, which is regulated by a threshold pressure head (ψ_{min}). The climatic data for the satellite pass day was used as an input to the CATHY model to compute the ET.

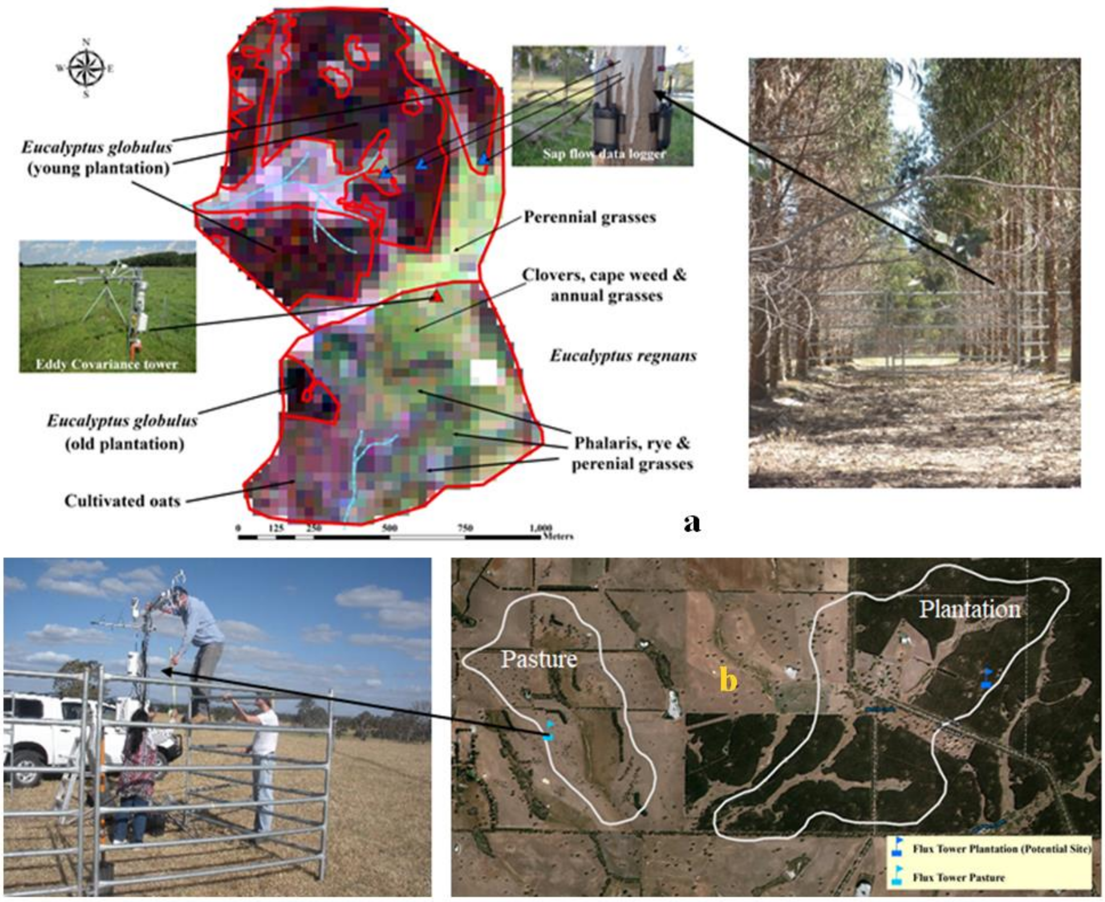

Figure 4.15. Field instrumentation for measurement of ET at (a) Mirranatwa and (b) Gatum study catchments.

Chapter 5. Results and Discussion

The model developed using the L1 product of Landsat 5 TM image of October 3rd, 2011. ArcGIS model builder was used to create the models for the various components of the radiation balance equation. First, a subset of the Landsat bands containing the Mirranatwa catchments was clipped (Figure 5.1).

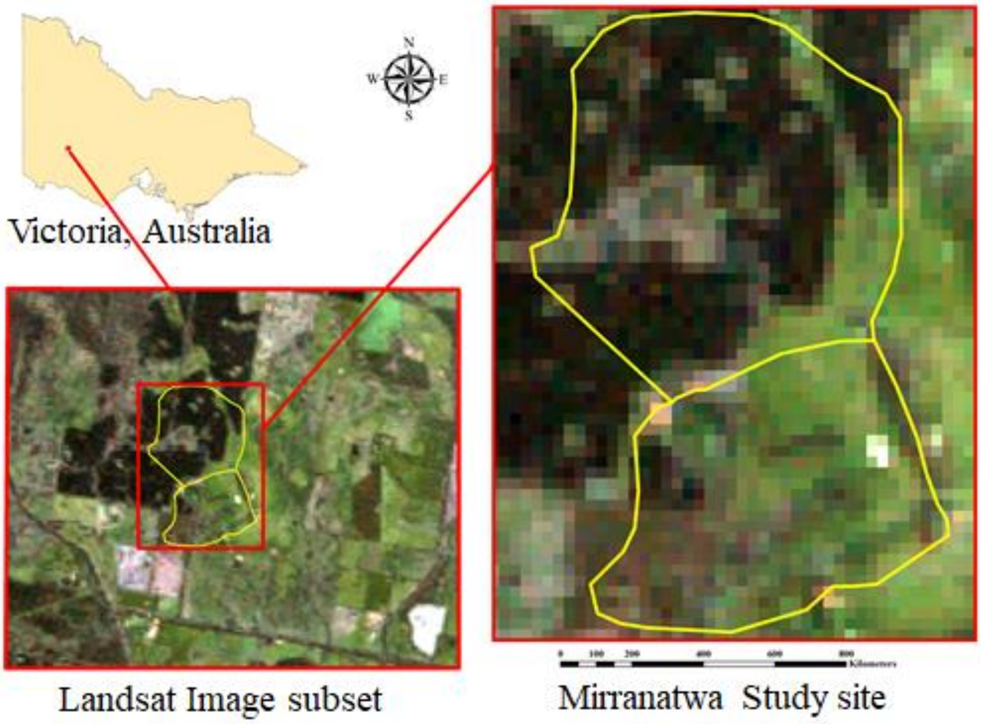

Figure 5.1. the location of the paired catchments and the image subset for model development.

5.1. Model output

5.1.1. Surface Radiation Balance (SRB)

The surface radiation balance consists of net incoming shortwave and longwave radiations (Figure 5.2). Out of the total incoming shortwave solar radiation, about half (51%) absorbed by the ocean and the land by surface processes, including latent heat of vaporization (23%), while the remainder is either absorbed by the atmosphere (15%), utilized by conduction and rising air (7%) or directly radiated from Earth's surface (6%). Out of the remaining 49% incoming radiation, 30% reflected back to the atmosphere (including surface albedo), and 19% absorbed by the atmosphere and clouds. In the following sections, the incoming and outgoing radiation parameters, extracted from the Landsat image using the models developed for these variables as explained in Chapter 4, are discussed .

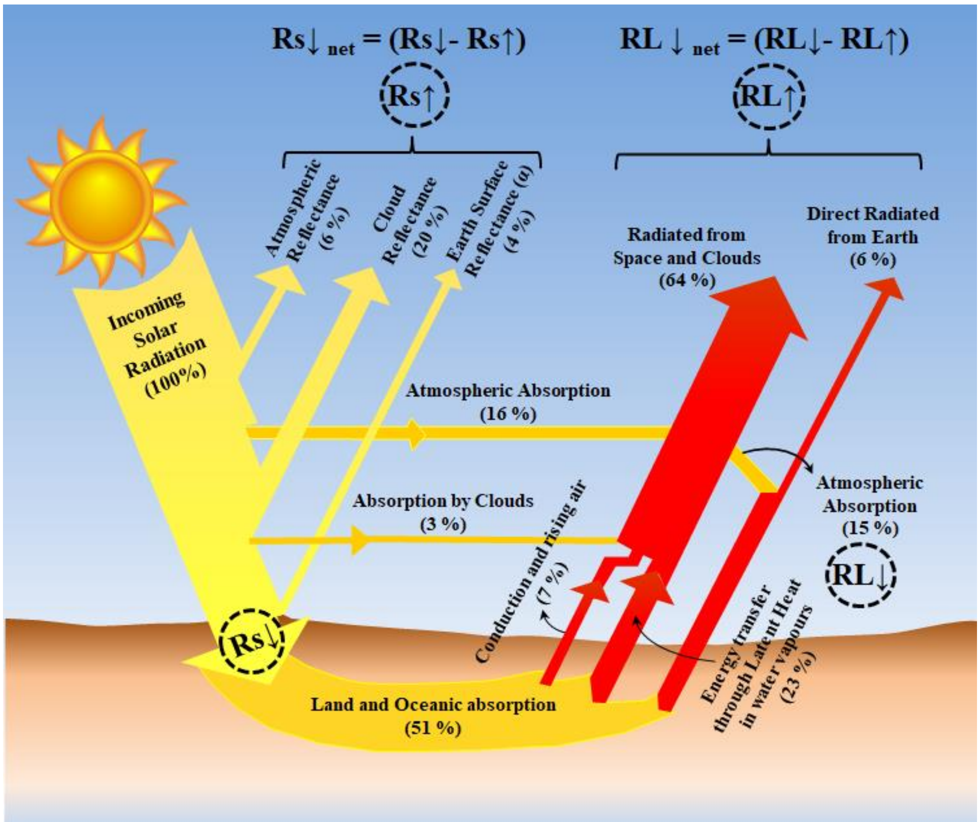

Figure 5.2. The Earth's energy budget.
Modified from: NASA 2003
https://pmm.nasa.gov/education/lesson-plans/global-energy-budget

5.1.1.1. Radiance

The radiance is the energy directly measured by remote sensing instruments. During the energy transfer process from the Earth to the instrument, some of the scattered light in the atmosphere will also be recorded by the instrument and included in the observed radiance of the target (Harris, 2017). Besides atmospheric scattering, there is some absorption as well, which will decrease the observed radiance. Radiance depends on the illumination (both its intensity and direction), the orientation and position of the target and the path of the light through the atmosphere.

Generally, the radiance of all the bands is higher for pasture as compared to plantation or cropped area (Figure 5.3), indicating that the incoming radiation is mostly reflected by pasture, however, the plantation retains more incoming energy. Among the visible bands (RGB), B2 (Green) differentiates the plantation blocks, pastures and cropped area whereas SWIR highlight trees and pastures/crops.

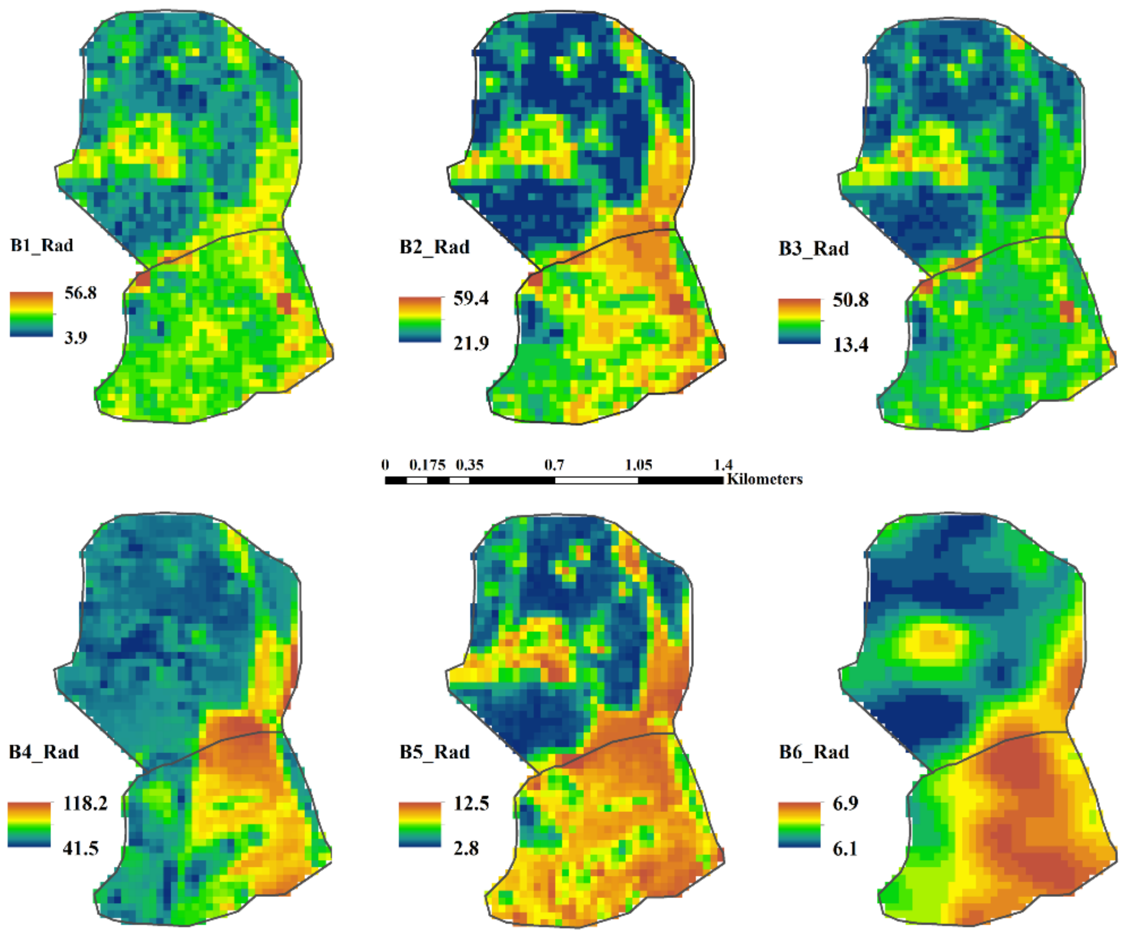

*Figure 5.3. Spatial patterns of Radiance (Watts/ (m^2 * srad * µm)) of bands of Landsat 5TM.*

5.1.1.2. Reflectance (ρλ)

Reflectance is the ratio of the amount of light leaving a target to the amount of light striking the target. It has no units. Reflectance (or more specifically, hemispherical reflectance) is a property of the material being observed. Many of the atmospheric effects and the solar illumination can be compensated for in remote sensing data. For many applications, radiance and reflectance can be used interchangeably, however, since reflectance is a property of the target material itself, the most reliable (and repeatable) vegetation index values can be calculated using reflectance (Harris, 2017).

Among the visible bands, the blue and red bands have relatively low reflectance due to high absorption by the plant pigments, whereas green reflects more. For healthy vegetation, the reflectance is much higher in NIR than VIS bands due to the cellular structure of leaves, especially spongy mesophyll. In SWIR bands, the water content and structure of vegetation is responsible for absorption of energy, especially in wavelengths 1.45 to 1.95 and 2.50 μm (Figure 5.4).

Generally, the re-radiated absorbed energy will vary according to Stefan-Boltzmann and Wien Laws and will be controlled by surface absolute temperature or emissivity (Ahmad and Lockwood, 1979). If the radiation directly reflected back, there would be no change in wavelength and shortwave will reflect as shortwave radiation.

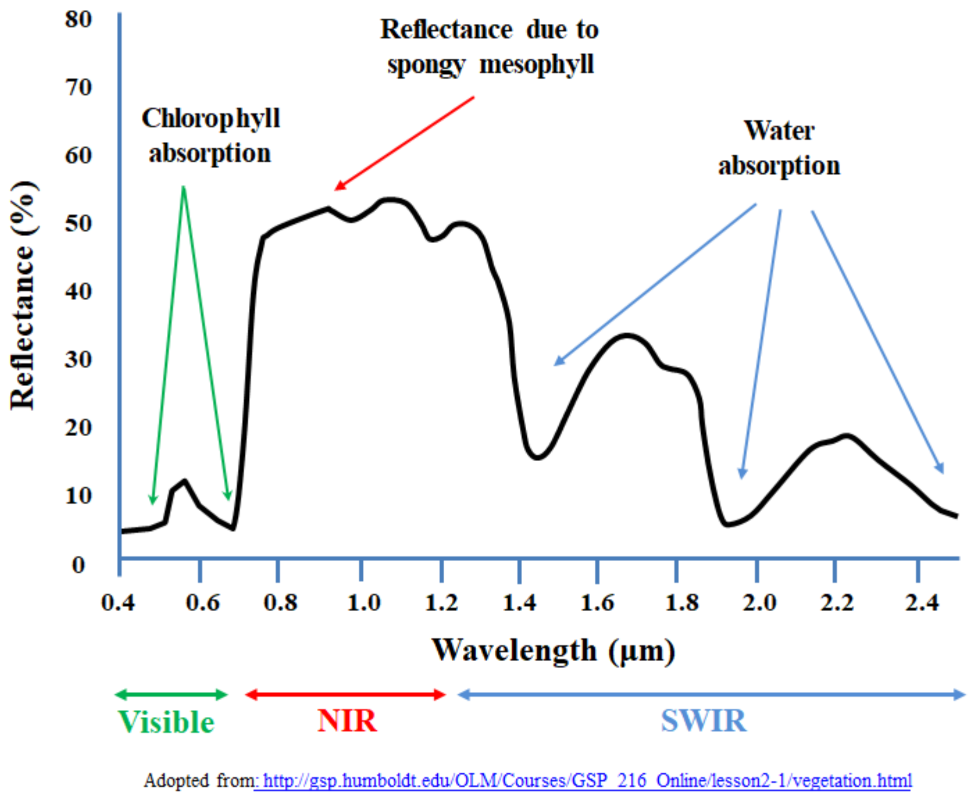

Figure 5.4. The reflectance of different surfaces.

The surface reflectance, in general, follows the spatial pattern of radiance (Figure 5.5), and the ratio of reflected light is low for plantations as compared to the pasture. Previous studies (Datt, 1999; Madhavan *et al.*, 2016; Stone *et al.*, 2001) reported that in *Eucalyptus* species the reflectance of the NIR band (close to 0.71µm wavelength) shows higher sensitivity to chlorophyll content than the green band (0.55µm); the NIR band (0.85µm) is insensitive to chlorophyll. In the study site, all the visible, NIR, SWIR bands show higher energy absorption by *Eucalyptus* plantation than the pastures probably due to a better three-dimensional structure of trees. The reflectance values were used to compute albedo and vegetation indices.

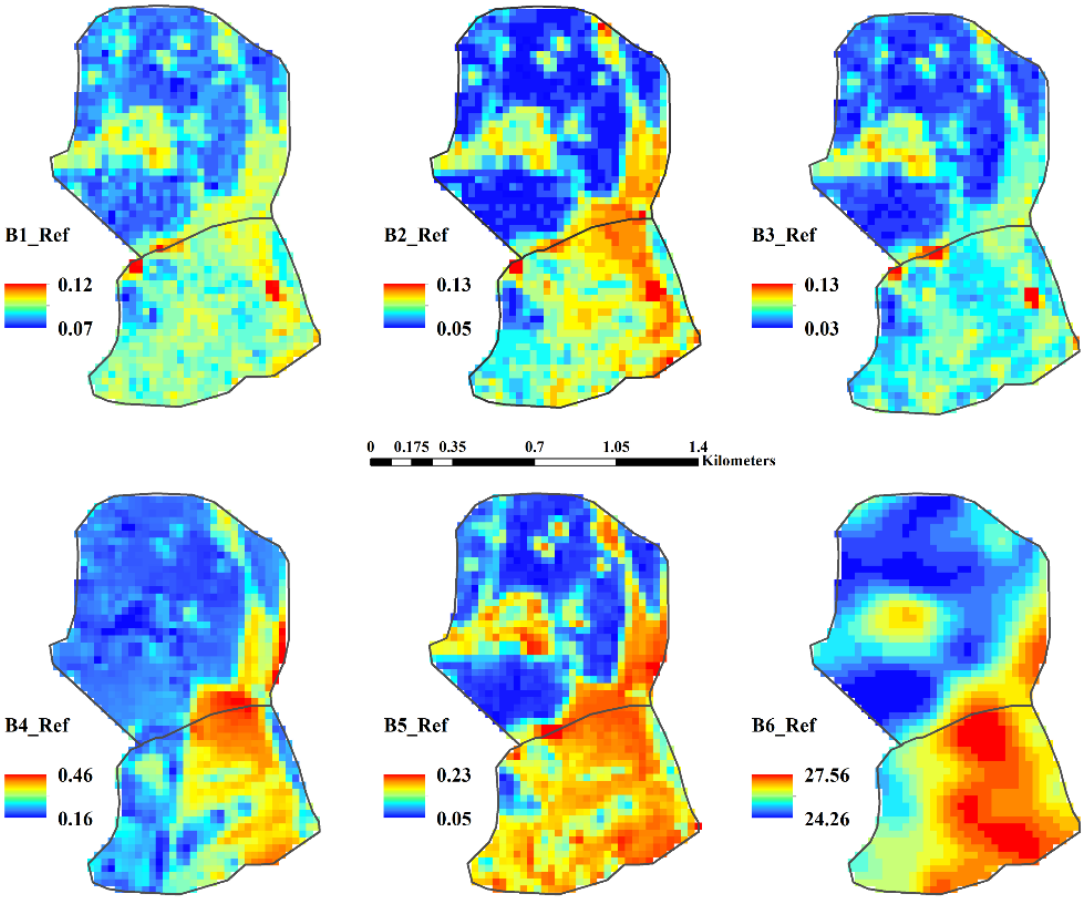

Figure 5.5. Spatial patterns of reflectance of Landsat 5TM bands.

5.1.1.3. Albedo (α_{toa} and α_{surf})

Albedo is the fraction of the incoming shortwave solar energy scattered by the Earth back to space. It is highly sensitive to small changes in system components, and to some extent, is regulated by biotic adaptation over time. Incoming solar radiation to vegetative surfaces is either absorbed by vegetation, transmitted, reflected or absorbed by the soil (Ahmad and Lockwood, 1979). Similarly, the incoming radiation to other surfaces is either absorbed or reflected. The measure of the reflecting power of the surfaces is called the albedo, which depends upon the properties of the surfaces, e.g., different shades of green vegetation reflect the energy in different wavelengths.

Any shift in a balanced system can lead to variable response towards albedo (Lovelock, 1983; Watson and Lovelock, 1983; Budyko,1969; Evans *et al.*, 2017; Cahalan and North, 1979; Stephen *et al.*, 2015; Stevens and Feingold, 2009; Stone, 1978; Endterton and Marshall, 2010). At a small scale, like the Mirranatwa study site, the external forces like latitudinal impact and the tilt of Earth's axis are not significant. However, local conditions and different landuses cause the differences in both top of the atmosphere (α_{toa}) and the surface albedo (α_{surf}), as shown in Figure 5.6. It is reported that the total shortwave apparent albedo under both clear and cloudy conditions is significantly different from the inherent overall shortwave albedo (Liang *et al.*, 1998 & 1999; Nielsen *et al.*, 1981). It is highly recommended to use either the cloud-free images or use a mask for cloud cover area. For Landsat 8, there is an additional band that highlights the cloud cover; however, low clouds may not be detected, which needs to be considered.

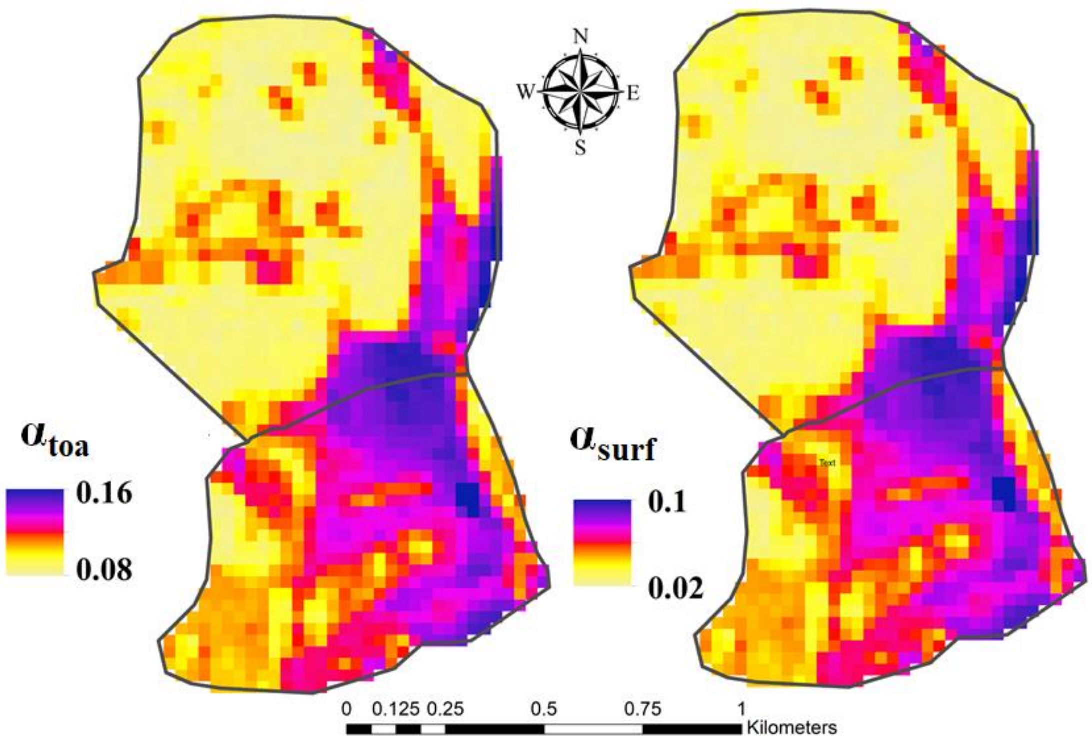

Figure 5.6. Spatial pattern of the top of the atmosphere albedo (α_{toa}) and surface albedo (α_{surf}) at the study site.

Both the albedo values (α_{toa} and α_{surf}) show a distinctive pattern representing land cover: higher values for α_{toa} correlate with lower values for α_{surf} ($R^2 = 0.98$). The α_{toa} ranges from 0.08 to 0.16, whereas surface albedo ranges from 0.02 to 0.1. The *Eucalyptus* plantation retains more energy and therefore, the scattering energy in terms of albedo is low. On the contrary, due to the shallow root system, the pastures have access only to soil moisture, which limits the utilization of available energy for ET. A similar response observed in earlier research (Kotak *et al.*, 2015; Ritter, 2003; McCaughey, 1987; Nyman *et al.*, 2014; Kalma and Badham, 1972; Moore, 1976). The proportion of α_{toa} lost in both the catchment ranges from 26% to 64% (Figure 5.7a), being highest for pasture at elevated areas or low-lying areas with high salinity. Ideally, there should be a linear relationship between α_{toa} and α_{surf}; however, some exceptions are there, as highlighted in Figure 5.7b.

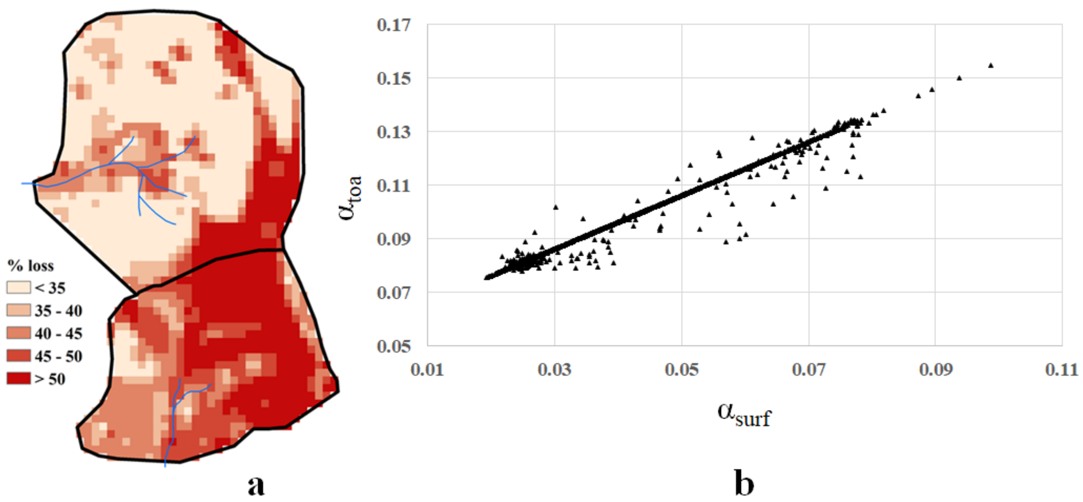

Figure 5.7. Percentage loss of α_{toa} from the surface to the atmosphere.

Howard (1977) measured albedo for various communities using a radiometer and 70mm camera on an aircraft. The aerial recordings were converted into albedo using a conversion factor, and aerial photos interpreted for various landcovers. A two-way table using stand height and crown cover of the subformations clearly showed a very distinctive trend of albedos: higher for grassland and bare ground, and lower for different categories of forests. The Landsat image-based albedo estimates (α_{toa}) are in agreement with the measured values. For dry and wet sclerophyll forest, average albedo values range from 0.08 to 0.09 and for ungrazed and grazed pastures the average measured value ranges between 0.155 to 0.135; this is similar to the trend presented by the paired catchments at Mirranatwa (Figure 5.8).

McCaughey (1987) reported that the daily mean α varies from 0.12 to 0.15 under a full canopy in summer, whereas, in winter, the value falls to a minimum (0.10). Further, in winter advection of additional energy from surrounding vegetation repressed the latent heat and can be responsible for a further drop in the α value (Yunusa *et al.*, 2015). Generally, at Mirranatwa study site the plantation has low α (< 0.09) as compared to pasture (0.09 – 0.135) in early October.

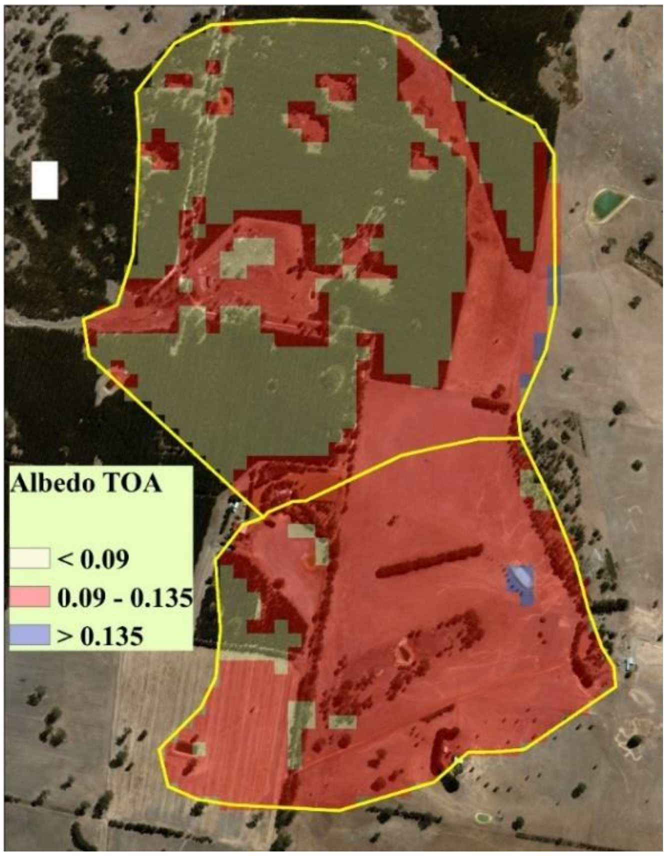

Figure 5.8. The albedo (α_{toa}) representing the different landcover.

5.1.1.4. Incoming Shortwave Radiation ($R_s\downarrow$)

Shortwave radiation is crucial for estimating the evapotranspiration process. About half of the solar radiation reaching the Earth surface is shortwave and includes both direct and diffuse solar radiation.

The incoming shortwave radiation at the satellite pass time was calculated in an Excel spreadsheet assuming a clear sky. Using the values of the solar constant (1367 W/m^2), the cosine of the solar incidence angle (cosθ) and inverse squared relative earth-sun distance (d_r) from header file of the image and the atmospheric transmissivity ($\tau_{s\omega}$) value from the output of the NASA online atmospheric correction calculator, the total incoming shortwave radiation was computed using equation 4.1.15. At the image-pass day and time shortwave radiation estimated was 830.235 W/m^2. Shortwave radiation is absorbed by water bodies more than the land surface (Trenberth *et al.,* 2009; Levitus *et al.,* 2005, Fasullo and Trenberth, 2008; Hansen *et al.,* 2005; Huang, 2006), therefore more shortwave radiation is lost from land with limited vegetation cover.

5.1.1.5. Outgoing Longwave Radiation ($R_L\uparrow$)

The longwave radiation emitted by the Earth is absorbed by water and greenhouse gases and needs to be accounted for in the surface energy budget (Kiehl and Trenberth, 1997; Niemelä *et al.,* 2001; Trenberth *et al.,* 2009; Ellingson, 1995). The energy lost by the Earth depends upon the emissivity properties and temperature of the Earth's surface. Spectral Vegetation Indices (SVIs) including NDVI, SAVI, and LAI were calculated to compute the surface emissivity and temperature.

- *NDVI:* The response of NDVI for various landcovers is shown in Figure 5.9. It is a standardized measure of the health of vegetation and ranges from 0 to 1. Healthy vegetation reflects more energy in the near-infrared region. Low NDVI values represent sparse, thin, or dry vegetation and the values close to +1 (0.8 – 0.9) indicates the healthy vegetation. In the study site, the NDVI value ranges from 0.39 – 0.81. The pasture represents the highest vegetation cover by having the highest NDVI value. Low vegetative cover in areas like roads, paths, bare patches, and low-lying saline spots has low NDVI. Medium range of NDVI differentiates areas having natural vegetation or crops.

- *SAVI:* It is like NDVI, but it accounts for the soil-vegetation interaction and under some canopies, it eliminates the variations induced by underlying soil heterogeneity (Huete, 1988; Xavier and Vettorazzi, 2004). The SAVI value ranges from 0.27 to 0.7 in both the catchments (Figure 5.9). Compared to NDVI, SAVI segregates the landcovers in the study area by having lower values for plantation and cropped area and higher for pasture.

- *LAI:* It is also a dimensionless value and characterizes by the amount of foliage in the plant canopies. LAI regulates the net primary productivity and carbon balance, considering the impact of soil variability; however, it depends upon the leaf shape and characteristics. The image (Figure 5.9) shows that the LAI ranges from 0.27 to 3.05; higher for pastures and lower for other landcovers. The *Eucalyptus* plantation has a medium range of LAI probably due to young open canopy, relatively dry environment (Marshal and Waring 1986) and low soil moisture condition and topography (Nemani *et al.*, 1993).

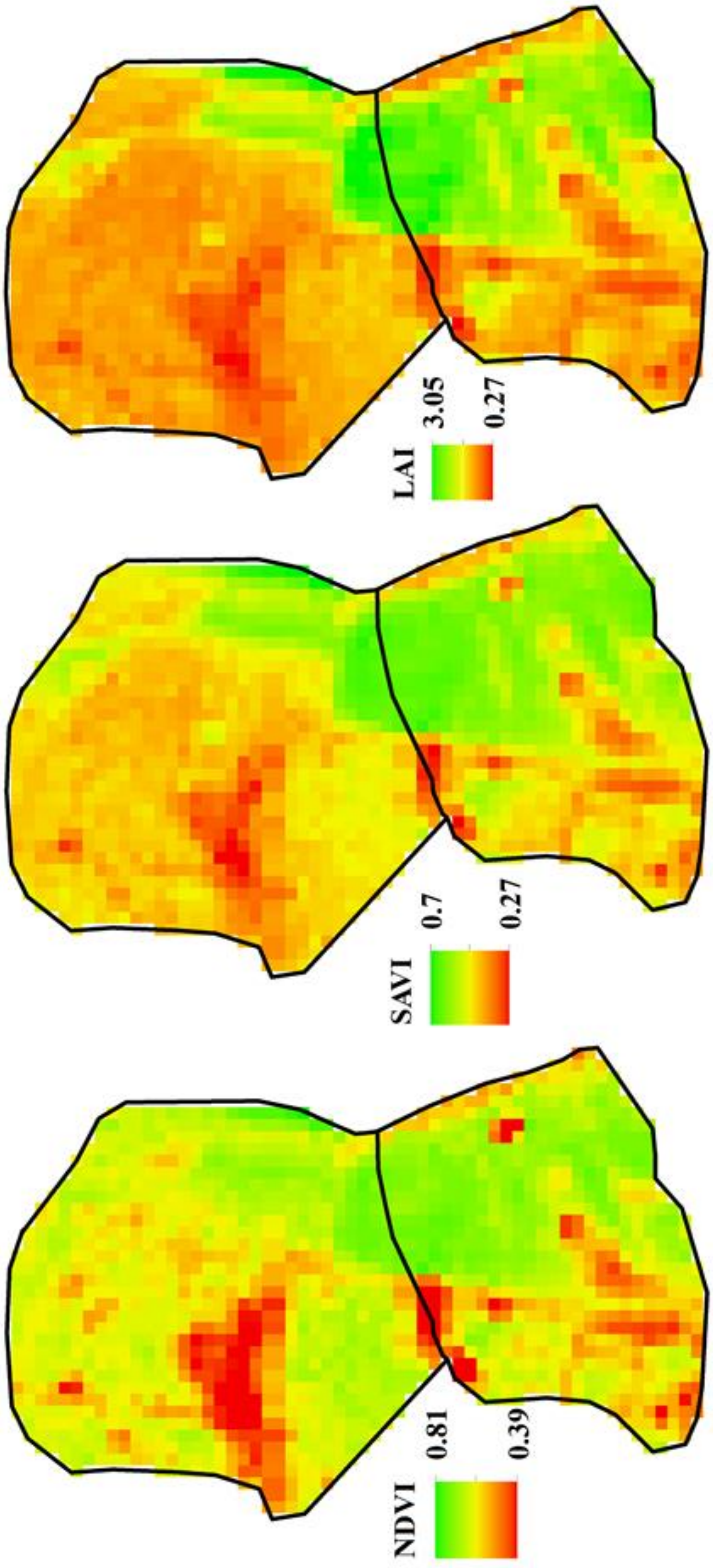

Figure 5.9. Spatial patterns of vegetation indices.

The general trend of LAI and NDVI (Figure 5.10) indicates that both have a similar spatial response, however, LAI, while taking into account the soil heterogeneity, can better present the variability within each landcover. Higher values of both LAI (> 1.5) and NDVI (> 0.7) characterise the pasture; however, LAI is a better representative of pastures than NDVI. Extremely low values of both the indices describe waterlogged areas, poor vegetative cover, or infrastructure, whereas high values represent actively growing pasture (Figure 5.10). It is interesting to note that maximum NDVI represented by pasture and some healthy plantations with thick canopy in the south-west of plantation catchment. On the contrary, maximum LAI is represented by pastures only and due to open canopy of young plantation higher LAI could not be achieved. LAI accounting for SAVI and have a strong correlation (R^2 = 0.96), whereas NDVI has a weaker correlation with both SAVI and LAI, having R^2 values of 0.78 and 0.67 respectively (Appendix 31).

Carlson and Ripley (1997) and Johnson (2003) indicated the sensitivity dependence of LAI on NDVI; when the LAI is less than 2- 4, it is primarily contributed by the bare soil component. Further, the sensitivity of NDVI to increasing LAI gets weaker beyond a threshold (2-3). However, at Mirranatwa, these limits do not hold true probably because of the rainfed conditions.

Surface Emissivity (ε_o): The ε_o is the ratio of the radiant energy emitted by a surface to that emitted by a blackbody at the same temperature. It was computed following the approach proposed by Van de Griend & Owe (1993 and 1994) and Gieske & Timmerman (2002) as compared to the one developed by Bastiaanssen *et al.,* (2005) and Allan *et al.,* (2002) just to avoid the computation of an intermediate variable (SAVI). The spatial pattern of surface emissivity (Figure 5.11) indicates that the pasture has higher emissivity compared to the plantation, which is in line with the previous studies (Sobrino *et al*., 2009; Van de and Owe 1993; Qin *et al.*, 2004; Humes *et al.*, 1994; Formetta *et al.,* 2016; Labed and Stoll, 1991).

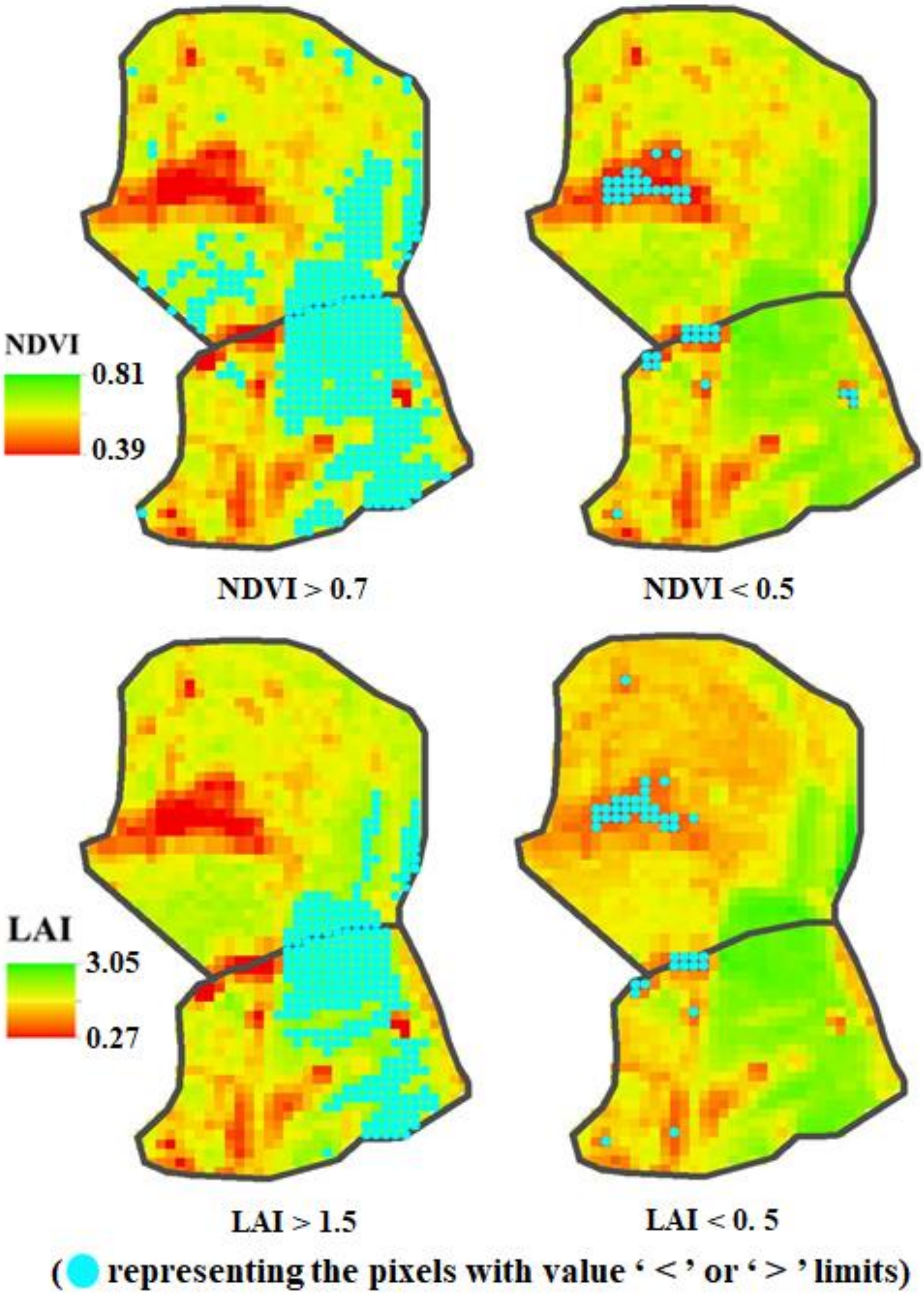

Figure 5.10. High and low NDVI and LAI zones in both the catchments at Mirranatwa.

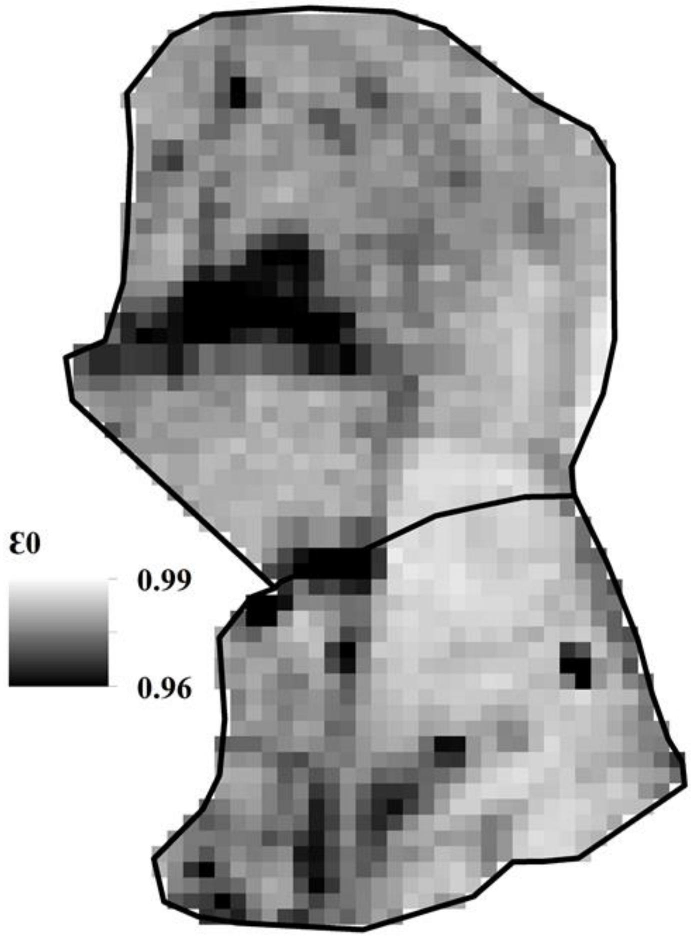

Figure 5.11. The spatial response of emissivity.

- *Land Surface and Air Temperature (T_s and T_a):* T_s depends upon the available energy of the thermal band and the emissivity of different surfaces (Zheng *et al.,* 2010). The direct role of water and vegetation is in cooling or reducing temperature and air pressure gradient (Huryna and Pokorný, 2016; Labitzke and Loon, 1992).

  To compute the surface temperature, first, the brightness temperature (T_b) was computed using thermal band radiance and band-specific constants which then was converted into T_s. Both the T_b and T_s are lower for the plantation, as compared to the pasture (Figure 5.12), having a strong correlation ($R^2 = 0.99$).

As confirmed by previous studies (White Newsome, 2013; Li *et al.*, 2004; Huryna and Pokorný, 2016), the T_s recorded at the Mirrantwa weather station (15.4°C) agrees with the modelled T_s (15.8°C). The highest temperature (18 °C) in the pasture catchment, represented by a single pixel, is a shed for the livestock.

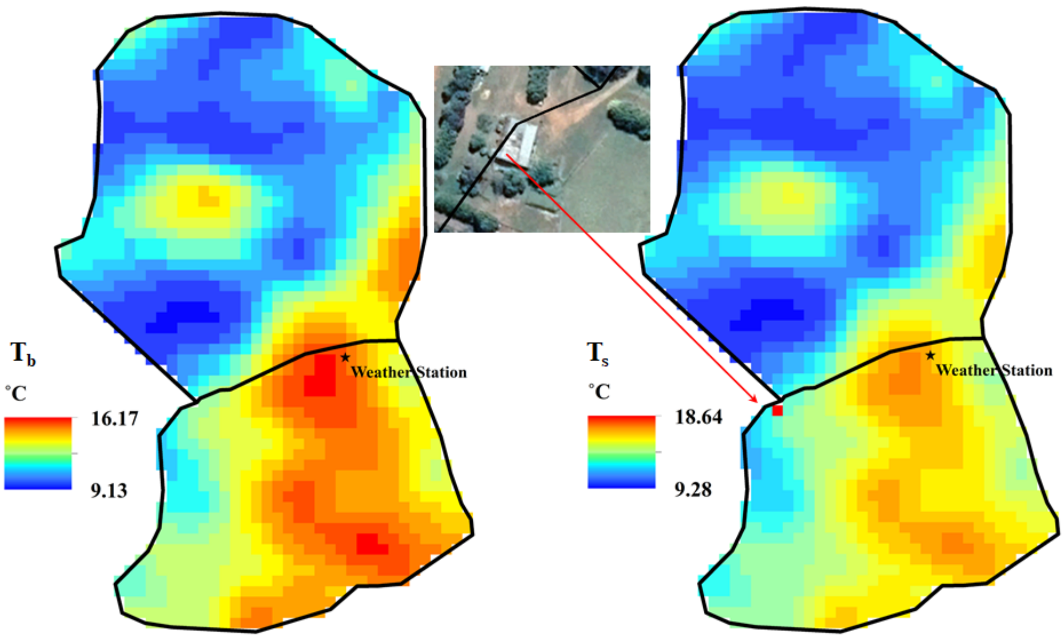

Figure 5.12. Brightness and surface temperature in the study catchments.

Generally, the area under plantation has a lower temperature as compared to pasture, which agrees with earlier research (Wilson and Ludlow, 1991; Chen, 1989; Wong and Wilson, 1980). Despite having lower albedo, emissivity and vegetation indices, plantations sustained lower T_s than pasture and cropland. It is indicative of the cooling effect of higher evaporative water loss from the trees. A similar response observed by Dewan and Corner (2012) where there was a significant difference in the mean surface temperature of various landcovers.

The emitted energy from the Earth surface as $R_L\uparrow$ depends upon the surface temperature. As observed from the surface temperature response in the previous section, the pastures emit more energy than the plantation. The distribution of $R_L\uparrow$ follows the pattern of surface temperature (Figure 5.13). Trees can access water from deeper layers, due to their deep root system, and hence utilize more available energy for ET. However, the shallow root system of the pasture, depending upon soil moisture, cannot use more available energy for the ET process; the excess energy heats the surface or lost to the atmosphere as $R_L\uparrow$. Out of the total incoming shortwave radiation (830.235 W/m^2), the average loss in terms of $R_L\uparrow$ from the pastures is 47% and from the plantation is 44.5%, which is in line with the surface energy budget shown in Figure 4.10. The elevated areas in the pasture catchment and the low-lying areas with shallow saline water in both the catchments have a higher energy loss in terms of $R_L\uparrow$. The pixel representing the animal shed has the highest value of more than 400 W/m^2.

5.1.1.6. Incoming Longwave Radiation ($R_L\downarrow$)

Incoming longwave radiation contributed by shallow atmospheric layers (Schmetz, 1989) and therefore, near air surface temperature and atmospheric emissivity properties are essential in estimating the $R_L\downarrow$. The incoming longwave radiation ($R_L\downarrow$) is 236 W/m^2, whereas $R_L\uparrow$ varied from 325 – 402 W/m^2. Generally, under clear sky conditions, the $R_L\downarrow$ is less than $R_L\uparrow$ (Monteith and Szeicz, 1961; Weiss 1982).

5.1.1.7. Net Longwave Radiation (R_{L_net})

Net longwave radiation (R_{L_net}) varies from -124 to -166 W/m^2 (Figure 5.14). There is less loss of longwave radiation in the plantation as compared to the pasture. The higher temperature in the pasture catchment resulted in a stronger vertical gradient in surface and air temperature, therefore more longwave radiation was lost. On the contrary, the plantation maintained a lower surface temperature and has more capacity to retain the incoming $R_L\downarrow$.

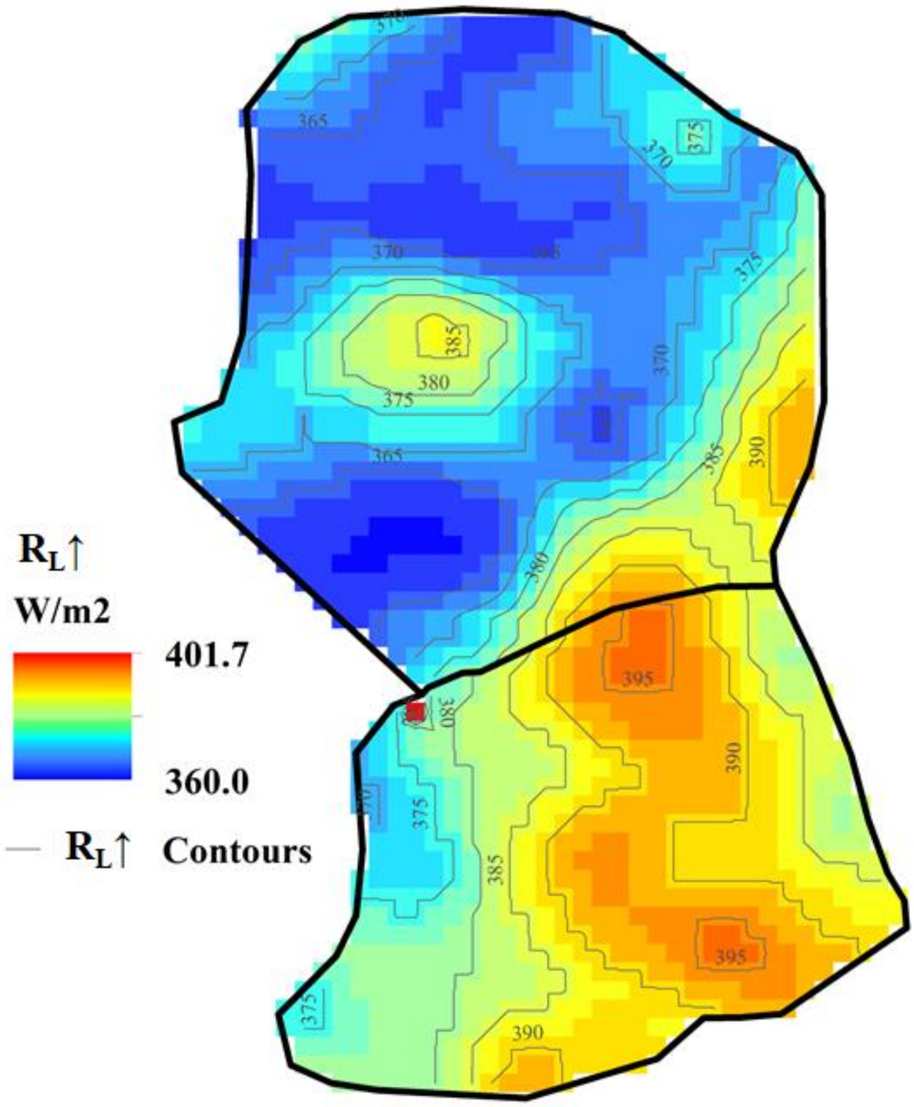

Figure 5.13. The pattern of $R_L\uparrow$ from the Earth's surface in the study area.

The $R_L\downarrow$ is contributed mostly by the shallow atmospheric layers close the Earth surface, whereas higher atmosphere accounts for only 16 to 20% of the total incoming longwave radiation (Liang *et al.*, 2012). Since the Earth's surface is hotter than the atmosphere, generally, net longwave radiation is negative because the Earth is emitting more longwave radiation than it gains from the air. R_{L_net} can be positive if the air is hotter than the Earth surface, and the shift can be abrupt (Tamai *et al.*, 1998).

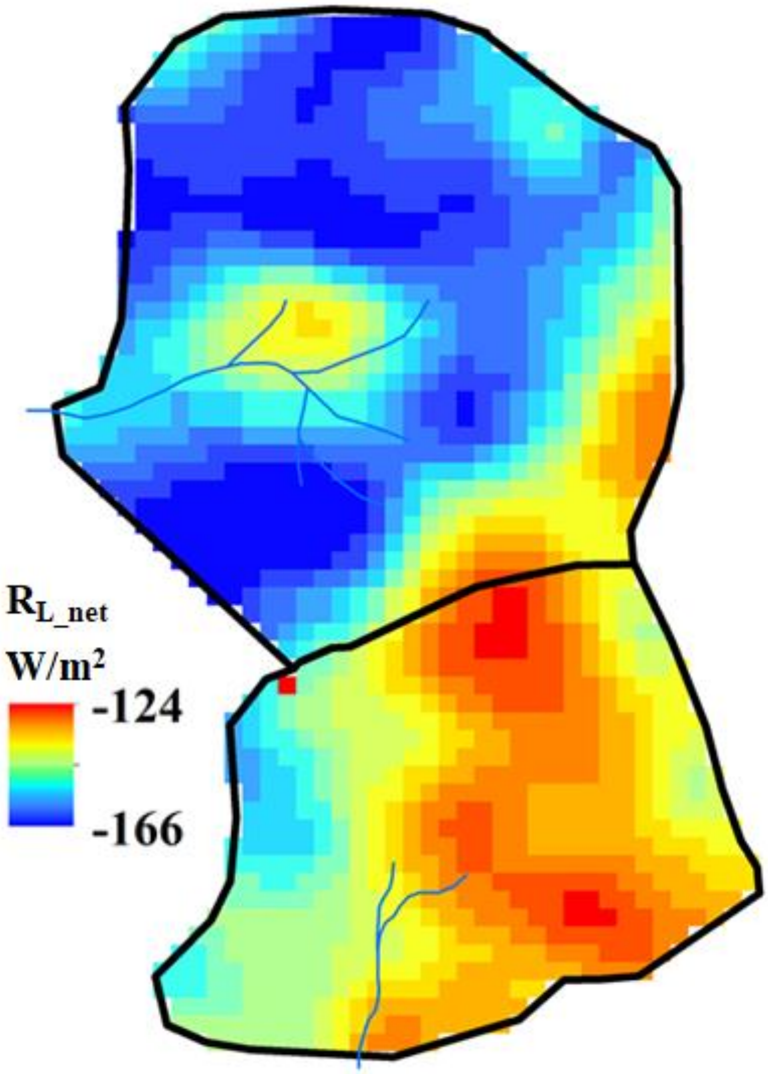

Figure 5.14. Radiation loss in terms of outgoing longwave radiation.

5.1.1.8. Net Radiation (R_n)

The surface radiative balance was computed using incoming and outgoing longwave and shortwave radiations and surface albedo and emissivity. Net radiation can be positive, negative, or zero. It is positive when there is more incoming radiation than outgoing radiation which typically occurs during the daytime when the sun is out, and the air temperature is the warmest. At night, net radiation is usually negative as there is no incoming solar radiation and the outgoing terrestrial longwave flux dominates. Net radiation is zero when the incoming and outgoing components are in perfect balance, which does not occur too often.

The output raster layer presents the net radiation (Figure 5.15). The R_n available for surface process, primarily ET, ranges from 473 to 698 W/m^2. The utilization of this energy depends upon the surface properties, vegetation types, available soil moisture and access to groundwater.

The spatial pattern of R_n (Figure 5.15) shows that the plantation has more R_n compared to pasture and cropped areas, as shown by several studies (Moore, 1976; Friend *et al.*, 1997; Zhang *et al.*, 1999; Langford and O'Shaughnessy, 1977; Nielsen *et al.*, 1981; Rosset *et al.*, 1997; Enz *et al.*, 1988; Crabtree and Kjerfve, 1978). The amount of available R_n determines the potential for ET, however, the availability of water resources, especially in rainfed environments, and vegetation type and health define the limits. As observed in other studies (Crabtree and Kjerfve, 1978; Kutas *et al.*, 1994) at Mirranatwa, R_n has a linear relationship with RL↑ (R^2 0.904). The relationship of R_n, with vegetation indices, RL_{net}, RL↑ and temperature; and Ts with dT and T_a are included in Appendix 31 to 35.

5.1.1.9. Closure of the surface radiation budget

The surface radiation budget was calculated after computing the incoming and outgoing R_s and R_L. Table 5.1 shows the averages, as well as the maxima and minima, values of various components of the surface energy budget. A few pixels sometimes show unrepresentative extreme values. The $R_L\downarrow_{net}$ is negative, whereas $R_s\downarrow_{ne}$t in terms of net radiation ranges from 473 to 698 W/m^2.

The net radiation available for the system performance is strongly correlated with the $R_L\uparrow$, albedo and temperature (R^2 between 0.85 to 0.9; Table 5.2).

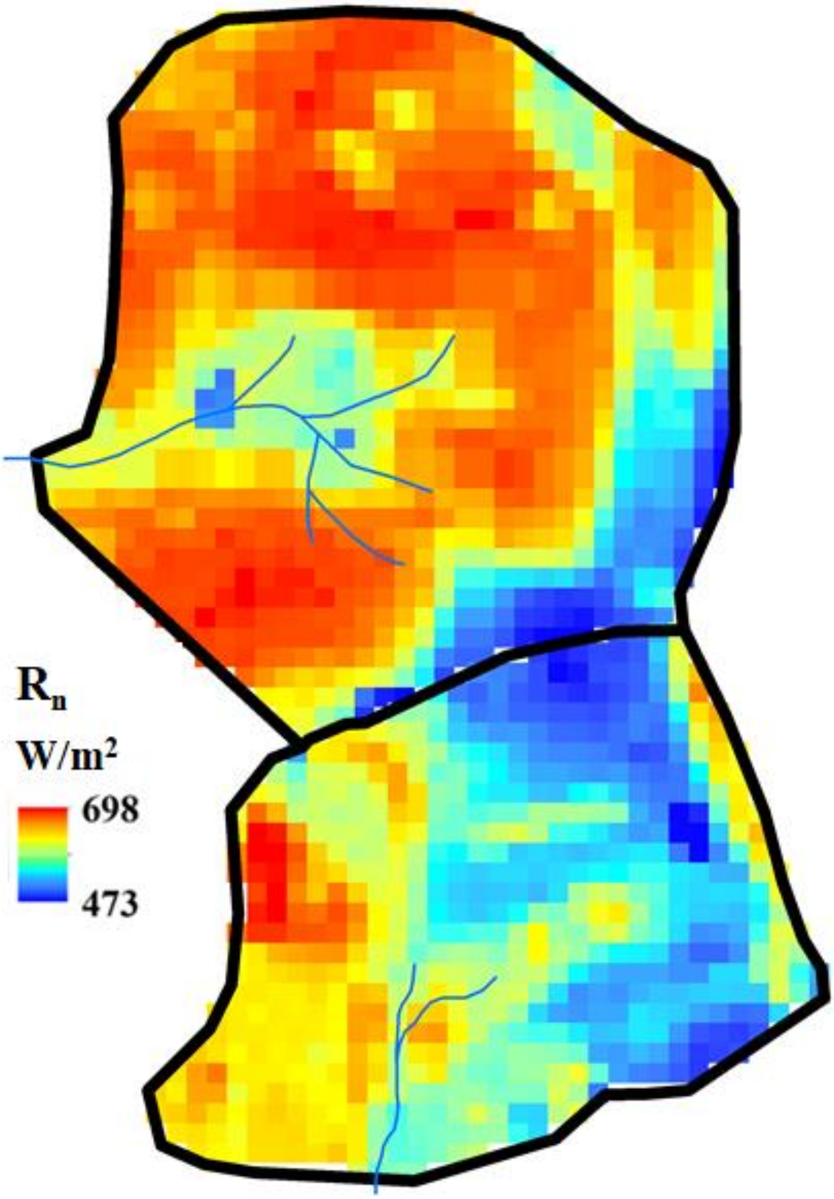

Figure 5.15. The spatial pattern of net radiative flux at the surface.

Table 5-1. Various components of the surface radiation budget.

Parameters			
Gsc (W/m^2)	1367		
Rs↓ (W/m^2)	830		
R_L↓ (W/m^2)	236		
	Minimum	Maximum	Average
RL↑ (W/m^2)	360	402	358
Albedo (α_{surf})	0.02	0.1	0.06
NDVI	0.39	0.81	0.6
SAVI	0.27	0.7	0.485
LAI	0.27	3.05	1.66
Emissivity	0.96	0.99	0.975
Ts (^oC)	9.28	18.64	13.96
Rn (W/m^2)	473	698	585.5

Table 5-2. The correlation between R_n and components of the radiation balance equation.

Net radiation equation components	R^2
Outgoing Longwave radiation	**0.904**
Surface emissivity	0.033
Surface Albedo	**0.861**
Top of the atmosphere Albedo	**0.854**
dT	0.564
Temperature (Surface)	**0.903**
Temperature (Brightness)	**0.902**
NDVI	0.052
LAI	0.405
SAVI	0.485

5.1.2. Surface Energy Balance (SEB)

The available energy (R_n) at the Earth's surface is utilized by surface processes, primarily evaporation and transpiration. The energy utilized for this process depends primarily on soil heat flux (G), sensible heat flux (H) and latent heat flux (λET) as discussed in chapter 4.

5.1.2.1. Soil Heat Flux (G)

G is the portion of R_n that is absorbed or released by the soil at a given time. Generally, it is the smallest component of the energy balance equation (Brutsaert, 1982; Simmers, 1977), however, during day-time under dry conditions with sparse vegetation, it can constitute 50% of R_n (Clothier *et al.*, 1986; Santanello and Friedl, 2002). It is challenging to measure G directly, however, in regional energy balance studies under different crop cover, Kustas *et al.,* (1989 and 1990) concluded that the midday value of the G/R_n ratio was linearly related to the simple ratio and NDVI. Further, they found that the G/R_n estimates for cotton were insensitive to changes in the VIs due to change in solar zenith and azimuth angles. Based on these findings, they proposed a correlation equation to compute the G/R_n ratio. This ratio uses surface temperature, albedo, and NDVI along with the respective coefficients as described in Chapter 4.

Generally, in the study site, the G/R_n ratio ranges from 0.01 to 0.07 at the image pass time (Figure 5.16). In the pasture catchment, the G/R_n ratio is higher than in the plantation catchment, indicating a higher proportion of R_n is used to heat the soil, whereas, in the plantation catchment, the available R_n is utilized for evapotranspiration. Earlier studies also confirm that for bare and sparsely covered soils, G/R_n is maximum during mid-morning and decreases to zero by late afternoon. Fuchs and Hadas (1972) and Idso *et al.* (1975) reported $G/R_n \simeq 0.3$ for bare soil; however, Idso *et al.* (1975) indicated that depending upon the soil moisture, the ratio may vary from 0.5 to 0.3.

Contrary to these findings, Brutsaert (1982) suggested a coefficient of 0.4 and Monteith (1973) proposed a range from 0.1 to 0.5, which was supported by voluminous hourly data from a shortgrass pasture where the average daytime ratio was 0.1 (De Bruin and Holtslag, 1982). For agricultural areas, the ratio may range from $\simeq$0.3 at an early growth stage to $\simeq$ 0.1 at full crop cover. Chaudhry et al. (1987) reported that the ratio is an exponential function of LAI with a correlation of 0.9, and it is considered that remotely sensed VIs might be surrogates for plant phytomass, LAI and percent cover (Hinzman *et al.,* 1986; Kollenkark *et al.,* 1982). Clothier *et al.* (1986) showed a strong linear correlation ($R^2 \simeq 0.76$) between midday G/R_n ratio and exponential NDVI under full and sparse alfalfa cover. However, due to an extreme heterogeneity in landcover and soil properties in the present study site in a rainfed environment, there is a weak correlation between G/R_n ratio and VIs.

For the plantation catchment, with a good tree cover, the G/R_n ratio is close to 0.01, which agrees with previous studies (Santanello and Friedl; 2003; Kutas and Daughtry, 1990; Clothier *et al.,* 1986; Kustas *et al.,* 1993). The pasture catchment and low-lying area in the plantation catchment have higher G/R_n values due to thin vegetation cover and high salinity respectively, which is also in confirmation to previous research (Fuchs and Hadas, 1972; Idso *et al.,* 1975).

The correlation between G/R_n ratio and RL↑, $\alpha_{surf,}$ T_s, dT and T_a is shown in table 5.3 and Appendix 35. The ratio is strongly correlated with outgoing longwave radiation and surface temperature.

Table 5-3. The correlation between G/R_n ratio and components of the radiation balance equation.

Net radiation equation components	R^2
Outgoing Longwave radiation	**0.86**
Surface Albedo	0.55
T_s	**0.86**
dT	0.54
T_a	0.54

Heat conduction through soil is determined by the ability of the soil to change temperature. The interaction between surface and subsurface energy transfer processes has led to detailed investigations of soil heat flux (G) for a wide variety of agricultural systems (Sauer and Hortont, 2005; Malek, 1993). The G determines the available energy for latent and sensible heat transfer, as well as the energy flow path that couples soil and atmospheric systems. Higher accuracy in G estimation can lead to a reduction in errors encountered in H and λET.

Soil Heat Flux (G) is computed by multiplying G/R_n ratio with R_n. The soil heat flux is lower for the plantation catchment except for the low-lying saline areas. Pasture catchment has an overall high G except for plantation and cropped areas (Figure 5.16). Soil surface layer properties including soil textural properties, surface water content and type of vegetation cover impact the partitioning of the incident radiation (Sauer and Hortont, 2005).

Within plantations, the patches having better tree growth have lowest G. In contrast, the pastures on higher slopes or in low lying areas with higher salinity due to shallow groundwater have the highest G values. Water is an excellent heat absorbent, and therefore the farm dams have the highest G value.

Once the G value is calculated, the available energy (R_n – G) can be computed. It is clear from Figure 5.17 that the plantation, cropped areas and areas of natural vegetation have the higher available energy (> 640 W/m^2) for evaporation and transpiration processes, as compared to pastures where it ranges between 537 to 640 W/m^2.

5.1.2.2. Sensible Heat Flux (H)

It is a surface energy balance component which is associated with the change in energy of a system due to heat exchange. This flux is extremely sensitive to factors like dynamics of the turbulent heat transport system, natural landscape, and vegetation structure. The model was run twice to incorporate the impact of different major landcover (pasture and plantation) on turbulent heat transport, once using the vegetation properties of pasture and then the plantation.

The surrounding temperature plays a crucial role in determining the H. The two complex components required to compute equation 4.2.5 are aerodynamic resistance to heat transport and the temperature difference between two heights for anchor pixels. These two heights are assumed as cold and hot layers, so first in the image two sets of clusters of pixels, representing the hot and cold area, were selected as explained in section 4.2.2 (Figure 5.18).

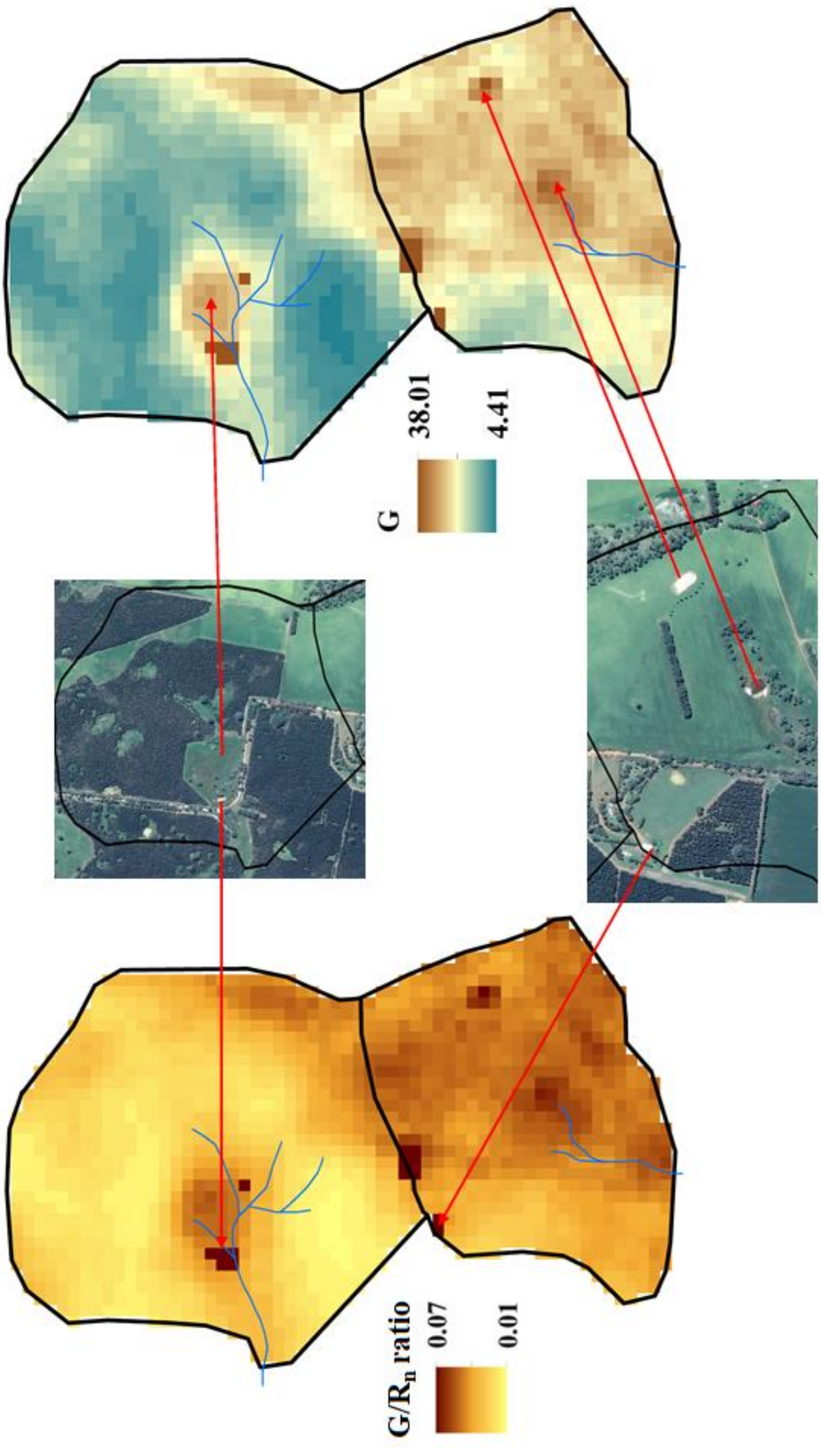

Figure 5.16. The spatial response of G/R_n ratio and Soil Heat Flux (G).

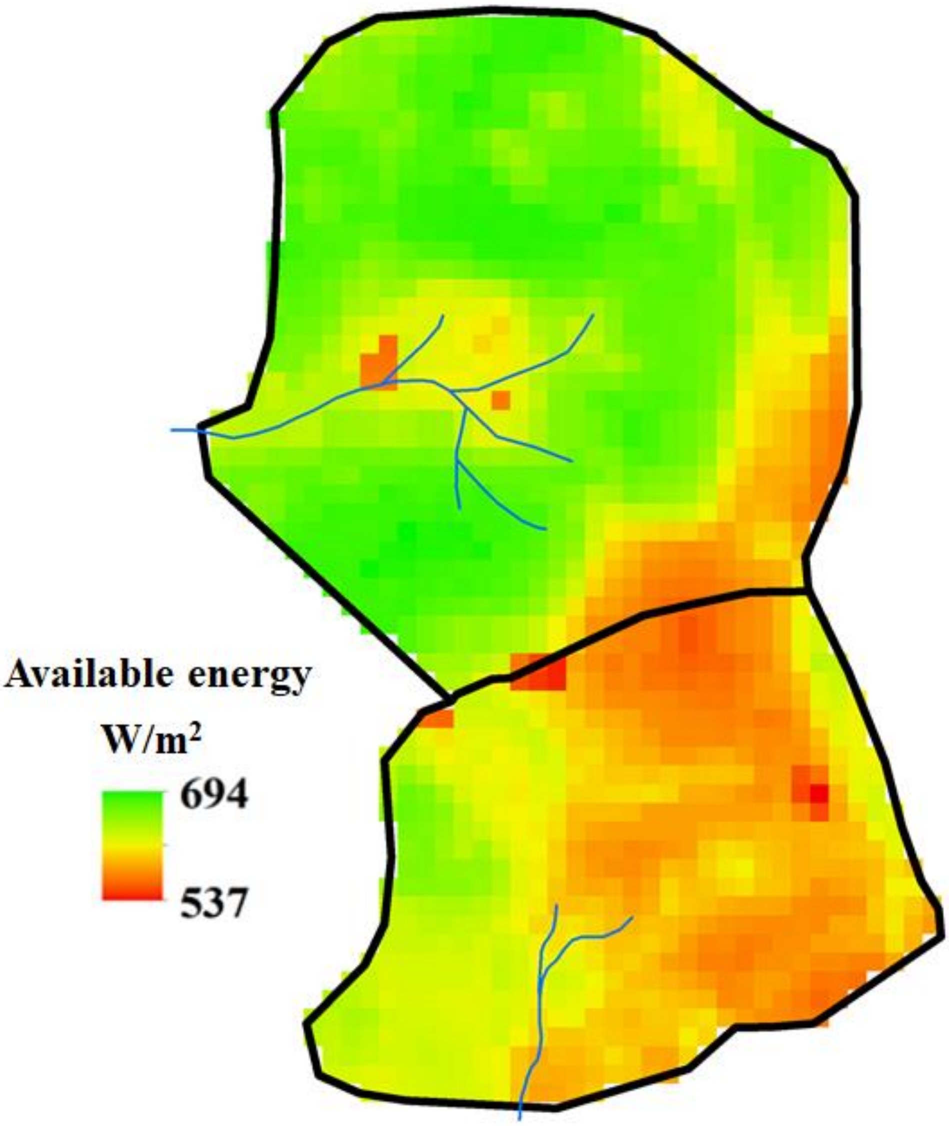

Figure 5.17. The available energy for evapotranspiration processes.

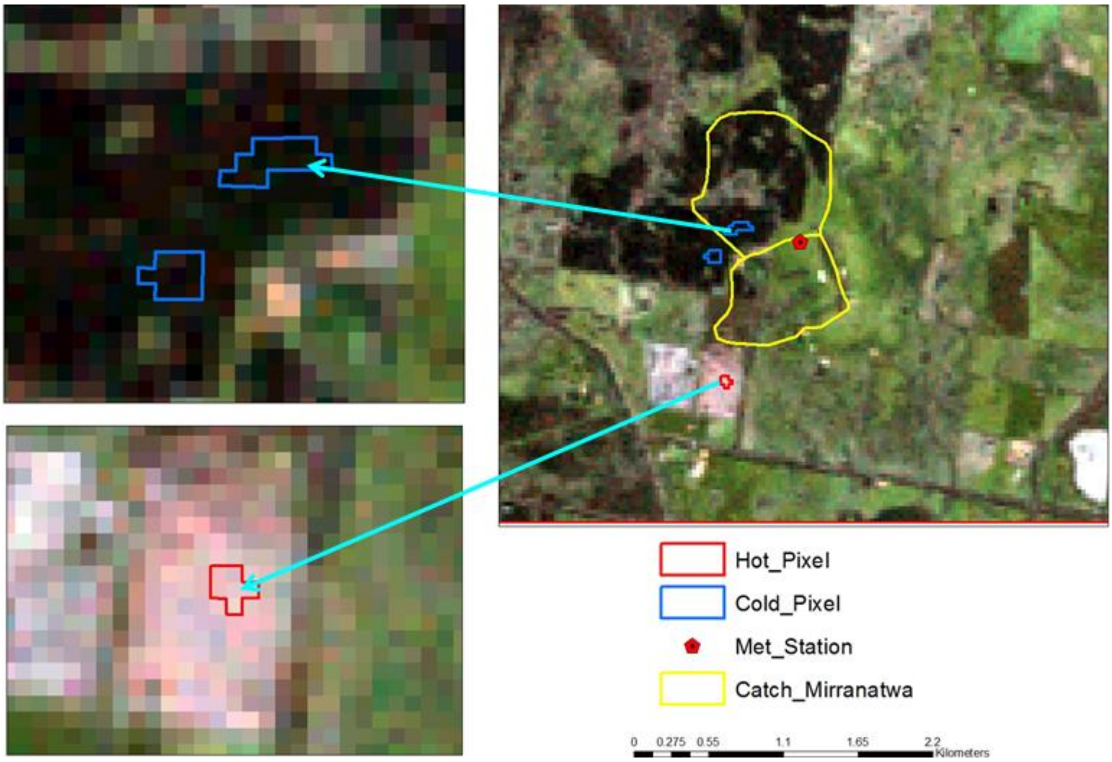

Figure 5.18. Forested area and bare ground representing 'Cold' and 'Hot' Pixels.

For the aerodynamic resistance to heat transport, the friction velocity of each pixel is required. First, the friction velocity both at the weather station and at the blending height was computed. Assuming neutral conditions, the friction velocity at the weather station on the satellite pass day/time was 0.07, whereas, at the blending height, it was 1.82.

The other components computed for aerodynamic resistance equation are momentum roughness length (Zom_{pix}) and friction velocity of each pixel ($\mu*_{pix}$) (Figure 5.19). The roughness length varies from 0.05 to 0.005: higher for pastures and lower for the cropped area and plantations: this may be due to the small study area and open young tree canopy. The friction velocity ranges from 0.07 to 0.1 and follows the response of Zom_{pix} for pasture and plantation (Figure 5.19).

High variability in the Zom_{pix} for different land covers is reported. This variability may be due to local vegetation conditions (structure, heterogeneity and type) as well as the time of the year (Hansen 1993; Stanhill, 1969; Monteith, 1973; Garratt, 1978; ESDU, 1972; Rider *et al.*, 1963; Barad, 1959; Ripley and Redmann, 1976; Luers *et al.*, 1981; Panchal and Chandrasekharan, 1983). The *Eucalyptus* plantation has a low μ^*_{pix} probably due to vertical and horizontal gradients as compared to the pasture.

The final parameter required to compute H is the air temperature. Since there is no direct method for computation of the spatial pattern of air temperature under variable landcovers, an indirect method was adopted to calculate the near-surface temperature difference (dT) for each pixel, assuming a linear relationship between surface temperature and dT as proposed by Bastiaanssen *et al.,* 2005, and Allen *et al.,* 2011). The correlation coefficients for this linear relationship were computed by plotting temperature and dT of the respective ‘hot’, and ‘cold’ pixels identified earlier. For the satellite pass day and time, using the correlation equation (eq. 4.2.12), dT was computed. Finally, the temperature difference (dT) and surface temperature (T_s) images used to calculate air temperature (T_a). There is a 5°K temperature difference between the maximum and minimum dT: higher in the plantation and lower in the pasture, which is reflected in T_a as well. The air above the pasture is warmer than plantation due to more energy loss in terms of outgoing longwave and shortwave radiation.

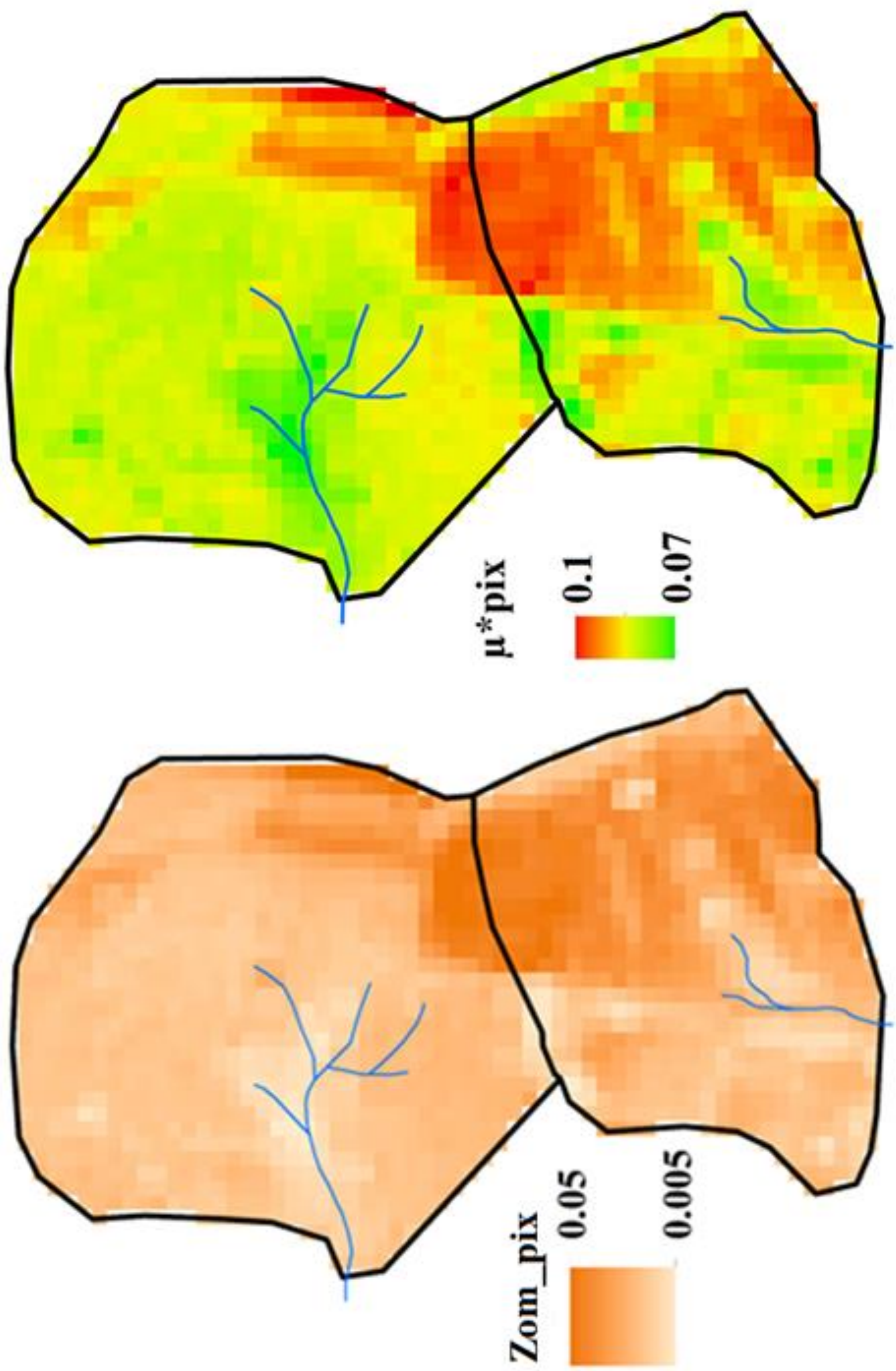

Figure 5.19. Momentum roughness length (Zom_{pix}) and Friction velocity ($\mu*_{pix}$).

Over large landscapes, it is well-documented that T_s, T_a, and dT are related to cloud cover and wind speed, and spatial correlation patterns are consistent over time (Pepin and Norris, 2005; Samson, 1965; McCutchan, 1983; Richner and Phillips, 1984; Tabony, 1985; Barry, 1992). The main controls over dT highlighted are cloudiness, topographical characteristics and snow cover; out of these the only relevant parameter for the study site could be topography, as the area is snow-free and the Landsat image was cloud-free for the study site. However, the small size of the catchments with low topographical range may not be as important as the contrasting vegetation which might be responsible for the difference in dT. There are not many studies highlighting dT and Ta under contrasting landcovers in a rainfed agricultural system; however, there are several studies on the impact of trees and grass on urban heat islands compared to the rural landscape. These studies indicate that trees and grass can play a substantial role in reducing regional and local temperatures during the summer within the urban landscape (Armson *et al.,* 2012; Tan *et al.,* 2016; Derkzen *et al.,* 2015; Rahman *et al.,* 2015). Guan (2011), while studying the T_s and T_a of various surfaces, concluded that there is a strong correlation between T_a and T_s. A study conducted in Manchester, UK, indicated that grass reduced maximum surface temperatures by up to 24 °C, while tree shade reduced by up to 19 °C. The other studies also found similar trends; however, substantial variability observed in the magnitude of the near-surface air temperature, probably due to atmospheric turbulence and landcover (Rosenzweig *et al.,* 2006).

Using all the required components and assuming the neutral conditions, an initial sensible heat flux (H) calculated for both the catchments considering the aerodynamic resistance (model 019 - Appendix 27). The overall H value ranges from 108 to 477 W/m^2 in the study area: for the plantation catchment > 382 W/m^2 and for pasture < 382 W/m^2 (Figure 5.20). Fisch *et al.* (2004) reported that in dry conditions, H is very high for areas that were converted from tropical forest in the Amazon region probably due to modification of the dynamics of the boundary layer as compared to the forest. Yunusa *et al.* (2011 & 2015) reported a significant H under conditions of limited soil moisture and inactive canopy cover/mutual shading in plantations caused by the solar angle or dormant phase of grassland.

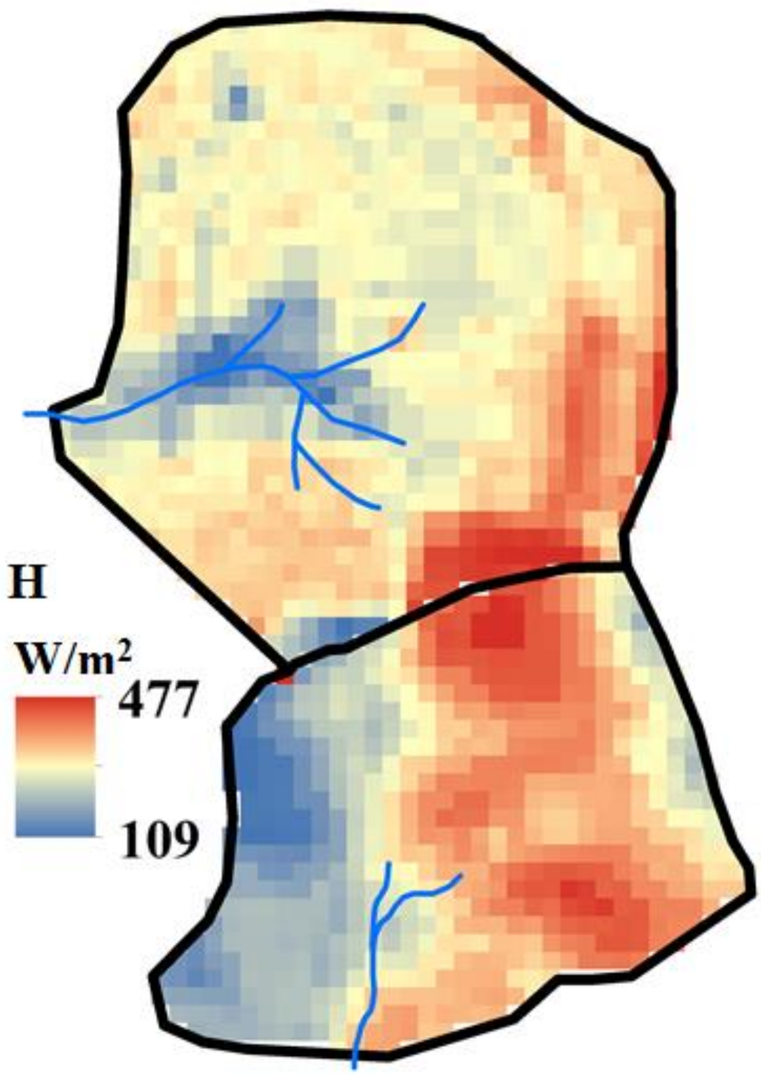

Figure 5.20. Variability of Sensible Heat flux (H) in both the catchments.

Monin-Obukhov Length (L) was computed using (Appendix 28) to assess the buoyancy effects due to atmospheric turbulence under major landcover and the prevailing stability condition at satellite pass time. The stability conditions were neutral at the satellite pass time as the wind was < 1 m/sec (Figure 5.21); therefore, the initial H computed earlier was used.

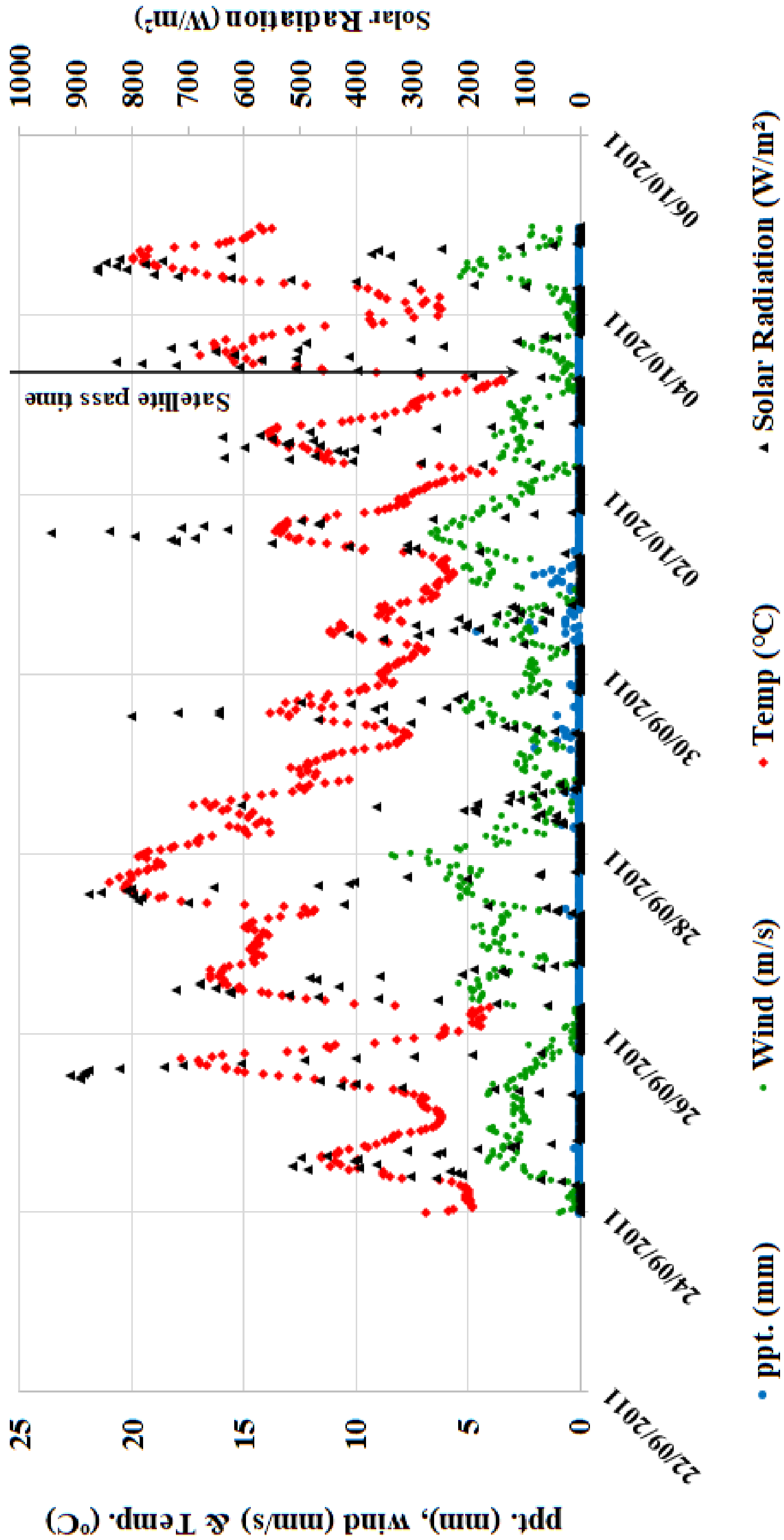

Figure 5.21. The climatic variables measured at the weather station before and after the satellite pass time.

5.1.2.3. Latent Heat Flux (λET)

The λET computed by rearranging the net energy equation (eq. 4.2.2). Generally, it is observed that there is a daily as well as the seasonal shift in λET depending upon the soil water availability, vegetation type, rainfall and latitudinal gradient (Waterloo *et al.,* 1999; Yunusa *et al.,* 2008 and 2011; Wilson *et al.,* 2002; Schneider *et al.,* 2012; Rosset *et al.,* 2001).

At Mirranatwa study site, λET ranges from 118 to 344 W/m^2 (Figure 5.22), generally higher for plantation, cropped area and natural vegetation, and lower for pasture which is in agreement with previous studies (Wilson *et al.,* 2002; Wilson and Baldocchi, 2000; Wilson and Ludlow, 1991). Yunusa *et al.* (2008) partitioned turbulent heat between λET and sensible H in a setting of a 6-year old plantation and a 16-year-old grassland and found that λET in the plantation was at least twice as large as on the grassland during a heatwave. The afternoon ambient temperature over the plantation was 5 °C lower and an average 1.2 °C lower for the entire day as compared to grassland. The consistent low λET and H can make grassland a source for advective energy, whereas the plantation response is opposite. However, this response further depends upon the latitudinal range: the mid-latitudinal response is to have higher λET for evergreen woody vegetation as compared to grassland, whereas in northern latitudes (>35°), a smaller λET for the coniferous forest was observed (Yunusa *et al.,* 2008).

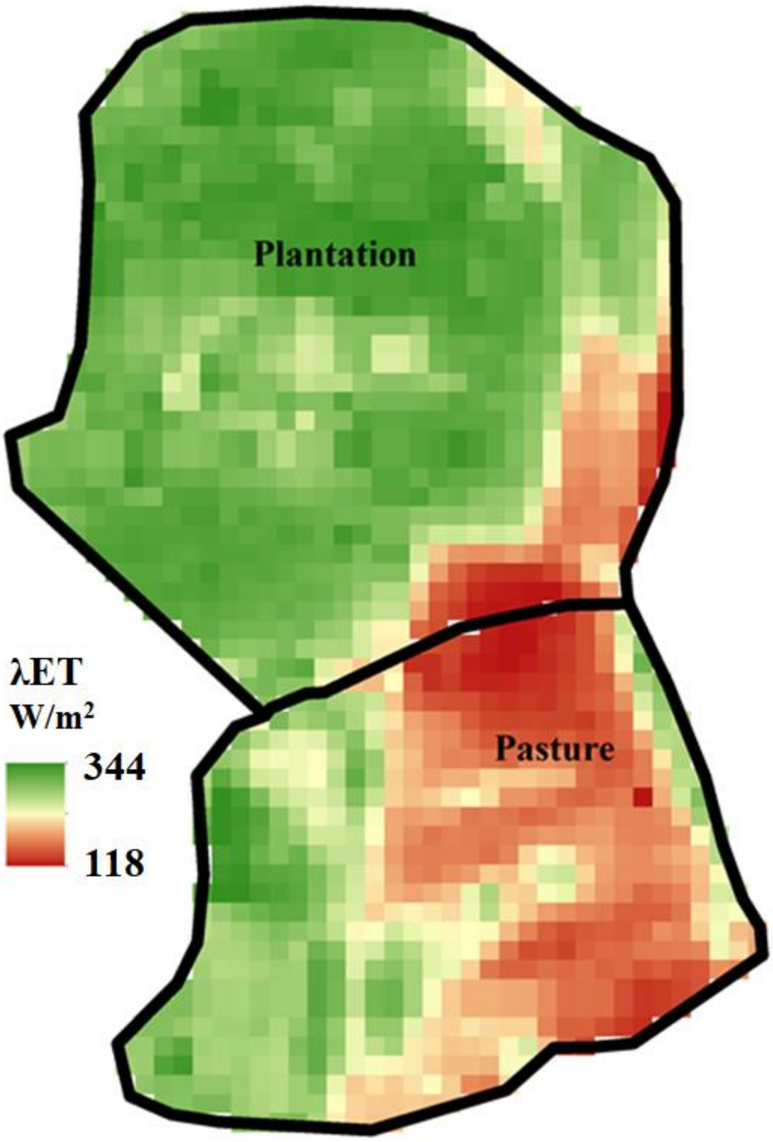

Figure 5.22. Latent Heat Flux (W/m^2) variability in the study catchments.

5.1.2.4. Evapotranspiration

A. Instantaneous ET (ET_{inst})

ET_{inst} computed using equation 4.2.32 (Chapter 4) and the latent heat of vaporization of water. The ET_{inst} ranges from 0.19 to 0.55 mm/hr (Figure 5.23), following the pattern of λET; higher for plantation, cropped area and natural vegetation and lower for pasture, which is in agreement with previous studies (Wilson *et al.,* 2002; Yunusa *et al.*, 2008; 2010a; 2010b; 2012 & 2015).

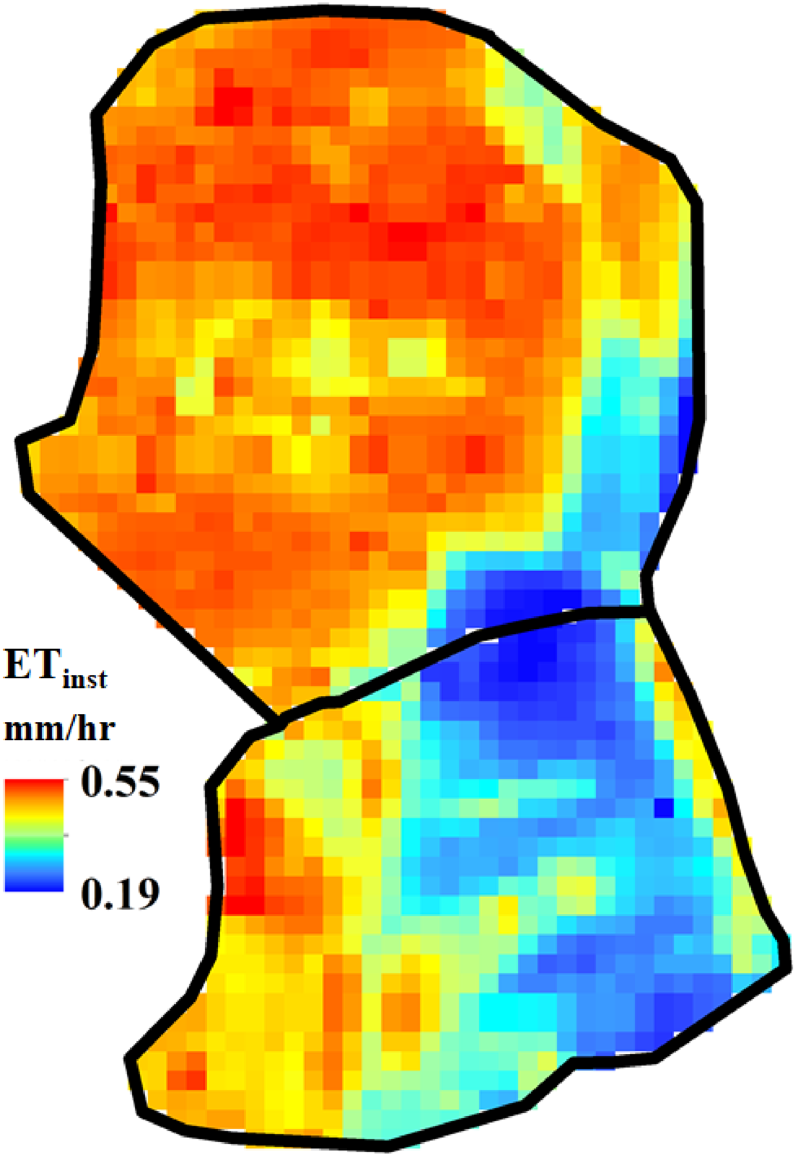

Figure 5.23. The spatial pattern of instant ET (mm/hr) in plantation and pasture catchment.

B. Reference ET Fraction (ETrf)

The ETrf is a ratio of the ET_{inst} of each pixel to the reference ET (ET_r or ET_o) which was computed using RefET model. The reference ET (ET_r or ET_o) value for the closet time to the satellite pass time, was used from the RefET model output file.

ET_rf for plantation, crop and forest are higher than pasture. Generally, it is assumed that for a pixel representing dry soil, the fraction can be 0 and the one representing wet with full vegetation cover may have a value of 1. However, on the other extreme, since there are quite a few assumptions made in the computation of various variables, negative values can also be expected. In the study catchments, ET_rf ranged between 0.2 to 0.6; for healthy plantations with shallow groundwater close to 0.6 and pastures at higher elevations close to 0.19 (Figure 5.24).

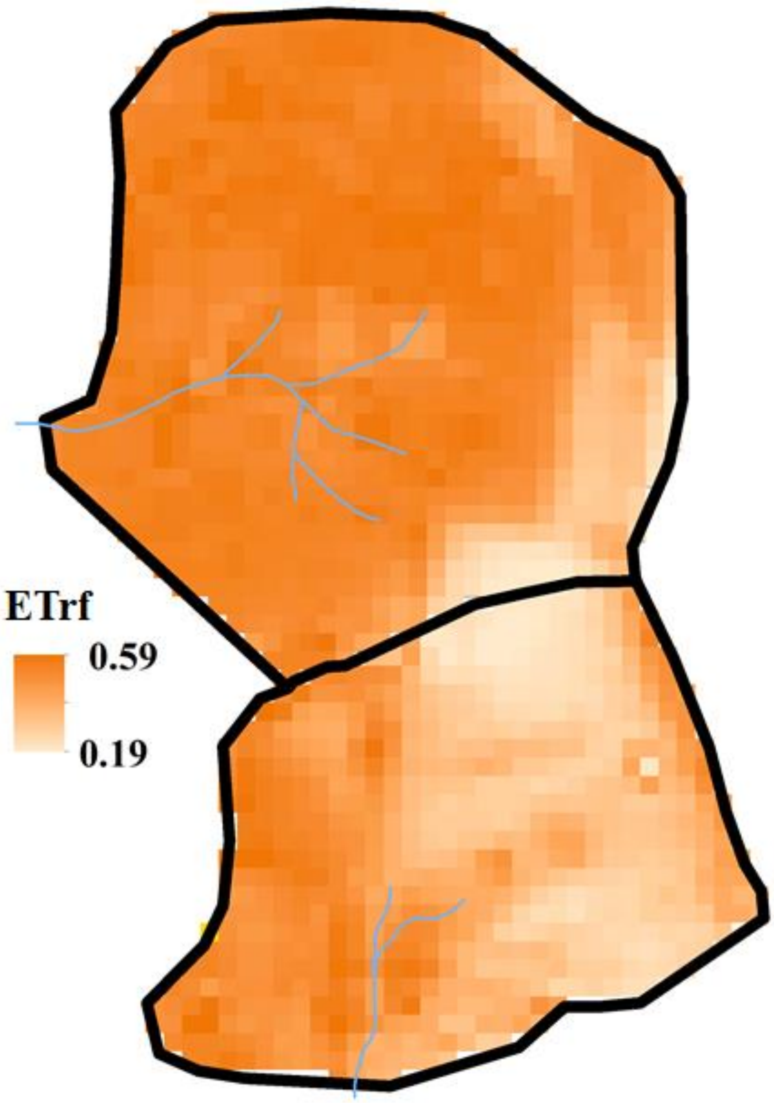

Figure 5.24. The fraction of ET_r or ET_o in study catchments.

C. Daily Evapotranspiration (ET_{24})

ET_{24} computed using accumulative daily adjusted reference ET from the RefET model output (Section 4.2.2.2.) for the satellite pass-day (Figure 6.25). The daily ET ranges from 1.5 to 4.2 mm/day. Generally, all the plantation blocks, low-lying cropped areas and natural vegetation have higher ET_{24}. Pastures, on the contrary, show lower ET_{24}, which is in agreement with previous catchment-scale studies (Roohi *et al.,* 2015 & 2016a; Roohi and Webb, 2016b; Dean, 2013; Dean *et al.,* 2014, 2015; Yunusa *et al.,* 2015, 2010a & 2010b; Cattin 2007; Eugster and Cattin, 2007; Gwenzi *et al.,* 2012; Kelliher *et al.,* 1993; Moore, 1976; Priante-Filho *et al.,* 2004; Roberts *et al.,* 2005; Rost and Mayer, 2006; Schneider *et al.,* 2012; Waterloo *et al.,* 1999; Camporese *et al.,* 2014; Adelana *et al.,* 2015; Dresel *et al.,* 2018).

The instant and daily ET were compared at the catchment scale as well as for various landcovers. The higher ET_{inst} and ET_{24} of the plantation, forest and crops can be attributed to rainfall before satellite pass time, higher available R_n, and lower G. The young, healthy plantation has the highest ET within the plantation catchment. Both the ET_{inst} and ET_{24} rates are low at the periphery of the plantation blocks, at higher elevations with deep groundwater and saline patches at low elevation (Figure 5.26 & 5.27).

The pasture catchment has an overall higher ET compared to the plantation catchment ranging from 2.59 to 4.20 mm/day. Generally, higher ET characterises cropped areas, low lying plantation areas with shallow groundwater and an old forest. Among the pastures, clover, capeweed and annual grasses, despite having an almost similar response of G, H and λET, have the lowest ET (Figure 6.26 & 6.27), probably due to a shortage of soil moisture in elevated areas and limited root system of annuals. In contrast, *Phalaris* sp., ryegrass and perennial grasses in low lying areas have higher ET, similar to the young plantation. McNaughton and Jarvis (1983) observed a similar response: higher transpiration from grassland and arable crops as compared to the forest.

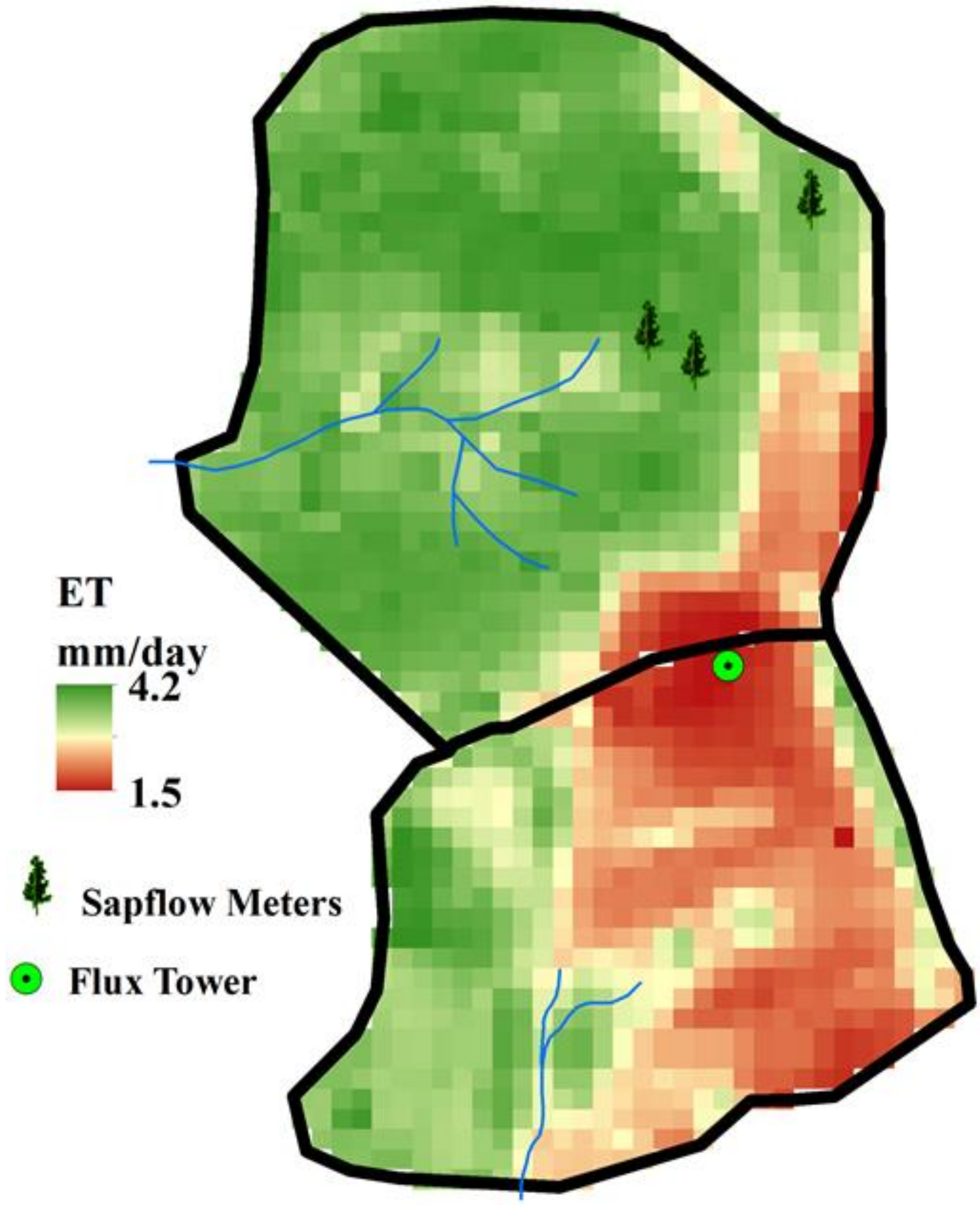

Figure 5.25. Daily evapotranspiration pattern in plantation and pasture catchment at Mirranatwa study site.

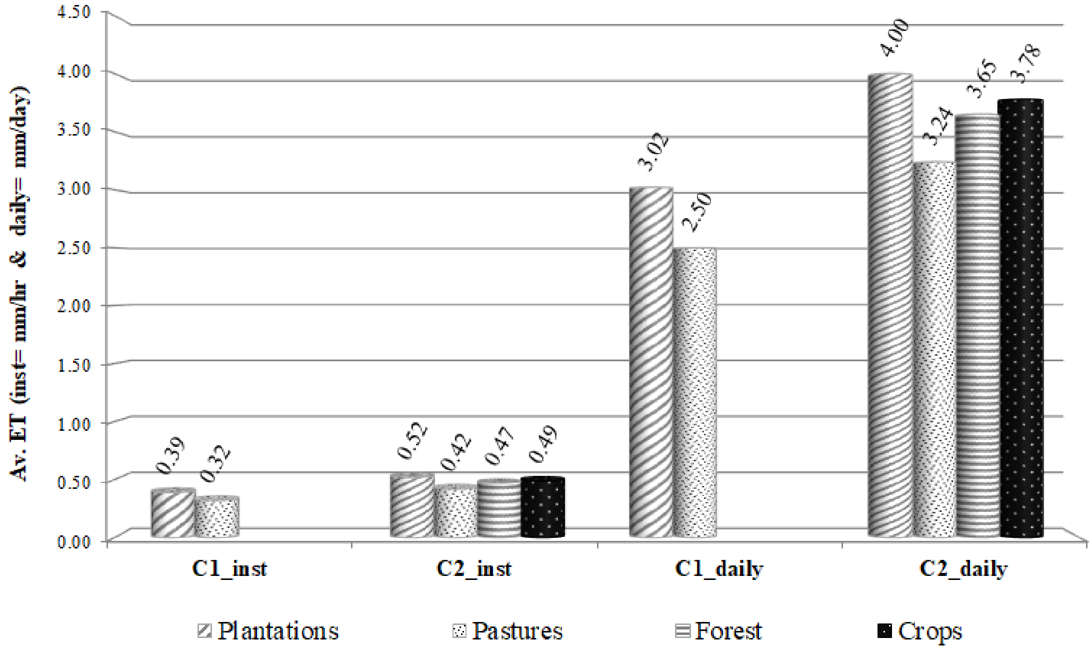

Figure 5.26. Catchment-wise ET response of various landcover in plantation (C1) and Pasture (C2) catchments.

The natural forest of *Eucalyptus regnans*, in the eastern part of the pasture catchment, has well-established trees probably with access to groundwater, resulting in higher ET. In the cropped area, a farm dam close to the south-western boundary and good crop cover is responsible for a higher ET.

Liu et al. (2010) observed that, within the same climatic and meteorological conditions, ET exhibits remarkable spatial variability across different landcovers and agricultural species; this is in line with the observed responses in the small Mirranatwa catchments (Roohi *et al.*, 2015 and 2016a; Roohi and Webb, 2016b).

Annual grassland ET is generally lower than that of plantation by 54% (Yunusa et al., 2015) to 15-20% (Roohi and Webb, 2016b). In a long-term comprehensive pasture and plantation catchment study (Dresel et al., 2018), it was observed that the annual actual pasture ET was 87 to 93% of precipitation. In contrast, plantation ET exceeded 102-108% of annual rainfall

(Dean, 2013). The fact that actual ET was higher than rainfall was attributed to the high groundwater uptake by the extensive root system of the trees.

At the Mirranatwa study site, on average, the pasture has 18% lower ET_{inst} and 5% ET_{24} than the plantation. The smaller difference in daily ET may be due to the low ET from plantations at a higher elevation with deep groundwater. The response of plantation vs forest and plantation vs crop is opposite to that of plantation vs pasture; 6 % and 13% higher ET_{inst} and 5% and 13% $ET_{24,}$ respectively. Even though *E. regnans* trees were well established with deep and extensive root systems, due to an open canopy they could not achieve the same high ET as the plantation. On the other hand, the cultivated oats, due to access to better moisture in the low-lying area, the presence of a farm dam and better crop cover had a similar high ET to the plantation.

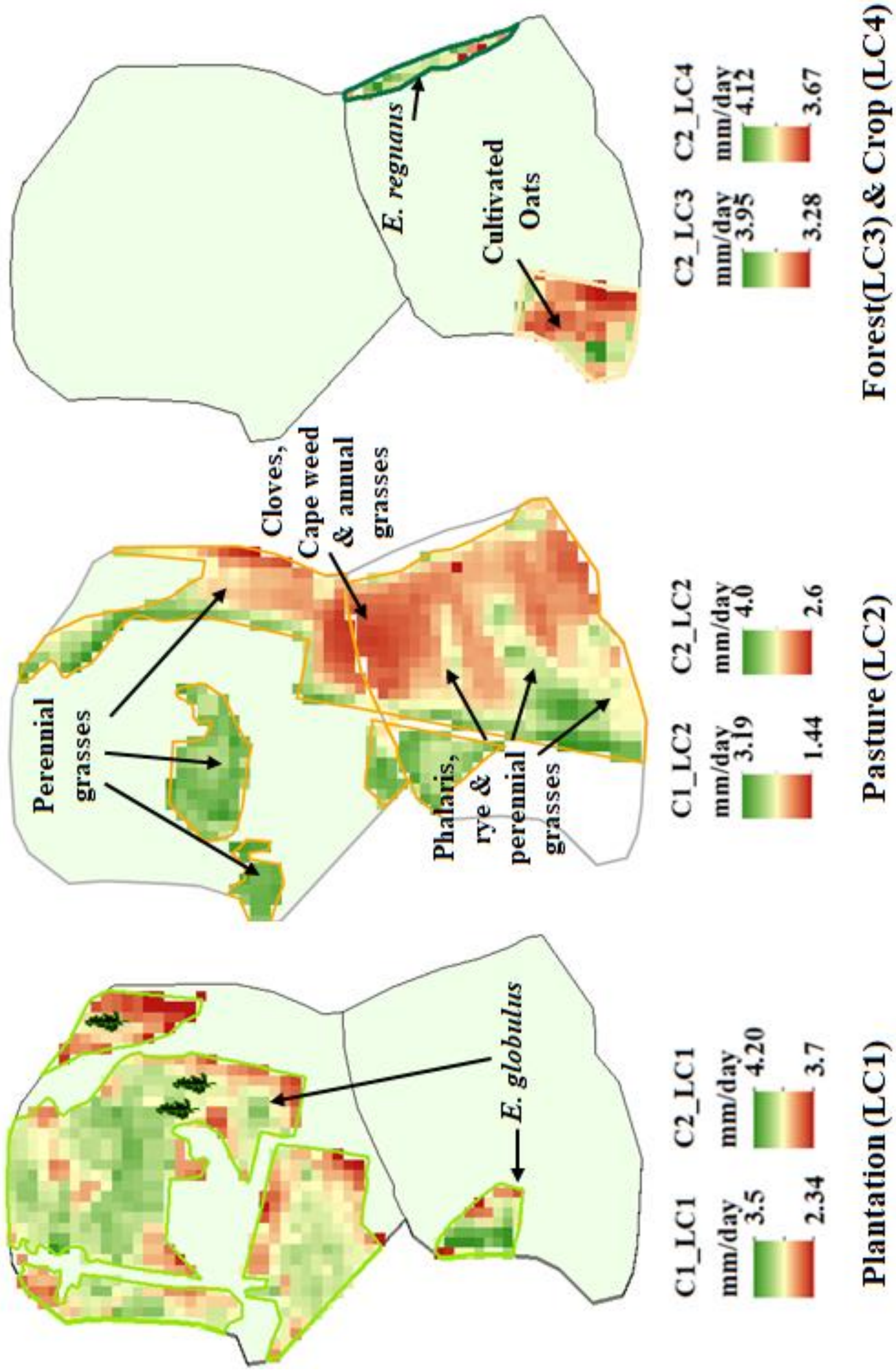

Figure 5.27. Differential response of landcover in plantation and pasture catchments.

5.1.2.5. Closure of the surface energy budget

A summary of the various components of the surface energy budget along with ETinst, ETrf and ET_{24} are included in the table 5.4. The table shows the averages, as well as the maxima and minima values of various components. A few pixels sometimes show unrepresentative extreme values. Considering the average values of net available energy (R_n) and it's users in terms of soil heat flux (G), sensible heat flux (H) and latent heat flus (λET) there is only difference of 38 W/m^2, which may be due to small area with heterogenous landcover and several assumptions made while computing various radiation and energy balance components.

Table 5-4. Surface energy balance components.

Parameters	Minimum	Maximum	Average
G (W/m^2)	4.41	38.01	22.21
H (W/m^2)	109	477	293
λET (W/m^2)	118	344	231
ET_{inst} (mm/hr)	0.19	0.55	0.37
ETrf	0.19	0.59	0.39
ET_{24} (mm/day)	1.5	4.2	2.85

Note: A few pixels sometimes show unrepresentative extreme values, the averages, as well as the maxima and minima, have been given.

5.2. Comparison of model estimates

The output of the SEBARA algorithm was compared with field measured values, the CATHY Model (Camporese *et al.*, 2014 and 2013), Bowen ratio (β) and Evaporative fraction (ETf) which is the ratio of λET to the sum of available energy in terms of λET and H.

5.2.1. SEBARA vs. Field Measurements

At the location of flux tower and sapflow meters, the output values of SEBARA model was compared with field measurements including flux tower and adjusted sapflow readings (Table 5.5). The catchments are small (plantation 0.813 km^2 and pasture 0.514 km^2) and the only high spatial and temporal resolution data available for comparison was from these instruments. The nearest weather stations are more than 20 and 29.9 km away respectively from the catchments and have daily climate data. The image pass time is a fraction of a second, so the best option for comparable data is the climatic data available at the site. Since the size of the pixel corresponding to the weather station/sapflow is 30m and the corrected data from the instruments was used, it is assumed that there is no advection effect.

The daily ET estimates of SEBARA is 4.55% lower than the measured value at the flux tower, however, for the plantation, in comparison with ET obtained from average adjusted sapflow readings (Dean, 2013), SEBARA overestimated (12.97 %). The sapflow readings represent only the transpiration component of ET and considering daily soil evaporation, SEBARA estimates for actual ET may be more representative. Dean (2013), using three sapflow meters set up at different locations within *Eucalyptus* plantation, found variability in annual transpiration (388.3 ±20 mm). After incorporating the canopy interception and soil evaporation, the variability in actual ET for plantation was even higher (642.0±78.1 mm). The high variability in transpiration (±20 mm) and actual evapotranspiration (±78.1 mm) may be due to spatial variability within plantation as shown in Figure 5.26 and 5.27 therefore, the overestimation of SEBARA can be justified.

Furthermore, in SEBARA, several assumptions are made which may be responsible for overestimation; however, Similar accuracy levels were achieved in previous studies as well (Karimi and Bastiaanssen, 2015).

Table 5-5. Comparison of SEBARA output with various approaches.

Catchment	ET (Instrument /Technique)	ET (mm/day)	Over (+)/ Underestimates (-)
Pasture	Eddy Covariance	2.86	-4.55
	RefET (ET_o)	2.97	-8.08
	CATHY	2.37	+15.18
	SEBARA (Pasture)	**2.73**	
Plantation	Sapflow (Adjusted)	2.62	+12.97
	RefET (ET_r)	2.97	-0.34
	CATHY Model	2.37	+24.89
	SEBARA (Plantation)	**2.96**	

5.2.2. SEBARA vs. RefET model output

Using the climatic data and the RefET model (FAO 56 PM approach), reference ET (ET_r and ET_o) was calculated for both the catchments. Comparison with SEBARA values shows reasonable agreement (8% lower for pasture and 0.34% higher for plantation).

5.2.3. SEBARA vs. CATHY Model output

Catchment Hydrology (CATHY) distributed model (Camporese *et al.*, 2013) was used to compute the daily ET using climatic data from the flux tower at the study site. SEBARA overestimated ET for both the pasture and plantation catchments (15.18% and 24.89% respectively).

5.2.4. Bowen ratio (β)

It is a ratio of H and λET (Fritschen, 1965; Sturman and Tapper, 1996; Bowen, 1926) and generally used to calculate heat loss/gain by a substance. When the magnitude of β is less than one, a higher proportion of the available energy at the surface is passed to the atmosphere as λET than H, and the reverse is valid for the $\beta > 1$. In the study area, β ranges from 0.32 to 4.1; higher for elevated and dry areas and less for areas with good vegetation cover (Figure 5.28). The β ratio in semiarid landscapes ranges from 2.0 to 6.0 and for temperate forests and grasslands is 0.4 - 0.8 (https://en.wikipedia.org/wiki/Bowen_ratio). The lower λET for pastures in both the catchments resulted in a higher Bowen ratio, which reflects the fact that the pasture loses more heat (Figure 5.28). The shallow root system of pastures depends on the soil moisture or shallow groundwater and therefore, cannot utilize the available energy for enhanced ET (Bastiaanssen, 2000). This extra energy was either lost as longwave radiation or used to heat the ground, resulting in higher surface temperature. Pastures at lower elevations, especially close to the drainage network, have a relatively lower β ratio reflecting that more energy was utilized for ET due to the available soil moisture. The β ratio of pastures on elevated areas with deep groundwater was the highest. Generally, large variability in the β ratio is reported for Mediterranean climates, with values up to 6 with increasing aridity (Wang *et al.*, 2006; Dugas *et al.*, 1991).

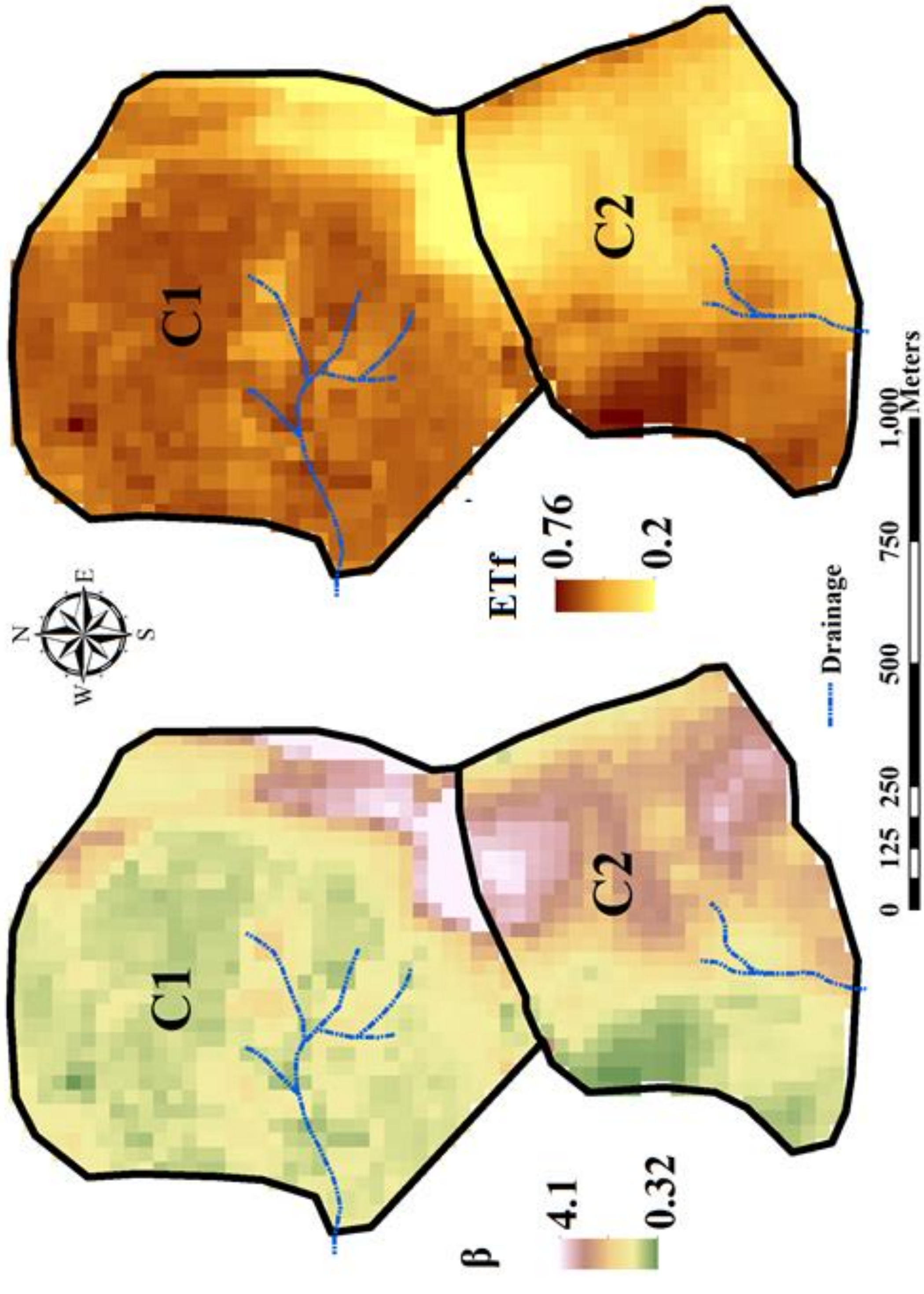

Figure 5.28. Spatial variability of Bowen Ratio (β) and an evaporative fraction (ETf) in plantation (C1) and pasture (C2) catchments.

5.2.5. Evaporative fraction (ETf)

ETf (the ratio of λET to the sum of available energy in terms of λET and H) can be used as a diagnostic test for surface energy partitioning during the daytime, especially under variable landcover. Partitioning of available surface energy into λET and H depends upon the soil moisture and therefore impacts the ETf. Figure 5.28 represents the spatial pattern of ETf, more for plantations and less for pastures. The low ETf indicates that pastures could not utilize the available energy due to limited soil moisture in shallow soil layers. Therefore, energy is lost either as longwave radiation or used to heat the surface, which is also confirmed by earlier studies (Wang *et al.*, 2006; Dugas *et al.*, 1991). Within plantations, low-lying areas with shallow groundwater can utilize more available energy for higher ET than plantations at elevated areas with deep groundwater, and this is reflected in higher ETf values for the plantation at low elevation. However, Nichol and Cuenca (1993) observed no correlation between the ETf and soil surface moisture as well as soil moisture. Gentine *et al.* (2011), in a study based on a model of the soil–vegetation–atmosphere, concluded that any phase difference between the λET and H, as mean values or daily amplitudes, can alter the pattern of ETf.

Chapter 6. ET vs. Groundwater

Groundwater plays an essential role in regulating ET, especially in arid and semi-arid regions where ET not only reduces the available groundwater resource but also causes soil salt accumulation particularly in SE Australia (Adelana *et al.,* 2015; Benyon *et al.,* 2006; Tweed *et al.,* 2007; Dresel *et al.,* 2018). The groundwater - ET relationship depends upon factors like groundwater depth, and upward movement; capillary rise, soil type and adaptative plant strategies.

Daniel (1976) observed capillary flux or negative groundwater recharge upward from the aquifer to the root zone to maintain a high rate of ET, as observed in several subsequent studies (Yeh and Famiglietti, 2008; Luo *et al.*, 2009; Satchithanantham *et al.*, 2017; Lubczynski, 2000 & 2011; Groeneveld *et al.,* 2007; Tyler *et al.,* 1997).

Plants can extract moisture from deep soil layers to maintain their evaporative demand, especially during the growing season (Yeh and Famiglietti, 2008 and 2009). However, this depends upon the proximity of the capillary fringe to the plant root system, the anaerobic conditions of the saturated zone, soil type, water table depth and plant species (Nichols, 1993a, 1993b & 1994; Miller and Eagleson, 1982; Theiveyanathan *et al.*, 2005; Colville and Holmes, 1972). Gardner and Fireman (1958) demonstrated that the upward movement of groundwater to plant is possible when the water table is more than 10 meters deep. This phenomenon was also observed by Nepstad *et al.* (1994) for Brazilian closed forests, where during dry seasons the forest depends upon the deep root systems to access water from deeper soil moisture or groundwater to maintain green canopies. Some of these evergreen forests can absorb water from depths of more than 8 meters.

Plant water availability depends upon the type of vegetation cover. Comparison of three ecosystems (mature evergreen mixed forest with 171 species, pasture and second-growth forest on abandoned pasture-land) showed that in both dry and wet seasons, plant water availability was lowest under the forest and highest under the pasture (Jipp *et al.,* 1998).

To optimize the available resources in the soil column, plant's adaptative strategies, especially in water-limited environments, include the development of deep root system and the use of hydraulic redistribution (hydraulic lift) or reverse sap flow in roots (Brooks *et al.,* 2002; Oliveira *et al.*, 2005; Burgess *et al.,* 1998 & 2001; Dawson, 1993 & 1996; Ryel, *et al.,* 2002 and 2003; Caldwell *et al.,* 1998; Horton and Hart, 1998; Ludwig *et al.*, 2003; Richards Espeleta *et al.,* 2004; Richards and Caldwell, 1987; Scholz *et al.*, 2002; Brooks *et al.,* 2002; Nambiar, 1990; Falkiner *et al.*, 2006). A comprehensive analysis of the maximum rooting depth of 253 woody and herbaceous species concluded that the rooting depth varies from 0.3 meters for some tundra species to 68 meters for *Bosscia albitrunca* in the central Kalahari Desert (Canadell *et al.*, 1996). Further, it was also observed that for trees, shrubs and herbaceous species, the average rooting depths are 7.0±1.2 m, 5.1±0.8 m and 2.6±0.1 m, respectively.

A hydraulic lift is a process in which some deep-rooted plant species transfer water from deeper to shallower soil layers. It predominantly depends upon the hydraulic gradient in soil water potential and the plant species.

Burgess *et al.* (1998) demonstrated that reverse hydraulic lift could occur whereby water transported from shallower to deeper soil layers. A hydraulic lift considered as an important process for maintaining root viability and growth under dry conditions. Comparing oak species and C4 grasses Espeleta *et al.* (2004) concluded that, in general, oaks showed a higher hydraulic lift activity. Hydraulic lift by *Acacia tortlis* trees shown to benefit the understory grass in the arid east African savanna (Ludwig *et al.*, 2003). Thus, the hydrological redistribution of rainwater from moist to drier regions of the soil profile by roots can be a significant recharge mechanism to the deeper soil layers in arid or semi-arid environments. This is enhanced by the dimorphic root system of *Eucalyptus spp.*, where a deep vertical anchor root grows straight down to the water table, and the lateral roots extract moisture from the superficial soil layers, enabling the plant to maintain relatively high transpiration even in dry conditions (Knight, 1999). Further, *Eucalyptus* roots can follow moisture gradients up to 20 meters into adjacent fields (Knight, 1999). The pattern of sapflow observed during the dry season in species having a dimorphic root system is consistent with the hydraulic redistribution of the soil water (Ryel *et al.*, 2003).

6.1. Groundwater Mapping

In order to determine the relationship between groundwater and ET in the study area, the spatial pattern of groundwater (depth below natural surface) was mapped using borehole data of the image pass day (Figure 6.1). Generally, the groundwater depth does not fluctuate over a short time interval; however, the groundwater depth borehole data for the image pass day was used to create a groundwater-surface layer. The Department of Primary Industries provided the groundwater depth data. From an interpolated surface, a raster layer was developed in ArcGIS environment with a cell size equivalent to the Landsat image.

In both the catchments, the groundwater depth ranges from 0 to 22.72 m; the mid-western part of the plantation catchment and the middle of pasture catchment has the shallowest groundwater and may be waterlogged. The groundwater is deepest on the eastern parts of both the catchments due to the higher elevational grid.

ET estimates for the study catchments were compared with the spatial variability of groundwater depth, and the response of each landcover to the groundwater depth investigated.

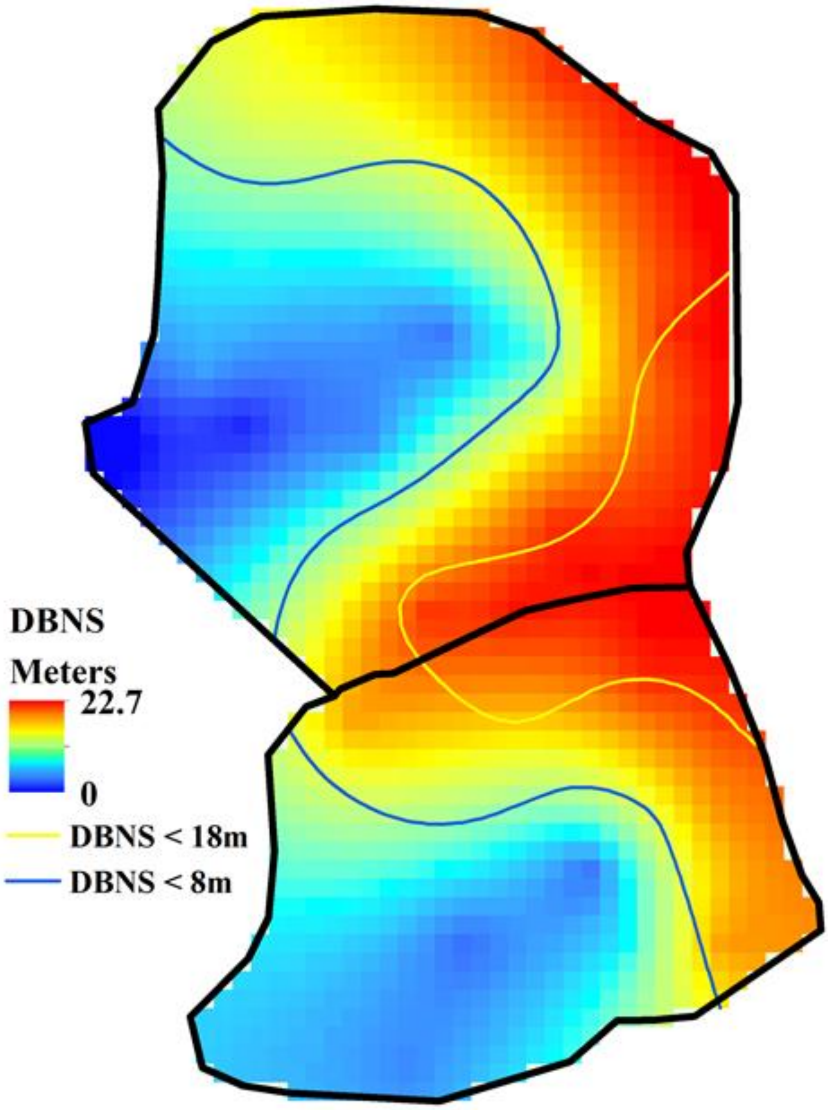

Figure 6.1. The spatial pattern of groundwater depth (DBNS) at the study site.

6.2. ET – Groundwater Interaction

Pixel-based comparison of groundwater depth and ET at the catchment scale (Figure 6.2 & 6.3) revealed that there is a weak linear correlation between these two parameters for the pasture catchment; however, there are two distinct ET trends in plantation catchment for ET > 3 and ET < 3 mm/day (Figure 6.3).

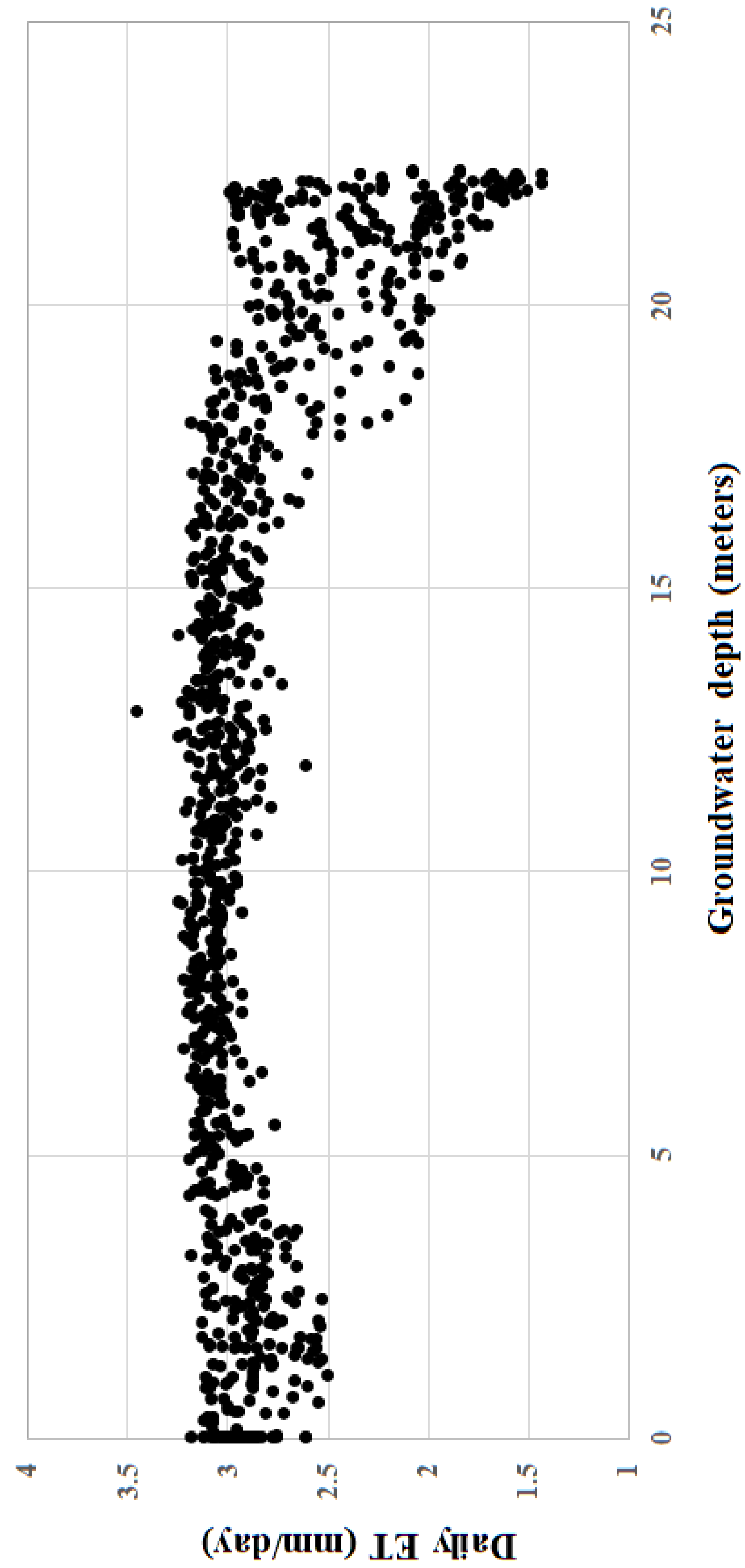

Figure 6.2. Daily ET vs groundwater depth in plantation catchment.

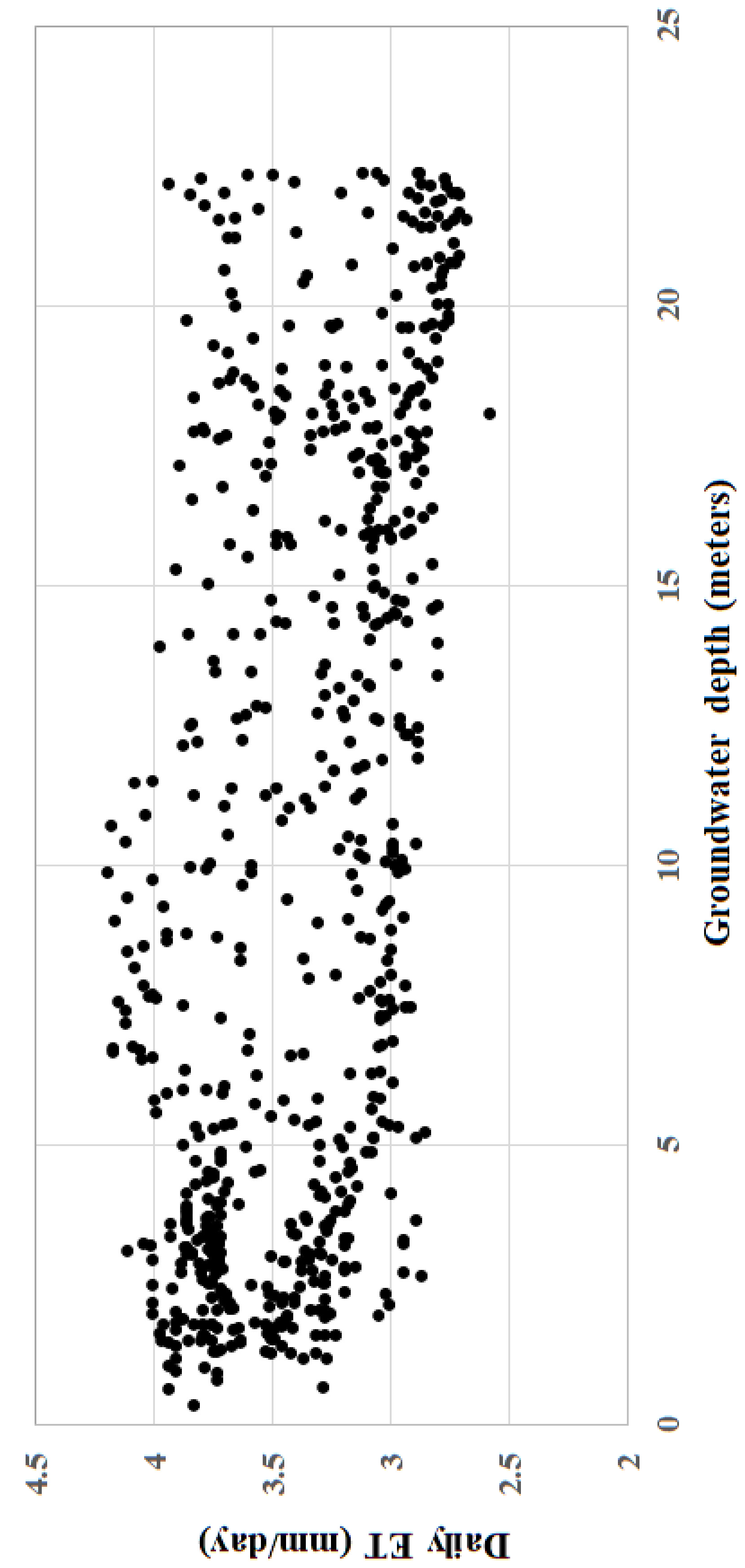

Figure 6.3. Daily ET vs groundwater depth in pasture catchment.

The variable ET response of different landcover and the groundwater depth will now be discussed in detail. To do so, first the ET and groundwater raster layers, having the same pixel size, were transformed into the respective point vector layers and then through spatial join, the attribute tables of different land covers were used for plotting ET vs groundwater (Figure 6.4 – 6.11). The red, green and blue boxes on the graph and the corresponding images represent the pixels in cyan colour highlighting the respective pixels on the daily ET raster layer or picture of the respective pixel.

6.2.1. Plantation Catchment (C1)

On the graph of ET and groundwater depth, the area with shallow groundwater (<10 m) has ET > 2.5 mm/day and includes plantations, natural vegetation and pasture (Figure 6.4a). The higher ET pixels within this part of the graph are representing *Eucalyptus globulus* plantation, and this is also true for increasing groundwater depth up to 20 meters (Figure 6.4b). At groundwater depths >10 meters, the ET response is more or less constant (> 2.8 mm/day) up to ~ 15 meters depth. At greater depths, there is a sharp decline in ET (Figures 6.4c), with ET < 2.5 mm/day represented by perennial grasses growing on the elevated area with rock outcrops in the north-western part of the catchment (Figure 6.4c).

There is a degree of uncertainty in the factors impacting water uptake by tree plantations (Benyon, 2002; Dye, 1996). In this study, groundwater depths can relate to satellite image ET estimates in terms of the interaction between the water table and tree water uptake as reported in earlier studies (Macfarlane *et al.*, 2018; Sharma, 1984; Silberstein *et al.*, 2001).

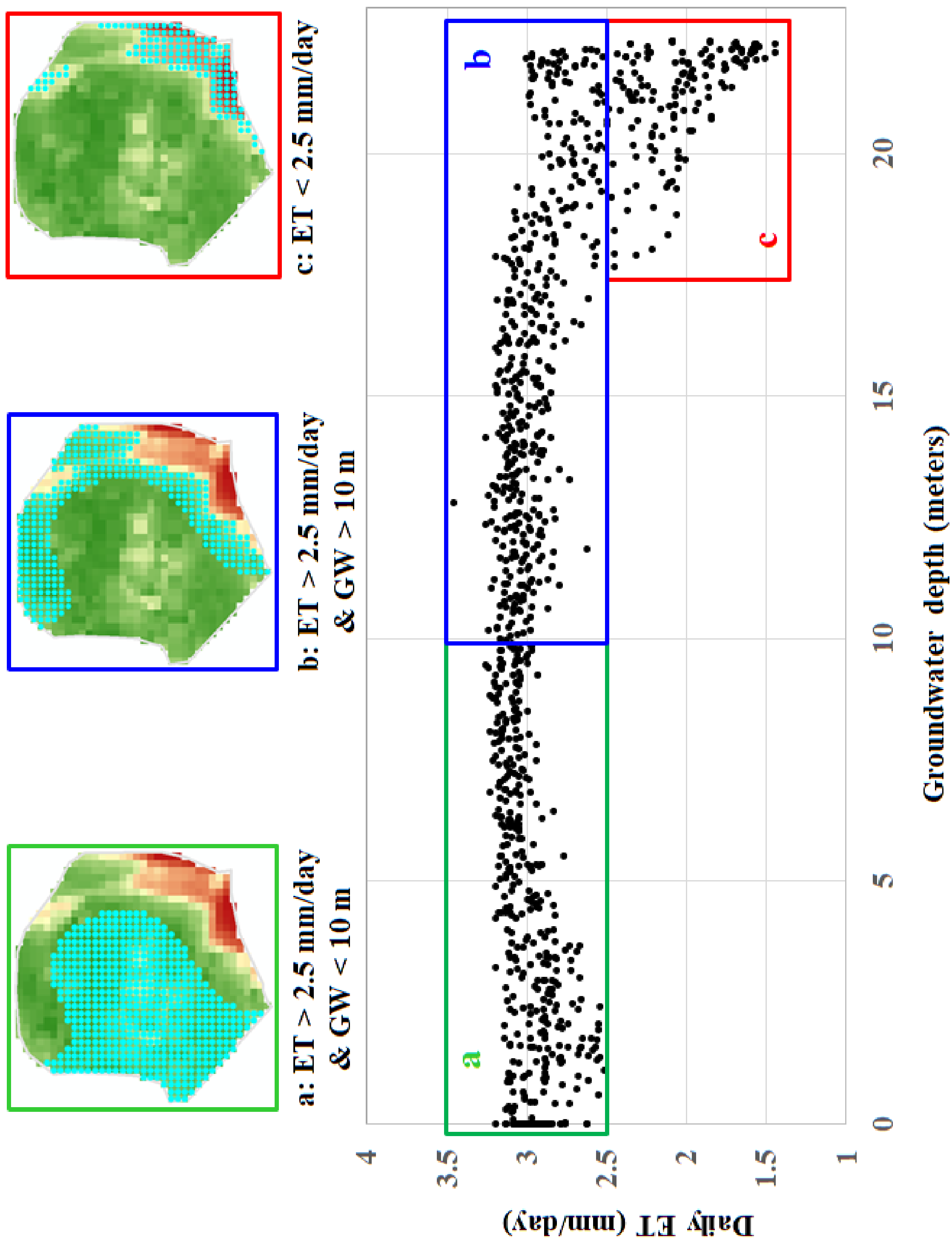

Figure 6.4. ET vs Groundwater depth in the plantation catchment (‘a’ to ‘c’ show the corresponding pixels on the graph).

6.2.2. Pasture Catchment (C2)

The response of ET in the pasture catchment to landuse is similar to that in the plantation catchment, but it is more pronounced; the upper half of the graph (Figure 6.5a) is represented by plantation, crops and native forest and the lower half by pastures (Figure 6.5b and c). The lowest ET is represented by pasture species including phalaris and ryegrass (Figure 6.5c); the *Eucalyptus globulus* plantation achieves the highest ET (> 4 mm/day) with a groundwater depth < 8 meters. The open native forest canopy, mainly dominated by *Eucalyptus regnans,* has an ET rate of 3.5 – 4 mm/day despite a groundwater depth > 18 meters comparable to a young plantation with relatively shallow groundwater.

The higher ET achieved by open canopy *Eucalyptus regnans* forest underlain by deep groundwater could be attributed to the upward movement of groundwater from water table deeper than 10m due to hydraulic lift by old trees with a well-established dimorphic root system (Ludwig *et al.,* 2003), consistent with the earlier studies (Gardner and Fireman, 1958; Nepstad *et al.*, 1994; Jipp *et al.,* 1998). On the other hand, the presence of a farm dam in this forest may be having a localized effect.

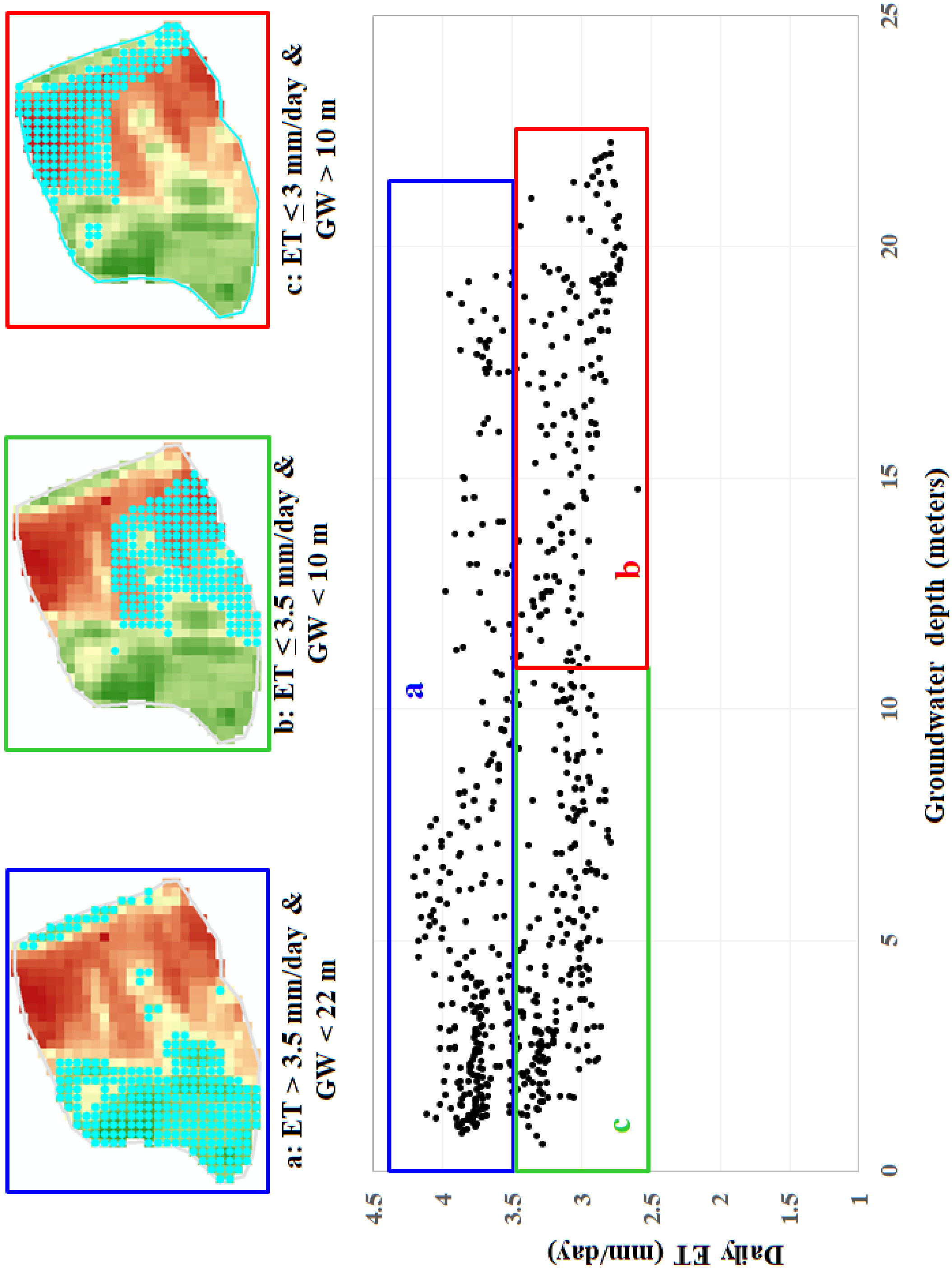

Figure 6.5. ET vs groundwater depth in pasture catchment (‘a’ to ‘c’ show the corresponding pixels on the graph).

6.2.3. *Landcover*

To further investigate the response of ET to major landcover, within each catchment, the different landcover considered include plantation, pasture, native forest and crops.

6.2.3.1. Plantations

The ET response of the *Eucalyptus globulus* plantation in the plantation catchment over a range of groundwater depth is consistent (Figure 6.6). The plantation has a high ET (> 3 mm/day) irrespective of groundwater depth up to 13m, above which the ET declines but is still > 2.5 mm/day (Figure 6.6a & b). One pixel at the periphery of the plantation block next to the bare ground has a lower ET of < 2.5 mm/day. One pixel has a very high ET of 3.5 mm/day, probably due to a contribution from the farm dam (Figure 6.6c).

Deep groundwater (> 15 m) has a small negative impact on ET, which nevertheless remains within a narrow limit of 3.0 to 3.25 mm/day. Thus, *Eucalyptus globulus* probably has access to moisture in deeper layers of groundwater, helped by its dimorphic root system, as also shown by earlier studies (Knight, 1999; Eastham *et al.*, 1990; El-Lakany and Mohammad, 1993).

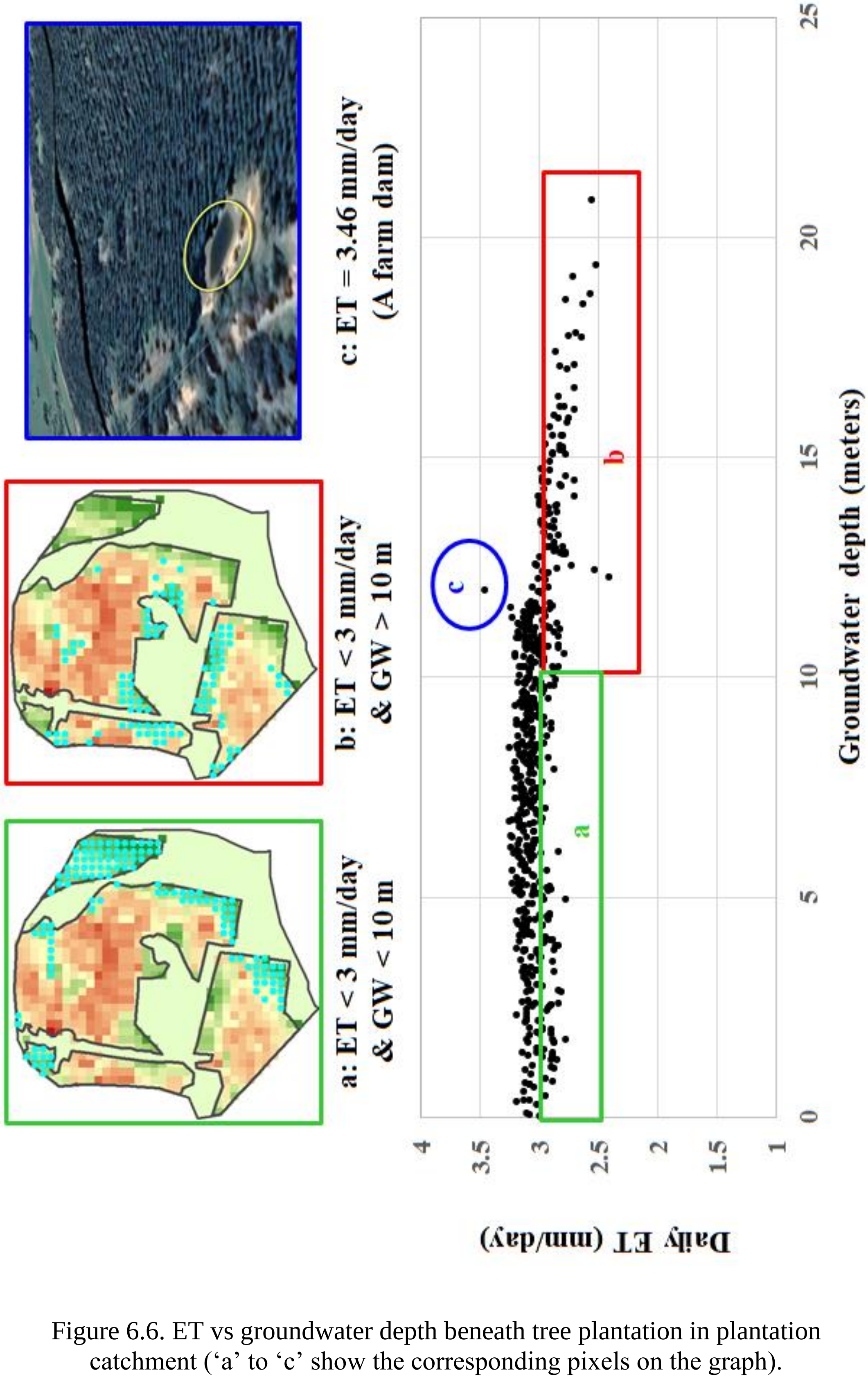

Figure 6.6. ET vs groundwater depth beneath tree plantation in plantation catchment (‘a’ to ‘c’ show the corresponding pixels on the graph).

A small block of *Eucalyptus globulus* plantation in the pasture catchment (C2) underlain by shallow groundwater (Figure 6.7a). Due to reasonable access to soil moisture, higher ET rates were maintained (3.6 to 4.2 mm/day).

Figure 6.7. ET vs groundwater depth of tree plantation in pasture catchment ('a' shows the corresponding pixels on the graph).

6.2.3.2. Pastures

The pasture response in the plantation catchment (C1) is quite variable over increasing groundwater depth (Figure 6.8). There is a distinct cluster at groundwater depth < 5 meters, where the relatively high ET reflects the easily accessible groundwater (Figure 6.8a & b). There is a linear correlation between ET and groundwater depth > 10 meters; ET declines below 2.5 mm/day (Figure 6.8c) for deeper groundwater, the lesser the ET.

For the pastures in the pasture catchment (C2), the higher ET (> 3.5 mm/day) represents either perennial pastures in low lying areas with groundwater < 10 meters, or areas with scattered old trees (*Eucalyptus regnans*) and groundwater deeper than 10 meters (Figure 6.9a & b). The higher ET of the pasture in the deep groundwater zone can be attributed to the hydraulic lift and groundwater redistribution by trees from the aquifer to the root zone as reported in the literature (Yeh *et al.*, 1998; Yeh and Famiglietti, 2008, Tyler *et al.*, 1997; Malek *et al.*, 1990; Luo *et al.*, 2009; Satchithanantham *et al.*, 2017; Lubczynski, 2000 & 2011; Groeneveld *et al.*, 2007). The higher ET in these pastures may also be due to the presence of a farm dam.

The medium ET rate (3 – 3.5 mm/day) of the pasture achieved over a wide range of groundwater depth (Figure 6.9c). Low ET (< 3 mm/day) occurs at both shallow groundwater depths (Zone I; < 10 m) and deeper (Zone II; >10 m) adjacent to the natural forest (Figure 7.9d). The dominant flora of Zone I is perennial grasses (phalaris and ryegrass). In contrast, in zone II, annuals are dominant (clovers and capeweed), suggesting that annuals can cope in areas with less soil moisture during the summer season, particularly in the vicinity of trees.

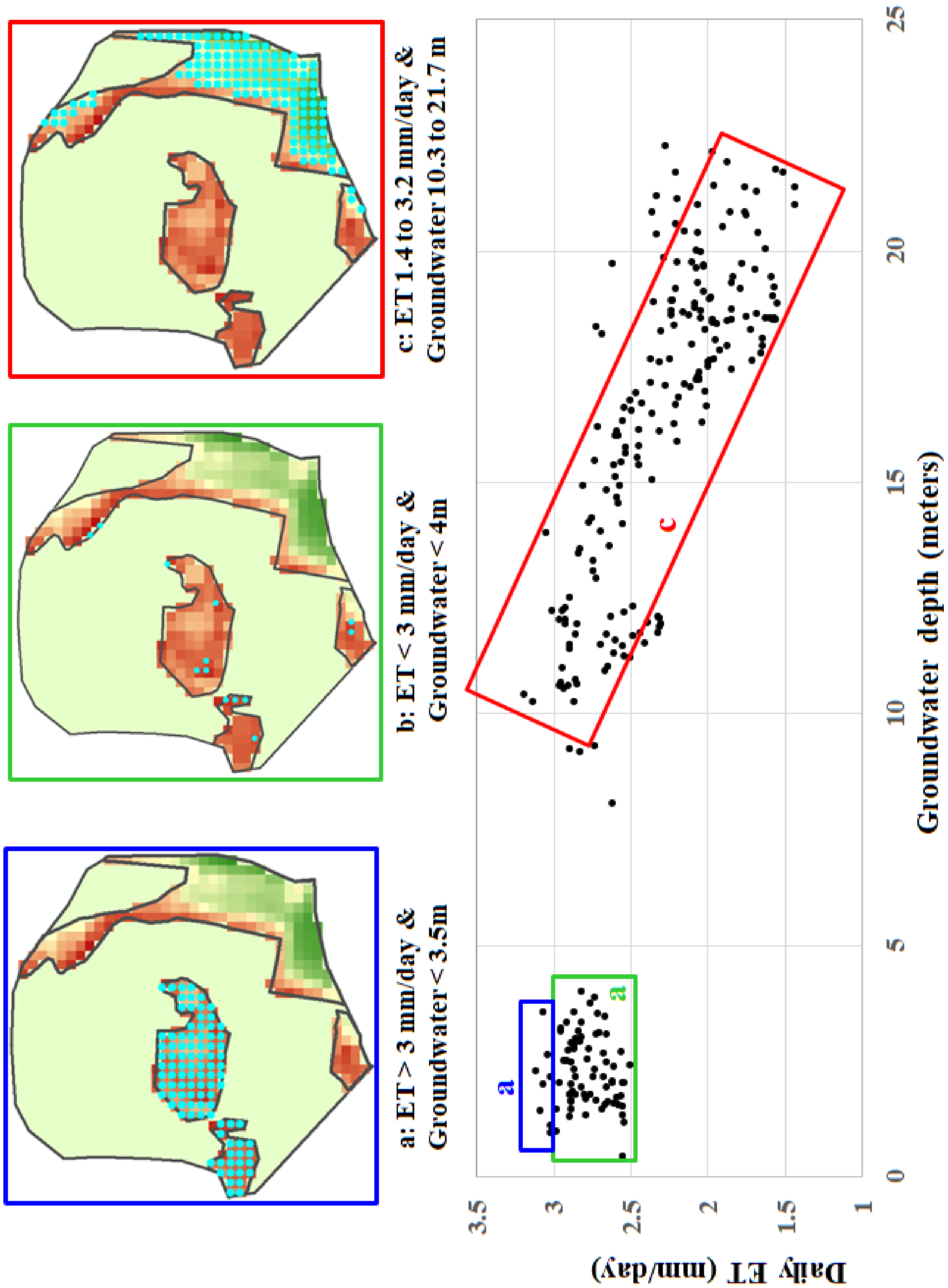

Figure 6.8. ET vs groundwater depth of pasture in plantation catchment (‘a’ to ‘c’ show the corresponding pixels on the graph).

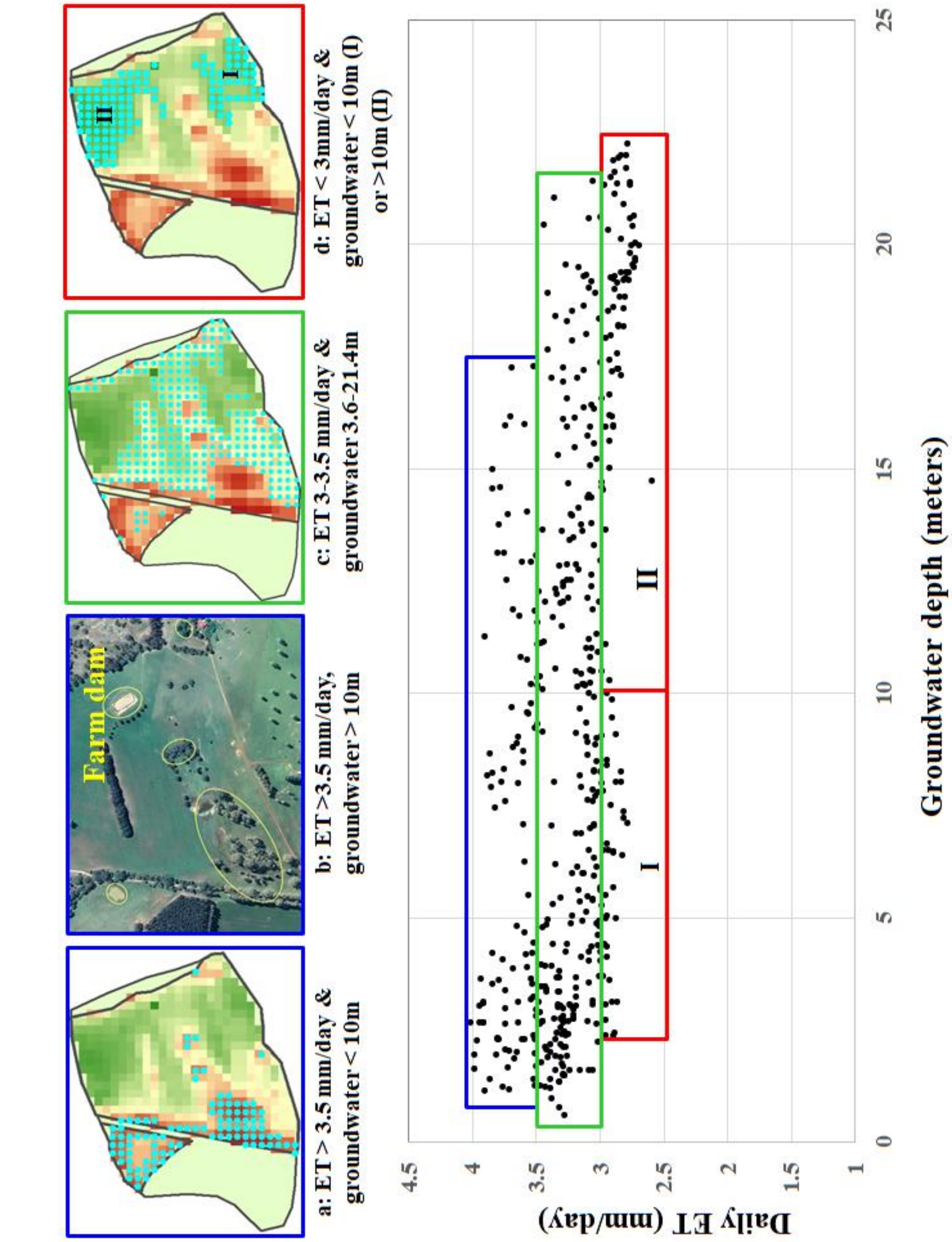

Figure 6.9. ET vs groundwater depth of pasture in pasture catchment ('a', 'c' and 'd' show the corresponding pixels on the graph).

6.2.3.3. Native Forest (*Eucalyptus regnans*)

An open canopy *Eucalyptus regnans* native forest maintained a higher ET than a young *Eucalyptus globulus* plantation despite having deep groundwater (18 – 19.5 m) (Figure 6.10). Pixels with lower ET within this forest are probably due to canopy gaps covered with herbaceous vegetation. Some evergreen forests can maintain ET even during extended dry periods by accessing water from depths of more than 8 meters through their deep root systems as reported earlier (Oliveira *et al.*, 2005; Amenu and Kumar, 2007; Nepstad *et al.*, 1994; Ullman, 1985; Allison and Barnes, 1985; Gardner, 1958; Gardner and Fireman, 1958; Albaugh *et al.*, 2013; Hutley *et al.*, 2000). It is in line with the current findings.

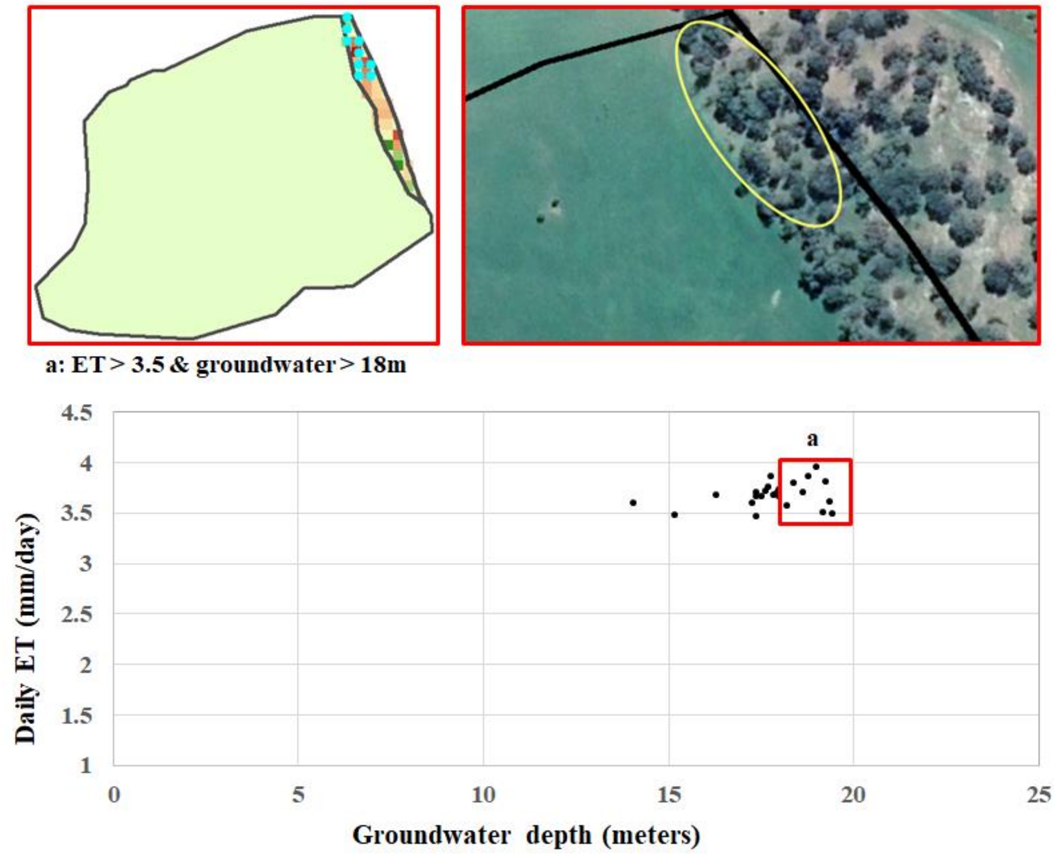

Figure 6.10. ET vs groundwater of native forest in pasture catchment (‘a’ shows the corresponding pixels on the graph).

6.2.3.4. Crops (cultivated oats)

The paddock of cultivated oats within the pasture catchment lies in a shallow groundwater (< 5 m) zone (Figure 6.11). The uniform crop cover and shallow groundwater were probably responsible for achieving a high ET rate like the native forest and young plantations. A few pixels with ET > 4 mm/day located near a farm dam (Figure 6.11).

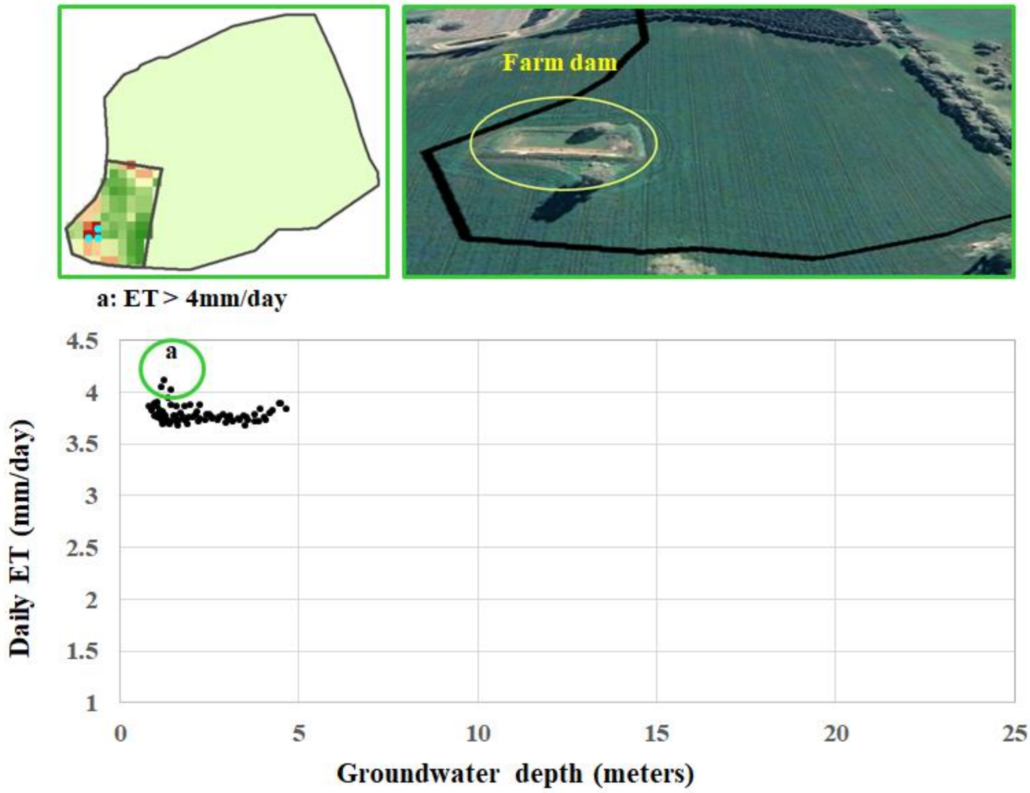

Figure 6.11. ET vs groundwater depth for crops (Oats) in pasture catchment ('a' shows the corresponding pixels on the graph).

Chapter 7. Application of SEBARA to a second site

7.1. Site Description

To test the SEBARA model for paired catchment at Gatum and Mirranatwa (Figure 7.1) the Landsat 8 image of winter (10:15:037am, June 26, 2016) was used for the analysis. Climate data from a flux tower, installed at the Gatum pasture catchment (C2), was used for the RefET calculations and comparison of various components of the energy balance equation. The flux tower was not installed at the plantation catchment at the satellite pass time; therefore, ET for this catchment could not be validated; however, the spatial pattern was compared with the response at Mirranatwa. At the satellite pass time, in the pasture catchment, data from the weather station showed that the relative humidity was 66% with specific humidity deficit of 0.002 and vapour pressure deficit of 0.36. The wind speed recorded was 3.9 m/s. For winter analysis, the groundwater-surface was not used because the ET estimate was the main objective. Further, due to the winter season, the slow growth was assumed, and therefore, ET dependence on groundwater was limited.

For cloud cover, the Cirrus band (B9), was checked; the study catchments appeared to be cloud-free; however, there were some low clouds present at the Mirranatwa catchments. The digital numbers of the VIS, NIR and SWIR bands of Landsat image were converted directly to reflectance using band-specific multiplicative and additive rescaling factors (given in the metadata file). The digital number of TIRS (B10) used for the calculation of surface temperature.

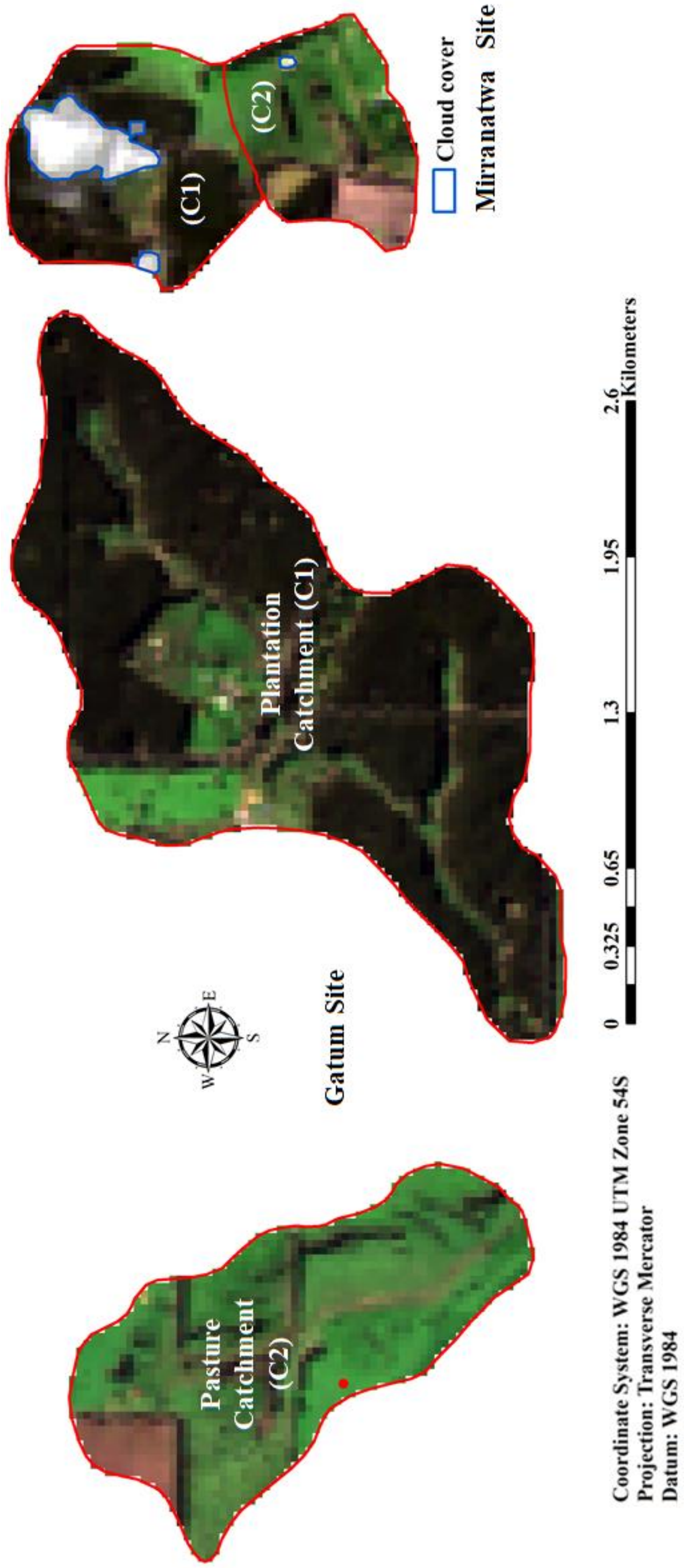

Figure 7.1. Natural Colour Composite (RGB432) of 26/06/2016 Landsat 8 image for Plantation (C1) and Pasture (C2) catchments at Gatum and Mirranatwa sites.

The Gatum site is about 30 km west of Mirranatwa site in the Geelong Hopkins region of south-western Victoria, approximately 300 km west of Melbourne near Hamilton (Figure 7.2). The climate of the area is Mediterranean with cold, wet winters and hot, dry summers. The long-term average annual rainfall is 611mm, and the yearly pan evaporation is almost double (1400 mm) of annual rainfall (Adelana *et al.*, 2015).

The Gatum site also has two catchments: one managed as pasture with some cropping (1.61 km^2) and the other covered by a *Eucalyptus* tree plantation, (3.42 km^2). The aspect, topography, geology, and soil characteristics are almost the same for both the catchments. To monitor the groundwater, there are 23 boreholes (10 in the pasture and 13 in the plantation catchment) (Figure 7.3). The water table depth below the natural surface in the pasture catchment is shallow (1-13m) as compared to the plantation catchment (5.6-14.3m). Overall, both soil water EC and groundwater EC are higher for the plantation catchment (Adelana *et al.*, 2015).

In the pasture catchment, the elevation ranges from 235 to 265m AHD (Australian Height Datum), and Banool Creek runs through the centre from the north-west to south-east (Figure 7.3). It is dominated by annual pasture for cattle and sheep grazing, with some cropping of canola and wheat (Figure 7.2). *Eucalyptus* shelter belts which include the species *Eucalyptus camaldulensis* and *Eucalyptus cladocalyx*, cover approximately 3% of the area mainly along the creeks.

The plantation catchment has an elevation range of 236–270 m ADH with McGill Creek as the main drainage (Figure 7.2 & 7.3). A *Eucalyptus globulus* plantation planted in 2005 covers 62% of the catchment, while the remaining land area is grassland with grassed access tracks.

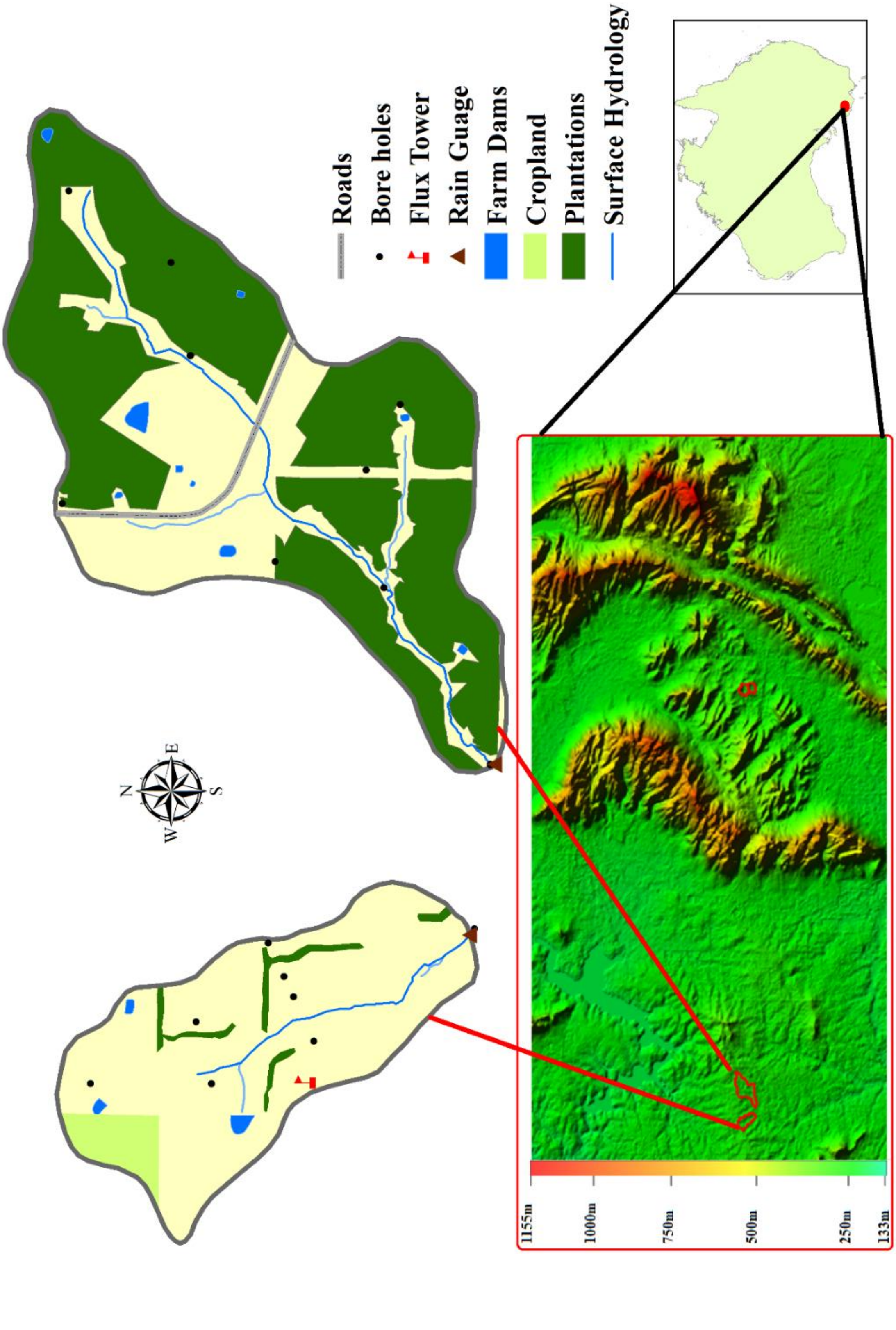

Figure 7.2. Location of paired catchments at Gatum in western Victoria, Australia, and the catchments with landcover types, road network, location of farm dams and rain gauge.

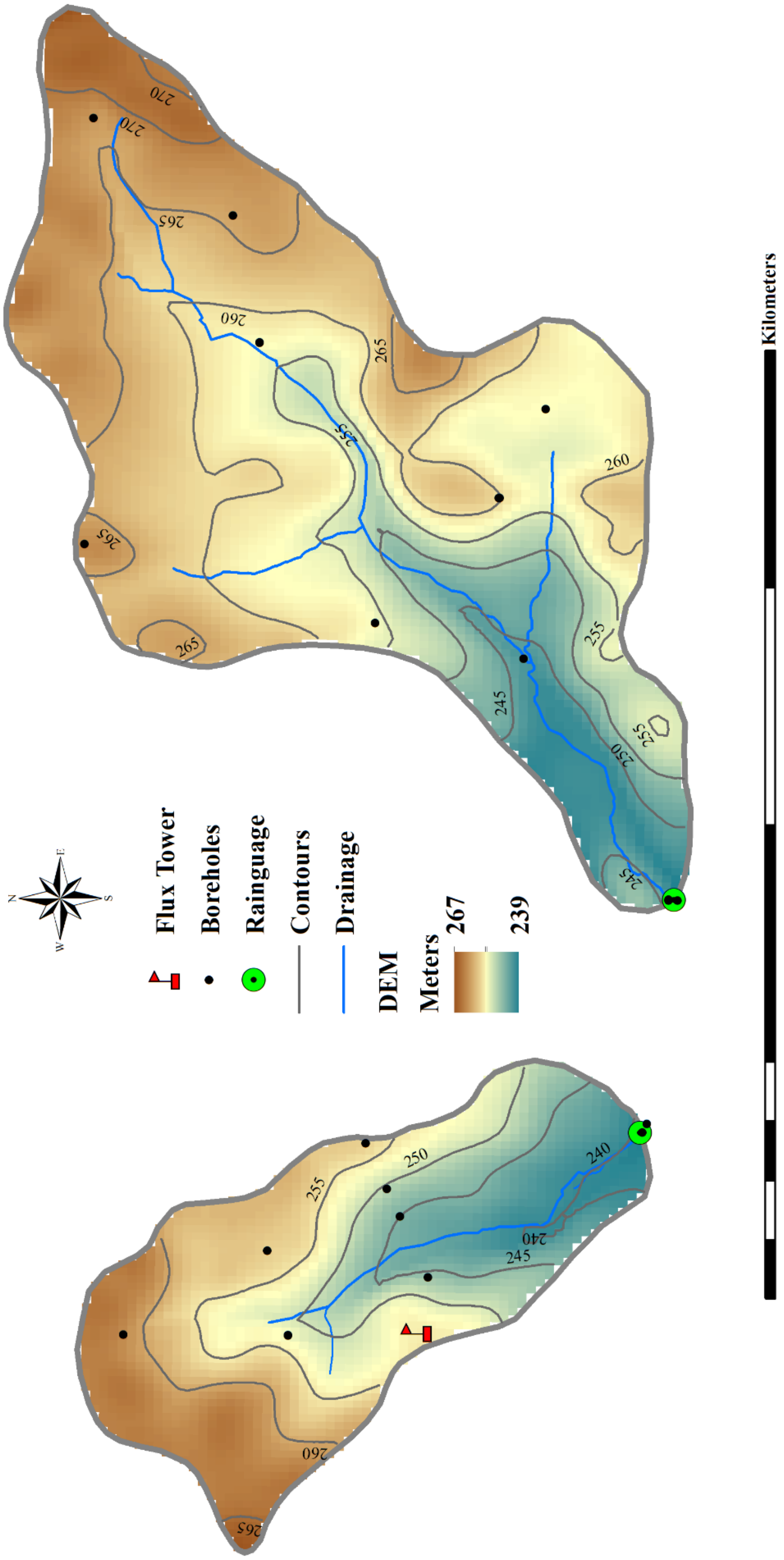

Figure 7.3. The topography of both catchments at Gatum site along with the location of boreholes, flux tower and rain gauges.

A flux tower was installed in the pasture catchment to measure ET with the support of the Australian Federal Government via the National Collaborative Research Infrastructure Scheme and Education Investment Fund (Figure 7.4). EddyPro software used to access the data by Monash University. The details of the data variables collected are available in LiCor (2015). The flux tower data used for the development and comparison of SEBARA as well as, interpretation of results include energy fluxes (latent heat, soil heat and sensible heat), momentum roughness, friction velocity, net radiative flux, down word shortwave radiation, rainfall, relative and specific humidity, air and soil temperature, vapour pressure and vapour pressure deficit, wind speed and solar altitude.

Figure 7.4. Installation of flux tower in pasture catchment at Gatum site.

7.2. Surface Radiation Balance (SRB)

7.2.1. Albedo (α_{toa} and α_{surf})

The top of the atmosphere (α_{toa}) and surface albedo (α_{surf}) are similar at Gatum and Mirranatwa (Figure 7.5 & 7.6), which are 33 km apart, and values were higher for pastures and lower for tree plantation, as previously observed at Mirranatwa.

Compared to the summer values obtained at Mirranatwa, both α_{toa} and α_{surf} for winter are lower; α_{toa} is almost half of the summer range, which is in line with studies on seasonal albedo (Zhou *et al.,* 2003; Evans *et al.,* 2017).

7.2.2. Incoming Shortwave Radiation ($R_S\downarrow$)

The total incoming shortwave radiation estimated for the satellite pass time was 437 W/m^2, as compared to 830 W/m^2 calculated for summer at Mirranatwa. The shorter day length, lower sun elevation and azimuth angle in winter are responsible for the lower incoming shortwave radiation. The measured shortwave radiation at the flux tower was 419 W/m^2, which is only 4% lower than the remote sensing estimate.

7.2.3. Outgoing Longwave Radiation ($R_L\uparrow$)

First, the spectral vegetation indices were computed.

7.2.3.1. Vegetation Indices

- *NDVI:* The NDVI ranges from 0 to 0.83; lower for cropped fields/sparse vegetation cover and higher for winter pastures followed by the plantation (Figure 7.7).

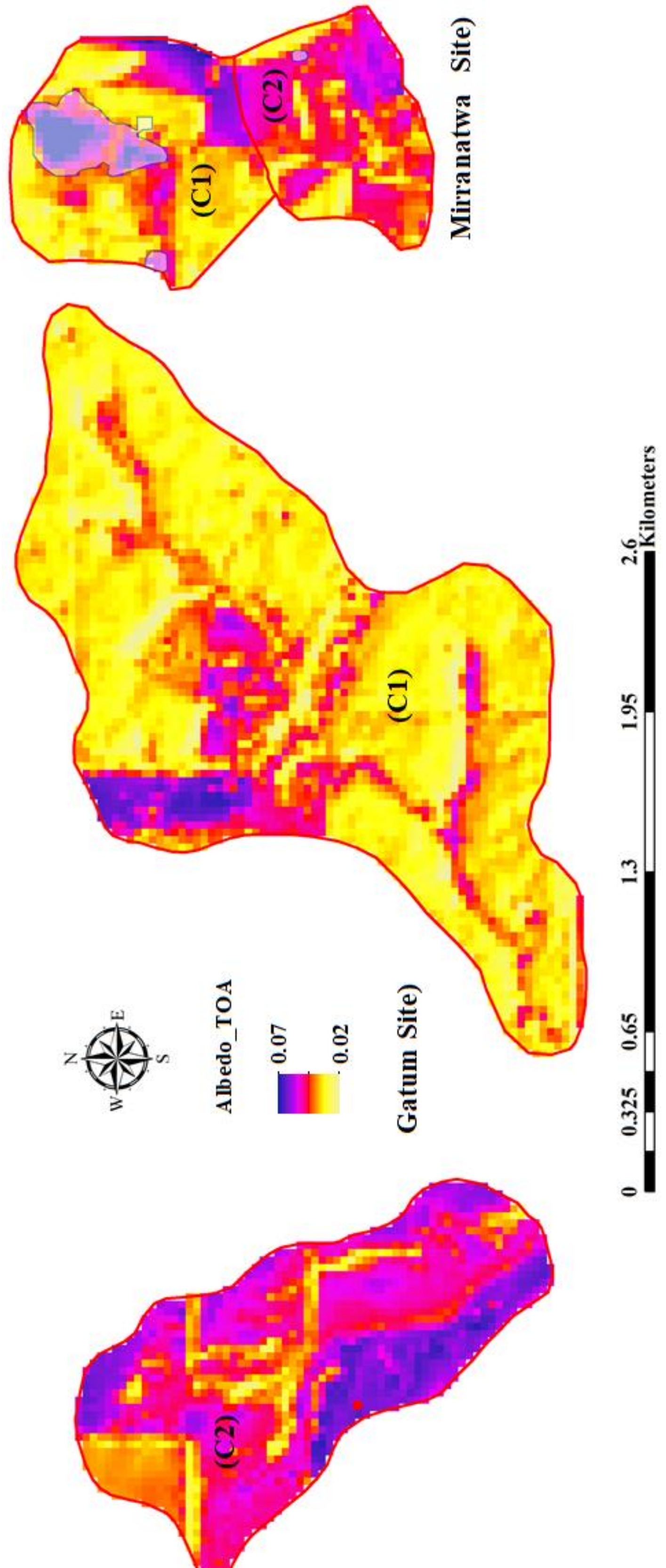

Figure 7.5. Top of the atmosphere (ToA) Albedo (α_{toa}).

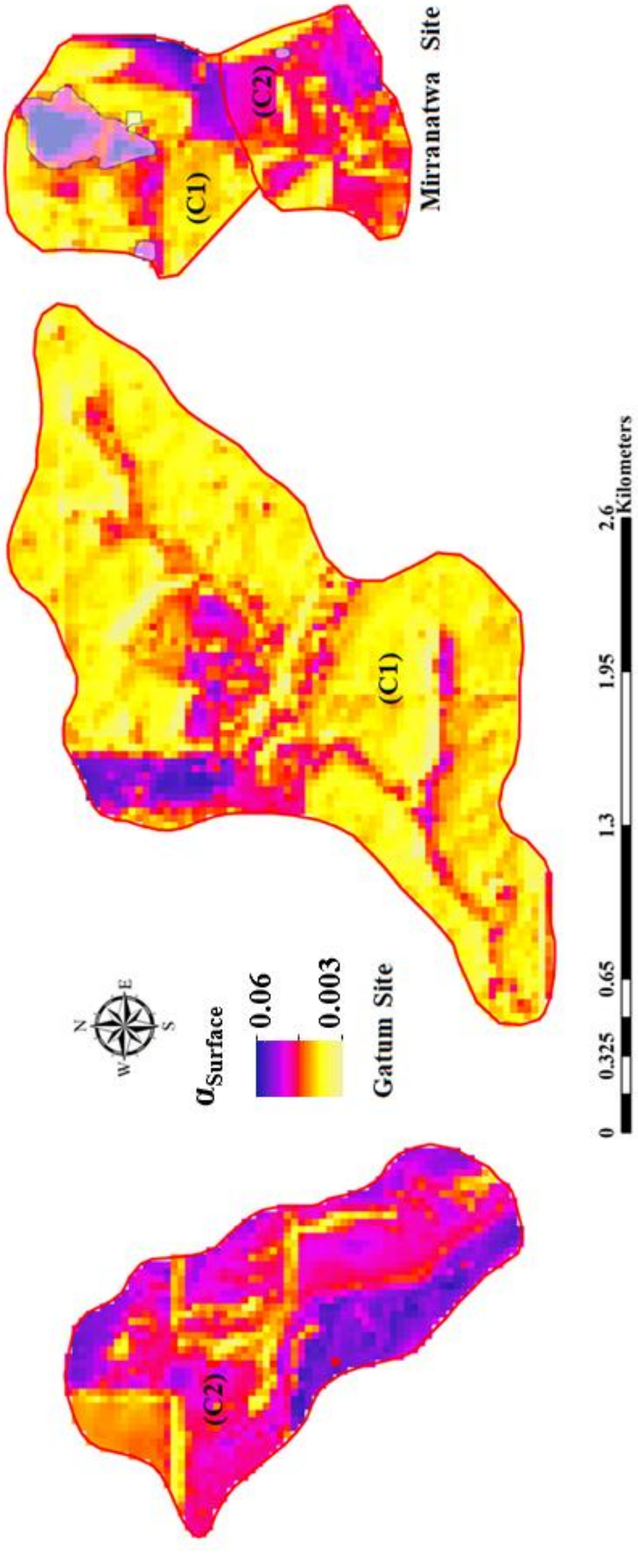

Figure 7.6. Surface albedo (α_{surf}).

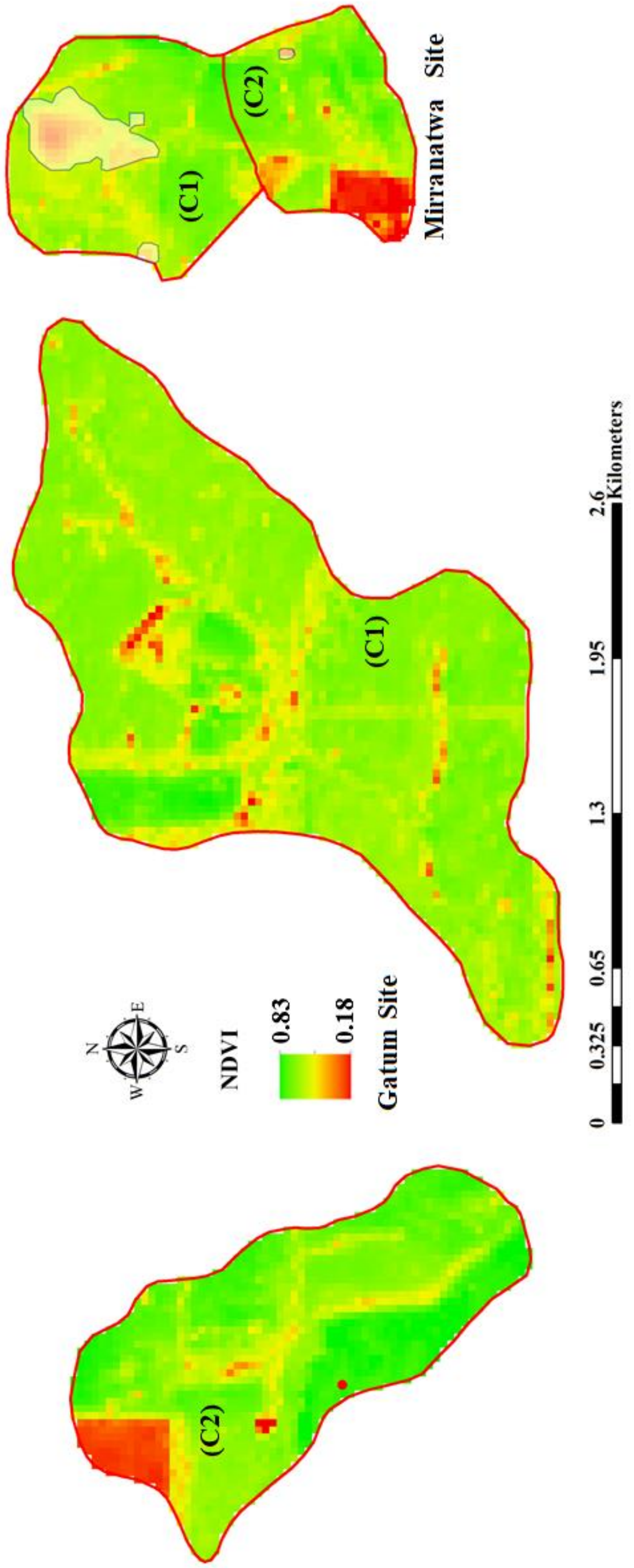

Figure 7.7. Normalized Difference Vegetation Index (NDVI).

- *SAVI:* It ranged from 0 to 0.57 which is lower than the summer values at Mirranatwa, however, highlighted the landcover accurately: pastures have the highest values whereas plantations due to canopy openings and slow winter growth, have a medium range of SAVI (Figure 7.8).

- *LAI:* The winter LAI values range from 0 to 0.83 (Figure 7.9) which are much lower with a narrower range than summer values at Mirranatwa (the highest being 3.05). The close range of LAI in winter meant that the different landcover could not be differentiated.

7.2.3.2. Surface Emissivity (ε_o):

The surface emissivity ranges from 0.94 to 1 (Figure 7.10), which is in line with summer values; however, the winter minimum value is 0.02 lower than that in summer. The cropped fields at both sites have the most moderate ε_o values, whereas pastures are highly emissive surfaces, followed by the tree plantations and natural vegetation along the creeks.

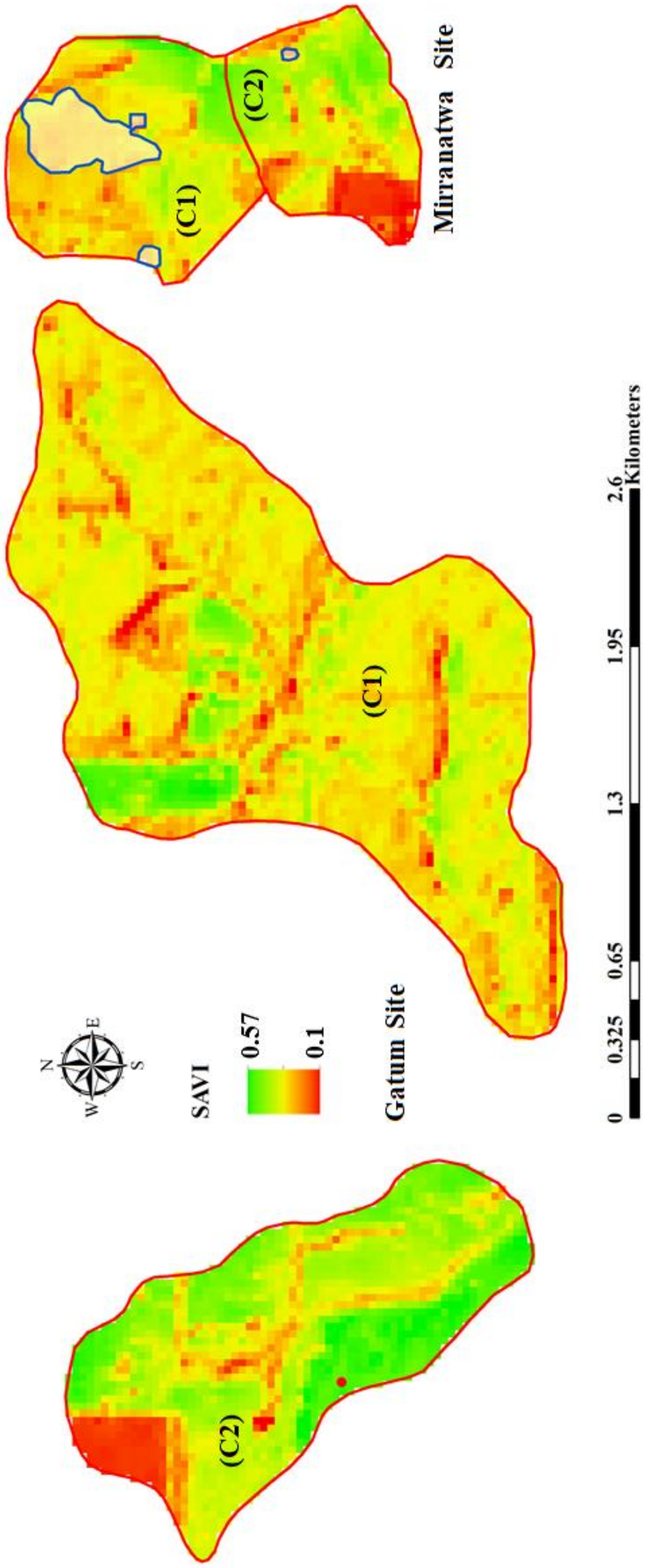

Figure 7.8. Soil Adjusted Vegetation Index (SAVI).

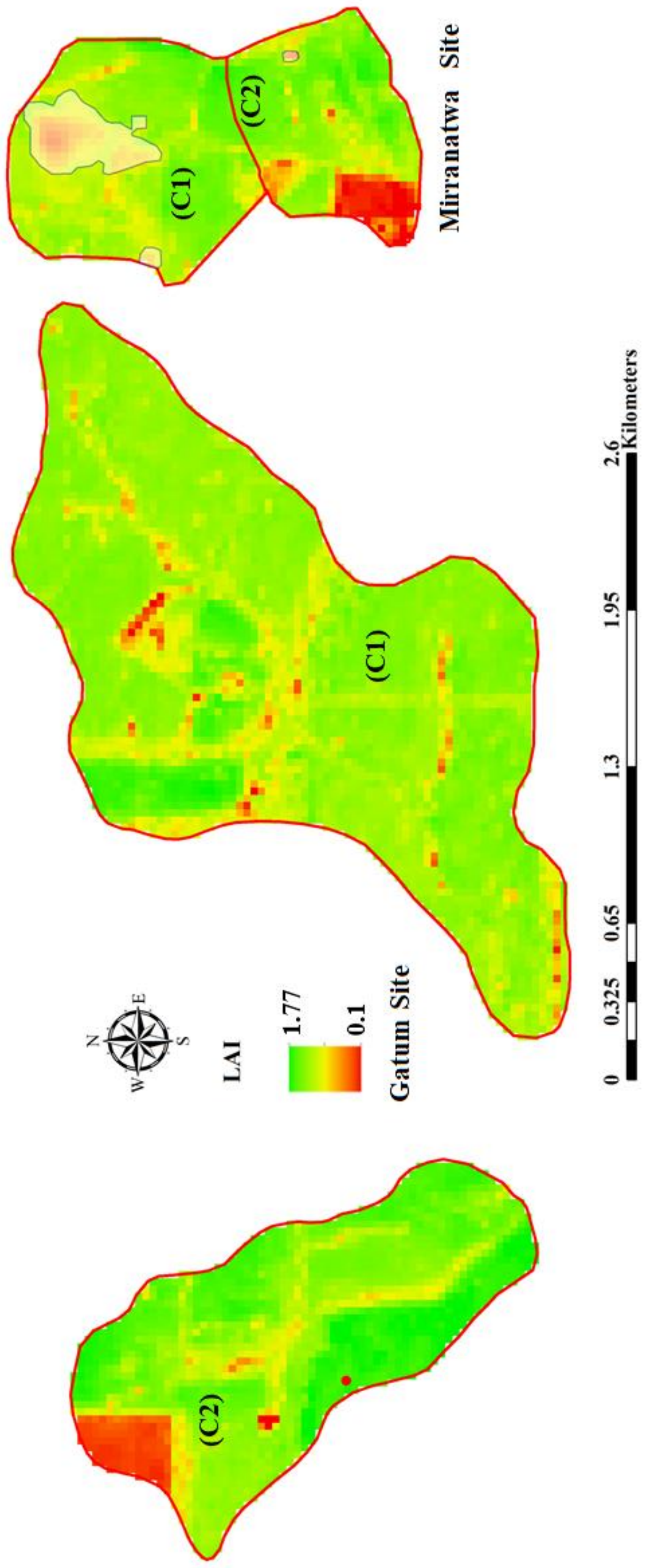

Figure 7.9. Leaf Area Index (LAI).

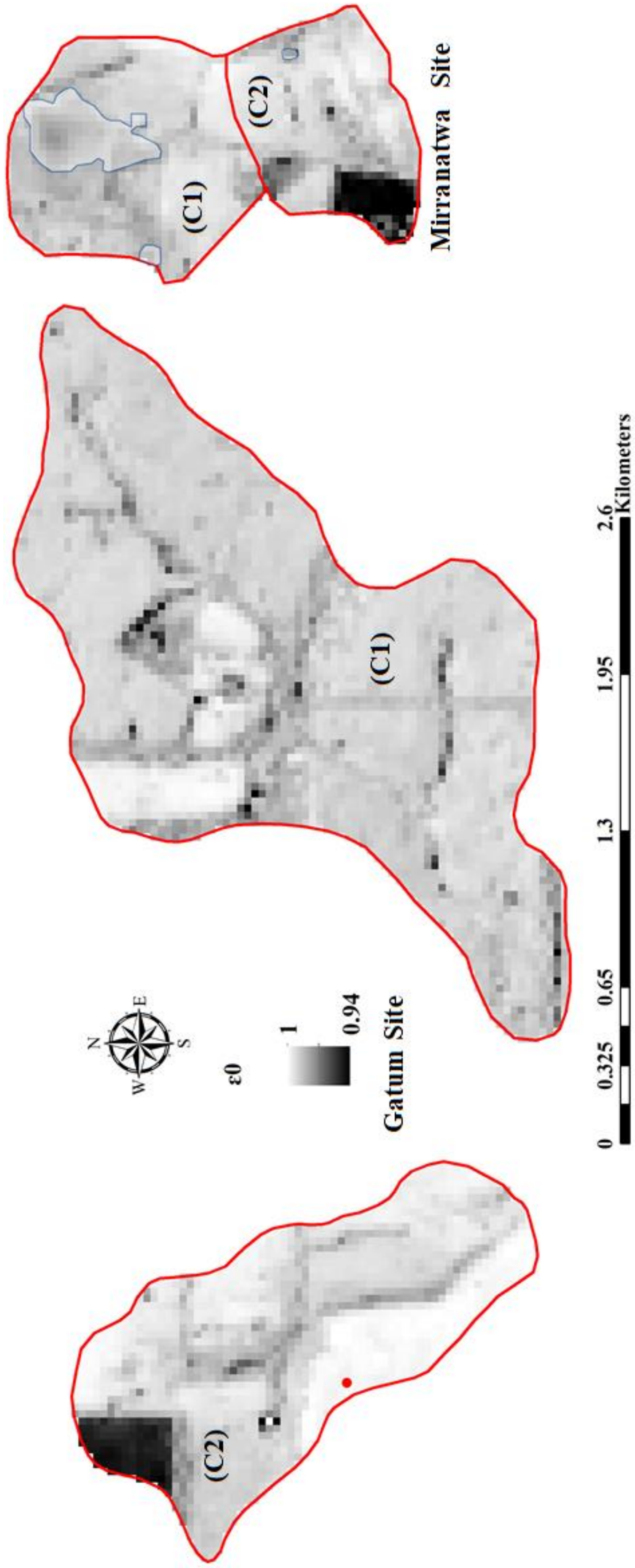

Figure 7.10. Surface Emissivity (ε_o).

7.2.3.3. Brightness and Land Surface Temperature (T_b & T_s):

There is little difference in brightness (T_b) and land surface (T_s) temperature. Generally, the pastures have a higher temperature compared to plantations or natural vegetation along the creeks (Figure 7.11). The area under cloud cover presents the lowest temperature (< 2 °C) at Mirranatwa. The temperature recorded at the flux tower at Gatum (6.6°C) is very similar to the image estimate for the corresponding pixel (6.1°C; estimation accuracy of 92%).

The spatial pattern of outgoing longwave radiation indicates higher losses from the pastures than from the plantations and cropped area (Figure 7.12). The pattern agrees with the summer response though with lower values.

7.2.4. Incoming Longwave Radiation ($R_L\downarrow$)

Since calculations of incoming longwave radiation are dependent upon the emissivity and temperature of the cluster of ‘cold’ pixels, the values are similar for both seasons. The $R_L\downarrow$ computed for the satellite pass time is 236 W/m^2.

7.2.5. Net Radiation (R_n)

The radiative balance for both Gatum catchments at the satellite pass time ranges from 277 to 329 W/m^2, which is substantially lower than that calculated for summer at Mirranatwa (473 to 698 W/m^2), although the net energy distribution pattern among the various landcover in winter (Figure 7.13) is similar. Overall, pastures have the lowest net energy because of higher energy loss in terms of $R_L\uparrow$ compared to plantations and cropped areas.

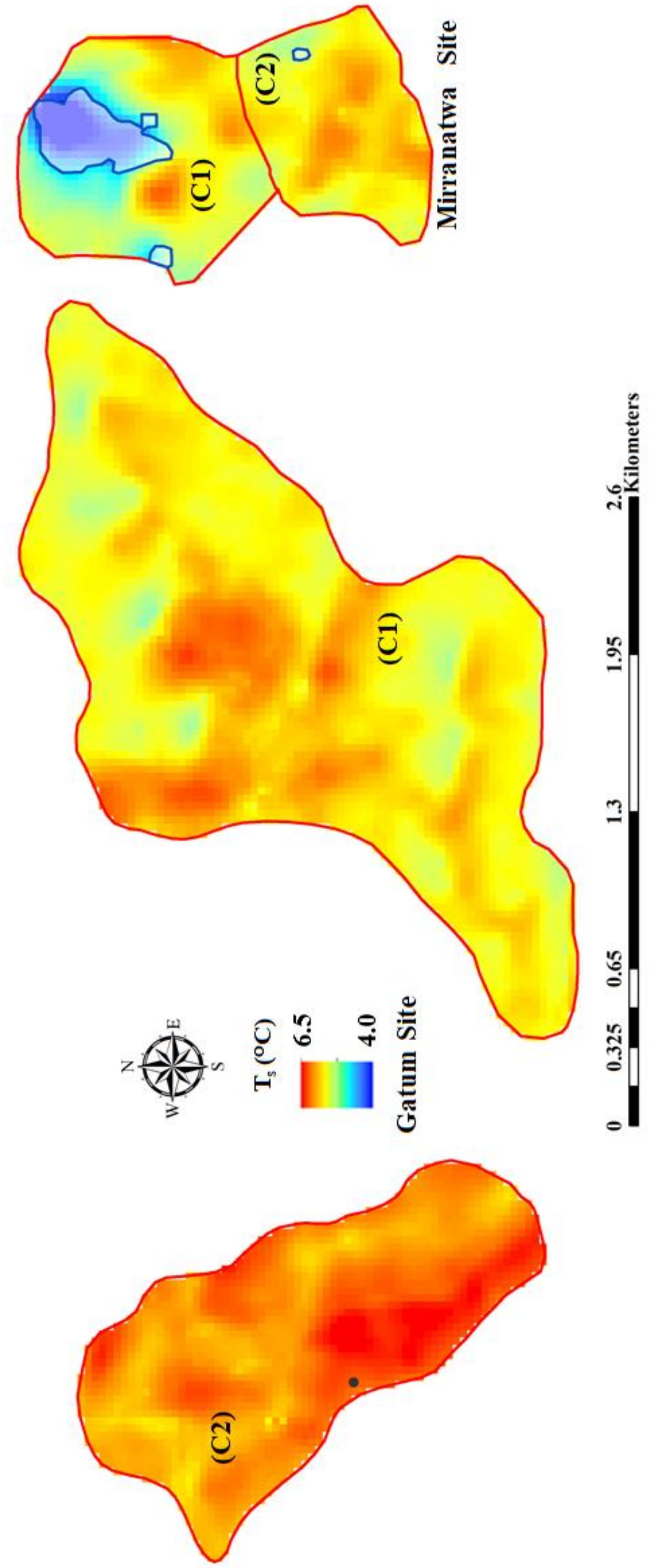

Figure 7.11. Land surface temperature (T_s)

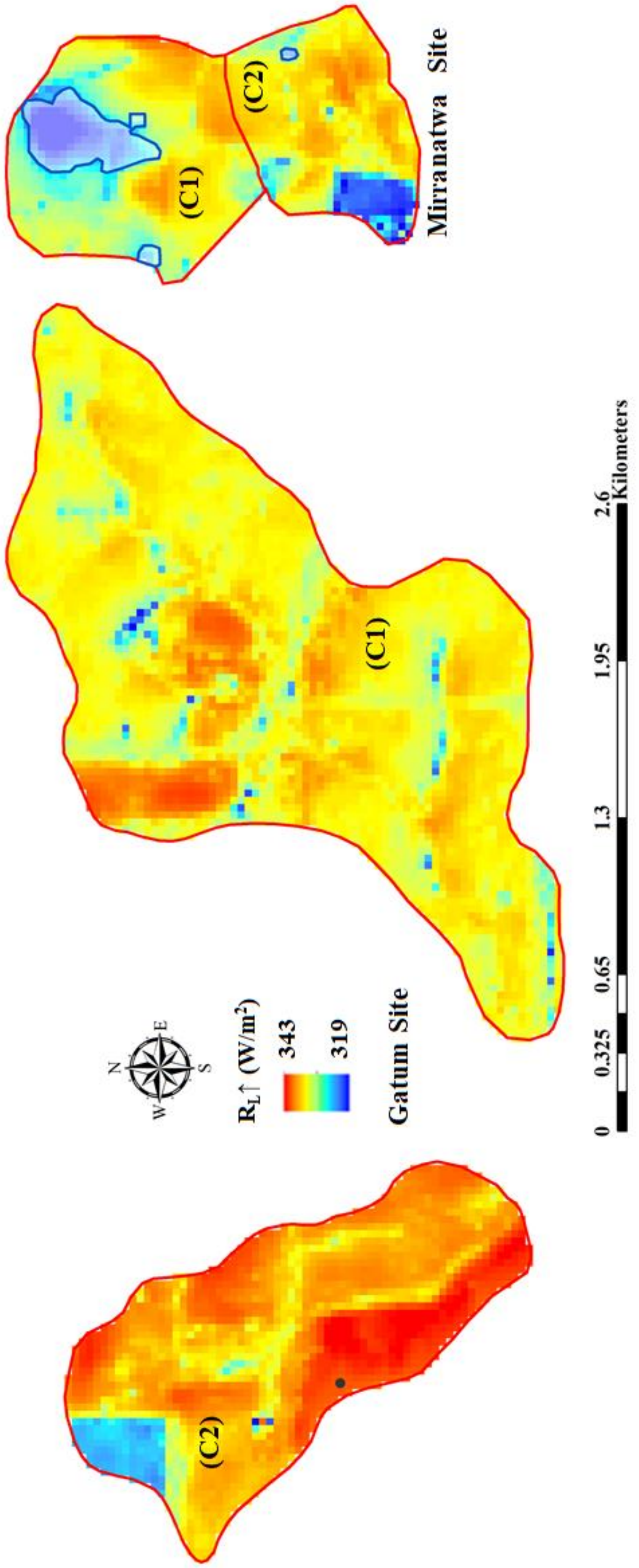

Figure 7.12. Outgoing Longwave Radiation ($R_L\uparrow$).

At the satellite pass time, the net radiation recorded at the flux tower was 302 $W/m^{2,}$ and for the corresponding pixel, the SEBARA output is comparable (293 W/m^2). The difference may be because of the flux tower value, calculated from incoming shortwave radiation, which was highly variable (419 – 291 W/m^2) during the hour corresponding to the satellite pass time.

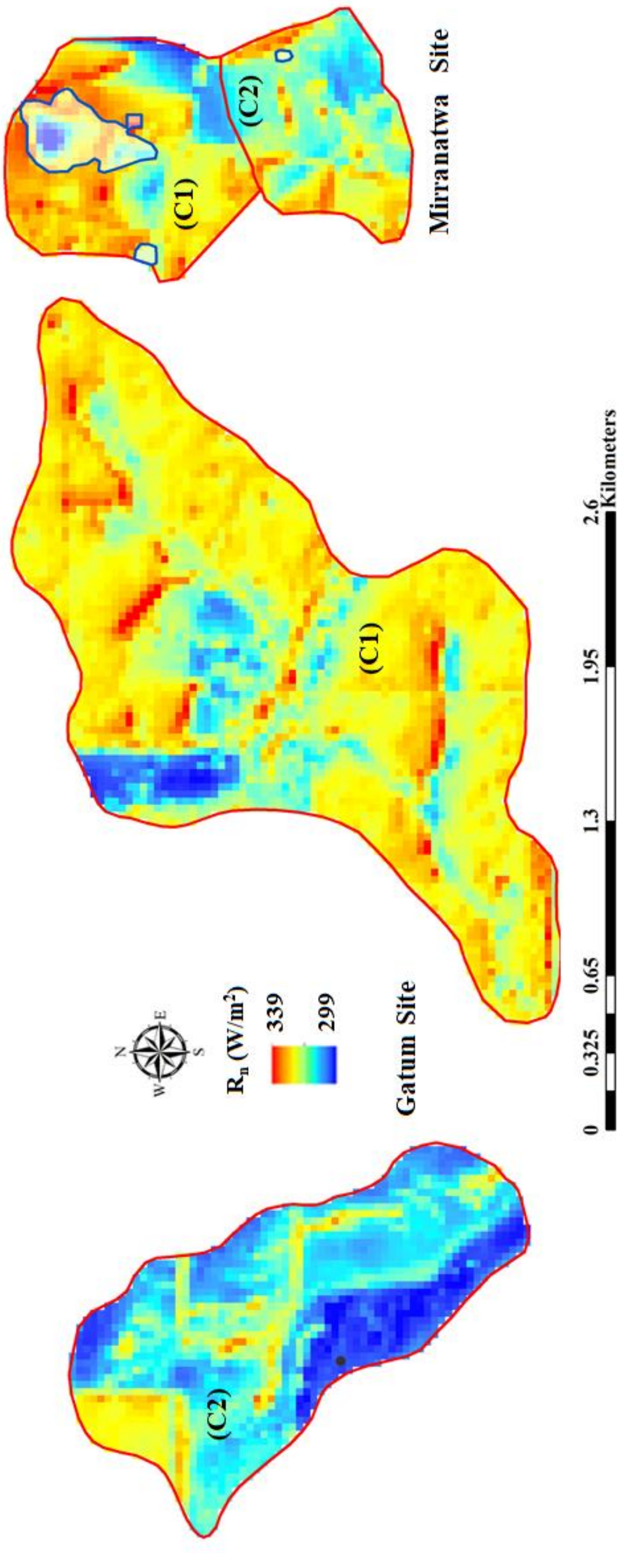

Figure 7.13. Net Radiation (R_n).

7.3. Surface Energy Balance (SEB)

The computation of the surface energy balance requires detailed knowledge of the area, especially landuse and the climate, and is, therefore, the most challenging component to compute. Special attention must be given to the selection of appropriate ‘hot’ and ‘cold’ spots and values for crop coefficient for reference ET. To accommodate the variability in the study site (e.g. predominant landcover, vegetation height), For the current testing of the model, the target area was the pasture-dominated catchment; therefore, the variables predominantly based on pasture. However, where relevant information was available for the plantation, the model was re-run for the plantation, but the output for the plantation catchment should be used with care.

7.3.1. Soil Heat Flux

To compute soil heat flux, first the G/R_n ratio was computed; this varied from 0.11 to 0.45 (Figure 7.14), higher for pastures and cropped areas and lower for plantation, reflecting higher values of T_s, α_{surf} and NDVI for pasture.

The G values range from 36.4 – 125.8 W/m^2, which is higher than for summer at Mirranatwa (4.4 – 38 W/m^2). This response is in agreement with previous studies (Sauer and Hortont, 2005; Malek *et al.,* 1990; Malek, 1993; Kustas and Daughtry, 1990) showing that due to differences in vegetation growth and cover, soil heat flux is lower for the plantation and higher for pastures (Figure 7.15). Despite the lower net available energy for pasture, the higher G/R_n ratio contributed to the more G. The low-lying areas along the creek and the cropped area had more G. In contrast, the plantations represent the area with the lowest G.

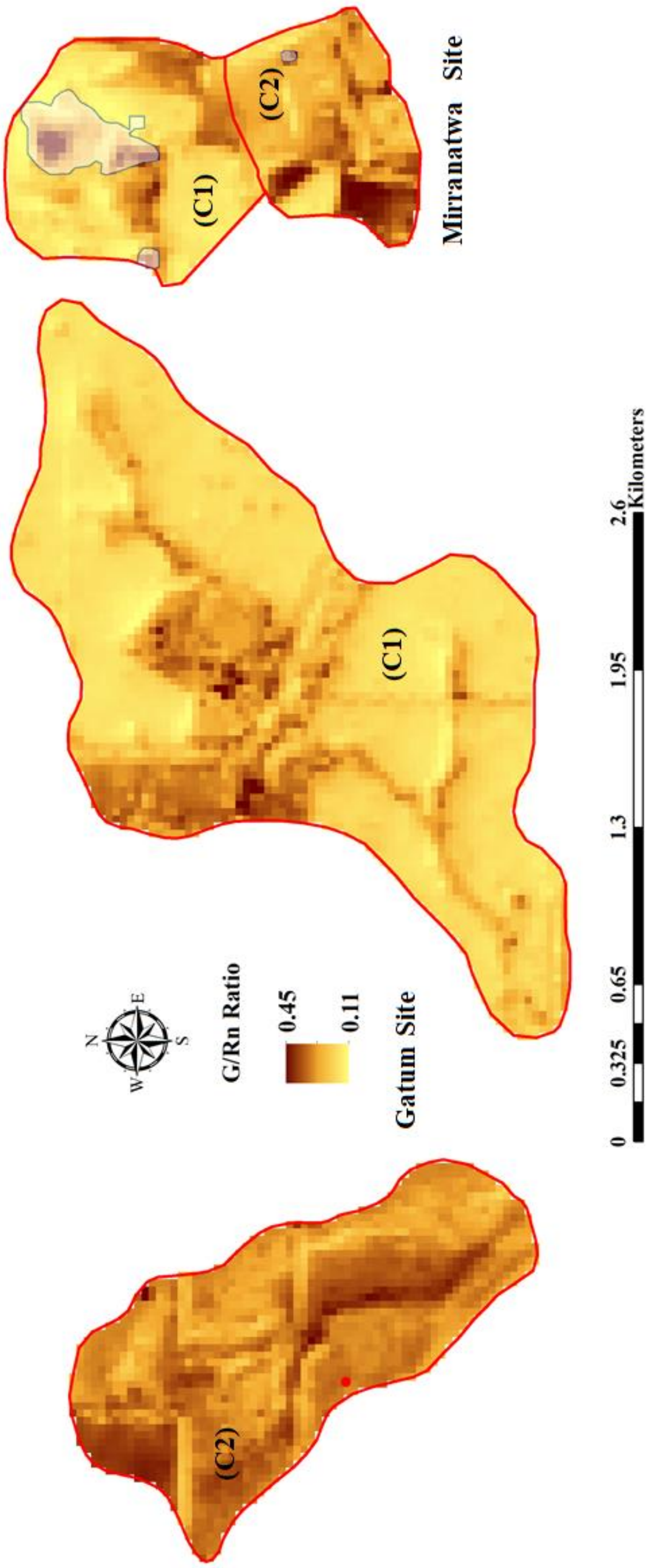

Figure 7.14. G/R_n ratio.

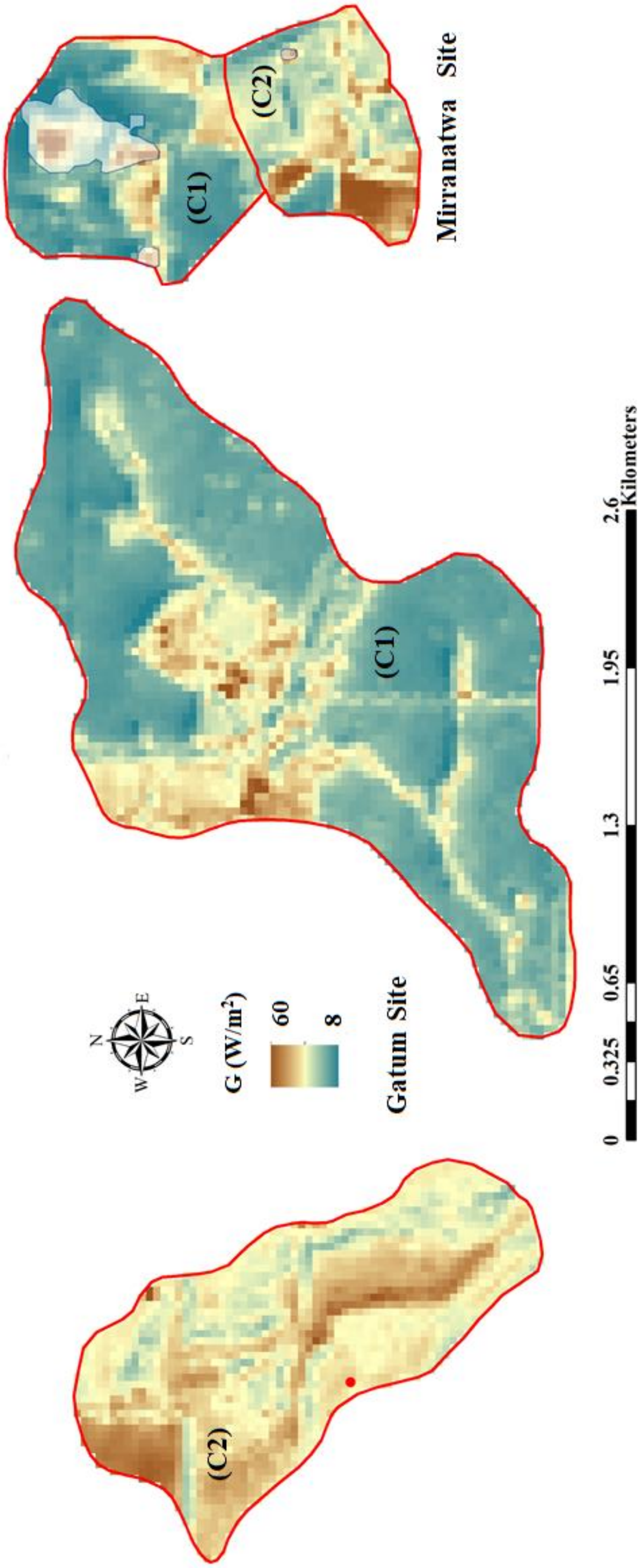

Figure 7.15. Soil Heat Flux (G).

7.3.2. Available Energy

The available energy for surface processes in winter at Gatum ranges from 153 to 290 W/m^2 (Figure 7.16), which is 36% of the available energy during summer at Mirranatwa (Figure 5.17). Still, it has a similar general pattern: higher for plantations and lower for pastures. The average measured available energy at the flux tower between 11:00 and 11:30 am was 202.3 W/m^2; the ET estimate for the satellite pass time (10:15:03 am) for the corresponding pixel was 214 W/m^2. The difference of 12 W/m^2 may be due to a decline in available energy from 10:00 am to 11-11:30 am.

7.3.3. Sensible Heat Flux (H)

7.3.3.1. Momentum Roughness Length (Zom_{pix})

The momentum roughness length computed using the regression equation between the ratio of NDVI to albedo and the natural log of Zom. The Zom_{pix} measured at the flux tower is 0.17 at the satellite pass time, whereas the model output for the corresponding pixel is 0.11. A decline in Zom_{pix} over a half-hour time step (11 to 11:30 am) on the image pass day, was recorded at flux tower. The momentum roughness depends upon the relative object height or surface roughness elements (Kanda *et al.,* 2007; Stewart *et al.,* 1994; Lhomme *et al.,* 2000; Garratt, 1992; Blyth and Dolman, 1995) and is generally one-tenth of the height of the roughness element. Considering the spatial resolution of the satellite data (30m), the average height of the objects within the pixel including the flux tower was considered for computation of Zom_{pix} which may be responsible for the differences between the two values. The landcover or vegetation type has a substantial impact on Zom_{pix}; pasture has a low Zom_{pix} compared to the trees (Figure 7.17), which is in line with limits given by WMO (2008).

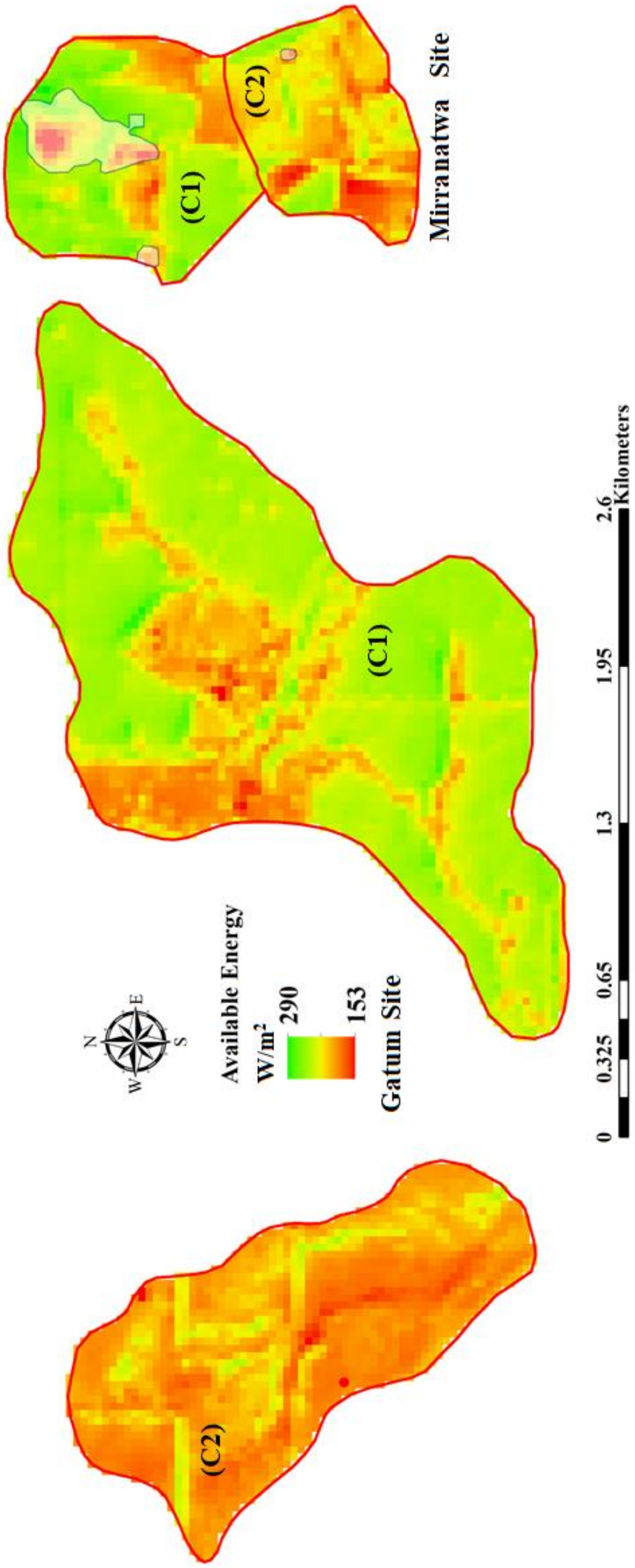

Figure 7.16. Available Energy.

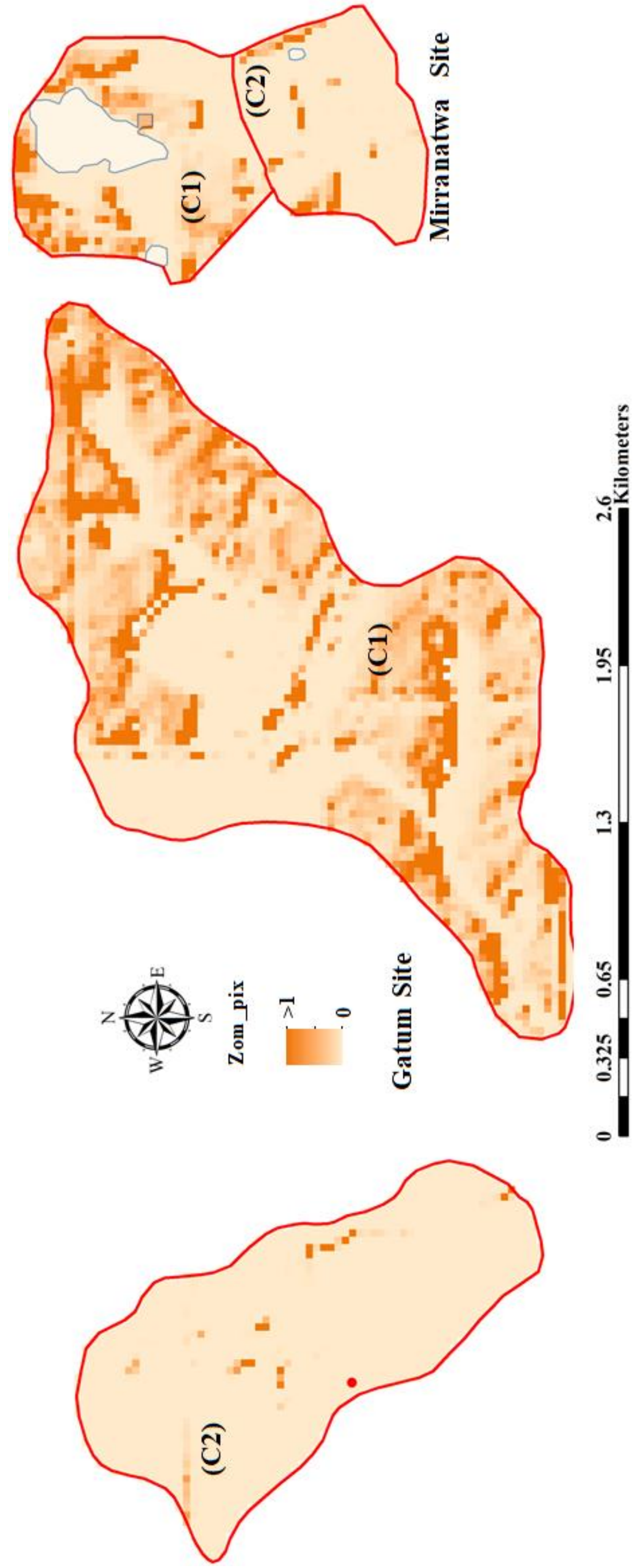

Figure 7.17. Momentum Roughness Length (Zom_{pix}).

7.3.3.2. Friction Velocity (μ^*_{pix})

The μ^*_{pix} is highly variable depending upon the ground surface; low for pastures and higher for plantations (Figure 7.18). The friction velocity recorded at the weather station at Gatum is 0.371, closely comparable to the model output for the corresponding pixel (0.367). The wind at the satellite pass time was 3.9 m/s, which although not characterised as a strong wind, elevated both the Zom_{pix} and μ^*_{pix} values. In summer at the Mirranatwa the pastures showed higher μ^*_{pix} values than the plantations, which may be due to active pasture growth. In winter for both plantation and pasture, μ^*_{pix} showed a contrasting response to the spatial pattern in summer. It can be due to the variability in carbon source and sink (Barr *et al.,* 2013; Paco *et al.,* 2009; Law *et al.,* 2002; Beer *et al.,* 2010; Reichstein *et al.,* 2007a & 2007b; Richardson *et al.,* 2010); eco-physiological processes and their climatic controls (Irvine *et al.,* 2005; Mahecha *et al.,* 2010); as well as landuse shift (Davis, 2008; Amiro *et al.,* 2010).

7.3.3.3. Temperature Difference (dT) and Air Temperature (T_a)

Due to the winter season, dT values are low (the cloud-covered area has the lowest value of < 1.8 °K). The dT follows the surface temperature pattern: high for pastures and lower for plantations.

The dT pattern also reflected in the T_a. The clouds prevented incoming radiation from reaching the surface, resulting in lower T_a. Pastures, especially at elevated patches, had the highest air temperature.

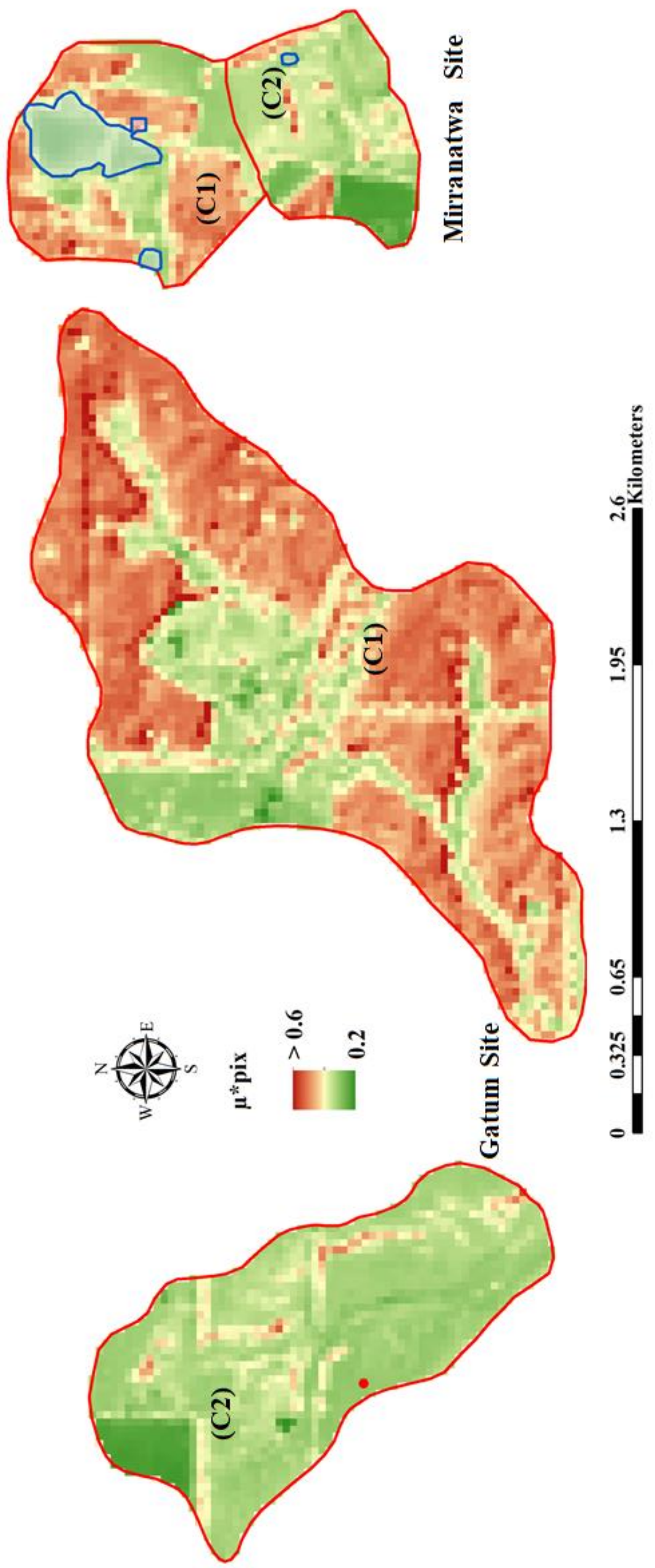

Figure 7.18. Friction Velocity (μ^*_{pix}).

7.3.3.4. Sensible Heat Flux (H)

Both the Gatum catchments present a distinct pattern of H (Figure 7.19), with pastures and crops representing the lower ranges (47 to 155 W/m^2) and plantations higher values (> 500 W/m^2).

The spatial response of H for plantation and pasture during winter contrasts with summer at Mirranatwa, where pasture had low sensible heat flux as compared to the plantation. The spatial pattern of R_n, available energy, T_s, T_a, and VIs are similar for the Mirranatwa plantation and pasture catchments during both seasons. However, lower values occur in winter: 50% less R_n and 66% less available energy. The sensible heat flux is a function of the temperature gradient, surface roughness and wind speed (Allen *et al.,* 2002a; Bastiaanssen, 2000; and Buntor *et al.*, 2019). The low-temperature gradient (dT) and NDVI, along with relatively higher wind speed and phenological stage, may have contributed to a higher aerodynamic resistance and friction velocity, leading to a higher sensible heat flux for the plantation during winter at the Gatum site.

The flux tower measurement of sensible heat flux at Gatum shows a peak (32.33 W/m^2) at 11:00 am whereas on either side of the time step; the H value is less than half of this value (11.3 W/m^2 at 10:30 am and 12.8 W/m^2 at 11:30 am). The corresponding pixel estimate is 72 W/m^2. The agreement of values recorded at the flux tower to SEBARA estimates for all the components of the energy balance equation except sensible heat flux is an indication of an anomaly in flux tower readings. Further, exploring the flux tower data, it was noticed the values of sensible heat flux for the image pass day were quite erratic whereas, on the previous and the following days, similar H values recorded.

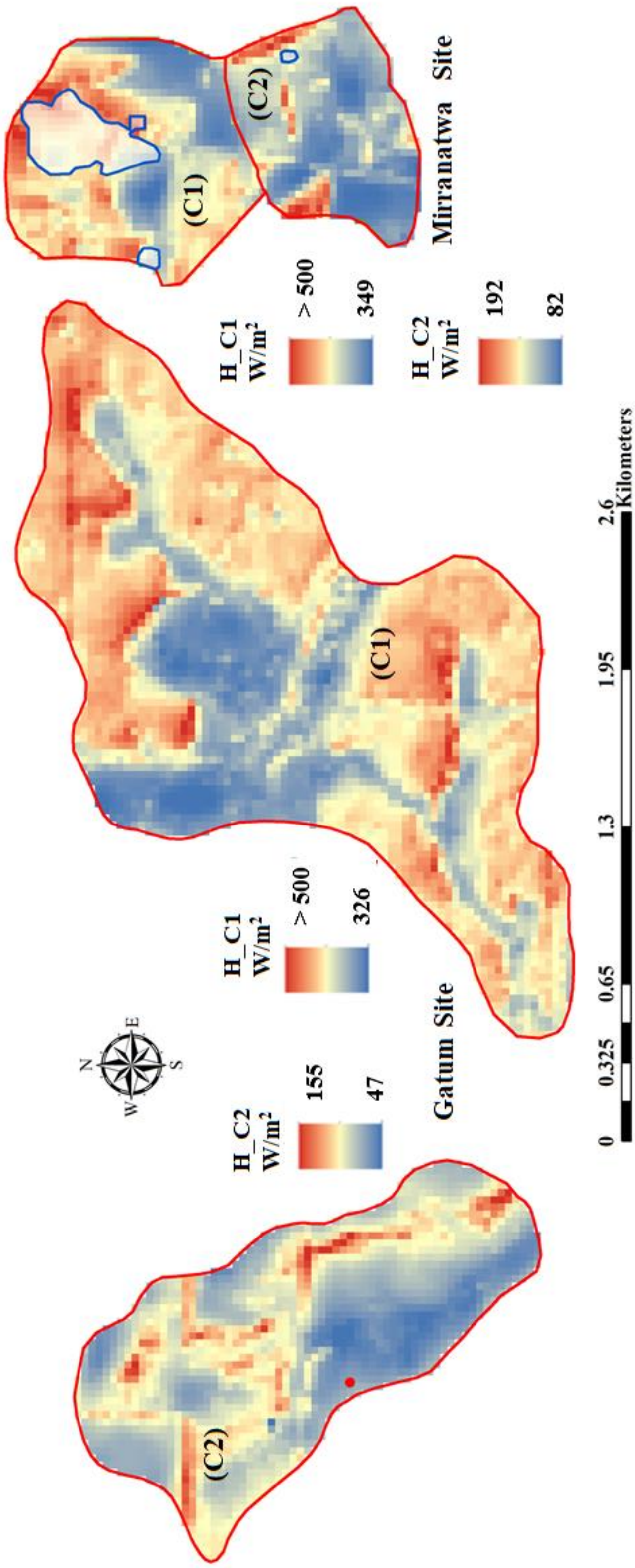

Figure 7.19. Sensible Heat Flux (H).

7.3.3.5. Latent Heat Flux (λET)

The λET at both sites ranges from negative to more than 50 W/m^2 (Figure 7.20). A few pixels in the pasture catchment have values higher than 50 W/m^2, whereas scattered trees or shelter belts have a negative flux. Low/negative fluxes (for both H and λET) in winter are possible (Van der Molen *et al.,* 2006; Ma *et al.,* 2017) due to ground cooling and condensation of water vapour. The latent heat flux recorded at the flux tower at the image pass time is 45 W/m^2, whereas the SEBARA estimate for the corresponding pixel is 41 W/m^2.

7.4. Evapotranspiration (ET)

7.4.1. ET instantaneous (ET_{inst})

The higher available energy in the pasture and the cropped area is utilized by the winter species growing in this area, leading to higher ET_{inst} values (Figure 7.21). The ET_{inst} measured at the flux tower at the satellite pass time is 0.050 mm/hr; for the corresponding pixel, the estimated value is 0.055 mm/hr.

7.4.2. Reference ET fraction (ET_rf)

The pastures have a variable ET fraction ranging from 0 to 0.75, whereas winter crops at both Mirranatwa and Gatum represent the highest ET_rf (Figure 7.22). The plantation, shelterbelts in the pasture catchment and scattered trees along the creeks show lower ET_rf.

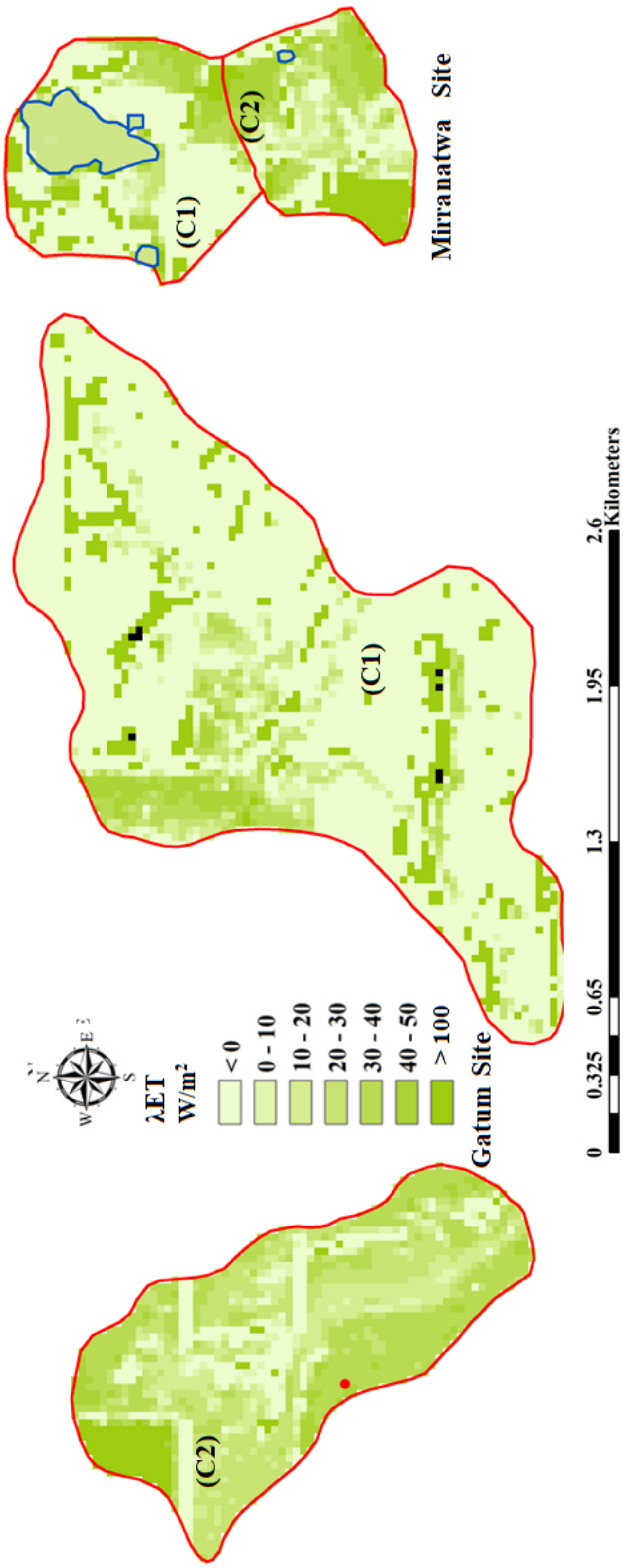

Figure 7.20. Latent Heat Flux (λET).

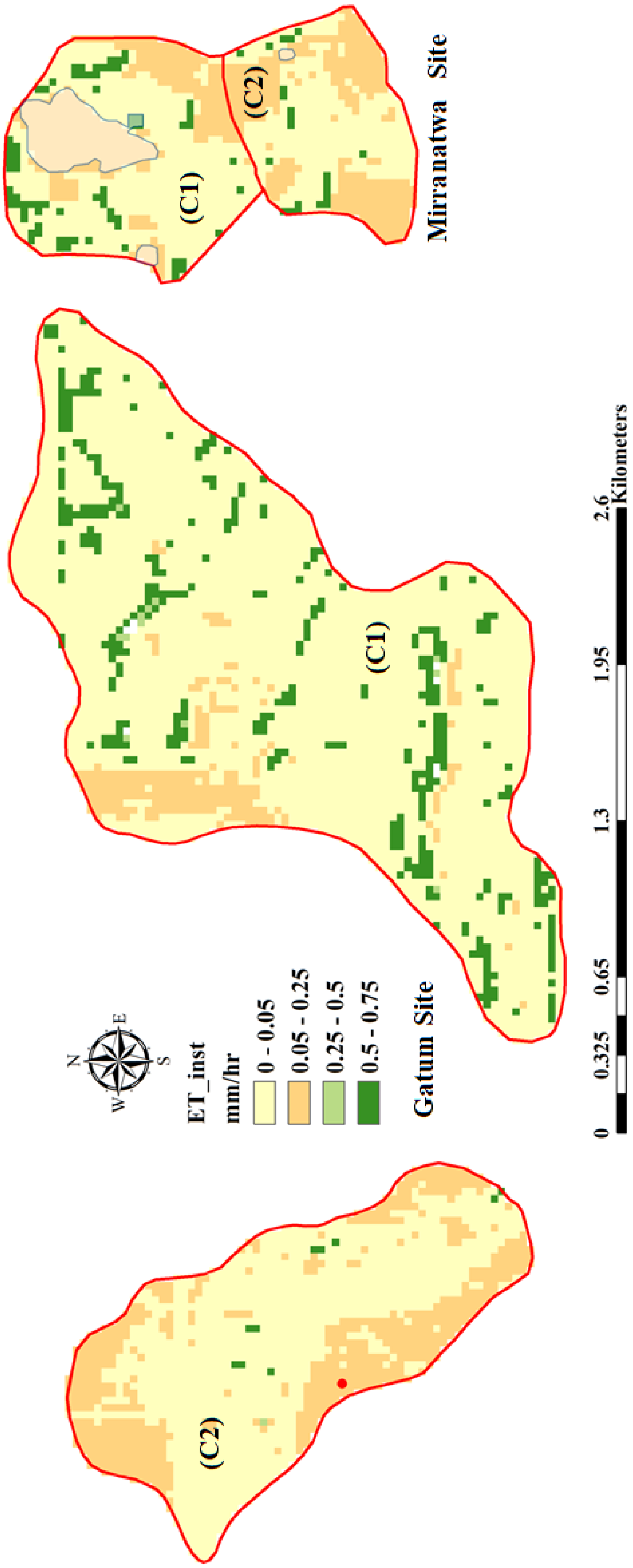

Figure 7.21. Instantaneous ET (ET_{inst}).

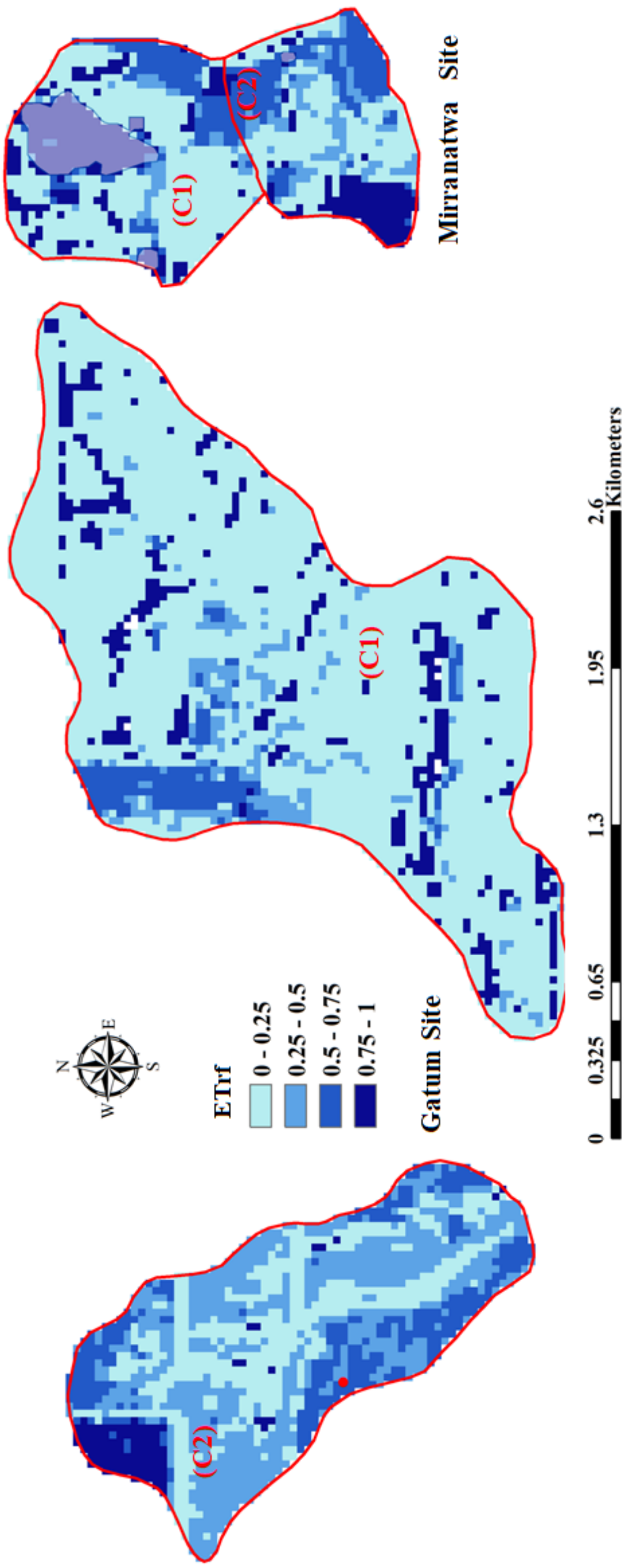

Figure 7.22. ETr fraction (ETrf).

7.4.3. Daily ET (ET_{24})

The spatial pattern of daily ET_{24} is like the ET_{inst} pattern and ranges from <0.25 to > 1 mm/day (Figure 7.23). A few pixels in the pasture catchment have values >2 mm/day and represent either the higher evaporation from farm dams/drains surrounded by trees or dense tree plantation on elevated areas. In plantation catchment, an ET > 2 mm/day represented by pastures with scattered trees at elevated areas.

In general, the pasture catchment has relatively high ET_{24}, although, the low-lying areas have the lowest ET_{24}. Compared to 0.429 mm/day ET recorded at the flux tower, the SEBARA daily output for the corresponding pixel is 0.495 mm/day. In the plantation catchment, the plantation and pasture exhibited a similar response except for the pasture at elevated areas. The pixels with higher ET occur in the north-western and southern parts with a mix of pasture and trees.

The soil heat flux recorded at the flux tower was negative at the satellite pass time. The flux tower also recorded low vapour pressure deficit (0.38), high relative humidity (67%) and the low net radiation at the satellite pass time. Although rainfall was recorded during the week prior to the satellite pass day, in the tree plantation low root activity due to a negative soil flux, low soil evaporation; and low temperature may be responsible for lower ET, which is following the outcome of earlier studies (Knohl et al., 2003; Shirke et al., 2004).

At Mirranatwa, the spatial pattern of the components of surface radiation balance was similar for summer and winter; however, with lower ranges for winter. The response of main component of surface radiation and energy balance components for summer and winter are given in Table 7.1. The climatic controls on ET including solar radiation, humidity, and vapour pressure deficit (Allen *et al.*, 1998; Reichstein, *et al.*, 2010) were variable and contributed to the lower winter ET of plantation. Since the daily partitioning of net radiation into soil heat flux and sensible heat flux, it is a dynamic process that depends upon wind speed and sensible heat balance residual (Cellier *et al.,* 1996; Heitman *et al.,* 2008) which may further also be responsible for lower ET . In winter, the contrasting response of sensible heat flux, higher wind speed and relative humidity were responsible for elevating the contrast of evaporative fluxes. Furthermore, the physiological and morphological stages, as well as the net photosynthesis rate of plantations and pasture in both the seasons, are responsible for the differences in ET. This response is in agreement with reported studies (Huizhi and Jianwu, 2012; de Sousa Lima *et al.,* 2013; Baldocchi and Meyers, 1998; Li *et al.,* 2005; Verhoef *et al.,* 1999; Sun and Wu, 2001; Cornic, 2000; Ma *et al.,* 2007; Baldocchi and Xu, 2007; Ryu *et al.,* 2008; Wilson and Baldocchi, 2000 and Wever *et al.,* 2002; Frank and Inouye, 1994; Pereira *et al.,* 1986). The groundwater data was not used for winter because the ET estimate was the main objective. Further, due to wintertime, the growth was slow, and therefore, ET was low as well.

In conclusion, SEBARA performed well at the Gatum site in estimating ET with an accuracy of +10% compared to field measurements, despite the assumptions made in SEBARA. Use of a detailed landuse map and consideration of vegetation types to adjust the model variables, especially the sensible and latent heat fluxes, is strongly recommended.

In general, the surface energy models SEBARA predicted ET with an accuracy level of ± 10%, better than the uncertainty of ± 20% achieved in-field measurements of transpiration in the same region (Benyon *et al.,* 2006, Forrester *et al.,* 2010; Dean, 2013).

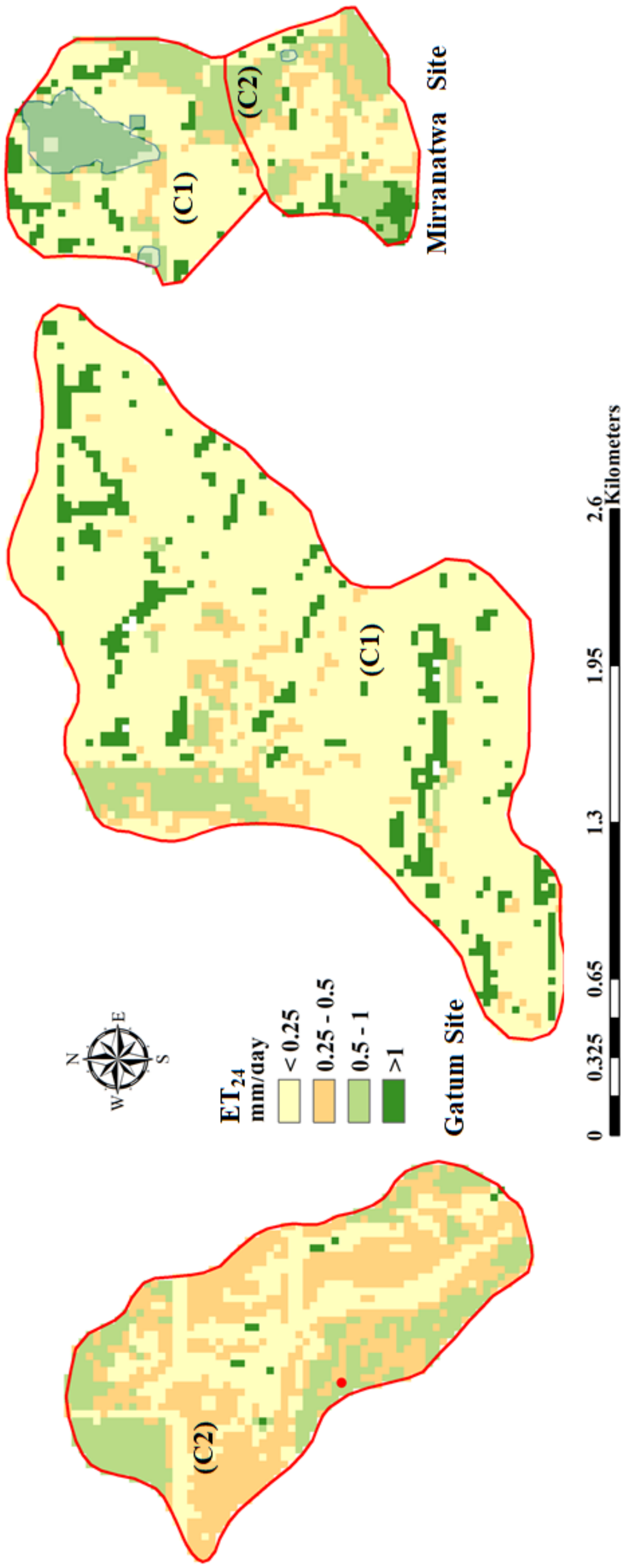

Figure 7.23. Daily ET (ET_{24}).

Table 7-1. Comparison of summer and winter surface radiation and energy budgets.

	Summer Mirranatwa	Winter Mirranatwa & Gatum
Surface radiation balance		
Solar constant (W/m^2)	1367	
$R_S\downarrow$ (W/m^2)	830	437
$R_L\downarrow$ (W/m^2)	236	222
$R_L\uparrow$ (W/m^2)	360 - 402	319 - 343
Albedo (α_{surf})	0.02 - 0.1	0.003 - 0.057
NDVI	0.39 - 0.81	0.18 - 0.83
SAVI	0.27 - 0.7	0.1 - 0.57
LAI	0.27 - 3.05	0.1 - 1.77
Emissivity	0.96 - 0.99	0.94 - 1.0
Ts (^{o}C)	9.28 - 18.64	4.0 - 6.5
Rn (W/m^2)	473 - 698	299 - 339
Surface energy balance		
G/R_n ratio	0.01 - 0.07	0.11 - 0.45
G (W/m^2)	4.41 - 38.01	8 - 60
H (W/m^2)	109 - 477	47 - >500
λET (W/m^2)	118 - 344	< 0 - >100
ET_{inst} (mm/hr)	0.19 - 0.55	0 - 0.75
ETrF	0.19 - 0.59	0.25 - 1
ET_{24} (mm/day)	1.5 - 4.2	< 0.25 - > 1

Note: A few pixels sometimes show unrepresentative extreme values either as maximum or minimum except for latent heat flux where plantations generally showed a negative flux during winter.

Chapter 8. Conclusions

8.1. Key outcomes:

- Using the SEBARA algorithm with input data including satellite images (visible, NIR, SWIR and thermal bands), climatic data (from a weather station) and the target site landuse, spatial patterns of evapotranspiration can be estimated with a high level of accuracy (85-95%).

- Pastures during summer season, in general, has 22% lower ET as compared to tree plantations due to limited access to soil moisture of the shallow root system, higher energy loss as outgoing longwave radiation and higher soil heat flux.

- Tree plantation mirrored the response of pastures in general; however, the young plantation did not exceed the ET rates of pasture, whereas the old forest and plantations at lower elevations consistently showed ET 15-20% higher than pastures.

- Groundwater depth from borehole data can help in understanding the spatial variability of ET, especially in tree plantations, and its role in the hydrological lift and groundwater redistribution by trees.

- During winter, ET is 16-24% of the summer ET and winter pastures have higher ET as compared to the plantations.

8.2. Research Highlights

- Following the principals of Surface Energy Balance Algorithms for Land (SEBAL), a modified approach (Surface Energy Balance Algorithms for Rainfed Agriculture - SEBARA) is developed. This approach uses medium spatial resolution Landsat image, climate data, weather station information, landuse and topography of the study catchments to estimate the evapotranspiration (ET) of rainfed agrosystems.

- The model was used to estimate the ET of two adjacent catchments with similar climatic conditions but contrasting land uses (*Eucalyptus globulus* plantation and pasture), located at Mirranatwa, about 230 km west of Melbourne, south-eastern Australia.

- The daily ET estimate of SEBARA during summer in the pasture catchment is only 4.55% less than the measured value at a flux tower in the catchment. In contrast, estimated ET for the plantation catchment is 12.97% higher than the sapflow reading. Considering the spatial and temporal variability in ET, the accuracies achieved (88-95%) using SEBARA are satisfactory.

- The model output also compared with calculations of ET using reference crop evapotranspiration (RefET - ET_o for pasture and ET_r for plantation) and the Catchment Hydrology (CATHY) distributed model. SEBARA underestimates ET as compared to RefET (< 8% for pasture and < 1% for plantation), these levels of accuracy regarded as satisfactory. In comparison with CATHY it overestimates ET (15% for pasture and 25% for planation).

- Overall, tree plantations have the highest daily ET, ranging from 2.34 mm/day to 4.2 mm/day during summer. The lower ranges represent the areas with deep groundwater or shallow saline groundwater, whereas the higher ranges represent the areas with medium groundwater depth.

- Pastures show spatial variability in daily ET ranging from 1.44 to 4 mm/day. The annual pastures at a higher elevation with deep groundwater had lower ET due to limited soil moisture; however, at lower elevations with better soil moisture, perennial pastures could attain higher ET, comparable to plantations.

- A cultivated oats crop at lower elevations, having a good vegetation cover and a farm dam, had higher daily ET than the pasture, and old forest, despite being located in an area with deep groundwater, also achieved higher ET due to its extensive and deep roots.

- The groundwater depth surface generated using borehole data helped in understanding the spatial variability of ET, especially in the tree plantation. In young plantation, ET is only limited by either shallow saline groundwater or a groundwater depth of > 15 m.

- After comparison, the SEBARA algorithm was used for another paired catchment at Gatum to the west of the Grampians, which had a similar climate to the Mirranatwa site. At this site, the SEBARA algorithm updated for Landsat 8 data and the winter image used for ET estimation. In general, the pasture catchment had relatively higher daily ET as compared to the tree plantation catchment. The spatial variability of ET ranged from < 0.25 to >1 mm/day, and compared to flux tower readings, an accuracy of ~10% was achieved.

8.3. Way forward

- The SEBARA algorithm may be applied in diversified environments having variable landuse so that spatial evapotranspiration response can be understood on a larger scale.

- Landsat data is available for over more than four decades, and SEBARA can be used with this data to see the temporal changes in ET following any shift in land use. This information can be used for future planning in rainfed agricultural systems.

- The data from the OzFlux network of 30 flux towers in diversified environments can be a useful input source for SEBARA.

- Although SEBARA algorithm developed for medium resolution Landsat data, it can be tested for higher spatial and temporal resolution satellite data, provided the thermal band or land surface temperature product is available with a data bundle.

8.4. Recommendations

- Based on the outcome of this research project, it is recommended that for future *Eucalyptus* plantation planning programmes, especially in rainfed environment, it's impact on water resources should be considered.

- *Eucalyptus* plantation should be avoided in the area with deep groundwater.

- In the existing *Eucalyptus* plantations in rainfed areas, farm dams can help to recharge the groundwater.

References

Adelana, S. M., Dresel, P. E., Hekmeijer, P., Zydor, H., Webb, J. A., Reynolds, M., & Ryan, M. (2015). A comparison of streamflow, salt and water balances in adjacent farmland and forest catchments in south-western Victoria, Australia. *Hydrological processes*, *29*(6), 1630-1643. https://doi.org/10.1002/hyp.10281

Adkins, C.J. (1975). *Equilibrium Thermodynamics*, second edition, McGraw-Hill, London, ISBN 0-07-084057-1, Section 3.6, pages 43-46.

Ahmad A. S. and Lockwood J.G. (1979). Albedo. In Progress in Physical Geography, 3, 4, (510-543). 10.1177/030913337900300403.

Albaugh JM, Dye PJ, King JS (2013) *Eucalyptus* and Water Use in South Africa. International Journal of Forestry Research Volume, 11 pages. Article ID 852540, http://dx.doi.org/10.1155/2013/852540.

Allen G. R. (2011). Ref-ET: Reference evapotranspiration calculation software for FAO and ASCE standardized equations. Vol 3.1 for windows. pp. 86. Publisher University of Idaho USA.

Allen, C. D., Betancourt, J. L., & Swetnam, T. W. (1998). Landscape changes in the southwestern United States: techniques, long-term data sets, and trends. Cahpter 9 In Perspectives on the Land-Use History of North America: A Context for Understanding Our Changing Environment. Fort Collins (CO): US Geological Survey, 71-84.

Allen, R. G., & Tasumi, M. (2005). Evaporation from American Falls Reservoir in Idaho via a combination of Bowen ratio and eddy covariance. *In* Impacts of Global Climate Change (pp. 1-17).

Allen, R. G., (2002). Evapotranspiration from a satellite-BASED surface energy balance for the snake plain aquifer in Idaho *In* Proceedings of the National USCID Conference, United States Committee on Irrigation and Drainage (USCID), Denver.

Allen, R. G., Bastiaanssen W, Waters R *et al*. (2002) SEBAL - Surface Energy Balance Algorithms for Land – Idaho Implementation, Advance Training and User Manual. Department of Water Resources, University of Idaho, US. pp 98.

Allen, R. G., Burnett, B., Kramber, W., Huntington, J., Kjaersgaard, J., Kilic, A., ... & Trezza, R. (2013). Automated calibration of the metric-landsat evapotranspiration process. *JAWRA Journal of the American Water Resources Association*, *49*(3), 563-576. https://doi.org/10.1111/jawr.12056

Allen, R. G., Morse, A., Tasumi, M., Trezza, R., Bastiaanssen, W., Wright, J. L., & Kramber, W. (2002). Evapotranspiration from a satellite-based surface energy balance for the Snake Plain Aquifer in Idaho. *In* Proc. USCID Conference. USCID.

Allen, R. G., Pereira L. S. Raes D. & Smith M. 1998. Crop evapotranspiration - Guidelines for computing crop water requirements - FAO Irrigation and drainage paper 56. Chapter 5_ Introduction to Crop Evapotranspiration. FAO - Food and Agriculture Organization of the United Nations. http://www.fao.org/3/X0490E/x0490e0a.htm Rome. ISBN 92-5-104219-5.

Allen, R. G., Tasumi, M., & Trezza, R. (2007). Satellite-based energy balance for mapping evapotranspiration with internalized calibration (METRIC)—Model. *Journal of irrigation and drainage engineering*, *133*(4), 380-394. https://doi.org/10.1061/(ASCE)0733-9437(2007)133:4(380)

Allen, R. G., Tasumi, M., Morse, A., & Trezza, R. (2005). A Landsat-based energy balance and evapotranspiration model in Western US water rights regulation and planning. *Irrigation and Drainage systems*, *19*(3-4), 251-268. https://doi.org/10.1007/s10795-005-5187-z.

Allen, R. G., Tasumi, M., Morse, A., & Trezza, R. (2005). A Landsat-based energy balance and evapotranspiration model in Western US water rights regulation and planning. *Irrigation and Drainage systems*, *19*(3-4), 251-268. https://doi.org/10.1007/s10795-005 -5187-z.

Allen, R., Irmak, A., Trezza, R., Hendrickx, J. M., Bastiaanssen, W., & Kjaersgaard, J. (2011). Satellite-based ET estimation in agriculture using SEBAL and METRIC. *Hydrological Processes*, *25*(26), 4011-4027. https://doi.org/10.1002/hyp.8408

Allen, R., Irmak, A., Trezza, R., Hendrickx, J. M., Bastiaanssen, W., & Kjaersgaard, J. (2011). Satellite-based ET estimation in agriculture using SEBAL and METRIC. *Hydrological Processes*, *25*(26), 4011-4027. https://doi.org/10.1002/hyp.8408

Allen, R.G. (2011). Ref_ET: Reference Evapotranspiration Calculation Software for FAO and ASCE Standardized Equations.Version 3.1 for Windows: Window XP, Vista, Window 7. University of Idaho. pp86.

Allen, R.G., Pereira, L.S., Raes, D. and Smith, M. (1998a). Crop Evapotranspiration-Guidelines for computing crop water requirements-FAO Irrigation and drainage paper 56. *FAO, Rome*, *300*(9), p.D05109.

Allen, R.G., Pereira, L.S., Raes, D. and Smith, M. (1998b). Dual crop coefficient ($K_c = K_{cb} + K_e$) In Crop Evapotranspiration-Guidelines for computing crop water requirements-FAO Irrigation and drainage paper 56. FAO, Rome, 300(9), p.D05109.

Allen, R.G., Pereira, L.S., Raes, D. and Smith, M., 1998. Crop evapotranspiration-Guidelines for computing crop water requirements-FAO Irrigation and drainage paper 56. FAO, Rome, 300(9), p.D05109.

Allison, G. B., & Barnes, C. J. (1985). Estimation of evaporation from the normally "dry" Lake Frome in South Australia. Journal of Hydrology, 78(3-4), 229-242. https://doi.org/10.1016/0022-1694(85)90103-9

Alves, M. E. B., Mantovani, E. C., Sediyama, G. C., & Neves, J. C. L. (2013). Estimate of the crop coefficient for Eucalyptus cultivated under irrigation during initial growth. Cerne, 19(2), 247-253. http://dx.doi.org/10.1590/S0104-77602013000200008

Amenu, G. G., & Kumar, P. (2007). A model for hydraulic redistribution incorporating coupled soil-root moisture transport. Hydrology and Earth System Sciences Discussions, 4(5), 3719-3769. http://www.hydrol-earth-syst-sci-discuss.net/

Amiro, B. D., Barr, A. G., Barr, J. G., Black, T. A., Bracho, R., Brown, M., ... & Dore, S. (2010). Ecosystem carbon dioxide fluxes after disturbance in forests of North America. Journal of Geophysical Research: Biogeosciences, 115, G00K02. http://dx.doi.org/10.1029/2010JG001390.

Anderson, M. C., Allen, R. G., Morse, A., & Kustas, W. P. (2012). Use of Landsat thermal imagery in monitoring evapotranspiration and managing water resources. *Remote Sensing of Environment*, *122*, 50-65. https://doi.org/10.1016/j.rse.2011.08.025

André, J. C., Goutorbe, J. P., & Perrier, A. (1986). HAPEX—MOBLIHY: A Hydrologic Atmospheric Experiment for the Study of Water Budget and Evaporation Flux at the Climatic Scale. *Bulletin of the American Meteorological Society*, *67*(2), 138-144. https://doi.org/10.1175/1520-0477(1986)067<0138:HAHAEF>2.0.CO;2

Andre, J. C., Goutorbe, J. P., Perrier, A., Becker, F., Bessemoulin, P., Bougeault, P., ... & Gash, J. (1988). Evaporation over land-surfaces: First results from HAPEX-MOBILHY special observing period. Annls Geophysicae 6, 477-492. ⟨hal-01011981⟩

Anthes, R. A. (1984). Enhancement of convective precipitation by mesoscale variations in vegetative covering in semiarid regions. *Journal of Climate and Applied Meteorology*, *23*(4), 541-554. https://doi.org/10.1175/1520-0450(1984)023<0541:EOCPBM>2.0.CO;2

Armson, D., Stringer, P., & Ennos, A. R. (2012). The effect of tree shade and grass on surface and globe temperatures in an urban area. *Urban Forestry & Urban Greening*, *11*(3), 245-255. https://doi.org/10.1016/j.ufug.2012.05.002

Baldocchi, D. D., & Xu, L. (2007). What limits evaporation from Mediterranean oak woodlands–The supply of moisture in the soil, physiological control by plants or the demand by the atmosphere? *Advances in Water Resources*, *30*(10), 2113-2122. https://doi.org/10.1016/j.advwatres.2006.06.013

Baldocchi, D., & Meyers, T. (1998). On using eco-physiological, micrometeorological and biogeochemical theory to evaluate carbon dioxide, water vapor and trace gas fluxes over vegetation: a perspective. *Agricultural and Forest Meteorology*, *90*(1-2), 1-25. https://doi.org/10.1016/S0168-1923(97)00072-5

Barad, M. L. (1959). Project Prairie Grass, A Field Program in Diffusion, Volume I1, Geophysics Research Directorate, Air Force Cambridge Research Center, Bedford, Massachusetts.

Baret, F., & Guyot, G. (1991). Potentials and limits of vegetation indices for LAI and APAR assessment. *Remote sensing of environment*, *35*(2-3), 161-173. https://doi.org/10.1016/0034-4257(91)90009-U

Barr, A. G., Richardson, A. D., Hollinger, D. Y., Papale, D., Arain, M. A., Black, T. A., ... & Law, B. E. (2013). Use of change-point detection for friction–velocity threshold evaluation in eddy-covariance studies. *Agricultural and Forest Meteorology*, *171*, 31-45. https://doi.org/10.1016/j.agrformet.2012.11.023

Barry, R. G. (1992). Mountain Weather and Climate, 2nd ed., Psychology Press. 402 pp.

Barsi JA, Barker JL, Schott JR (2003) An Atmospheric Correction Parameter Calculator for a single thermal band earth-sensing instrument. *Geoscience and Remote Sensing Symposium, 2003. IGARSS '03. Proceedings. 2003 IEEE International Vol: 5*. DOI: 10.1109/IGARSS.2003.1294665.

Bastiaanssen, W. G. (2000). SEBAL-based sensible and latent heat fluxes in the irrigated Gediz Basin, Turkey. *Journal of hydrology*, *229*(1-2), 87-100. https://doi.org/10.1016/S0022-1694(99)00202-4

Bastiaanssen, W. G. M. (1995). Regionalization of surface flux densities and moisture indicators in composite terrain. *A remote sensing approach under clear skies in Mediterranean climates*, *271*. DLO Winand Staring Centre, Wageningen, The Netherlands.

Bastiaanssen, W. G. M. (1995). Regionalization of surface flux densities and moisture indicators in composite terrain: A remote sensing approach under clear skies in Mediterranean climates. PhD Diss. SC-DLO. ISBN 9789054854654 - 273

Bastiaanssen, W. G. M., Cheema, M. J. M., Immerzeel, W. W., Miltenburg, I. J., & Pelgrum, H. (2012). Surface energy balance and actual evapotranspiration of the transboundary Indus Basin estimated from satellite measurements and the ETLook model. *Water Resources Research*, *48*(11). https://doi.org/10.1029/2011WR010482

Bastiaanssen, W. G. M., Noordman, E. J. M., Pelgrum, H., Davids, G., Thoreson, B. P., & Allen, R. G. (2005). SEBAL model with remotely sensed data to improve water-resources management under actual field conditions. *Journal of irrigation and drainage engineering*, *131*(1), 85-93. https://doi.org/10.1061/(ASCE)0733-9437(2005)131:1(85)

Bastiaanssen, W. G., Menenti, M., Feddes, R. A., & Holtslag, A. A. M. (1998a). A remote sensing surface energy balance algorithm for land (SEBAL). 1. Formulation. *Journal of hydrology*, *212*, 198-212. https://doi.org/10.1016/S0022-1694(98)00253-4

Bastiaanssen, W. G., Pelgrum, H., Wang, J., Ma, Y., Moreno, J. F., Roerink, G. J., & Van der Wal, T. (1998). A remote sensing surface energy balance algorithm for land (SEBAL).: Part 2: Validation. *Journal of hydrology*, *212*, 213-229. https://doi.org/10.1016/S0022-1694(98)00254-6

Beer, C., Reichstein, M., Tomelleri, E., Ciais, P., Jung, M., Carvalhais, N., ... & Bondeau, A. (2010). Terrestrial gross carbon dioxide uptake: global distribution and covariation with climate. *Science*, *329*(5993), 834-838. http://dx.doi.org/10.1126/science.1184984

Beljaars, A. C. M., & Holtslag, A. A. M. (1991). Flux parameterization over land surfaces for atmospheric models. *Journal of Applied Meteorology*, *30*(3), 327-341. https://doi.org/10.1175/1520-450(1991)030<0327:FPOLSF>2.0.CO;2

Benyon, R. G., Theiveyanathan, S., & Doody, T. M. (2006). Impacts of tree plantations on groundwater in south-eastern Australia. *Australian Journal of Botany*, *54*(2), 181-192. https://doi.org/10.1071/BT05046

Benyon, R.G. (2002). Water use by tree plantations in the Green Triangle: a review of current knowledge. Glenelg Hopkins catchment Management Authority: Hamilton, VIC.; and CSIRO Forestry and Forest Products: Mt Gambier, SA.

Best, A., Zhang, L., McMahon, T., Western, A., & Vertessy, R. (2003). A critical review of paired catchment studies with reference to seasonal flows and climatic variability. CSIRO Land and Water Technical Report No. 25/03, Murray Darling Basin Commission, Canberra, Australia.

Blyth, E. M., & Dolman, A. J. (1995). The roughness length for heat of sparse vegetation. *Journal of Applied Meteorology*, *34*(2), 583-585. https://doi.org/10.1175/1520-0450-34.2.583

Bosch, J. M., & Hewlett, J. D. (1982). A review of catchment experiments to determine the effect of vegetation changes on water yield and evapotranspiration. *Journal of hydrology*, *55*(1-4), 3-23.

Bowen, I. S. (1926). The ratio of heat losses by conduction and by evaporation from any water surface. *Physical review*, *27*(6), 779. https://doi.org/10.1103/PhysRev.27.779

Brooks, J. R., Meinzer, F. C., Coulombe, R. O. B., & Gregg, J. (2002). Hydraulic redistribution of soil water during summer drought in two contrasting Pacific Northwest coniferous forests. *Tree physiology*, *22*(15-16), 1107-1117. https://doi.org/10.1093/treephys/22.15-16.1107

Brown, A. E., Zhang, L., McMahon, T. A., Western, A. W., & Vertessy, R. A. (2005). A review of paired catchment studies for determining changes in water yield resulting from alterations in vegetation. *Journal of hydrology*, *310*(1-4), 28-61. https://doi.org/10.1016/j.jhydrol.2004.12.010

Brutsaert, W. (1982). Evaporation into the Atmosphere: Theory, History, and Applications (Dordrecht, Holland: Reidel).

Brutsaert, W. (1986). Catchment-scale evaporation and the atmospheric boundary layer. *Water Resources Research*, *22*(9S), 39S-45S. https://doi.org/10.1029/WR022i09Sp0039S

Brutsaert, W. (1993). Horton, pipe hydraulics, and the atmospheric boundary layer (The Robert E. Horton Memorial Lecture).

Brutsaert, W. (1998). Land-surface water vapor and sensible heat flux: Spatial variability, homogeneity, and measurement scales. *Water Resources Research*, *34*(10), 2433-2442. https://doi.org/10.1029/98WR01340

Brutsaert, W. (2013). *Evaporation into the atmosphere: theory, history and applications* (Vol. 1). Springer Science & Business Media.

Brutsaert, W., & Sugita, M. (1996). Sensible heat transfer parameterization for surfaces with anisothermal dense vegetation. *Journal of the Atmospheric Sciences*, *53*(2), 209-216. https://doi.org/10.1175/1520-0469(1996)053<0209:SHTPFS>2.0.CO;2

Budyko, M. I. (1969). The effect of solar radiation variations on the climate of the Earth. *tellus*, *21*(5), 611-619. https://doi.org/10.3402/tellusa.v21i5.10109

Burba, G. (2013). *Eddy covariance method for scientific, industrial, agricultural and regulatory applications: A field book on measuring ecosystem gas exchange and areal emission rates*. LI-Cor Biosciences. Lincolin, NE, USA, 331pp.

Burgess, S. S., Adams, M. A., Turner, N. C., & Ong, C. K. (1998). The redistribution of soil water by tree root systems. *Oecologia*, *115*(3), 306-311. https://doi.org/10.1007/s004420050521

Burgess, S. S., Adams, M. A., Turner, N. C., White, D. A., & Ong, C. K. (2001). Tree roots: conduits for deep recharge of soil water. *Oecologia*, *126*(2), 158-165. https://doi.org/10.1007/s004420000501

Butnor, J. R., Johnsen, K. H., Anderson, P. H., Hall, K. B., Halman, J. M., Hawley, G. J., ... & Schaberg, P. G. (2019). Growth, photosynthesis, and cold tolerance of Eucalyptus benthamii planted in the piedmont of North Carolina. Forest Science, 65(1), 59-67. https://doi.org/10.1093/forsci/fxy030

Cahalan, R. F., & North, G. R. (1979). A stability theorem for energy-balance climate models. *Journal of the Atmospheric Sciences*, 36(7), 1178-1188. https://doi.org/10.1175/1520-0469(1979)036<1178:ASTFEB>2.0.CO;2

Calder, I. R. (1998). Water use by forests, limits and controls. *Tree physiology*, *18*(8-9), 625-631. https://doi.org/10.1093/treephys/18.8-9.625

Calder, I. R., Hall, R. L., & Prasanna, K. T. (1993). Hydrological impact of *Eucalyptus* plantation in India. *Journal of Hydrology*, *150*(2-4), 635-648. https://doi.org/10.1016/0022-1694(93)90129-W

Calder, I. R., Rosier, P. T., Prasanna, K. T., & Parameswarappa, S. (1997). *Eucalyptus* water use greater than rainfall input-possible explanation from southern India.

Caldwell, M. M., Dawson, T. E., & Richards, J. H. (1998). Hydraulic lift: consequences of water efflux from the roots of plants. *Oecologia*, *113*(2), 151-161. https://doi.org/10.1007/s004420050363

Camporese, M., Daly, E., Dresel, P. E., & Webb, J. A. (2014). Simplified modeling of catchment-scale evapotranspiration via boundary condition switching. *Advances in water resources*, *69*, 95-105. doi:10.1016/j.advwaters.2014.04.008

Camporese, M., Dean, J. F., Dresel, P. E., Webb, J., & Daly, E. (2013). Hydrological modelling of paired catchments with competing landuses.

In *Proceedings of the 20th International Congress on Modelling and Simulation*, *Adelaide*, *Australia* (pp. 1-6). www.mssanz.org.au/modsim2013

Canadell, J., Jackson, R. B., Ehleringer, J. B., Mooney, H. A., Sala, O. E., & Schulze, E. D. (1996). Maximum rooting depth of vegetation types at the global scale. *Oecologia*, *108*(4), 583-595. https://doi.org/10.1007/BF00329030

Carlson, T. N., & Ripley, D. A. (1997). On the relation between NDVI, fractional vegetation cover, and leaf area index. *Remote sensing of Environment*, *62*(3), 241-252. https://doi.org/10.1016/S0034-4257(97)00104-1

Castellví, F., & Snyder, R. L. (2009). On the performance of surface renewal analysis to estimate sensible heat flux over two growing rice fields under the influence of regional advection. *Journal of hydrology*, *375*(3-4), 546-553. https://doi.org/10.1016/j.jhydrol.2009.07.005

Cellier, P., Richard, G., & Robin, P. (1996). Partition of sensible heat fluxes into bare soil and the atmosphere. *Agricultural and forest meteorology*, *82*(1-4), 245-265. https://doi.org/10.1016/0168-1923(95)02328-3.

Cess, R. D. (1978). Biosphere-albedo feedback and climate modeling. *Journal of the Atmospheric Sciences*, *35*(9), 1765-1768. https://doi.org/10.1175/1520-0469(1978)035<1765:BAFACM>2.0.CO;2

Chander, G., & Markham, B. (2003). Revised Landsat-5 TM radiometric calibration procedures and postcalibration dynamic ranges. *IEEE Transactions on geoscience and remote sensing*, *41*(11), 2674-2677. DOI: 10.1109/TGRS.2003.818464

Chander, G., Haque, M. O., Micijevic, E., & Barsi, J. A. (2009). A procedure for radiometric recalibration of Landsat 5 TM reflective-band data. *IEEE Transactions on Geoscience and Remote Sensing*, *48*(1), 556-574. DOI: 10.1109/TGRS.2009.2026166

Chander, G., Markham, B. L., & Barsi, J. A. (2007). Revised Landsat-5 thematic mapper radiometric calibration. *IEEE Geoscience and remote sensing letters*, *4*(3), 490-494. DOI: 10.1109/LGRS.2007.898285

Charney, J. G. (1975). Dynamics of desert and drought in the Sahel. *Q. Jl R. met. Soc. 101*, 193-202.

Chen, C.P. 1989. Problems and prospect of integration of forage into permanent crops. In: Halim, R.A., 1989, February. Grasslands and Forage Production in South-east Asia. In *Proceedings of First Meeting of the Regional Group on Grazing and Feed Resources in South-East Asia* (Vol.

27).

Chen, Y. C., Christensen, M. W., Xue, L., Sorooshian, A., Stephens, G. L., Rasmussen, R. M., & Seinfeld, J. H. (2012). Occurrence of lower cloud albedo in ship tracks. *Atmospheric Chemistry and Physics*, *12*(17), 8223-8235. https://doi.org/10.5194/acp-12-8223-2012

Choudhury, B. J. (1987). Relationships between vegetation indices, radiation absorption, and net photosynthesis evaluated by a sensitivity analysis. *Remote Sensing of Environment*, *22*(2), 209-233. https://doi.org/10.1016/0034-4257(87)90059-9

Choudhury, B. J., Idso, S. B., & Reginato, R. J. (1987). Analysis of an empirical model for soil heat flux under a growing wheat crop for estimating evaporation by an infrared-temperature based energy balance equation. *Agricultural and Forest Meteorology*, *39*(4), 283-297. https://doi.org/10.1016/0168-1923(87)90021-9

Christensen, M. W., & Stephens, G. L. (2011). Microphysical and macrophysical responses of marine stratocumulus polluted by underlying ships: Evidence of cloud deepening. *Journal of Geophysical Research: Atmospheres*, *116*(D3). https://doi.org/10.1029/2010JD014638

Clothier, B. E., Clawson, K. L., Pinter Jr, P. J., Moran, M. S., Reginato, R. J., & Jackson, R. D. (1986). Estimation of soil heat flux from net radiation during the growth of alfalfa. *Agricultural and forest meteorology*, *37*(4), 319-329. https://doi.org/10.1016/0168-1923(86)90069-9

Cobos, D. R., & Baker, J. M. (2003). In situ measurement of soil heat flux with the gradient method. *Vadose Zone Journal*, *2*(4), 589-594.

Coll, C., Galve, J. M., Sanchez, J. M., & Caselles, V. (2009). Validation of Landsat-7/ETM+ thermal-band calibration and atmospheric correction with ground-based measurements. *IEEE Transactions on Geoscience and Remote Sensing*, *48*(1), 547-555. DOI: 10.1109/TGRS.2009.2024934

Colville, J. S., & Holmes, J. W. (1972). Water table fluctuations under forest and pasture in a karstic region of southern Australia. *Journal of Hydrology*, *17*(1-2), 61-80. https://doi.org/10.1016/0022-1694(72)90066-2

Cornic, G. (2000). Drought stress inhibits photosynthesis by decreasing stomatal aperture–not by affecting ATP synthesis. *Trends in plant science*, *5*(5), 187-188. https://doi.org/10.1016/S1360-1385(00)01625-3

Courault, D., Seguin, B., & Olioso, A. (2005). Review on estimation of evapotranspiration from remote sensing data: From empirical to numerical modeling approaches. *Irrigation and Drainage systems*, *19*(3-4), 223-249.

https://doi.org/10.1007/s10795-005-5186-0

Crabtree, S. J., & Kjerfve, B. (1978). Radiation balance over a salt marsh. *Boundary-Layer Meteorology*, *14*(1), 59-66. https://doi.org/10.1007/BF00123989

Cramer, V. A., Thorburn, P. J., & Fraser, G. W. (1999). Transpiration and groundwater uptake from farm forest plots of Casuarina glauca and *Eucalyptus camaldulensis* in saline areas of southeast Queensland, Australia. *Agricultural water management*, *39*(2-3), 187-204. https://doi.org/10.1016/S0378-3774(98)00078-X

Cristóbal, J., Jiménez-Muñoz, J. C., Sobrino, J. A., Ninyerola, M., & Pons, X. (2009). Improvements in land surface temperature retrieval from the Landsat series thermal band using water vapor and air temperature. *Journal of Geophysical Research: Atmospheres*, *114*(D8). https://doi.org/10.1029/2008JD010616

Daniel, J. F. (1976). Estimating groundwater evapotranspiration from streamflow records. *Water Resources Research*, *12*(3), 360-364. https://doi.org/10.1029/WR012i003p00360

Dash, P., Göttsche, F. M., Olesen, F. S., & Fischer, H. (2002). Land surface temperature and emissivity estimation from passive sensor data: Theory and practice-current trends. *International Journal of remote sensing*, *23*(13), 2563-2594. https://doi.org/10.1080/01431160110115041

Datt, B. (1999). A new reflectance index for remote sensing of chlorophyll content in higher plants: tests using *Eucalyptus* leaves. *Journal of Plant Physiology*, *154*(1), 30-36. https://doi.org/10.1016/S0176-1617(99)80314-9

Daughtry, C. S. T., Kustas, W. P., Moran, M. S., Pinter Jr, P. J., Jackson, R. D., Brown, P. W., ... & Gay, L. W. (1990). Spectral estimates of net radiation and soil heat flux. *Remote sensing of environment*, *32*(2-3), 111-124.

Davis, K. J. (2008). Integrating field measurements with flux tower and remote sensing data, (pp. 207-225). *In* Field Measurements for Forest Carbon Monitoring XVIII, 242 p. 20 illus., Springer, Dordrecht, Hardcover. ISBN: 978-1-4020-8505-5.

Dawson, T. E. (1993). Hydraulic lift and water use by plants: implications for water balance, performance and plant-plant interactions. *Oecologia*, *95*(4), 565-574. https://doi.org/10.1007/BF00317442

Dawson, T. E. (1996). Determining water use by trees and forests from isotopic, energy balance and transpiration analyses: the roles of tree size and hydraulic lift. *Tree physiology*, *16*(1-2), 263-272.

https://doi.org/10.1093/treephys/16.1-2.263

De Bruin, H. A. R., & Holtslag, A. A. M. (1982). A simple parameterization of the surface fluxes of sensible and latent heat during daytime compared with the Penman-Monteith concept. *Journal of Applied Meteorology*, *21*(11), 1610-1621. https://doi.org/10.1175/1520-0450(1982)021<1610:ASPOTS>2.0.CO;2

de Jesus, J. B., & Santana, I. D. M. (2017). Estimation of land surface temperature in Caatinga area using Landsat 8 data. Journal of Hyperspectral Remote Sensing, 7(3), 150-157. https://pdfs.semanticscholar.org/ae34/7613b8388eb7f5440ec1a72bda2dcb4f42d9.pdf.

de Sousa Lima, J. R., Antonino, A. C. D., de Souza, E. S., de Oliveira Lira, C. A. B., & da Silva, I. D. F. (2013). Seasonal and interannual variations of evapotranspiration, energy exchange, yield and water use efficiency of castor grown under rainfed conditions in northeastern Brazil. *Industrial Crops and Products*, *50*, 203-211. https://doi.org/10.1016/j.indcrop.2013.07.012

Dean, J. F. (2013). An ecohydrological and biogeochemical investigation into the impacts of changing land-use on groundwater and surface water resources in south-western Victoria, Australia. Ph.D. thesis. pp. 133. 20150713-09389. digitalTheses-20150713-09389

Dean, J. F., Webb, J. A., Jacobsen, G. E., Chisari, R., & Dresel, P. E. (2014a). Where to locate a tree plantation within a low rainfall catchment to minimise impacts on groundwater resources. *Hydrology and Earth System Sciences Discussions*, *11*(8), 10001-10041. doi:10.5194/hessd-11-10001- 2014.

Dean, J. F., Webb, J. A., Jacobsen, G. E., Chisari, R., & Dresel, P. E. (2014b). Biomass uptake and fire as controls on groundwater solute evolution on a southeast Australian granite: aboriginal land management hypothesis. *Biogeosciences*, *11*(15), 4099-4114. https://doi.org/10.5194/bg-11-4099-2014

Dean, J., Camporese, M., Grover, S., Webb, J., Dresel, E., & Daly, E. (2015, April). Hydrological modeling in small, semiarid catchments of south-eastern Australia: reforestation affects groundwater but not streamflow. In *EGU General Assembly Conference Abstracts* (Vol. 17, p. 8954).

Derkzen, M. L., van Teeffelen, A. J., & Verburg, P. H. (2015). Quantifying urban ecosystem services based on high-resolution data of urban green space: an assessment for Rotterdam, the Netherlands. *Journal of Applied Ecology*, *52*(4), 1020-1032. https://doi.org/10.1111/1365-2664.12469

Dewan, A. M., & Corner, R. J. (2012, July). The impact of landuse and land cover changes on land surface temperature in a rapidly urbanizing megacity. In *2012 IEEE International Geoscience and Remote Sensing Symposium* (pp. 6337-6339). IEEE. https://doi.org/10.3390/su9122324

Diak, G. R., Bland, W. L., Mecikalski, J. R., & Anderson, M. C. (2000). Satellite-based estimates of longwave radiation for agricultural applications. *Agricultural and Forest Meteorology*, *103*(4), 349-355. https://doi.org/10.1016/S0168-1923(00)00141-6

Diak, G. R., Mecikalski, J. R., Anderson, M. C., Norman, J. M., Kustas, W. P., Torn, R. D., & DeWolf, R. L. (2004). Estimating land surface energy budgets from space: Review and current efforts at the University of Wisconsin—Madison and USDA–ARS. *Bulletin of the American Meteorological Society*, *85*(1), 65-78. https://doi.org/10.1175/BAMS-85-1-65

Dickinson, R. E. (1983). Land surface processes and climate—Surface albedos and energy balance. In *Advances in geophysics* (Vol. 25, pp. 305-353). Elsevier. https://doi.org/10.1016/S0065-2687(08)60176-4

Dickinson, R. E., Pinty, B., & Verstraete, M. M. (1990). Relating surface albedos in GCM to remotely sensed data. *Agricultural and Forest Meteorology*, *52*(1-2), 109-131. https://doi.org/10.1016/0168-1923(90)90103-D

Donohoe, A., & Battisti, D. S. (2012). What determines meridional heat transport in climate models? *Journal of Climate*, *25*(11), 3832-3850. https://doi.org/10.1175/JCLI-D-11-00257.1

Doorenbos, J., & Pruitt, W. O. (1977). Crop water requirements. FAO irrigation and drainage paper 24. *Land and Water Development Division, FAO, Rome*, *144*.

Dresel, P. E., Dean, J. F., Perveen, F., Webb, J. A., Hekmeijer, P., Adelana, S. M., & Daly, E. (2018). Effect of *Eucalyptus* plantations, geology, and precipitation variability on water resources in upland intermittent catchments. *Journal of hydrology*, *564*, 723-739. https://doi.org/10.1016/j.jhydrol.2018.07.019

Dresel, P. E., Hekmeijer, P., Dean, J. F., Harvey, W., Webb, J. A., & Cook, P. (2012). Use of laser-scan technology to analyse topography and flow in a weir pool. *Hydrology and Earth System Sciences*, *16*(8), 2703-2708. https://doi.org/10.5194/hess-16-2703-2012

Dugas, W.A., Fritschen, L.J., Gay, L.W., Held, A.A., Matthias, A.D., Reicosky, D.C., Steduto, P. and Steiner, J.L., (1991). Bowen ratio, eddy correlation, and portable chamber measurements of sensible and latent heat flux over irrigated spring wheat. *Agricultural and forest meteorology*, *56*(1-2), 1-20. https://doi.org/10.1016/0168-1923(91)90101-U

Dye, P. J. (1996). Response of *Eucalyptus grandis* trees to soil water deficits. *Tree Physiology*, *16*(1-2), 233-238.

Eastham, J., Rose, C. W., Cameron, D. M., Rance, S. J., Talsma, T., & Charles-Edwards, D. A. (1990). Tree/pasture interactions at a range of tree densities in an agroforestry experiment. II. Water uptake in relation to rooting patterns. *Australian Journal of Agricultural Research*, *41*(4), 697-707. https://doi.org/10.1071/AR9900697

El-Lakany, M. H., & Mohamed, S. Y. (1993). Root characteristics of four tree species as affected by irrigation systems. *Alexandria Journal of Agricultural Research*, *38*(1), 183-210. https://www.cabdirect.org/cabdirect/abstract/19940603797

Ellingson, R. G. (1995). Surface longwave fluxes from satellite observations: A critical review. *Remote Sensing of Environment*, *51*(1), 89-97. https://doi.org/10.1016/0034-4257(94)00067-W

Ellingson, R. G., Yanuk, D. J., Lee, H. T., & Gruber, A. (1989). A technique for estimating outgoing longwave radiation from HIRS radiance observations. *Journal of Atmospheric and Oceanic Technology*, *6*(4), 706-711. https://doi.org/10.1175/1520-0426(1989)006<0706:ATFEOL>2.0.CO;2

Endterton, D., & Marshall, J. (2009). Explorations of atmosphere–ocean–ice climates on an aquaplanet and their meridional energy transports. *Journal of the Atmospheric Sciences*, *66*(6), 1593-1611. https://doi.org/10.1175/2008JAS2680.1

Enz, J. W., Brun, L. J., & Larsen, J. K. (1988). Evaporation and energy balance for bare and stubble covered soil. *Agricultural and forest meteorology*, *43*(1), 59-70. Show more. https://doi.org/10.1016/0168-1923(88)90006-8

ESDU (Engineering Sciences Data Unit). (1972). Characteristics of Wind Speed in the Lower Layers of the Atmosphere Near the Ground: Strong Winds (Neutral Atmosphere) ESDU, Regent Street, London, UK.

Espeleta, J. F., West, J. B., & Donovan, L. A. (2004). Species-specific patterns of hydraulic lift in co-occurring adult trees and grasses in a sandhill community. *Oecologia*, *138*(3), 341-349. https://doi.org/10.1007/s00442-003-1460-8

Eugster, W., & Cattin, R. (2007). Evapotranspiration and energy flux differences between a forest and a grassland site in the subalpine zone in the Bernese Oberland. Erde 138: 333–354. http://homepage.agrl.ethz.ch/eugsterw/publications/pdf/Eugster.2007.DieErde_138.pdf

Evans, J. P., Meng, X., & McCabe, M. (2017). Land surface albedo and vegetation feedbacks enhanced the millennium drought in south-east Australia. http://www.hydrol-earth-syst-sci.net/21/409/2017/

Falkiner, R. A., Nambiar, E. K. S., Polglase, P. J., Theiveyanathan, S., & Stewart, L. G. (2006). Root distribution of *Eucalyptus grandis* and *Corymbia maculata* in degraded saline soils of south-eastern Australia. *Agroforestry systems*, *67*(3), 279-291. https://doi.org/10.1007/s10457-005-5258-z

Farah, H. O., & Bastiaanssen, W. G. (2001). Impact of spatial variations of land surface parameters on regional evaporation: a case study with remote sensing data. *Hydrological processes*, *15*(9), 1585-1607. https://doi.org/10.1002/hyp.159

Fasullo, J. T., & Trenberth, K. E. (2008). The annual cycle of the energy budget. Part I: Global mean and land–ocean exchanges. *Journal of Climate*, *21*(10), 2297-2312. https://doi.org/10.1175/2007JCLI1935.1

Fisch, G., Tota, J., Machado, L. A. T., Dias, M. S., Lyra, R. D. F., Nobre, C. A., ... & Gash, J. H. C. (2004). The convective boundary layer over pasture and forest in Amazonia. *Theoretical and Applied Climatology*, *78*(1-3), 47-59. https://doi.org/10.1007/s00704-004-0043-x

Fisher, D. K. (2012). Simple weighing lysimeters for measuring evapotranspiration and developing crop coefficients. *International Journal of Agricultural and Biological Engineering*, *5*(3), 35-43. http://www.ijabe.org/index.php/ijabe/article/view/627

Formetta, G., Bancheri, M., David, O., & Rigon, R. (2016). Performance of site-specific parameterizations of longwave radiation. *Hydrology and Earth System Sciences*, *20*(11), 4641-4654. https://doi.org/10.5194/hess-20-4641-2016

Forrester, D. I., Collopy, J. J., & Morris, J. D. (2010). Transpiration along an age series of *Eucalyptus globulus* plantations in southeastern Australia. *Forest Ecology and Management*, *259*(9), 1754-1760. https://doi.org/10.1016/j.foreco.2009.04.023

Frank, D. A., & Inouye, R. S. (1994). Temporal variation in actual evapotranspiration of terrestrial ecosystems: patterns and ecological implications. Journal of Biogeography, 401-411. DOI: 10.2307/2845758 https://www.jstor.org/stable/2845758

French, A. N., & Inamdar, A. (2010). Land cover characterization for hydrological modelling using thermal infrared emissivities. *International Journal of Remote Sensing*, *31*(14), 3867-3883. https://doi.org/10.1080/01431161.2010.483491

French, A. N., Jacob, F., Anderson, M. C., Kustas, W. P., Timmermans, W., Gieske, A., ... & Prueger, J. (2005). Surface energy fluxes with the Advanced Spaceborne Thermal Emission and Reflection radiometer (ASTER) at the Iowa 2002 SMACEX site (USA). *Remote sensing of environment*, *99*(1-2), 55-65. https://doi.org/10.1016/j.rse.2005.05.015

Friend, A. D., Stevens, A. K., Knox, R. G., & Cannell, M. G. R. (1997). A process-based, terrestrial biosphere model of ecosystem dynamics (Hybrid v3. 0). *Ecological Modelling*, *95*(2-3), 249-287. https://doi.org/10.1016/S0304-3800(96)00034-8

Fritschen, L. (1982). Energy at the Surface of the Earth: An Introduction to the Energetics of Ecosystems. *Eos, Transactions American Geophysical Union*, *63*(21), 514-514. https://doi.org/10.1029/EO063i021p00514-01

Fritschen, L. J. (1965). Accuracy of evapotranspiration determinations by the Bowen ratio method. *Hydrological Sciences Journal*, *10*(2), 38-48. https://doi.org/10.1080/02626666509493388

Fritschen, L.J. and Gay, L.W. (1979). *In* D.E. Reichler (Editor), Environmental Instrumentation. Springer-Verlag, New York, 216 pp.

Fuchs, M., & Hadas, A. (1972). The heat flux density in a non-homogeneous bare loessial soil. *Boundary-layer meteorology*, *3*(2), 191-200. https://doi.org/10.1007/BF02033918

Fuchs, M., & Tanner, C. B. (1967). Evaporation from a drying soil. *Journal of Applied Meteorology*, *6*(5), 852-857. https://doi.org/10.1175/1520-0450(1967)006<0852:EFADS>2.0.CO;2

Fuchs, M., & Tanner, C. B. (1968). Calibration and Field Test of Soil Heat Flux Plates 1. *Soil Science Society of America Journal*, *32*(3), 326-328. doi:10.2136/sssaj1968.03615995003200030021x

Gallant, J. (2012). *Doing physics with scientific notebook: a problem-solving approach*. John Wiley & Sons.

Gardner, W. R. (1958). Some steady-state solutions of the unsaturated moisture flow equation with application to evaporation from a water table. *Soil science*, *85*(4), 228-232.

Gardner, W. R., & Fireman, M. (1958). Laboratory studies of evaporation from soil columns in the presence of a water table. *Soil Science*, *85*(5), 244-249.

Garratt, J. R. (1978). Flux profile relations above tall vegetation. *Quarterly Journal of the Royal Meteorological Society*, *104*(439), 199-211. https://doi.org/10.1002/qj.49710443915

Garratt, J. R. (1992). The Atmospheric Boundary Layer Cambridge University Press Cambridge 316.

Gausman, H. W., Gerbermann, A. H., Wiegand, C. L., Leamer, R. W., Rodriguez, R. R., & Noriega, J. R. (1975). Reflectance Differences Between Crop Residues and Bare Soils 1. *Soil Science Society of America Journal*, *39*(4), 752-755. doi:10.2136/sssaj1975.03615995003900040043x

Gentine, P., Entekhabi, D., & Polcher, J. (2011). The diurnal behavior of evaporative fraction in the soil–vegetation–atmospheric boundary layer continuum. *Journal of Hydrometeorology*, *12*(6), 1530-1546. https://doi.org/10.1175/2011JHM1261.1

Gowda, P. H., Chavez, J. L., Colaizzi, P. D., Evett, S. R., Howell, T. A., & Tolk, J. A. (2007). Remote sensing-based energy balance algorithms for mapping ET: Current status and future challenges. *Transactions of the ASABE*, *50*(5), 1639-1644. DOI. 10.13031/2013.23964

Gray, C. G., Gubbins, K. E., & Joslin, C. G. (2011). *Theory of Molecular Fluids: Volume 2: Applications* (Vol. 10). Oxford University Press.

Gray, L. J., Beer, J., Geller, M., Haigh, J. D., Lockwood, M., Matthes, K., ... & Luterbacher, J. (2010). Solar influences on climate. *Reviews of Geophysics*, *48*(4). https://doi.org/10.1029/2009RG000282

Groeneveld, D. P., Baugh, W. M., Sanderson, J. S., & Cooper, D. J. (2007). Annual groundwater evapotranspiration mapped from single satellite scenes. *Journal of Hydrology*, *344*(1-2), 146-156. https://doi.org/10.1016/0022-1694(85)90105-2

Guan, K. K. (2011). Surface and ambient air temperatures associated with different ground material: a case study at the University of California, Berkeley. *Environmental Science*, *196*, 1-14. https://nature.berkeley.edu/classes/es196/projects/2011final/GuanK_2011.pdf

Gupta, S. K., Ritchey, N. A., Wilber, A. C., Whitlock, C. H., Gibson, G. G., & Stackhouse Jr, P. W. (1999). A climatology of surface radiation budget derived from satellite data. *Journal of Climate*, *12*(8), 2691-2710. https://doi.org/10.1175/1520-0442(1999)012<2691:ACOSRB>2.0.CO;2

Gurney, R. J., & Camillo, P. J. (1984). Modelling daily evapotranspiration using remotely sensed data. *Journal of hydrology*, *69*(1-4), 305-324. https://doi.org/10.1016/0022-1694(84)90170-7

Gwenzi, W., Veneklaas, E. J., Bleby, T. M., Yunusa, I. A., & Hinz, C. (2012). Transpiration and plant water relations of evergreen woody vegetation on a recently constructed artificial ecosystem under seasonally dry conditions in Western Australia. *Hydrological Processes*, *26*(21), 3281-3292. https://doi.org/10.1002/hyp.8330

Hall, F. G., & Sellers, P. J. (1995). First international satellite land surface climatology project (ISLSCP) field experiment (FIFE) in 1995. *Journal of Geophysical Research: Atmospheres*, *100*(D12), 25383-25395. https://doi.org/10.1029/95JD03300

Hansen, F. V. (1993). Surface roughness lengths (No. ARL-TR-61). *Army Research Lab White Sands Missile Range NM: Adelphi, MD, USA*, 88002-85501.

Hansen, J., Nazarenko, L., Ruedy, R., Sato, M., Willis, J., Del Genio, A., Koch D, Lacis A, Lo K, Menon S, & Novakov, T. (2005). Earth's energy imbalance: Confirmation and implications. *science*, *308*(5727), 1431-1435.

Harper, L. A., White, A. W., Bruce, R. R., Thomas, A. W., & Leonard, R. A. (1976). Soil and Microclimate Effects on Trifluralin Volatilization 1. *Journal of Environmental Quality*, *5*(3), 236-242. doi:10.2134/jeq1976.00472425000500030004x

Harris Geospatial solutions. 2017. Radiance vs. Reflectance. https://www.harrisgeospatial.com/Support/Self-Help-Tools/Help-Articles/Help-Articles-Detail/ArtMID/10220/ArticleID/19247/3377

Harte, J., Torn, M. S., Chang, F. R., Feifarek, B., Kinzig, A. P., Shaw, R., & Shen, K. (1995). Global warming and soil microclimate: Results from a meadow-warming experiment. *Ecological Applications*, *5*(1), 132-150. https://doi.org/10.2307/1942058

Heitman, J. L., Xiao, X., Horton, R., & Sauer, T. J. (2008). Sensible heat measurements indicating depth and magnitude of subsurface soil water evaporation. *Water Resources Research*, *44*(4). https://doi.org/10.1029/2008WR006961

Herschel, W. (1801). XIII. Observations tending to investigate the nature of the sun, in order to find the causes or symptoms of its variable emission of light and heat; with remarks on the use that may possibly be drawn from solar observations. *Philosophical Transactions of the Royal Society of London*, (91), pp.265-318. https://doi.org/10.1098/rstl.1801.0015

Heuperman, A. (1999). Hydraulic gradient reversal by trees in shallow water table areas and repercussions for the sustainability of tree-growing systems. *Agricultural water management*, *39*(2-3), 153-167. https://doi.org/10.1016/S0378-3774(98)00076-6

Heusinkveld, B. G., Jacobs, A. F. G., Holtslag, A. A. M., & Berkowicz, S. M. (2004). Surface energy balance closure in an arid region: role of soil heat flux. *Agricultural and Forest Meteorology*, *122*(1-2), 21-37. https://doi.org/10.1016/j.agrformet.2003.09.005

Hillel, D. (1998). Environmental soil physics. Academic Press, San Diego. *Environmental soil physics. Academic Press, San Diego.*

Hinzman, L. D., Bauer, M. E., & Daughtry, C. S. T. (1986). Effects of nitrogen fertilization on growth and reflectance characteristics of winter wheat. *Remote sensing of environment*, *19*(1), 47-61. https://doi.org/10.1016/0034-4257(86)90040-4

Högström, U. L. F. (1988). Non-dimensional wind and temperature profiles in the atmospheric surface layer: A re-evaluation. In *Topics in Micrometeorology. A Festschrift for Arch Dyer* (pp. 55-78). Springer, Dordrecht. https://doi.org/10.1007/978-94-009-2935-7_6

Holland, S., Heitman, J. L., Howard, A., Sauer, T. J., Giese, W., Ben-Gal, A., ... & Havlin, J. (2013). Micro-Bowen ratio system for measuring evapotranspiration in a vineyard interrow. *Agricultural and forest meteorology*, *177*, 93-100. https://doi.org/10.1016/j.agrformet.2013.04.009

Horton, R. E. (1919). The measurement of rainfall and snow. Monthly Weather Review, 47(5), 294-296. https://doi.org/10.1175/1520-0493(1919)47<294:TMORAS>2.0.CO;2

Horton, J. L., & Hart, S. C. (1998). Hydraulic lift: a potentially important ecosystem process. *Trends in Ecology & Evolution*, *13*(6), 232-235. https://doi.org/10.1016/S0169-5347(98)01328-7

Howard, J. A. (1977). Aerial albedos of natural vegetation in South-eastern Australia. FAO, UN.

Huang, S. (2006). Land warming as part of global warming. *Eos, Transactions American Geophysical Union*, *87*(44), 477-480. https://doi.org/10.1029/2006EO440003

Huete, A. R. (1987). Soil and sun angle interactions on partial canopy spectra. *International Journal of Remote Sensing*, *8*(9), 1307-1317. https://doi.org/10.1080/01431168708954776

Huete, A. R. (1988). A soil-adjusted vegetation index (SAVI). *Remote sensing of environment*, *25*(3), 295-309. DOI: 10.1016/0034-4257(88)90106-X. (For more information on this paper, please contact the IDMP HelpDesk).

Huete, A. R., Jackson, R. D., & Post, D. F. (1985). Spectral response of a plant canopy with different soil backgrounds. *Remote sensing of environment*, *17*(1), 37-53. https://doi.org/10.1016/0034-4257(85)90111-7

Huizhi, L., & Jianwu, F. (2012). Seasonal and interannual variations of evapotranspiration and energy exchange over different land surfaces in a semiarid area of China. *Journal of Applied Meteorology and Climatology*, *51*(10), 1875-1888. DOI: 10.1175/JAMC-D-11-0229.1. https://journals.ametsoc.org/doi/pdf/10.1175/JAMC-D-11-0229.1

Humes, K. S., Kustas, W. P., Moran, M. S., Nichols, W. D., & Weltz, M. A. (1994). Variability of emissivity and surface temperature over a sparsely vegetated surface. *Water Resources Research*, *30*(5), 1299-1310. https://doi.org/10.1029/93WR03065

Huryna, H., & Pokorný, J. (2016). The role of water and vegetation in the distribution of solar energy and local climate: a review. *Folia geobotanica*, *51*(3), 191-208. https://doi.org/10.1007/s12224-016-9261-0

Hutley, L. B., O'grady, A. P., & Eamus, D. (2000). Evapotranspiration from Eucalypt open-forest savanna of Northern Australia. *Functional Ecology*, *14*(2), 183-194. https://doi.org/10.1046/j.1365-2435.2000.00416.x

Idso, S. B., Schmugge, T. J., Jackson, R. D., & Reginato, R. J. (1975). The utility of surface temperature measurements for the remote sensing of surface soil water status. *Journal of Geophysical Research*, *80*(21), 3044-3049. https://doi.org/10.1029/JC080i021p03044

Irvine, J., Law, B. E., & Kurpius, M. R. (2005). Coupling of canopy gas exchange with root and rhizosphere respiration in a semi-arid forest. Biogeochemistry, 73(1), 271-282. https://doi.org/10.1007/s10533-004-2564-x

Jaber, H.S., Mansor, S., Pradhan, B. and Ahmad, N., 2016. Evaluation of SEBAL model for Evapotranspiration mapping in Iraq using remote sensing and GIS. *Int. J. Appl. Eng. Res*, *11*, pp.3950-3955. http://www.ripublication.com

Jacob, F., Olioso, A., Gu, X. F., Su, Z., & Seguin, B. (2002). Mapping surface fluxes using airborne visible, near infrared, thermal infrared remote sensing data and a spatialized surface energy balance model. *Agronomie*, *22*(6), 669-680. DOI: 10.1051/agro:2002053

Jacob, F., Weiss, M., Olioso, A., & French, A. (2002). Assessing the narrowband to broadband conversion to estimate visible, near infrared and shortwave apparent albedo from airborne PolDER data. *Agronomie*, *22*(6), 537-546. DOI: 10.1051/agro:2002049

Jimenez, C., Prigent, C., Mueller, B., Seneviratne, S. I., McCabe, M. F., Wood, E. F., ... & Fisher, J. B. (2011). Global intercomparison of 12 land surface heat flux estimates. *Journal of Geophysical Research: Atmospheres*, *116*(D2). https://doi.org/10.1029/2010JD014545

Jiménez-Muñoz, J. C., & Sobrino, J. A. (2003). A generalized single-channel method for retrieving land surface temperature from remote sensing data. *Journal of Geophysical Research: Atmospheres*, *108*(D22). https://doi.org/10.1029/2003JD003480

Jiménez-Muñoz, J. C., & Sobrino, J. A. (2009). A single-channel algorithm for land-surface temperature retrieval from ASTER data. *IEEE Geoscience and Remote Sensing Letters*, *7*(1), 176-179. DOI: 10.1109/LGRS.2009.2029534

Jiménez-Muñoz, J. C., Cristóbal, J., Sobrino, J. A., Sòria, G., Ninyerola, M., & Pons, X. (2008). Revision of the single-channel algorithm for land surface temperature retrieval from Landsat thermal-infrared data. *IEEE Transactions on geoscience and remote sensing*, *47*(1), 339-349. DOI: 10.1109/TGRS.2008.2007125

Jiménez-Muñoz, J. C., Sobrino, J. A., Skoković, D., Mattar, C., & Cristóbal, J. (2014). Land surface temperature retrieval methods from Landsat-8 thermal infrared sensor data. *IEEE Geoscience and remote sensing letters*, *11*(10), 1840-1843. DOI: 10.1109/LGRS.2014.2312032

Jipp, P. H., Nepstad, D. C., Cassel, D. K., & De Carvalho, C. R. (1998). Deep soil moisture storage and transpiration in forests and pastures of seasonally-dry Amazonia. In *Potential impacts of climate change on tropical forest ecosystems* (pp. 255-272). Springer, Dordrecht. https://doi.org/10.1007/978-94-017-2730-3_11.

Jobbágy, E. G., & Jackson, R. B. (2004). Groundwater use and salinization with grassland afforestation. *Global Change Biology*, *10*(8), 1299-1312. doi: 10.1111/j.1365-2486.2004.00806.x

Johnson, L. F. (2003). Temporal stability of an NDVI-LAI relationship in a Napa Valley vineyard. *Australian Journal of Grape and Wine Research*, *9*(2), 96-101. https://doi.org/10.1111/j.1755-0238.2003.tb00258.x

Kalma, J. D., & Badham, R. (1972). The radiation balance of a tropical pasture, I. The reflection of short-wave radiation. *Agricultural Meteorology*, *10*, 251-259. https://doi.org/10.1016/0002-1571(72)90030-1

Kalma, J. D., McVicar, T. R., & McCabe, M. F. (2008). Estimating land surface evaporation: A review of methods using remotely sensed surface temperature data. *Surveys in Geophysics*, *29*(4-5), 421-469. https://doi.org/10.1007/s10712-008-9037-z

Kamila, A., Paul, A. K., & Bandyopadhyay, J. (2018). Estimation and Validation of Land Surface Temperature (LST) from Landsat 8 OLI and TIRS sensor’s Data. International Journal of Research: 5(4), pp.162-169.

Kanda, M., Kanega, M., Kawai, T., Moriwaki, R., & Sugawara, H. (2007). Roughness lengths for momentum and heat derived from outdoor urban scale models. *Journal of Applied Meteorology and Climatology*, *46*(7), 1067-1079. https://doi.org/10.1175/JAM2500.1

Karimi, P., & Bastiaanssen, W. G. (2015). Spatial evapotranspiration, rainfall and landuse data in water accounting–Part 1: Review of the accuracy of the remote sensing data. *Hydrology and Earth System Sciences*, *19*(1), 507-532. DOI:10.5194/hess-19-507-2015

Katul, G. G., Oren R., Manzoni, S., Higgins, C. W., & Parlange, M. B. (2012). Evapotranspiration: a process driving mass transport and energy exchange in the soil-plant-atmosphere-climate system. *Reviews of Geophysics*, *50*(3). doi:10.1029/2011RG000366.

Kelliher, F. M., Leuning, R., & Schulze, E. D. (1993). Evaporation and canopy characteristics of coniferous forests and grasslands. *Oecologia*, *95*(2), 153-163. https://doi.org/10.1007/BF00323485

Kiehl, J. T., & Trenberth, K. E. (1997). Earth's annual global mean energy budget. *Bulletin of the American Meteorological Society*, *78*(2), 197-208. https://doi.org/10.1175/1520-0477(1997)078<0197:EAGMEB>2.0.CO;2

Kite, G. W., & Droogers, P. (2000). Comparing evapotranspiration estimates from satellites, hydrological models and field data. *Journal of Hydrology*, *229*(1-2), 3-18. https://doi.org/10.1016/S0022-1694(99)00195-X

Knight, J. H. "Root distributions and water uptake patterns in eucalypts and other species: a literature review. *In:* Landsberg, J.J. (ed.), *The ways trees* *use water, Rural Industries Research and Development Corporation, ISBN* 64278117 (1998). Identifier: rocite:5d70520b-f402-405a-9cfd-ce5a05a4ae8a

Knohl, A., Schulze, E. D., Kolle, O., & Buchmann, N. (2003). Large carbon uptake by an unmanaged 250-year-old deciduous forest in Central Germany. *Agricultural and Forest Meteorology*, *118*(3-4), 151-167. doi:10.1016/S0168-1923(03)00115-1.

Kollenkark, J. C., Vanderbilt, V. C., Daughtry, C. S. T., & Bauer, M. E. (1982). Influence of solar illumination angle on soybean canopy reflectance. *Applied Optics*, *21*(7), 1179-1184.

Koloskov, G., Mukhamejanov, K., & Tanton, T. W. (2007). Monin–Obukhov length as a cornerstone of the SEBAL calculations of evapotranspiration. *Journal of hydrology*, *335*(1-2), 170-179. https://doi.org/10.1016/j.jhydrol.2006.11.010

Kopp, G., & Lean, J. L. (2011). A new, lower value of total solar irradiance: Evidence and climate significance. Geophysical Research Letters, 38(1). https://doi.org/10.1029/2010GL045777

Köppen, W. (1873). Über mehrjährige Perioden der Witterung, insbesondere über die 11-jährige Periode der Temperatur. *Zeitschrift der Österreichischen Gesellschaft für Meteorologie*, *8*, 241-248.

Kotak, Y., Gul, M. S., Muneer, T., & Ivanova, S. M. (2015). Investigating the impact of ground albedo on the performance of pv systems. *In Proceedings of CIBSE Technical Symposium Chartered Institution of Building Services Engineers (CIBSE): London, UK*, pp. 16-17.

Kustas, W. P., & Daughtry, C. S. (1990). Estimation of the soil heat flux/net radiation ratio from spectral data. *Agricultural and Forest Meteorology*, *49*(3), 205-223. https://doi.org/10.1016/0168-1923(90)90033-3

Kustas, W. P., & Norman, J. M. (1997). A two-source approach for estimating turbulent fluxes using multiple angle thermal infrared observations. *Water Resources Research*, *33*(6), 1495-1508. https://doi.org/10.1029/97WR00704

Kustas, W. P., Choudhury, B. J., Moran, M. S., Reginato, R. J., Jackson, R. D., Gay, L. W., & Weaver, H. L. (1989). Determination of sensible heat flux over sparse canopy using thermal infrared data. *Agricultural and Forest Meteorology*, *44*(3-4), 197-216. https://doi.org/10.1016/0168-1923(89)90017-8

Kustas, W. P., Daughtry, C. S., & Van Oevelen, P. J. (1993). Analytical treatment of the relationships between soil heat flux/net radiation ratio and vegetation indices. *Remote sensing of environment*, *46*(3), 319-330. https://doi.org/10.1016/0034-4257(93)90052-Y

Kustas, W. P., Norman, J. M., Anderson, M. C., & French, A. N. (2003). Estimating subpixel surface temperatures and energy fluxes from the vegetation index–radiometric temperature relationship. *Remote sensing of environment*, *85*(4), 429-440. https://doi.org/10.1016/S0034-4257(03)00036-1

Kustas, W. P., Pinker, R. T., Schmugge, T. J., & Humes, K. S. (1994). Daytime net radiation estimated for a semiarid rangeland basin from remotely sensed data. *Agricultural and Forest Meteorology*, *71*(3-4), 337-357. https://doi.org/10.1016/0168-1923(94)90019-1

Labed, J., & Stoll, M. P. (1991). Spatial variability of land surface emissivity in the thermal infrared band: spectral signature and effective surface temperature. *Remote Sensing of Environment*, *38*(1), 1-17. https://doi.org/10.1016/0034-4257(91)90068-H

Labitzke, K., & Loon, H. (1992). Association between the 11-year solar cycle and the atmosphere. Part V: Summer. *Journal of Climate*, *5*(3), 240-251. https://doi.org/10.1175/1520-0442(1992)005<0240:ABTYSC>2.0.CO;2

Landsberg, P.T. (1978). *Thermodynamics and Statistical Mechanics*, Oxford University Press, Oxford, ISBN 0-19-851142-6, page 11.

Langford, K. J., & O'SHAUGHNESSY, P. J. (1977). Some effects of forest change on water values. *Australian forestry*, *40*(3), 192-218. https://doi.org/10.1080/00049158.1977.10675672

Latham, J. (2002). Amelioration of global warming by controlled enhancement of the albedo and longevity of low-level maritime clouds. *Atmospheric Science Letters*, *3*(2-4), 52-58. https://doi.org/10.1006/asle.2002.0048

Law, B. E., Falge, E., Gu, L. V., Baldocchi, D. D., Bakwin, P., Berbigier, P., ... & Goldstein, A. (2002). Environmental controls over carbon dioxide and water vapor exchange of terrestrial vegetation. *Agricultural and Forest Meteorology*, *113*(1-4), 97-120. https://doi.org/10.1016/S0168-1923(02)00104-1

Lee, H. T., & Ellingson, R. G. (2002). Development of a nonlinear statistical method for estimating the downward longwave radiation at the surface from satellite observations. *Journal of Atmospheric and Oceanic*

Technology, *19*(10), 1500-1515. https://doi.org/10.1175/1520-0426(2002)019<1500:DOANSM>2.0.CO;2

Levitus, S., Antonov, J., & Boyer, T. (2005). Warming of the world ocean, 1955–2003. *Geophysical Research Letters*, *32*(2). https://doi.org/10.1029/2004GL021592

Lhomme, J. P., Chehbouni, A., & Monteny, B. (2000). Sensible heat flux-radiometric surface temperature relationship over sparse vegetation: Parameterizing B-1. *Boundary-Layer Meteorology*, *97*(3), 431-457. https://doi.org/10.1023/A:1002786402695

Li, F., Jackson, T. J., Kustas, W. P., Schmugge, T. J., French, A. N., Cosh, M. H., & Bindlish, R. (2004). Deriving land surface temperature from Landsat 5 and 7 during SMEX02/SMACEX. *Remote sensing of environment*, *92*(4), 521-534. https://doi.org/10.1016/j.rse.2004.02.018

Li, S. G., Lai, C. T., Lee, G., Shimoda, S., Yokoyama, T., Higuchi, A., & Oikawa, T. (2005). Evapotranspiration from a wet temperate grassland and its sensitivity to microenvironmental variables. *Hydrological Processes: An International Journal*, *19*(2), 517-532. DOI: 10.1002/hyp.5673

Liang, S., Fang, H., Chen, M., Shuey, C. J., Walthall, C., Daughtry, C., ... & Strahler, A. (2002). Validating MODIS land surface reflectance and albedo products: Methods and preliminary results. *Remote sensing of environment*, *83*(1-2), 149-162. https://doi.org/10.1016/S0034-4257(02)00092-5

Liang, S., Li, X., & Wang, J. (Eds.). (2012). *Advanced remote sensing: terrestrial information extraction and applications*. Academic Press.

Liang, S., Strahler, A. H., & Walthall, C. (1999). Retrieval of land surface albedo from satellite observations: A simulation study. *Journal of Applied meteorology*, *38*(6), 712-725. DOI: 10.1109/IGARSS.1998.691379

Liang, S., Strahler, A., & Walthall, C. (1998). Retrieval of land surface albedo from satellite observations: a simulation study. In *IGARSS'98. Sensing and Managing the Environment. 1998 IEEE International Geoscience and Remote Sensing. Symposium Proceedings. (Cat. No. 98CH36174)* (Vol. 3, pp. 1286-1288). IEEE. DOI: 10.1109/IGARSS.1998.691379

Liang, S., Stroeve, J., & Box, J. E. (2005). Mapping daily snow/ice shortwave broadband albedo from Moderate Resolution Imaging Spectroradiometer (MODIS): The improved direct retrieval algorithm and validation with Greenland in situ measurement. *Journal of Geophysical Research: Atmospheres*, *110*(D10). https://doi.org/10.1029/2004JD005493

LiCor. (2015). EddyPro Eddy Covarience Software Instruction Manual. eP with support of SMARTFluex. file:///G:/LTU_External_F/Data_D%20drive/1A_Postgrad%20scholarship_old/1A_PhD/GIS_RS_Data_softwares/Data/Climate%20Data/Gatum/Flux%20tower%20data_Original_Gatum_Edo_Bertrand/EddyPro5_User_Guide.pdf.

Liu, F., Tao, F., Li, S., Zhang, S., Xiao, D., & Wang, M. (2014). Energy partitioning and environmental influence factors in different vegetation types in the GEWEX Asian Monsoon Experiment. *Frontiers of earth science*, *8*(4), 582-594. https://doi.org/10.1007/s11707-014-0429-8

Liu, S., Lu, L., Mao, D., & Jia, L. (2007). Evaluating parameterizations of aerodynamic resistance to heat transfer using field measurements. *Hydrology and Earth System Sciences Discussions*, *11*(2), 769-783. https://hal.archives-ouvertes.fr/hal-00305051

Liu, W., Hong, Y., Khan, S. I., Huang, M., Vieux, B., Caliskan, S., & Grout, T. (2010). Actual evapotranspiration estimation for different landuse and land cover in urban regions using Landsat 5 data. *Journal of Applied Remote Sensing*, *4*(1), 041873. https://doi.org/10.1117/1.3525566

Lovelock, J. E. (1983). Gaia as seen through the atmosphere. In *Biomineralization and biological metal accumulation* (pp. 15-25). Springer, Dordrecht.

Lubczynski, M. W. (2000). Groundwater evapotranspiration, underestimated component of the groundwater balance in a semi-arid environment, Serowe case, Botswana. *Groundwater: past achievements and future challenges. Balkema, Rotterdam*, 199-204.

Lubczynski, M. W. (2011). Groundwater evapotranspiration–underestimated role of tree transpiration and bare soil evaporation in groundwater balances of dry lands. In *Climate change and its effects on water resources* (pp. 183-190). Springer, Dordrecht. https://doi.org/10.1007/978-94-007-1143-3_21

Ludwig, F., Dawson, T. E., de Kroon, H., Berendse, F., & Prins, H. H. (2003). Hydraulic lift in *Acacia tortilis* trees on an East African savanna. *Oecologia*, *134*(3), 293-300. https://doi.org/10.1007/s00442-002-1119-x

Luo, Y. F., Peng, S. Z., Khan, S., Cui, Y. L., Wang, Y., & Feng, Y. H. (2009, July). A comparative study of groundwater evapotranspiration functions. In *18th IMACS World Congress MODSIM09 Proceedings* (pp. 3095-3101).

Ma, S., Baldocchi, D. D., Xu, L., & Hehn, T. (2007). Inter-annual variability in carbon dioxide exchange of an oak/grass savanna and open grassland in California. *Agricultural and Forest Meteorology*, *147*(3-4), 157-171. https://doi.org/10.1016/j.agrformet.2007.07.008

MacArthur, C. D., & Haines, P. A. (1982). The Roughness Lengths Associated with Regions of Heterogeneous Vegetation and Elevation. Contract DAAD07-80-D-0206, University of Dayton Research Institute, Dayton, OH 45469. https://apps.dtic.mil/dtic/tr/fulltext/u2/a117409.pdf

Macfarlane, C., Grigg, A., McGregor, R., Ogden, G., & Silberstein, R. (2018). Overstorey evapotranspiration in a seasonally dry Mediterranean eucalypt forest: Response to groundwater and mining. Ecohydrology, 11(5), e1971. https://doi.org/10.1002/eco.1971

Madhavan, D. B., Kitching, M., Mendham, D. S., Weston, C. J., & Baker, T. G. (2016). Mid-infrared spectroscopy for rapid assessment of soil properties after landuse change from pastures to *Eucalyptus globulus* plantations. *Journal of environmental management*, *175*, 67-75. https://doi.org/10.1016/j.jenvman.2016.03.032

Mahecha, M. D., Reichstein, M., Carvalhais, N., Lasslop, G., Lange, H., Seneviratne, S. I., ... & Janssens, I. A. (2010). Global convergence in the temperature sensitivity of respiration at ecosystem level. *Science*, *329*(5993), 838-840. DOI: 10.1126/science.1189587

Mahrt, L., & Khelif, D. (2010). Heat fluxes over weak SST heterogeneity. *Journal of Geophysical Research: Atmospheres*, *115*(D11). https://doi.org/10.1029/2009JD013161

Mahrt, L., & Vickers, D. (2002). Contrasting vertical structures of nocturnal boundary layers. *Boundary-Layer Meteorology*, *105*(2), 351-363. https://doi.org/10.1023/A:1019964720989

Mahrt, L., Vickers, D., Andreas, E. L., & Khelif, D. (2012). Sensible heat flux in near-neutral conditions over the sea. *Journal of Physical Oceanography*, *42*(7), 1134-1142. https://doi.org/10.1175/JPO-D-11-0186.1

Malek, E. (1993). Rapid changes of the surface soil heat flux and its effects on the estimation of evapotranspiration. *Journal of Hydrology*, *142*(1-4), 89-97. https://doi.org/10.1016/0022-1694(93)90006-U

Malek, E., Bingham, G. E., & McCurdy, G. D. (1990). Evapotranspiration from the margin and moist playa of a closed desert valley. *Journal of Hydrology*, *120*(1-4), 15-34. https://doi.org/10.1016/0022-1694(90)90139-O

Mareschal, J. C., & Jaupart, C. (2011). Energy budget of the Earth. *Encyclopedia of Solid Earth Geophysics*, 285-291. https://doi.org/10.1007/978-90-481-8702-7_64

Marshall, J. D., & Waring, R. H. (1986). Comparison of methods of estimating leaf-area index in old-growth Douglas-fir. *Ecology*, *67*(4), 975-979. https://doi.org/10.2307/1939820

Ma, X., Feng, Q., Su, Y., Yu, T., & Jin, H. (2017). Forest evapotranspiration and energy flux partitioning based on eddy covariance methods in an arid desert region of northwest China. Advances in Meteorology, 2017. https://doi.org/10.1155/2017/1619047

Meng, X., Cheng, J., Zhao, S., Liu, S., & Yao, Y. (2019). Estimating land surface temperature from Landsat-8 data using the NOAA JPSS enterprise algorithm. Remote Sensing, 11(2), 155. https://www.mdpi.com/2072-4292/11/2/155

McCabe, M. F., & Wood, E. F. (2006). Scale influences on the remote estimation of evapotranspiration using multiple satellite sensors. Remote Sensing of Environment, 105(4), 271-285. https://doi.org/10.1016/j.rse.2006.07.006

McCabe, M. F., Wood, E. F., Wójcik, R., Pan, M., Sheffield, J., Gao, H., & Su, H. (2008). Hydrological consistency using multi-sensor remote sensing data for water and energy cycle studies. *Remote Sensing of Environment*, *112*(2), 430-444. https://doi.org/10.1016/j.rse.2007.03.027

McCaughey, J. H. (1987). The albedo of a mature mixed forest and a clear-cut site at Petawawa, Ontario. *Agricultural and forest meteorology*, *40*(3), 251-263. https://doi.org/10.1016/0168-1923(87)90062-1

McCutchan, M. H. (1983). Comparing temperature and humidity on a mountain slope and in the free air nearby. *Monthly Weather Review*, *111*(4), 836-845. https://doi.org/10.1175/1520-0493(1983)111<0836:CTAHOA>2.0.CO;2

McMahon, T. A., Peel, M. C., Lowe, L., Srikanthan, R., & McVicar, T. R. (2013). Estimating actual, potential, reference crop and pan evaporation using standard meteorological data: a pragmatic synthesis. *Hydrology and Earth System Sciences*, *17*(4), 1331-1363. doi:10.5194/hess-17-1331-2013.

McNaughton, K. G., & Jarvis, P. G. (1983). Predicting effects of vegetation changes on transpiration and evaporation. *Water deficits and plant growth*, *7*, 1-47.

McNaughton, K. G., & Laubach, J. (1998). Unsteadiness as a cause of nonequality of eddy diffusivities for heat and vapour at the base of an advective inversion. *Boundary-Layer Meteorology*, *88*(3), 479-504. https://doi.org/10.1023/A:1001573521304

Miller, D. H. 1981. Energy at the Surface of the Earth: An Introduction to the Energetics of Ecosystems, International Geophysics. Vol 27, pp96-113. https://doi.org/10.1016/S0074-6142(08)60373-3

Miller, S. A., & Eagleson, P. S. (1982). Interaction of the saturated and unsaturated soil zones. *MIT, Parsons Laboratory Rep. No.* 284, 289pp.

Mohamed, Y. A., Bastiaanssen, W. G. M., & Savenije, H. H. G. (2004). Spatial variability of evaporation and moisture storage in the swamps of the upper Nile studied by remote sensing techniques. *Journal of hydrology*, *289*(1-4), 145-164. https://doi.org/10.1016/j.jhydrol.2003.11.038

Monin, A. S., & Obukhov, A. M. (1954). Basic laws of turbulent mixing in the surface layer of the atmosphere. *Contrib. Geophys. Inst. Acad. Sci. USSR*, *151*(163), e187.

Monteith, J. L. (1973). Principles of Environmental Physics. Edward Arnold Ltd., London. *Nakamura*, *5*(1954), 43-47.

Monteith, J. L., & Szeicz, G. (1961). The radiation balance of bare soil and vegetation. *Quarterly Journal of the Royal Meteorological Society*, *87*(372), 159-170. https://doi.org/10.1002/qj.49708737205

Moore, C. J. (1976). A comparative study of radiation balance above forest and grassland. *Quarterly Journal of the Royal Meteorological Society*, *102*(434), 889-899. https://doi.org/10.1002/qj.49710243416

Morse, A., Tasumi, M., Allen, R. G., & Kramber, W. J. (2000). Application of the SEBAL methodology for estimating consumptive use of water and streamflow depletion in the Bear River Basin of Idaho through remote sensing. *Idaho Department of Water Resources–University of Idaho*.

Nambiar, E. S. (1990). Interplay between nutrients, water, root growth and productivity in young plantations. *Forest Ecology and Management*, *30*(1-4), 213-232. https://doi.org/10.1016/0378-1127(90)90138-2

Nemani, R., Pierce, L., Running, S., & Band, L. (1993a). Forest ecosystem processes at the watershed scale: sensitivity to remotely-sensed leaf area index estimates. *International journal of remote sensing*, *14*(13), 2519-2534. https://doi.org/10.1080/01431169308904290

Nemani, R., Pierce, L., Running, S., & Goward, S. (1993b). Developing satellite-derived estimates of surface moisture status. *Journal of Applied*

Meteorology, *32*(3), 548-557. https://doi.org/10.1175/1520-0450(1993)032<0548:DSDEOS>2.0.CO;2

Nepstad, D. C., de Carvalho, C. R., Davidson, E. A., Jipp, P. H., Lefebvre, P. A., Negreiros, G. H., ... & Vieira, S. (1994). The role of deep roots in the hydrological and carbon cycles of Amazonian forests and pastures. *Nature*, *372*(6507), 666-669. https://doi.org/10.1038/372666a0

Nichols, W. D. (1993). Estimating annual ground-water discharge by greasewood in areas of shallow groundwater in the northern Great Basin using an energy-combination model. *Water Resour. Res*, *29*, 2771-2778.

Nichols, W. D. (1993). Estimating discharge of shallow groundwater by transpiration from greasewood in the northern Great Basin. *Water Resources Research*, *29*(8), 2771-2778. https://doi.org/10.1029/93WR00930

Nichols, W. D. (1994). Groundwater discharge by phreatophyte shrubs in the Great Basin as related to depth to groundwater. *Water Resources Research*, *30*(12), 3265-3274. https://doi.org/10.1029/94WR02274

Nichols, W. E., & Cuenca, R. H. (1993). Evaluation of the evaporative fraction for parameterization of the surface energy balance. *Water Resources Research*, *29*(11), 3681-3690. https://doi.org/10.1029/93WR01958

Nielsen, L. B., Prahm, L. P., Berkowicz, R., & Conradsen, K. (1981). Net incoming radiation estimated from hourly global radiation and/or cloud observations. *Journal of Climatology*, *1*(3), 255-272. https://doi.org/10.1002/joc.3370010305

Niemelä, S., Räisänen, P., & Savijärvi, H. (2001). Comparison of surface radiative flux parameterizations: Part I: Longwave radiation. *Atmospheric Research*, *58*(1), 1-18. https://doi.org/10.1016/S0169-8095(01)00084-9

Noy-Meir, I. (1973). Desert ecosystems: environment and producers. *Annual review of ecology and systematics*, *4*(1),25-51. https://doi.org/10.1146/annurev.es.04.110173.000325.

Nyman, P., Sherwin, C. B., Langhans, C., Lane, P. N., & Sheridan, G. J. (2014). Downscaling regional climate data to calculate the radiative index of dryness in complex terrain. *Australian Meteorological and Oceanographic Journal*, *64*(2), 109-122. https://www.researchgate.net/publication/270396058

Oladosu, O. R., Jegede, O. O., Sunmonu, L. A., & Adediji, A. T. (2007). Bowen ratio estimation of surface energy fluxes in a humid tropical agricultural site, Ile-Ife, Nigeria. https://nopr.niscair.res.in/handle/123456789/2837

Oliveira, R. S., Dawson, T. E., Burgess, S. S., & Nepstad, D. C. (2005). Hydraulic redistribution in three Amazonian trees. *Oecologia*, *145*(3), 354-363. https://doi.org/10.1007/s00442-005-0108-2

Panchal, N. S., & Chandrasekharan, E. (1983). Terrain roughness and atmospheric stability at a typical coastal site. *Boundary-Layer Meteorology*, *27*(1), 89-96. https://doi.org/10.1007/BF00119973

Partington, J. R. (1949). *An advanced treatise on physical chemistry. 1. Fundamental principles, the properties of gases*. Longmans, Green & Company, London, pages 155-157.

Paulson, C. A. (1970). The mathematical representation of wind speed and temperature profiles in the unstable atmospheric surface layer. *Journal of Applied Meteorology*, *9*(6), 857-861. *https://doi.org/10.1175/1520-0450(1970)009<0857:TMROWS>2.0.CO;2*

Payero, J. O., Neale, C. M. U., & Wright, J. L. (2005). Estimating soil heat flux for alfalfa and clipped tall fescue grass. *Applied engineering in agriculture*, *21*(3), 401-409.

Peel, M. C. (2009). Hydrology: catchment vegetation and runoff. *Progress in Physical Geography*, *33*(6), 837-844. https://doi.org/10.1177/0309133309350122

Pepin, N. C., & Norris, J. R. (2005). An examination of the differences between surface and free-air temperature trend at high-elevation sites: Relationships with cloud cover, snow cover, and wind. *Journal of Geophysical Research: Atmospheres*, *110*(D24).

Pereira, J. S., Tenhunen, J. D., Lange, O. L., Beyschlag, W., Meyer, A., & David, M. M. (1986). Seasonal and diurnal patterns in leaf gas exchange of Eucalyptus globulus trees growing in Portugal. Canadian Journal of Forest Research, 16(2), 177-184. https://doi.org/10.1139/x86-033

Powell, J. M. (1996). Historical geography and environmental history: an Australian interface. *Journal of Historical Geography*, *22*(3), 253-273. https://doi.org/10.1006/jhge.1996.0016

Priante-Filho, N., Vourlitis, G. L., Hayashi, M. M. S., Nogueira, J. D. S., Campelo Jr, J. H., Nunes, P. C., ... & Trienweiler, J. L. (2004). Comparison of the mass and energy exchange of a pasture and a mature transitional tropical forest of the southern Amazon Basin during a seasonal transition. *Global Change Biology*, *10*(5), 863-876. https://doi.org/10.1111/j.1529-8817.2003.00775.x

Qin, Z., Karnieli, A., & Berliner, P. (2001). A mono-window algorithm for retrieving land surface temperature from Landsat TM data and its application to the Israel-Egypt border region. *International journal of remote sensing*, *22*(18), 3719-3746. https://doi.org/10.1080/01431160010006971

Quattrochi, D. A., & Luvall, J. C. (2009). *Thermal remote sensing in Earth science research* (pp. 64-78). SAGE Publications Ltd.: London, UK.

Quattrochi, D. A., & Luvall, J. C. (Eds.). (2004). *Thermal remote sensing in land surface processing*. CRC Press.

Rahman, M. A., Armson, D., & Ennos, A. R. (2015). A comparison of the growth and cooling effectiveness of five commonly planted urban tree species. *Urban Ecosystems*, *18*(2), 371-389. https://doi.org/10.1007/s11252-014-0407-7

Rajeshwari, A., & Mani, N. D. (2014). Estimation of land surface temperature of Dindigul district using Landsat 8 data. *International Journal of Research in Engineering and Technology*, *3*(5), 122-126.

Reichstein, M., Ciais, P., Papale, D., Valentini, R., Running, S., Viovy, N., N., Cramer, W., Granier, A., Ogee, J., Allard, V., Aubinet, M., Bernhofer, C., BuchmannN, Carrara, A., GrunwaldT, Heimann, M., HeineschB, Knohl, A., KutschW, Loustau, D., Manca, G., Matteucci, G., Miglietta, F., Ourcival, J.M., Pilegaard, K., Pumpanen, J., Rambal, S., Schaphoff, S., Seufert, G., Soussana, J.F., SanzMJ, Vesala, T., & Zhao, M. (2007a). Reduction of ecosystem productivity and respiration during the European summer 2003 climate anomaly: a joint flux tower, remote sensing and modelling analysis. *Global Change Biology*, *13*(3), 634-651. http://dx.doi.org/10.1111/j. 1365-2486.2006.01224.x.

Reichstein, M., Papale, D., Valentini, R., Aubinet, M., Bernhofer, C., Knohl, A., ... & Seufert, G. (2007b). Determinants of terrestrial ecosystem carbon balance inferred from European eddy covariance flux sites. *Geophysical Research Letters*, *34*(1). http://dx.doi.org/10.1029/2006GL027880.

Richards, J. H., & Caldwell, M. M. (1987). Hydraulic lift: substantial nocturnal water transport between soil layers by Artemisia tridentate roots. *Oecologia*, *73*(4), 486-489. https://doi.org/10.1007/BF00379405

Richardson, A. D., Andy Black, T., Ciais, P., Delbart, N., Friedl, M. A., Gobron, N., ... & Migliavacca, M. (2010). Influence of spring and autumn phenological transitions on forest ecosystem productivity. *Philosophical Transactions of the Royal Society B: Biological Sciences*, *365*(1555), 3227-3246. http://dx.doi.org/10.1098/rstb.2010.0102.

Richner, H., & Phillips, P. D. (1984). A comparison of temperatures from mountaintops and the free atmosphere—Their diurnal variation and mean difference. *Monthly Weather Review*, *112*(7), 1328-1340. *https://doi.org/10.1175/1520-0493(1984)112<1328:ACOTFM>2.0.CO;2*.

Rider, N. E., Philip, J. R., & Bradley, E. F. (1963). The horizontal transport of heat and moisture-a micrometeorological study. *Quarterly Journal of the Royal Meteorological Society*, *89*(382), 507-531. https://doi.org/10.1002/qj.49708938207

Ripley, E. A., & Redmann, R. E. (1976). Grassland. Vegetation and the Atmosphere, Vol. 2, JL Monteith, Ed. Academic Press, London.

Ritter, M. E. (2006 instead of 2003). The physical environment: An introduction to physical geography. https://www.earthonlinemedia.com/ebooks/tpe_3e/energy/outline.html

Roberts J, Rosier P, Smith D. M. (2005). The impact of broadleaved woodland on water resources in lowland UK: II. Evaporation estimates from sensible heat flux measurements over beech woodland and grass on chalk sites in Hampshire. *Hydrol. Earth Syst. Sci. 9: 607–613*, doi: 10.5194/hess-9-6072005.

Roerink, G. J., Su, Z., & Menenti, M. (2000). S-SEBI: A simple remote sensing algorithm to estimate the surface energy balance. *Physics and Chemistry of the Earth, Part B: Hydrology, Oceans and Atmosphere*, *25*(2), 147-157. https://doi.org/10.1016/S1464-1909(99)00128-8

Roohi, R. and Webb. J. and Jones, S. 2016a. Modelling surface energy balance of shifting rainfed agro-ecosystems and its response to groundwater in Western Victoria, SE Australia. *In* Proceedings of the International Society for Ecological Modelling Global Conference, 8 – 12 May 2016, organized by International Society for Ecological Modelling, Towson University, Townson University, MD, USA.

Roohi, R. Webb, J. A. and Jones, S. A. (2015a). Use of remote sensing to determine the impact of landuse on evapotranspiration and groundwater in Western Victoria, SE Australia. *In Proceedings of the Australian Groundwater Conference organized by NCGRT, Canbera, Australia, 3-5 November 2015.*

Roohi, R., & Webb, J. A. (2016b). Thermal and visible remote sensing for estimation of evapotranspiration of rainfed agrosystems and its impact on groundwater in SE Australia. *In* Thermosense: Thermal Infrared Applications XXXVIII (Vol. 9861, p. 98610A). International Society for Optics and Photonics. https://doi.org/10.1117/12.2223725

Roohi, R., Webb, J.A., and Jones, Simon, J.A. (2015 b). Use of remote sensing to determine the impact of landuse on evapotranspiration and groundwater in western Victoria, SE Australia. In Abstarcts of Australian Groundwater Conference 2015, pp. 220.

Roohi, R., Webb, J.A., and Jones, Simon, J.A. (2016b). Modelling surface energy balance of shifting rainfed agro-ecosystems and its response to groundwater in Western Victoria, SE Australia In proceedings of Ecological Modelling Global Conference 8-12 May, 2016 organized by International Society for Ecological Modelling, Towson University, MD, USA. pp 105.

Rosas, J., Houborg, R., & McCabe, M. F. (2017). Sensitivity of Landsat 8 surface temperature estimates to atmospheric profile data: A study using MODTRAN in dryland irrigated systems. Remote Sensing, 9(10), 988. https://doi.org/10.3390/rs9100988.

Rosenberg, N. J., Blad, B. L., & Verma, S. B. (1983). Microclimate; The Biological Environment', John Wiley & Sons, New York, 495pp.

Rosenzweig, C., Solecki, W., & Slosberg, R. (2006). Mitigating New York City's heat island with urban forestry, living roofs, and light surfaces. *A report to the New York State Energy Research and Development Authority*.

Rosset, M., Montani, M., Tanner, M., & Fuhrer, J. (2001). Effects of abandonment on the energy balance and evapotranspiration of wet subalpine grassland. *Agriculture, ecosystems & environment*, *86*(3), 277-286. https://doi.org/10.1016/S0167-8809(00)00290-5

Rosset, M., Riedo, M., Grub, A., Geissmann, M., & Fuhrer, J. (1997). Seasonal variation in radiation and energy balances of permanent pastures at different altitudes. *Agricultural and Forest Meteorology*, *86*(3-4), 245-258. https://doi.org/10.1016/S0168-1923(96)02423-9

Rost, J., & Mayer, H. (2006). Comparative analysis of albedo and surface energy balance of a grassland site and an adjacent Scots pine forest. Climate Research, 30(3), 227-237. doi:10.3354/cr030227

Rouse, W. R. (1984). Microclimate of arctic tree line 2. Soil microclimate of tundra and forest. *Water Resources Research*, *20*(1), 67-73. https://doi.org/10.1029/WR020i001p00067

Rozenstein, O., Qin, Z., Derimian, Y., & Karnieli, A. (2014). Derivation of land surface temperature for Landsat-8 TIRS using a split window algorithm. *Sensors*, *14*(4), 5768-5780. https://doi.org/10.3390/s140405768

Ryel, R. J., Caldwell, M. M., Leffler, A. J., & Yoder, C. K. (2003). Rapid soil moisture recharge to depth by roots in a stand of Artemisia tridentata. *Ecology*, *84*(3), 757-764. https://doi.org/10.1890/0012-

9658(2003)084[0757:RSMRTD]2.0.CO;2

Ryel, R., Caldwell, M., Yoder, C., Or, D., & Leffler, A. (2002). Hydraulic redistribution in a stand of Artemisia tridentata: evaluation of benefits to transpiration assessed with a simulation model. *Oecologia*, *130*(2), 173-184. https://doi.org/10.1007/s004420100794

Ryu, Y., Baldocchi, D. D., Ma, S., & Hehn, T. (2008). Interannual variability of evapotranspiration and energy exchange over an annual grassland in California. *Journal of Geophysical Research: Atmospheres*, *113*(D9). https://doi.org/10.1029/2007JD009263

Sahin, V., & Hall, M. J. (1996). The effects of afforestation and deforestation on water yields. *Journal of hydrology*, *178*(1-4), 293-309. https://doi.org/10.1029/2007JD009263

Samson, C. A. (1965). A comparison of mountain slope and radiosonde observations. *Monthly Weather Review*, *93*(5), 327-330. *https://doi.org/10.1175/1520-0493(1965)093<0327:ACOMSA>2.3.CO;2*

Santanello, J. A., & Friedl, M. A. (2002, January). Diurnal relationships between soil heat flux and net radiation over a range of surface conditions applied to land surface energy balance modeling. *In* JP1. 5–Land Atmosphere Interactions (Jointly In: Conference on Hydrology-American Meteorological Society; J83-J87 Hydrology Conference; 16th, Hydrology, and Symposium on Global Change and Climate Variations; J154-J158, Global Change and Climate Variations Symposium; 13th, Global change and climate variations) American Meteorological Society, Orlando, FL. Accessed December 18, 2013. https://ams. confex. com/ams/pdfpapers/30663. pdf 16th Conference on Hydrology and the 13th Symposium on Global Change and Climate Variations).

Sapanov, M. K. (2000). Water uptake by trees on different soils in the Northern Caspian region. *Pochvovedenie*, (11), 1318-1327. ISSN : 0032-180X, Record Number : 20013067157

Satchithanantham, S., Wilson, H. F., & Glenn, A. J. (2017). Contrasting patterns of groundwater evapotranspiration in grass and tree dominated riparian zones of a temperate agricultural catchment. *Journal of hydrology*, *549*, 654-666. https://doi.org/10.1016/j.jhydrol.2017.04.016

Sauer, T. J., & Horton, R. (2005). Soil heat flux. *Agronomy Publications*. 304. Iowa State University Digital repository, pp. 131-151/ Publications from USDA-ARS / UNL Faculty. 1402. https://lib.dr.iastate.edu/agron_pubs/304 / http://digitalcommons.unl.edu/usdaarsfacpub/1402.

Schenk J, Jackson RB. (2002). The global biogeography of roots. Ecological Monographs 72: 311-328. https://doi.org/10.1890/0012-9615(2002)072[0311:TGBOR]2.0.CO;2

Schmetz, J. (1989). Towards a surface radiation climatology: Retrieval of downward irradiances from satellites. *Atmospheric Research*, *23*(3-4), 287-321. https://doi.org/10.1016/0169-8095(89)90023-9

Schneider, A., Arnold, S., Doley, D., Mulligan, D. R., & Baumgartl, T. (2012). The importance of plant water use on evapotranspiration covers in semi-arid Australia. *Hydrology and Earth System Sciences Discussions*, *9*(10), 11911-11940. doi:10.5194/hessd-9-11911-2012

Scholz, F. G., Bucci, S. J., Goldstein, G., Meinzer, F. C., & Franco, A. C. (2002). Hydraulic redistribution of soil water by neotropical savanna trees. *Tree Physiology*, *22*(9), 603-612. https://doi.org/10.1093/treephys/22.9.603

Schotanus, P., Nieuwstadt, F., & De Bruin, H. A. R. (1983). Temperature measurement with a sonic anemometer and its application to heat and moisture fluxes. *Boundary-Layer Meteorology*, *26*(1), 81-93. https://doi.org/10.1007/BF00164332

Schuepp, P. H. (1993). Tansley review No. 59. Leaf boundary layers. *New Phytologist*, 477-507. https://www.jstor.org/stable/2558258

Scott, D. F., & Lesch, W. (1997). Streamflow responses to afforestation with *Eucalyptus grandis* and *Pinus patula* and to felling in the Mokobulaan experimental catchments, South Africa. *Journal of Hydrology*, *199*(3-4), 360-377. https://doi.org/10.1016/S0022-1694(96)03336-7

Sellers, P.J., Hall, F.G., Asrar, G., Strebel, D.E. and Murphy, R.E., 1992. An overview of the first international satellite land surface climatology project (ISLSCP) field experiment (FIFE). *Journal of* Geophysical Research: Atmospheres, 97(D17), pp.18345-18371.

Sharma, M. L. (1984). Evapotranspiration from a Eucalyptus community. In Developments in Agricultural and Managed Forest Ecology (Vol. 13, pp. 41-56). Elsevier. https://doi.org/10.1016/B978-0-444-42250-7.50007-0

Shirke, P. A., & Pathre, U. V. (2004). Influence of leaf-to-air vapour pressure deficit (VPD) on the biochemistry and physiology of photosynthesis in Prosopis juliflora. *Journal of Experimental Botany*, *55*(405), 2111-2120. DOI: 10.1093/jxb/erh229 https://doi.org/10.1093/jxb/erh229

Shukla, J., & Mintz, Y. (1982). Influence of land-surface evapotranspiration on the earth's climate. *Science*, *215*(4539), 1498-1501.

DOI:10.1126/science.215.4539.1498

Silberstein, R., Held, A., Hatton, T., Viney, N., & Sivapalan, M. (2001). Energy balance of a natural jarrah (Eucalyptus marginata) forest in Western Australia: measurements during the spring and summer. Agricultural and Forest Meteorology, 109(2), 79-104. https://doi.org/10.1016/S0168-1923(01)00263-5

Simmers, I. (1977). Effect of soil heat flux on the water balance of a small catchment/L'effet du flux en chaleur du sol sur le bilan hydrologique d'un petit bassin versant. *Hydrological Sciences Journal*, *22*(3), 433-445. https://doi.org/10.1080/02626667709491736

Singh, R., & Senay, G. (2016). Comparison of four different energy balance models for estimating evapotranspiration in the Midwestern United States. *Water*, *8*(1), 9. doi:10.3390/w8010009.

Skoković, D., Sobrino, J. A., Jimenez-Munoz, J. C., Soria, G., Juşien, Y., Mattar, C., & Cristóbal, J. (2014). Calibration and validation of land surface temperature for landsat8-tirs sensor. *LPVE (Land Product Validation and Evolution*.

Sobrino, J. A., Jimenez-Munoz, J. C., & Paolini, L. (2004). Land surface temperature retrieval from LANDSAT TM 5. *Remote Sensing of environment*, *90*(4), 434-440. https://doi.org/10.1016/j.rse.2004.02.003

Sobrino, J. A., Mattar, C., Pardo, P., Jiménez-Muñoz, J. C., Hook, S. J., Baldridge, A., & Ibañez, R. (2009). Soil emissivity and reflectance spectra measurements. *Applied optics*, *48*(19), 3664-3670. https://doi.org/10.1364/AO.48.003664

Sofia, S., & Li, L. H. (2001). Solar variability and climate. *Journal of Geophysical Research: Space Physics*, *106*(A7), 12969-12974. doi:10.1029/2000JA000379.

Stanhill, G. (1969). A simple instrument for the field measurement of turbulent diffusion flux. *Journal of Applied Meteorology*, *8*(4), 509-513. *https://doi.org/10.1175/1520-0450(1969)008<0509:ASIFTF>2.0.CO;2*

Steduto, P., Hsiao, T. C., Fereres, E., & Raes, D. (2012). *Crop yield response to water* (Vol. 1028). Rome: FAO, UN.

Stephens, G. L., O'Brien, D., Webster, P. J., Pilewski, P., Kato, S., & Li, J. L. (2015). The albedo of Earth. *Reviews of geophysics*, *53*(1), 141-163. https://doi.org/10.1002/2014RG000449

Stevens, B., & Feingold, G. (2009). Untangling aerosol effects on clouds and precipitation in a buffered system. *Nature*, *461*(7264), 607.

https://doi.org/10.1038/nature08281

Stewart, J. B., Kustas, W. P., Humes, K. S., Nichols, W. D., Moran, M. S., & de Bruin, H. A. (1994). Sensible heat flux-radiometric surface temperature relationship for eight semiarid areas. *Journal of Applied Meteorology*, *33*(9), 1110-1117. *https://doi.org/10.1175/1520-0450(1994)033<1110:SHFRST>2.0.CO;2*

Stone, C., Chisholm, L., & Coops, N. (2001). Spectral reflectance characteristics of eucalypt foliage damaged by insects. *Australian Journal of Botany*, *49*(6), 687-698. https://doi.org/10.1071/BT00091

Stone, P. H. (1978). Constraints on dynamical transports of energy on a spherical planet. *Dynamics of atmospheres and oceans*, *2*(2), 123-139. https://doi.org/10.1016/0377-0265(78)90006-4

Stroeve, J. C., & Nolin, A. W. (2002). New methods to infer snow albedo from the MISR instrument with applications to the Greenland ice sheet. *IEEE Transactions on Geoscience and Remote Sensing*, *40*(7), 1616-1625. DOI: 10.1109/TGRS.2002.801144

Stull, R. B. (2012). *An introduction to boundary layer meteorology* (Vol. 13). Springer Science & Business Media.

Sturman, A. P., & Tapper, N. J. (1996). *The weather and climate of Australia and New Zealand*. Oxford University Press, USA. ISBN (Print) 0195539230, 0195533933

Su, Z. (2002). The Surface Energy Balance System (SEBS) for estimation of turbulent heat fluxes. *Hydrology and earth system sciences*, *6*(1), 85-100. https://doi.org/10.5194/hess-6-85-2002, 2002

Sun, L., & Wu, G. (2001). Influence of land evapotranspiration on climate variations. *Science in China Series D: Earth Sciences*, *44*(9), 838-846. https://doi.org/10.1007/BF02907096

Tabony, R. C. (1985). The variation of surface temperature with altitude. *Meteorological Magazine*, *114*(1351), 37-48.

Tamai, K., Abe, T., Araki, M., & Ito, H. (1998). Radiation budget, soil heat flux and latent heat flux at the forest floor in warm, temperate mixed forest. *Hydrological processes*, *12*(13-14), 2105-2114. https://doi.org/10.1002/(SICI)1099-1085(19981030)12:13/14<2105::AID-HYP723>3.0.CO;2-9

Tan, Z., Lau, K. K. L., & Ng, E. (2016). Urban tree design approaches for mitigating daytime urban heat island effects in a high-density urban environment. *Energy and Buildings*, *114*, 265-274.

https://doi.org/10.1016/j.enbuild.2015.06.031

Tennekes, H. (1973). The logarithmic wind profile. *Journal of the Atmospheric Sciences*, *30*(2), 234-238. *https://doi.org/10.1175/1520-0469(1973)030<0234:TLWP>2.0.CO;2*

Theiveyanathan, S., & Polglase, P. (2005). Water management and groundwater uptake in plantations. *New Forests: Wood Production and Environmental Services*, 135.

Thorburn, P. J. (1999). The limits to evaporation from shallow, saline water tables—the big picture. *Agroforestry over shallow watertables: the impact of salinity on sustainability. Water and Salinity Issues in Agroforestry*, (4), 18-20.

Thorburn, P. J., & Walker, G. R. (1993). The source of water transpired by *Eucalyptus camaldulensis*: soil, groundwater, or streams? In *Stable isotopes and plant carbon-water relations* (pp. 511-527). Academic Press. https://doi.org/10.1016/B978-0-08-091801-3.50042-8

Thorburn, P. J., Hatton, T. J., & Walker, G. R. (1993a). Combining measurements of transpiration and stable isotopes of water to determine groundwater discharge from forests. *Journal of Hydrology*, *150*(2-4), 563-587. doi: 10.1016/0022-1694(93)90126-T

Thorburn, P. J., Walker, G. R., & Brunel, J. P. (1993b). Extraction of water from *Eucalyptus* trees for analysis of deuterium and oxygen-18: laboratory and field techniques. *Plant, Cell & Environment*, *16*(3), 269-277. https://doi.org/10.1111/j.1365-3040.1993.tb00869.x

Thorburn, P. J., Walker, G. R., & Woods, P. H. (1992). Comparison of diffuse discharge from shallow water tables in soils and salt flats. *Journal of Hydrology*, *136*(1-4), 253-274. https://doi.org/10.1016/0022-1694(92)90014-M

Tomlinson, S. A. (1997). Comparison of Bowen-ratio, eddy-correlation, and weighing-lysimeter evapotranspiration for two sparse-canopy sites in eastern Washington. https://journals.ametsoc.org/doi/pdf/10.1175/2008BAMS2634.1

Trenberth, K. E., Fasullo, J. T., & Kiehl, J. (2009). Earth's global energy budget. *Bulletin of the American Meteorological Society*, *90*(3), 311-324. https://journals.ametsoc.org/doi/pdf/10.1175/2008BAMS2634.1

Tseng, R. S., Hsu, Y. H., & Wu, J. (1992). Methods of measuring wind stress over a water surface—Discussions of displacement height and von Karman constant. *Boundary-Layer Meteorology*, *58*(1-2), 51-68.

https://doi.org/10.1007/BF00120751

Tweed, S. O., Leblanc, M., Webb, J. A., & Lubczynski, M. W. (2007). Remote sensing and GIS for mapping groundwater recharge and discharge areas in salinity prone catchments, southeastern Australia. *Hydrogeology Journal*, *15*(1), 75-96. https://doi.org/10.1007/s10040-006-0129-x

Tyler, S. W., Kranz, S., Parlange, M. B., Albertson, J., Katul, G. G., Cochran, G. F., ... & Holder, G. (1997). Estimation of groundwater evaporation and salt flux from Owens Lake, California, USA. *Journal of Hydrology*, *200*(1-4), 110-135. https://doi.org/10.1016/S0022-1694(97)00007-3

Ulivieri, C. M. M. A., Castronuovo, M. M., Francioni, R., & Cardillo, A. (1994). A split window algorithm for estimating land surface temperature from satellites. *Advances in Space Research*, *14*(3), 59-65. https://doi.org/10.1016/0273-1177(94)90193-7

Ullman, W. J. (1985). Evaporation rate from a salt pan: estimates from chemical profiles in near-surface groundwaters. *Journal of Hydrology*, *79*(3-4), 365-373. https://doi.org/10.1016/0022-1694(85)90066-6

USGS. (2019a). Landsat 4-7 surface reflectance (LEDAPS) product guide. Department of the Interior, U.S. Geological Survey. LSDS Version 2.0. https://prd-wret.s3.us-west-2.amazonaws.com/assets/palladium/production/atoms/files/LSDS-1370_L4-7_SurfaceReflectance-LEDAPS_ProductGuide-v2.pdf

USGS. (2019b). Landsat 7 (L7) Data users Handbook. *Department of the Interior, U.S. Geological Survey* Version 2.0. pp.139. https://prd-wret.s3.us-west-2.amazonaws.com/assets/palladium/production/atoms/files/LSDS-1927_L7_Data_Users_Handbook-v2.pdf

USGS. (2019c). Landsat 8 (L8) data users handbook. Department of the Interior, U.S. Geological Survey. LSDS Version 5.0. pp. 114. https://prd-wret.s3-us-west-2.amazonaws.com/assets/palladium/production/atoms/files/LSDS-1574_L8_Data_Users_Handbook-v5.0.pdf

Valor, E., & Caselles, V. (1996). Mapping land surface emissivity from NDVI: Application to European, African, and South American areas. *Remote sensing of Environment*, *57*(3), 167-184. https://doi.org/10.1016/0034-4257(96)00039-9

Van de Griend, A. A., & OWE, M. (1993). On the relationship between thermal emissivity and the normalized difference vegetation index for natural surfaces. *International Journal of remote sensing*, *14*(6), 1119-1131. DOI: 10.1080/01431169308904400

Van de Griend, A. A., & Owe, M. (1994). Microwave vegetation optical depth and inverse modelling of soil emissivity using Nimbus/SMMR satellite observations. *Meteorology and Atmospheric Physics*, *54*(1-4), 225-239. https://doi.org/10.1007/BF01030062

Van den Broeke, M., Fettweis, X. and Mölg, T. (2011). Surface energy balance. *Encyclopedia of Snow, Ice and Glaciers*, pp.1112-1123.

van den Kroonenberg, A., & Bange, J. (2007). Turbulent flux calculation in the polar stable boundary layer: Multiresolution flux decomposition and wavelet analysis. *Journal of Geophysical Research: Atmospheres*, *112*(D6). https://doi.org/10.1029/2006JD007819

Van der Molen, M. K., Dolman, A. J., Waterloo, M. J., & Bruijnzeel, L. A. (2006). Climate is affected more by maritime than by continental landuse change: A multiple scale analysis. *Global and Planetary Change*, *54*(1-2), 128-149. https://doi.org/10.1016/j.gloplacha.2006.05.005

Verhoef, A., Allen, S. J., & Lloyd, C. R. (1999). Seasonal variation of surface energy balance over two Sahelian surfaces. *International Journal of Climatology: A Journal of the Royal Meteorological Society*, *19*(11), 1267-1277. https://doi.org/10.1002/(SICI)1097-0088(199909)19:11<1267::AID-JOC418>3.0.CO;2-S

Wang, K., Li, Z., & Cribb, M. (2006). Estimation of evaporative fraction from a combination of day and night land surface temperatures and NDVI: A new method to determine the Priestley–Taylor parameter. *Remote Sensing of Environment*, *102*(3-4), 293-305. https://doi.org/10.1016/j.rse.2006.02.007

Waterloo, M. J., Bruijnzeel, L. A., Vugts, H. F., & Rawaqa, T. T. (1999). Evaporation from *Pinus caribaea* plantations on former grassland soils under maritime tropical conditions. *Water Resources Research*, *35*(7), 2133-2144. https://doi.org/10.1029/1999WR900006

Watson, A. J., & Lovelock, J. E. (1983). Biological homeostasis of the global environment: the parable of Daisyworld. *Tellus B: Chemical and Physical Meteorology*, *35*(4), 284-289. https://doi.org/10.3402/tellusb.v35i4.14616

Webb, E. K. (1970). Profile relationships: The log-linear range, and extension to strong stability. *Quarterly Journal of the Royal Meteorological Society*, *96*(407), 67-90. https://doi.org/10.1002/qj.49709640708

Weiss, A. (1982). An Experimental Study of Net Radiation, Its Components and Prediction 1. *Agronomy journal*, *74*(5), 871-874. doi:10.2134/agronj1982.00021962007400050024x

Wever, L. A., Flanagan, L. B., & Carlson, P. J. (2002). Seasonal and interannual variation in evapotranspiration, energy balance and surface conductance in a northern temperate grassland. *Agricultural and Forest meteorology*, *112*(1), 31-49. https://doi.org/10.1016/S0168-1923(02)00041-2

White M, Oates A, Barlow T, *et al*. (2003). The Vegetation of North-West Victoria, Department of Sustainability and Environment, Melbourne, Australia.

White-Newsome, J. L., Brines, S. J., Brown, D. G., Dvonch, J. T., Gronlund, C. J., Zhang, K., Oswald, E.M. & O'Neill, M. S. (2013). Validating satellite-derived land surface temperature within situ measurements: A public health perspective. *Environmental health perspectives*, *121*(8), 925-931. https://doi.org/10.1289/ehp.1206176

Wilson, J. D. (2008). Monin-Obukhov functions for standard deviations of velocity. *Boundary-layer meteorology*, *129*(3), 353-369. https://doi.org/10.1007/s10546-008-9319-5

Wilson, J. R., & Ludlow, M. M. (1991). The environment and potential growth of herbage under plantations. *Forages for Plantation Crops (ed. Shelton, HM and Stur, WW) ACIAR Proceedings*, *32*, 10-24.

Wilson, K. B., & Baldocchi, D. D. (2000). Seasonal and interannual variability of energy fluxes over a broadleaved temperate deciduous forest in North America. *Agricultural and Forest Meteorology*, *100*(1), 1-18. https://doi.org/10.1016/S0168-1923(99)00088-X

Wilson, K. B., Baldocchi, D. D., Aubinet, M., Berbigier, P., Bernhofer, C., Dolman, H., Falge, E., Field, C., Goldstein, A., Granier, A., Grelle, A., Halldor, T., Hollinger, D., Katul, G., Law, B. E., Lindroth, A., Meyers, T., Moncrieff, J., Monson, R., Oechel, W., Tenhunen, J., Valentini, R., Verma, S., Vesala, T., Wofsy, S. (2002). Energy partitioning between latent and sensible heat flux during the warm season at FLUXNET sites. *Water Resources Research*, *38*(12), 30-1. https://doi.org/10.1029/2001WR000989

Wilson, K. B., Baldocchi, D. D., Aubinet, M., Berbigier, P., Bernhofer, C., Dolman, H., ... & Grelle, A. (2002). Energy partitioning between latent and sensible heat flux during the warm season at FLUXNET sites. *Water Resources Research*, *38*(12), 30-1. https://doi.org/10.1029/2001WR000989

WMO (World meteorological organization, Geneva). (2008). *Guide to meterological instruments and methods of observation*. Secretariat of the World Meteorological Organization. *WMO-No. 8.* Pp. 1-13. https://www.weather.gov/media/epz/mesonet/CWOP-WMO8.pdf

Wong, C. C., & Wilson, J. R. (1980). Effects of shading on the growth and nitrogen content of green panic and siratro in pure and mixed swards defoliated at two frequencies. *Australian Journal of Agricultural Research*, *31*(2), 269-285. https://doi.org/10.1071/AR9800269

Xavier, A. C., & Vettorazzi, C. A. (2004). Mapping leaf area index through spectral vegetation indices in a subtropical watershed. *International Journal of Remote Sensing*, *25*(9), 1661-1672. https://doi.org/10.1080/01431160310001620803

Yang, X., Zhao, L., Bruse, M., & Meng, Q. (2013). Evaluation of a microclimate model for predicting the thermal behavior of different ground surfaces. *Building and Environment*, *60*, 93-104. https://doi.org/10.1016/j.buildenv.2012.11.008

Yau, M. K., & Rogers, R. R. (1996). *A short course in cloud physics*. Elsevier.

Yeh, P. J. F., & Famiglietti, J. S. (2008). Regional terrestrial water storage change and evapotranspiration from terrestrial and atmospheric water balance computations. *Journal of Geophysical Research: Atmospheres*, *113*(D9). doi:10.1029/2007JD009045.

Yeh, P. J. F., Irizarry, M., & Eltahir, E. A. (1998). Hydroclimatology of Illinois: A comparison of monthly evaporation estimates based on atmospheric water balance and soil water balance. *Journal of Geophysical Research: Atmospheres*, *103*(D16), 19823-19837. https://doi.org/10.1029/98JD01721

Yeh, P. J., & Famiglietti, J. S. (2009). Regional groundwater evapotranspiration in Illinois. *Journal of Hydrometeorology*, *10*(2), 464-478. *https://doi.org/10.1175/2008JHM1018.1*

Yeh, T. C., Wetherald, R. T., & Manabe, S. (1984). The effect of soil moisture on the short-term climate and hydrology change—A numerical experiment. *Monthly Weather Review*, *112*(3), 474-490. https://doi.org/10.1175/1520-0493(1984)112<0474:TEOSMO>2.0.CO;2

Yunusa, I. A., Aumann, C. D., Rab, M. A., Merrick, N., Fisher, P. D., Eberbach, P. L., & Eamus, D. (2010a). Topographical and seasonal trends in transpiration by two co-occurring *Eucalyptus* species during two contrasting years in a low rainfall environment. *Agricultural and forest meteorology*, *150*(9), 1234-1244. https://doi.org/10.1016/j.agrformet.2010.05.007

Yunusa, I. A., Eamus, D., Taylor, D., Whitley, R., Gwenzi, W., Palmer, A. R., & Li, Z. (2015). Partitioning of turbulent flux reveals contrasting cooling potential for woody vegetation and grassland during heat waves. *Quarterly Journal of the Royal Meteorological Society*, *141*(692), 2528-2537. https://doi.org/10.1002/qj.2539

Yunusa, I. A., Fuentes, S., Palmer, A. R., Macinnis-Ng, C. M., Zeppel, M. J., & Eamus, D. (2011). Latent heat fluxes during two contrasting years from a juvenile plantation established over a waste disposal landscape. *Journal of hydrology*, *399*(1-2), 48-56. https://doi.org/10.1016/j.jhydrol.2010.12.033

Yunusa, I. A., Nuberg, I. K., Fuentes, S., Lu, P., & Eamus, D. (2008). A simple field validation of daily transpiration derived from sapflow using a porometer and minimal meteorological data. *Plant and soil*, *305*(1-2), 15-24.

Yunusa, I. A., Zeppel, M. J., Fuentes, S., Macinnis-Ng, C. M., Palmer, A. R., & Eamus, D. (2010b). An assessment of the water budget for contrasting vegetation covers associated with waste management. *Hydrological Processes: An International Journal*, *24*(9), 1149-1158. https://doi.org/10.1002/hyp.7570

Yunusa, I. A., Zolfaghar, S., Zeppel, M. J., Li, Z., Palmer, A. R., & Eamus, D. (2012). Fine root biomass and its relationship to evapotranspiration in woody and grassy vegetation covers for ecological restoration of waste storage and mining landscapes. *Ecosystems*, *15*(1), 113-127. https://doi.org/10.1007/s10021-011-9496-9

Zhang, L., Walker, G. R., & Dawes, W. (1999). Predicting the effect of vegetation changes on catchment average water balance. *Technical Report 99/12. (November ,1999), Cooperative Research Centre for Catchment Hydrology*, *CSIRO Land and Water*, *Australia*. pp. 35.

Zheng, G. Q., Lu, M., Zhang, T., Liu, G., & Ke, C. (2010). The impact of difference of land surface emissivity on the land surface temperature retrieval in Jinan City. Journal of Shandong Jianzhu University, 25(5), 519-523. http://en.cnki.com.cn/Article_en/CJFDTotal-SDJG201005011.htm

Zhou, L., Dickinson, R. E., Tian, Y., Zeng, X., Dai, Y., Yang, Z. L., ... & Myneni, R. B. (2003). Comparison of seasonal and spatial variations of albedos from Moderate-Resolution Imaging Spectroradiometer (MODIS) and Common Land Model. *Journal of Geophysical Research:Atmospheres*, *108*(D15). https ://doi.org/10.1029/2002JD003326

Publications

- Roohi, R., Webb, J.A., and Jones, Simon, J.A., 2015b. Modified Surface Energy Balance Algorithms for Rainfed Agriculture (SEBARA) input parameters for estimation of evapotranspiration of paired catchments in Western Victoria, SE Australia. Presented at Fourth International Conference on Aerospace Science and Engineering. September 2-4, 2015 Organised by Institute of Space Science, Islamabad, Pakistan.

- Roohi, R. Webb, J. A. and Jones, S. A. 2015. Use of remote sensing to determine the impact of landuse on evapotranspiration and groundwater in Western Victoria, SE Australia. In Proceedings of the Australian Groundwater Conference organized by NCGRT, Canberra, Australia, 3-5 November 2015.

- Roohi, R. and Webb, J.A., 2016, May. Thermal and visible remote sensing for estimation of evapotranspiration of rainfed agrosystems and its impact on groundwater in SE Australia. In Thermosense: Thermal Infrared Applications XXXVIII (Vol. 9861, p. 98610A). International Society for Optics and Photonics.

- Roohi, R. and Webb. J. and Jones, S. 2016. Modelling surface energy balance of shifting rainfed agro-ecosystems and its response to groundwater in Western Victoria, SE Australia. In Proceedings of the International Society for Ecological Modelling Global Conference, 8 – 12 May 2016, Townson University, MD, USA.

- A journal article "Roohi, R., Webb, A. W., Jones, S. A. and Daly E. 2019. Modified Surface Energy Balance Algorithms for Rainfed Agriculture (SEBARA) for the estimation of evapotranspiration for contrasting landuse in SE Australia was developed and is ready for publication.

Appendices

Appendix 1. Surface albedo range for various land surfaces (a) & Surface albedo of different land surfaces over time (b).

(1a)

Surface	**Albedo**	**Source**
Court roof	0.1 – 0.15	*Kotak, Y., Gul, M.S., Muneer, T. and Ivanova, S.M., 2015, April. Investigating the impact of ground albedo on the performance of pv systems. In Proceedings of CIBSE Technical Symposium, London, UK (pp. 16-17).*
Coloured paint	0.15 – 0.35	
Trees	0.15 – 0.18	
Asphalt	0.05 _ 0.2	
Concrete	0.25 – 0.7	
Grass	0.25 – 0.3	
Ice	0.3 – 0.5	
Fresh Asphalt	0.04	*Ritter, M.E., 2003. The physical environment: An introduction to physical geography. Date visited July 25, p.2008.*
Worn Asphalt	0.12	
Bare Soil	0.17	
Conifer forest (Summer)	0.08	
Green grass	0.25	
New concrete	0.55	
Fresh Snow	0.80 - 0.90	
Conifer forest	0.10 – 0.15	*Horiguchi, Ikuo (ed.)m 1992. Agricultural Meteorology, Buneidou, Tokyo, Japan.*
Decideous forest	0.15 – 0.20	
Green Grass or pasture	0.15 – 0.25	
Corn field	0.15 – 0.22	
Black soil	.08 – 0.14	
Clay	0.16 – 0.23	
White-Yellow sand	0.34 – 0.40	
Grey-white sand	0.18 – 0.23	
Water	0.025 – 0.348	
Fresh Snow	0.80 - 0.85	
Old snow and ice	0.30 -0.70	

(1b)

Vegetation Type	February	May	August	November
Evergreen needleleaf (1)	0.096	0.090	0.096	0.092
Evergreen broadleaf in Amazonas (2)	0.122	0.119	0.124	0.127
Evergreen broadleaf excluding Amazonas (2)	0.121	0.116	0.118	0.127
Decidious needleleaf (3)	0.103	0.095	0.110	0.103
Decidious broadleaf (4)	0.116	0.137	0.140	0.119
Mixed forest(5)	0.096	0.101	0.119	0.100
Open shrubland 35S–45N (7)	0.220	0.219	0.209	0.217
Open shrubland Australia (7)	0.177	0.177	0.177	0.173
Open shrubland other (7)	0.137	0.126	0.141	0.129
Woody savanna (8)	0.106	0.117	0.110	0.112
Savanna (9)	0.140	0.141	0.142	0.133
Grassland (10)	0.185	0.165	0.165	0.178
Cropland Eurasia (12)	0.144	0.140	0.150	0.139
Cropland East Asia, India (12)	0.162	0.161	0.151	0.156
Cropland other (12)	0.162	0.151	0.165	0.159
Barren in Sahara and the Arabian desert (16)	0.365	0.356	0.353	0.365
Barren in Asia (16)	0.222	0.229	0.232	0.228
Barren excluding Sahara, the Arabian desert and Asia (16)	0.208	0.215	0.175	0.215

[a]Data in the analysis are based on high quality and snow free quality assurance flag.

Source: Myhre, G., Kvalevåg, M.M. and Schaaf, C.B., 2005. Radiative forcing due to anthropogenic vegetation change based on MODIS surface albedo data. Geophysical Research Letters, 32(21).

Appendix 2. The emissivity of different surfaces.

Surface	Emissivity	Source
Cropland	0.982	*Qin, Z.H., Li, W.J., Xu, B., Chen, Z.X. and Liu, J., 2004. The estimation of land surface emissivity for Landsat TM6. Remote Sens. Land Resour, 3, pp.28-32.*
Forest	0.988	
Bare soil	0.972	
Buildings	0.970	
Shrubland	0.986	*Humes, K.S., Kustas, W.P., Moran, M.S., Nichols, W.D. and Weltz, M.A., 1994. Variability of emissivity and surface temperature over a sparsely vegetated surface. Water Resources Research, 30(5), pp.1299-1310.*
Green space	0.985	
Asphalt and concrete	0.968	*WANG, X.X., Hu, D.S. and ZHU, Q.J., 2011. Comparison of infrared radiative temperatures from two scales on different land surfaces. Journal of Guangxi Normal University (Natural Science Edition), (2), p.02.*
Grassland	0.982	*Labed, J. and Stoll, M.P., 1991. Spatial variability of land surface emissivity in the thermal infrared band: spectral signature and effective surface temperature. Remote Sensing of Environment, 38(1), pp.1-17.*
Waterbody	0.995	*Zheng, G.Q., Lu, M., Zhang, T., Liu, G. and Ke, C., 2010. The impact of the difference of land surface emissivity on the land surface temperature retrieval in Jinan City. Journal of Shandong Jianzhu University, 25(5), pp.519-523.*
Tree vegetation	0.965	*Formetta, G., Bancheri, M., David, O. and Rigon, R., 2016. Performance of site-specific parameterizations of longwave radiation. Hydrology and Earth System Sciences, 20(11), pp.4641-4654.*

Appendix 3. Attributes of Landsat 5 TM image (a) and Landsat 8 OLI-TIRS (b) used for model development.

(3a - Landsat 5 TM image)

Dataset Attribute	Attribute Value
Landsat Scene Identifier	LT50940862011276ASA00
Spacecraft Identifier	5
Sensor Mode	BUMPER
Station Identifier	ASA
Day Night	DAY
WRS Path	094
WRS Row	086
Date Acquired	2011/10/03
Start Time	2011:276:00:03:45.88375
Stop Time	2011:276:00:04:12.49650
Sensor Anomalies	N
Acquisition Quality	9
Quality Band 1	9
Quality Band 2	9
Quality Band 3	9
Quality Band 4	9
Quality Band 5	9
Quality Band 6	9
Quality Band 7	9
Cloud Cover	7.16%
Cloud Cover Quadrant Upper Left	0.57%
Cloud Cover Quadrant Upper Right	25.24%
Cloud Cover Quadrant Lower Left	0.2%
Cloud Cover Quadrant Lower Right	2.62%
Sun Elevation	44.42735839
Sun Azimuth	50.46881769
Scene Center Latitude	-37.48990 (37°29'23"S)
Scene Center Longitude	142.86944 (142°52'09"E)
Browse Exists	Y
Scene Mode	U
Data Category	NOMINAL
Map Projection L0Ra	NA

Data Type L0Rp	TMR_L0RP
Data Type Level 1	L1T
Elevation Source	GLS2000
Output Format	GeoTIFF
Ephemeris Type	DEFINITIVE
Corner Upper Left Latitude Product	-36.52696 (36°31'37"S)
Corner Upper Left Longitude Product	141.46691 (141°28'00"E)
Corner Upper Right Latitude Product	-36.48451 (36°29'04"S)
Corner Upper Right Longitude Product	144.21587 (144°12'57"E)
Corner Lower Left Latitude Product	-38.49277 (38°29'33"S)
Corner Lower Left Longitude Product	141.47932 (141°28'45"E)
Corner Lower Right Latitude Product	-38.44721 (38°26'49"S)
Corner Lower Right Longitude Product	144.30115 (144°18'04"E)
Reflective Lines	7271
Reflective Samples	8211
Thermal Lines	7271
Thermal Samples	8211
Ground Control Points Model	36
Geometric RMSE Model	4.685
Geometric RMSE Model X	3.427
Geometric RMSE Model Y	3.195
Ground Control Points Verify	940
Geometric RMSE Verify	.288
Map Projection L1	UTM
Datum	WGS84
Ellipsoid	WGS84
UTM Zone	54
Grid Cell Size Reflective	30
Grid Cell Size Thermal	30
Orientation	NORTH_UP
Resampling Option	CUBIC_CONVOLUTION

FGDC Metadata

(3b - Landsat 8 OLI-TIRS)

```
GROUP = L1_METADATA_FILE
  GROUP = METADATA_FILE_INFO
    ORIGIN = "Image courtesy of the U.S. Geological Survey"
    REQUEST_ID = "0701607086151_00003"
    LANDSAT_SCENE_ID = "LC80940862016178LGN00"
    FILE_DATE = 2016-07-09T15:47:36Z
    STATION_ID = "LGN"
    PROCESSING_SOFTWARE_VERSION = "LPGS_2.6.2"
  END_GROUP = METADATA_FILE_INFO
  GROUP = PRODUCT_METADATA
    DATA_TYPE = "L1T"
    ELEVATION_SOURCE = "GLS2000"
    OUTPUT_FORMAT = "GEOTIFF"
    SPACECRAFT_ID = "LANDSAT_8"
    SENSOR_ID = "OLI_TIRS"
    WRS_PATH = 94
    WRS_ROW = 86
    NADIR_OFFNADIR = "NADIR"
    TARGET_WRS_PATH = 94
    TARGET_WRS_ROW = 86
    DATE_ACQUIRED = 2016-06-26
    SCENE_CENTER_TIME = "00:15:37.0172650Z"
    CORNER_UL_LAT_PRODUCT = -36.41602
    CORNER_UL_LON_PRODUCT = 141.47963
    CORNER_UR_LAT_PRODUCT = -36.37619
    CORNER_UR_LON_PRODUCT = 144.12114
    CORNER_LL_LAT_PRODUCT = -38.56571
    CORNER_LL_LON_PRODUCT = 141.49358
    CORNER_LR_LAT_PRODUCT = -38.52267
    CORNER_LR_LON_PRODUCT = 144.21171
    CORNER_UL_PROJECTION_X_PRODUCT = 543000.000
    CORNER_UL_PROJECTION_Y_PRODUCT = -4030200.000
    CORNER_UR_PROJECTION_X_PRODUCT = 780000.000
    CORNER_UR_PROJECTION_Y_PRODUCT = -4030200.000
    CORNER_LL_PROJECTION_X_PRODUCT = 543000.000
    CORNER_LL_PROJECTION_Y_PRODUCT = -4268700.000
    CORNER_LR_PROJECTION_X_PRODUCT = 780000.000
    CORNER_LR_PROJECTION_Y_PRODUCT = -4268700.000
    PANCHROMATIC_LINES = 15901
    PANCHROMATIC_SAMPLES = 15801
    REFLECTIVE_LINES = 7951
    REFLECTIVE_SAMPLES = 7901
```

THERMAL_LINES = 7951
THERMAL_SAMPLES = 7901
FILE_NAME_BAND_1 = "LC80940862016178LGN00_B1.TIF"
FILE_NAME_BAND_2 = "LC80940862016178LGN00_B2.TIF"
FILE_NAME_BAND_3 = "LC80940862016178LGN00_B3.TIF"
FILE_NAME_BAND_4 = "LC80940862016178LGN00_B4.TIF"
FILE_NAME_BAND_5 = "LC80940862016178LGN00_B5.TIF"
FILE_NAME_BAND_6 = "LC80940862016178LGN00_B6.TIF"
FILE_NAME_BAND_7 = "LC80940862016178LGN00_B7.TIF"
FILE_NAME_BAND_8 = "LC80940862016178LGN00_B8.TIF"
FILE_NAME_BAND_9 = "LC80940862016178LGN00_B9.TIF"
FILE_NAME_BAND_10 = "LC80940862016178LGN00_B10.TIF"
FILE_NAME_BAND_11 = "LC80940862016178LGN00_B11.TIF"
FILE_NAME_BAND_QUALITY =
"LC80940862016178LGN00_BQA.TIF"
METADATA_FILE_NAME = "LC80940862016178LGN00_MTL.txt"
BPF_NAME_OLI = "LO8BPF20160625233309_20160626001720.02"
BPF_NAME_TIRS = "LT8BPF20160620195437_20160707083823.01"
CPF_NAME = "L8CPF20160401_20160630.04"
RLUT_FILE_NAME = "L8RLUT20150303_20431231v11.h5"
END_GROUP = PRODUCT_METADATA
GROUP = IMAGE_ATTRIBUTES
CLOUD_COVER = 22.01
CLOUD_COVER_LAND = 22.01
IMAGE_QUALITY_OLI = 9
IMAGE_QUALITY_TIRS = 9
TIRS_SSM_MODEL = "FINAL"
TIRS_SSM_POSITION_STATUS = "ESTIMATED"
ROLL_ANGLE = -0.001
SUN_AZIMUTH = 33.41483480
SUN_ELEVATION = 21.29053046
EARTH_SUN_DISTANCE = 1.0165290
GROUND_CONTROL_POINTS_VERSION = 4
GROUND_CONTROL_POINTS_MODEL = 180
GEOMETRIC_RMSE_MODEL = 8.906
GEOMETRIC_RMSE_MODEL_Y = 6.961
GEOMETRIC_RMSE_MODEL_X = 5.556
GROUND_CONTROL_POINTS_VERIFY = 74
GEOMETRIC_RMSE_VERIFY = 16.315
END_GROUP = IMAGE_ATTRIBUTES
GROUP = MIN_MAX_RADIANCE
RADIANCE_MAXIMUM_BAND_1 = 735.54596
RADIANCE_MINIMUM_BAND_1 = -60.74163
RADIANCE_MAXIMUM_BAND_2 = 753.20807
RADIANCE_MINIMUM_BAND_2 = -62.20016

```
    RADIANCE_MAXIMUM_BAND_3 = 694.07477
    RADIANCE_MINIMUM_BAND_3 = -57.31692
    RADIANCE_MAXIMUM_BAND_4 = 585.28296
    RADIANCE_MINIMUM_BAND_4 = -48.33286
    RADIANCE_MAXIMUM_BAND_5 = 358.16397
    RADIANCE_MINIMUM_BAND_5 = -29.57730
    RADIANCE_MAXIMUM_BAND_6 = 89.07212
    RADIANCE_MINIMUM_BAND_6 = -7.35561
    RADIANCE_MAXIMUM_BAND_7 = 30.02207
    RADIANCE_MINIMUM_BAND_7 = -2.47923
    RADIANCE_MAXIMUM_BAND_8 = 662.37921
    RADIANCE_MINIMUM_BAND_8 = -54.69949
    RADIANCE_MAXIMUM_BAND_9 = 139.97861
    RADIANCE_MINIMUM_BAND_9 = -11.55948
    RADIANCE_MAXIMUM_BAND_10 = 22.00180
    RADIANCE_MINIMUM_BAND_10 = 0.10033
    RADIANCE_MAXIMUM_BAND_11 = 22.00180
    RADIANCE_MINIMUM_BAND_11 = 0.10033
  END_GROUP = MIN_MAX_RADIANCE
  GROUP = MIN_MAX_REFLECTANCE
    REFLECTANCE_MAXIMUM_BAND_1 = 1.210700
    REFLECTANCE_MINIMUM_BAND_1 = -0.099980
    REFLECTANCE_MAXIMUM_BAND_2 = 1.210700
    REFLECTANCE_MINIMUM_BAND_2 = -0.099980
    REFLECTANCE_MAXIMUM_BAND_3 = 1.210700
    REFLECTANCE_MINIMUM_BAND_3 = -0.099980
    REFLECTANCE_MAXIMUM_BAND_4 = 1.210700
    REFLECTANCE_MINIMUM_BAND_4 = -0.099980
    REFLECTANCE_MAXIMUM_BAND_5 = 1.210700
    REFLECTANCE_MINIMUM_BAND_5 = -0.099980
    REFLECTANCE_MAXIMUM_BAND_6 = 1.210700
    REFLECTANCE_MINIMUM_BAND_6 = -0.099980
    REFLECTANCE_MAXIMUM_BAND_7 = 1.210700
    REFLECTANCE_MINIMUM_BAND_7 = -0.099980
    REFLECTANCE_MAXIMUM_BAND_8 = 1.210700
    REFLECTANCE_MINIMUM_BAND_8 = -0.099980
    REFLECTANCE_MAXIMUM_BAND_9 = 1.210700
    REFLECTANCE_MINIMUM_BAND_9 = -0.099980
  END_GROUP = MIN_MAX_REFLECTANCE
  GROUP = MIN_MAX_PIXEL_VALUE
    QUANTIZE_CAL_MAX_BAND_1 = 65535
    QUANTIZE_CAL_MIN_BAND_1 = 1
    QUANTIZE_CAL_MAX_BAND_2 = 65535
    QUANTIZE_CAL_MIN_BAND_2 = 1
    QUANTIZE_CAL_MAX_BAND_3 = 65535
```

QUANTIZE_CAL_MIN_BAND_3 = 1
QUANTIZE_CAL_MAX_BAND_4 = 65535
QUANTIZE_CAL_MIN_BAND_4 = 1
QUANTIZE_CAL_MAX_BAND_5 = 65535
QUANTIZE_CAL_MIN_BAND_5 = 1
QUANTIZE_CAL_MAX_BAND_6 = 65535
QUANTIZE_CAL_MIN_BAND_6 = 1
QUANTIZE_CAL_MAX_BAND_7 = 65535
QUANTIZE_CAL_MIN_BAND_7 = 1
QUANTIZE_CAL_MAX_BAND_8 = 65535
QUANTIZE_CAL_MIN_BAND_8 = 1
QUANTIZE_CAL_MAX_BAND_9 = 65535
QUANTIZE_CAL_MIN_BAND_9 = 1
QUANTIZE_CAL_MAX_BAND_10 = 65535
QUANTIZE_CAL_MIN_BAND_10 = 1
QUANTIZE_CAL_MAX_BAND_11 = 65535
QUANTIZE_CAL_MIN_BAND_11 = 1
END_GROUP = MIN_MAX_PIXEL_VALUE
GROUP = RADIOMETRIC_RESCALING
RADIANCE_MULT_BAND_1 = 1.2151E-02
RADIANCE_MULT_BAND_2 = 1.2443E-02
RADIANCE_MULT_BAND_3 = 1.1466E-02
RADIANCE_MULT_BAND_4 = 9.6685E-03
RADIANCE_MULT_BAND_5 = 5.9166E-03
RADIANCE_MULT_BAND_6 = 1.4714E-03
RADIANCE_MULT_BAND_7 = 4.9595E-04
RADIANCE_MULT_BAND_8 = 1.0942E-02
RADIANCE_MULT_BAND_9 = 2.3124E-03
RADIANCE_MULT_BAND_10 = 3.3420E-04
RADIANCE_MULT_BAND_11 = 3.3420E-04
RADIANCE_ADD_BAND_1 = -60.75378
RADIANCE_ADD_BAND_2 = -62.21261
RADIANCE_ADD_BAND_3 = -57.32839
RADIANCE_ADD_BAND_4 = -48.34253
RADIANCE_ADD_BAND_5 = -29.58321
RADIANCE_ADD_BAND_6 = -7.35708
RADIANCE_ADD_BAND_7 = -2.47973
RADIANCE_ADD_BAND_8 = -54.71043
RADIANCE_ADD_BAND_9 = -11.56179
RADIANCE_ADD_BAND_10 = 0.10000
RADIANCE_ADD_BAND_11 = 0.10000
REFLECTANCE_MULT_BAND_1 = 2.0000E-05
REFLECTANCE_MULT_BAND_2 = 2.0000E-05
REFLECTANCE_MULT_BAND_3 = 2.0000E-05
REFLECTANCE_MULT_BAND_4 = 2.0000E-05

```
    REFLECTANCE_MULT_BAND_5 = 2.0000E-05
    REFLECTANCE_MULT_BAND_6 = 2.0000E-05
    REFLECTANCE_MULT_BAND_7 = 2.0000E-05
    REFLECTANCE_MULT_BAND_8 = 2.0000E-05
    REFLECTANCE_MULT_BAND_9 = 2.0000E-05
    REFLECTANCE_ADD_BAND_1 = -0.100000
    REFLECTANCE_ADD_BAND_2 = -0.100000
    REFLECTANCE_ADD_BAND_3 = -0.100000
    REFLECTANCE_ADD_BAND_4 = -0.100000
    REFLECTANCE_ADD_BAND_5 = -0.100000
    REFLECTANCE_ADD_BAND_6 = -0.100000
    REFLECTANCE_ADD_BAND_7 = -0.100000
    REFLECTANCE_ADD_BAND_8 = -0.100000
    REFLECTANCE_ADD_BAND_9 = -0.100000
  END_GROUP = RADIOMETRIC_RESCALING
  GROUP = TIRS_THERMAL_CONSTANTS
    K1_CONSTANT_BAND_10 = 774.8853
    K1_CONSTANT_BAND_11 = 480.8883
    K2_CONSTANT_BAND_10 = 1321.0789
    K2_CONSTANT_BAND_11 = 1201.1442
  END_GROUP = TIRS_THERMAL_CONSTANTS
  GROUP = PROJECTION_PARAMETERS
    MAP_PROJECTION = "UTM"
    DATUM = "WGS84"
    ELLIPSOID = "WGS84"
    UTM_ZONE = 54
    GRID_CELL_SIZE_PANCHROMATIC = 15.00
    GRID_CELL_SIZE_REFLECTIVE = 30.00
    GRID_CELL_SIZE_THERMAL = 30.00
    ORIENTATION = "NORTH_UP"
    RESAMPLING_OPTION = "CUBIC_CONVOLUTION"
  END_GROUP = PROJECTION_PARAMETERS
END_GROUP = L1_METADATA_FILE
END
```

Appendix 4. Model 001- Image subset

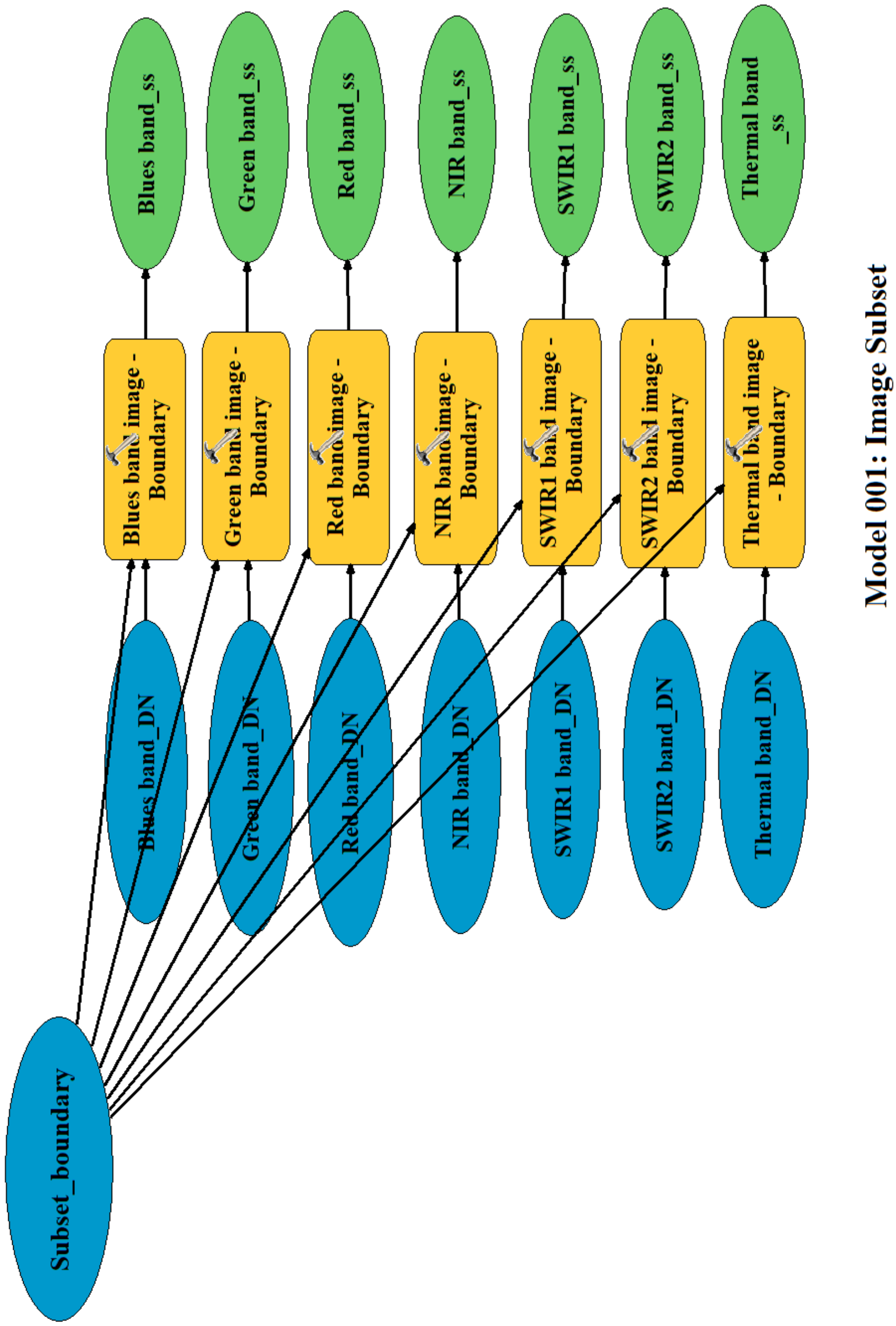

Appendix 5. Model 002 - DN to the radiance of Landsat 5 TM

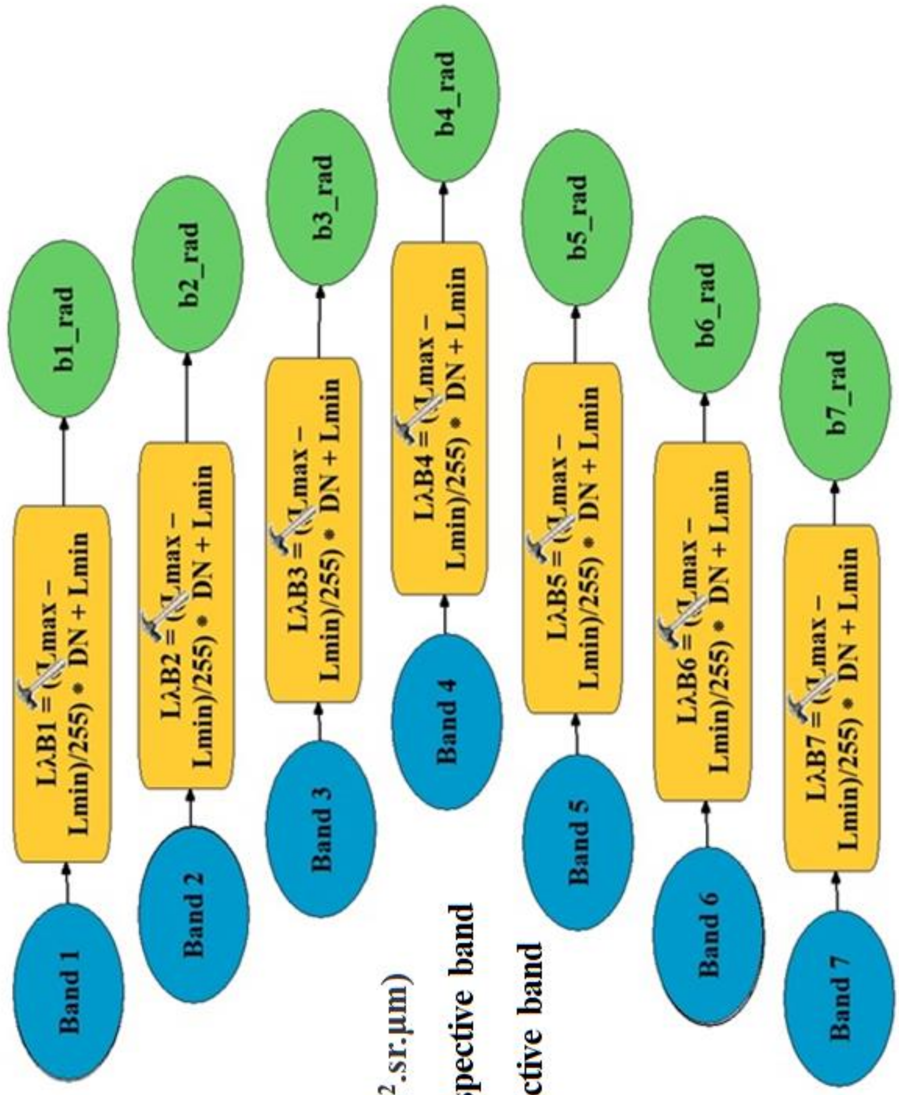

$$L_\lambda = \left[\frac{L_{max} - L_{min}}{255}\right] * DN + L_{min}$$

Where

L_λ TOA spectral radiance ($W/m^2.sr.\mu m$)

L_{max} Maximum L value for the respective band

L_{min} Minimum value for the respective band

DN Digital numbers

Appendix 6. Model 003 - DN to the radiance of Landsat 8 OLI

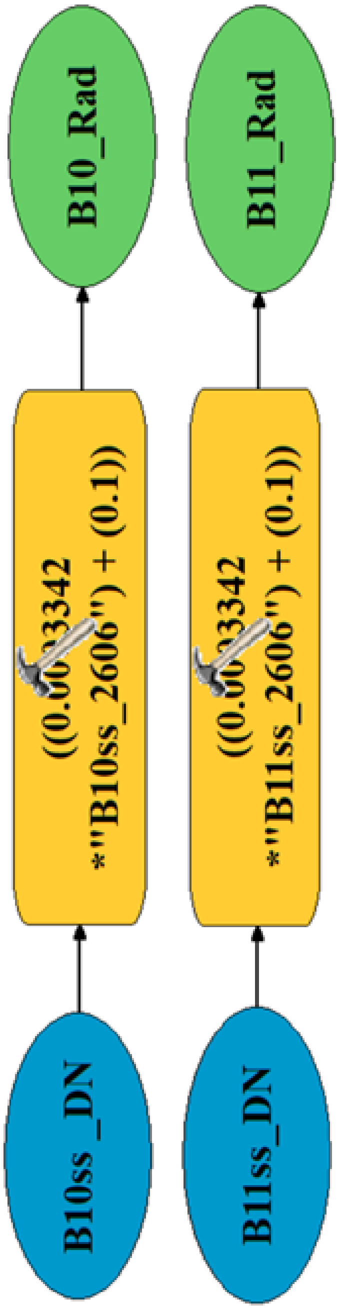

ToA Radiance Landsat 8 LOI

Lλ = ML * Qcal + AL

where:

Lλ = TOA spectral reflectance (Watts/(m^2 * srad * µm))

ML = Band-specific multiplicative rescaling factor from the metadata (RADIANCE_MULT_BAND_x, where x is the band number)

AL = Band-specific additive rescaling factor from the metadata (RADIANCE_ADD_BAND_x, where x is the band number)

Qcal = Quantized and calibrated standard product pixel values (DN)

Appendix 7. Julian Day Calendar

Day	Jan	Feb	Mar	Apr	May	Jun	Jul	Aug	Sep	Oct	Nov	Dec	Day
1	001	032	060	091	121	152	182	213	244	274	305	335	1
2	002	033	061	092	122	153	183	214	245	275	306	336	2
3	003	034	062	093	123	154	184	215	246	276	307	337	3
4	004	035	063	094	124	155	185	216	247	277	308	338	4
5	005	036	064	095	125	156	186	217	248	278	309	339	5
6	006	037	065	096	126	157	187	218	249	279	310	340	6
7	007	038	066	097	127	158	188	219	250	280	311	341	7
8	008	039	067	098	128	159	189	220	251	281	312	342	8
9	009	040	068	099	129	160	190	221	252	282	313	343	9
10	010	041	069	100	130	161	191	222	253	283	314	344	10
11	011	042	070	101	131	162	192	223	254	284	315	345	11
12	012	043	071	102	132	163	193	224	255	285	316	346	12
13	013	044	072	103	133	164	194	225	256	286	317	347	13
14	014	045	073	104	134	165	195	226	257	287	318	348	14
15	015	046	074	105	135	166	196	227	258	288	319	349	15
16	016	047	075	106	136	167	197	228	259	289	320	350	16
17	017	048	076	107	137	168	198	229	260	290	321	351	17
18	018	049	077	108	138	169	199	230	261	291	322	352	18
19	019	050	078	109	139	170	200	231	262	292	323	353	19
20	020	051	079	110	140	171	201	232	263	293	324	354	20
21	021	052	080	111	141	172	202	233	264	294	325	355	21
22	022	053	081	112	142	173	203	234	265	295	326	356	22
23	023	054	082	113	143	174	204	235	266	296	327	357	23
24	024	055	083	114	144	175	205	236	267	297	328	358	24
25	025	056	084	115	145	176	206	237	268	298	329	359	25
26	026	057	085	116	146	177	207	238	269	299	330	360	26
27	027	058	086	117	147	178	208	239	270	300	331	361	27
28	028	059	087	118	148	179	209	240	271	301	332	362	28
29	029		088	119	149	180	210	241	272	302	333	363	29
30	030		089	120	150	181	211	242	273	303	334	364	30
31	031		090		151		212	243		304		365	31

Appendix 8. Model 004 - Radiance to the reflectance of Landsat 5 TM

$$\rho\lambda = \frac{(\pi * L_\lambda)}{(ESUN_\lambda)} * \cos(\theta_{SZ}) * dr)$$

Where

ρλ	Reflectance
π	Maximum L value for the respective band
L_λ	Spectral radiance for each band
$ESUN_\lambda$	Mean solar exo-atmospheric irradiance for each ban (W/m²/μm)
Cosθ	Cosine of the solar incidence angle from nadir Cosθ = Cos (Radians (90 – sun elevation angle))
d_r	Inverse squared relative earth-sun distance d_r =1+0.033*cos (DOY/365)*(2)*(π)

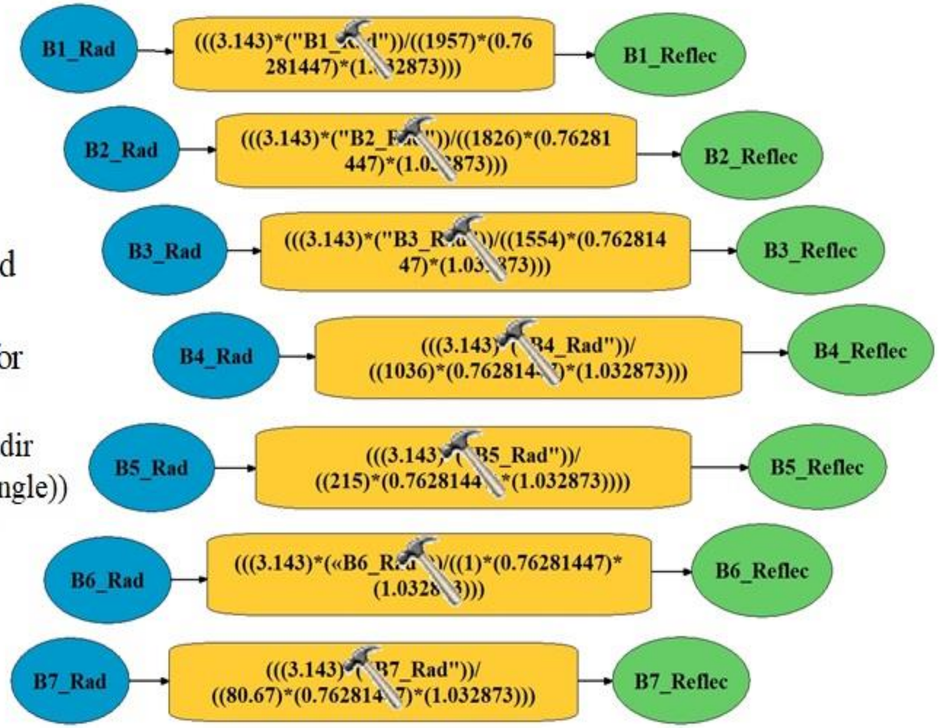

Appendix 9. Model 005 - Radiance to the reflectance of Landsat 8 OLI

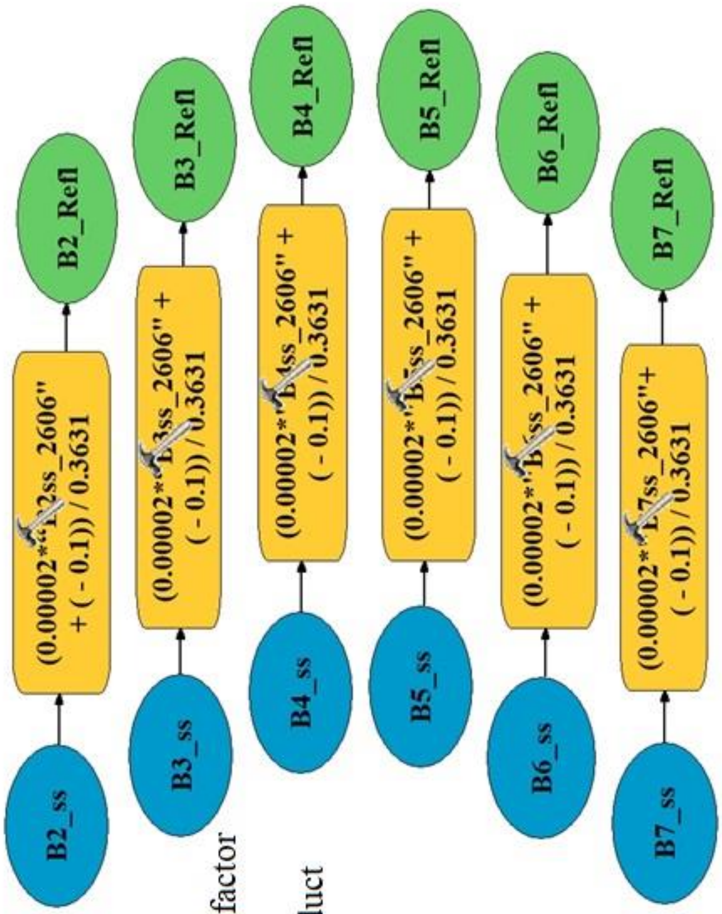

$$\rho\lambda' = M_\rho * Q_{cal} + A_\rho$$

Where

- $\rho\lambda'$ TOA planetary reflectance (without correction of solar angle.
- M_ρ Band-specific multiplicative rescaling factor
- A_ρ Band-specific additive rescaling factor
- Q_{cal} Quantized and calibrated standard product pixel values (DN

$$\rho\lambda = \frac{\rho\lambda'}{\cos(\theta_{SZ})} = \rho\lambda = \frac{\rho\lambda'}{\sin(\theta_{SE})}$$

Where

- $\rho\lambda$ Corrected TOA planetary reflectance
- θ_{SE} Local sun elevation angle.
- θ_{SZ} Local solar zenith angle; ($\theta_{SZ} = 90° - \theta_{SE}$)

https://landsat.usgs.gov/using-usgs-landsat-8-product

Appendix 10. The output of NASA online atmospheric calculator.

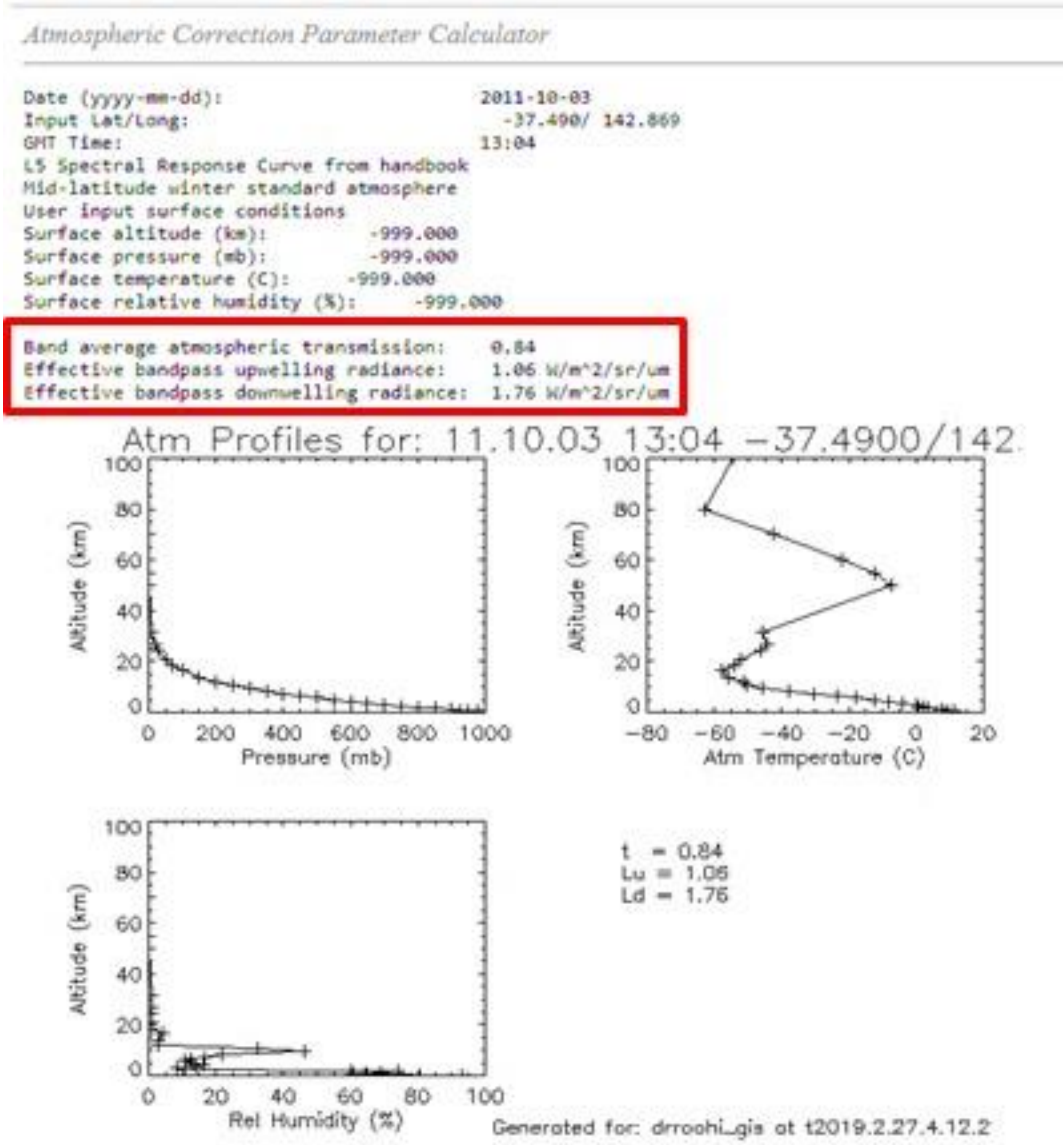

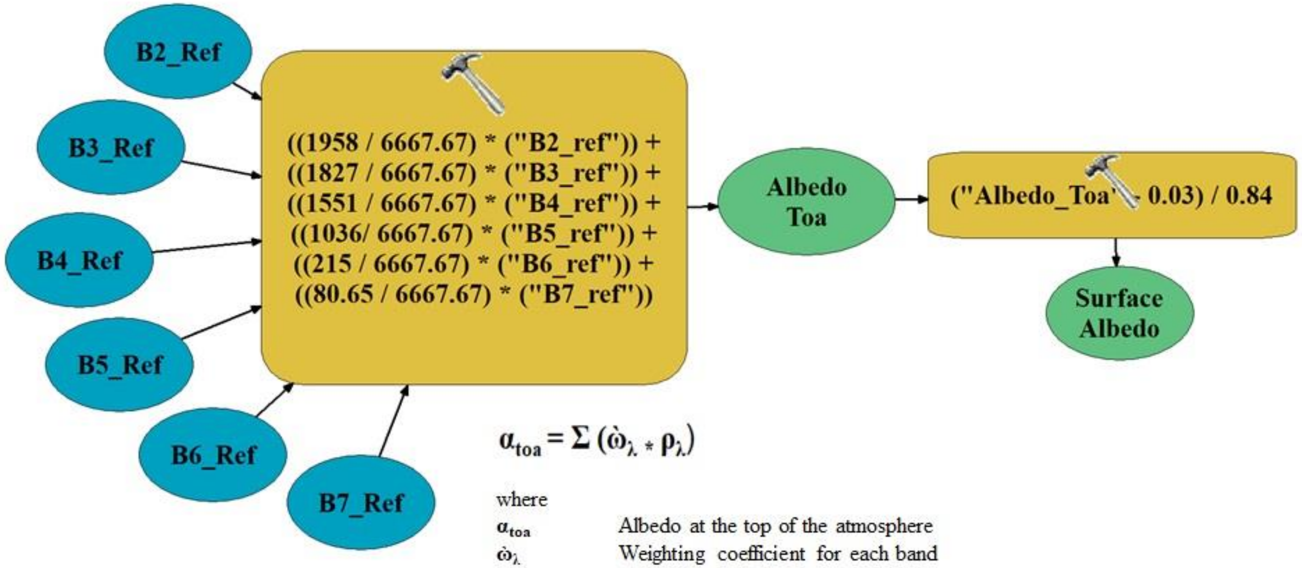

$$\alpha_{toa} = \Sigma\,(\dot{\omega}_{\lambda} * \rho_{\lambda})$$

where

α_{toa}	Albedo at the top of the atmosphere
$\dot{\omega}_{\lambda}$	Weighting coefficient for each band ($\dot{\omega}_{\lambda} = ESUN_{\lambda} / \Sigma\,(ESUN_{\lambda})$)
ρ_{λ}	Reflectivity of each band

$$\alpha = (\alpha_{toa} - \alpha_{path\_radiance}) / \tau_{s\omega}$$

Where

α_{toa}	Albedo at the top of the atmosphere
$\alpha_{path\_radiance}$	The values ranges between range between 0.025 and 0.04. An average value was used
$\tau_{s\omega}$	Using the information of the image pass day and weather station the value was computed using NASSA online atmospheric correction calculator (https://atmcorr.gsfc.nasa.gov/)

Appendix 12. Model 007 - Surface albedo using Landsat 8 OLI

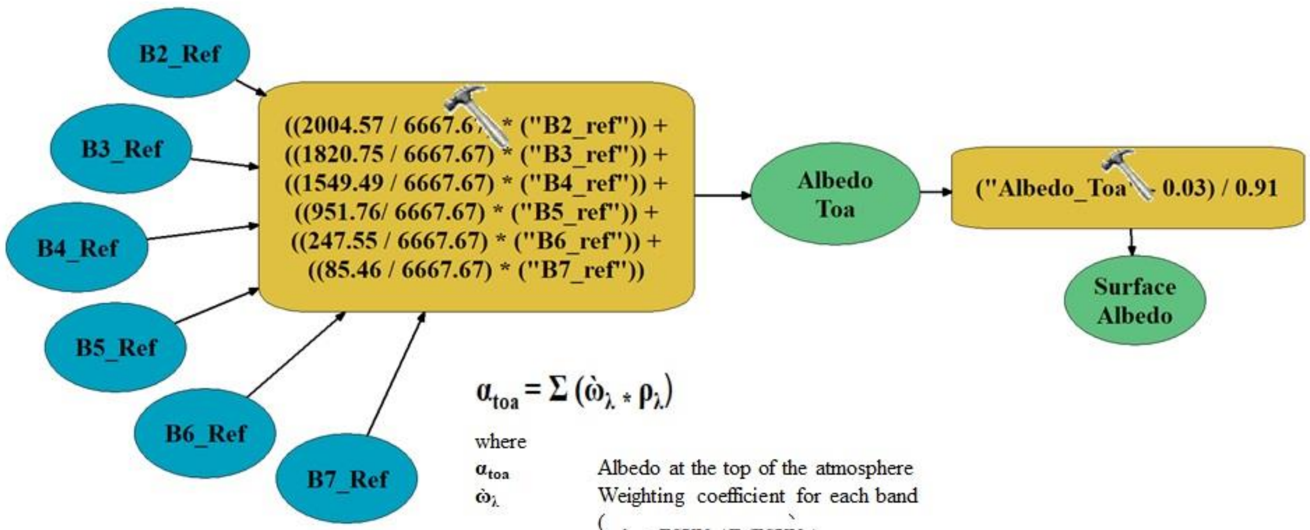

$$\alpha_{toa} = \Sigma\,(\dot{\omega}_{\lambda} * \rho_{\lambda})$$

where

α_{toa}	Albedo at the top of the atmosphere
$\dot{\omega}_{\lambda}$	Weighting coefficient for each band ($\dot{\omega}_{\lambda} = ESUN_{\lambda} / \Sigma\,(ESUN_{\lambda})$
ρ_{λ}	R

$$\alpha = (\alpha_{toa} - \alpha_{path\_radiance}) / \tau_{s\omega})$$

Where

α_{toa}	Albedo at the top of the atmosphere
$\alpha_{path\_radiance}$	The values ranges between range between 0.025 and 0.04. An average value was used
$\tau_{s\omega}$	Using the information of the image pass day and weather station the value was computed using NASSA online atmospheric correction calculator (https://atmcorr.gsfc.nasa.gov/)

Appendix 13. Model 008 – NDVI

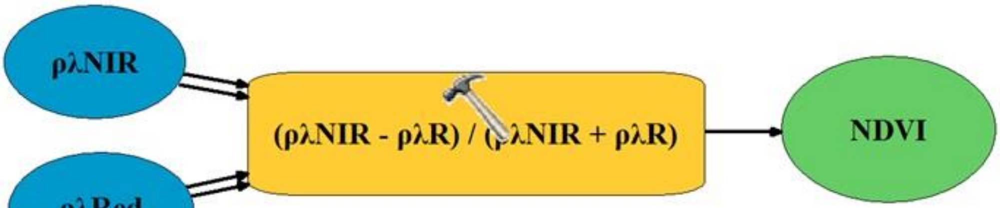

$$\mathrm{NDVI} = \frac{(\rho\lambda_{NIR} - \rho\lambda_{Red})}{(\rho\lambda_{NIR} + \rho\lambda_{Red})}$$

Where

$P\lambda_{NIR}$	Reflectance of the near-infrared band
$\rho\lambda_{Red}$	Reflectance of the red band

Appendix 14. Model 009 – SAVI

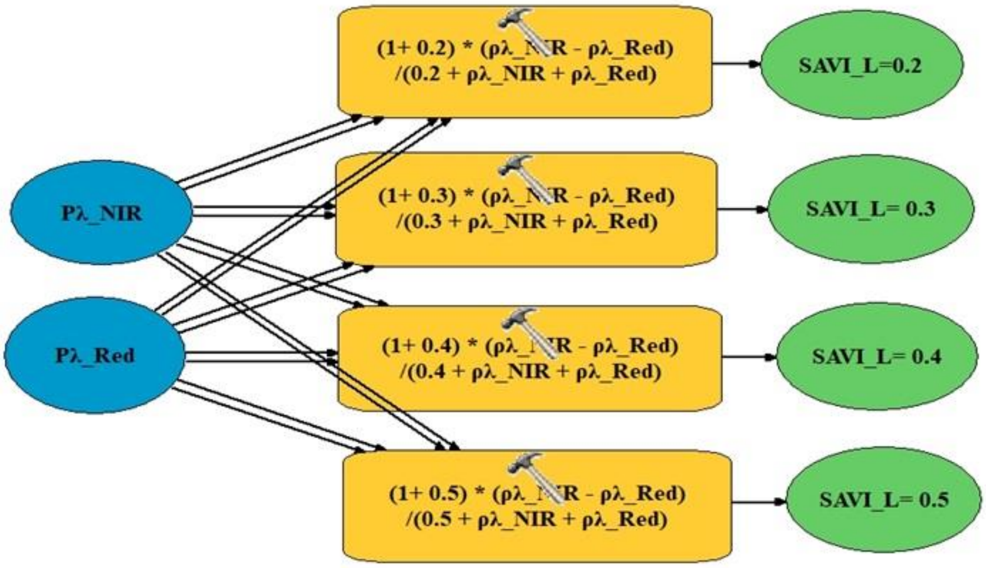

$$\mathrm{SAVI} = \frac{(1 + L) * (\rho\lambda_{NIR} - \rho\lambda_{Red})}{(L + \rho\lambda_{NIR} + \rho\lambda_{Red})}$$

Where

$P\lambda_{NIR}$	Reflectance of the near-infrared band
$\rho\lambda_{Red}$	Reflectance of the red band
L	Constant for SAVI

Appendix 15. Model 010 LAI

$$LAI = -\frac{\ln\left(\dfrac{0.7 - SAVI}{0.59}\right)}{0.91}$$

Where

SAVI is Soil Adjusted Vegetation Index using a value of 0.2 for L

Appendix 16. Model 011 - Surface emissivity

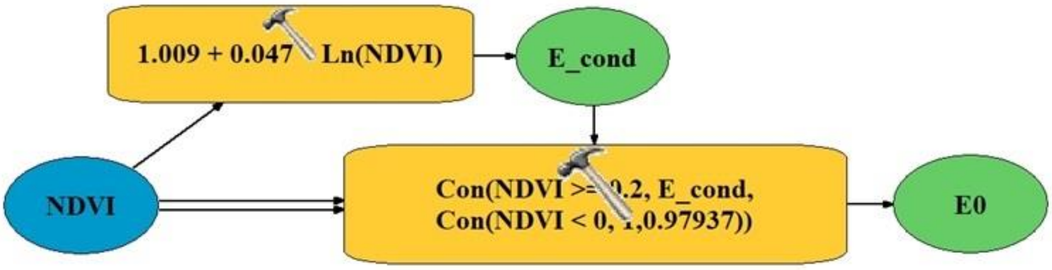

$$(\varepsilon_0) = 1.009 + 0.047 * \ln(NDVI)$$

NDVI less than 0.16 (positive) is normally bare soil, for this value of NDVI, emissivity can be set to 0.92 and for NDVI less than 0 (normally water surface), the emissivity has been set to 1 (Van de Griend and Owe, 1993 & Gieske and Timmerman, 2002)

Appendix 17. Model 012 – Land surface temperature using Landsat 5 TM data.

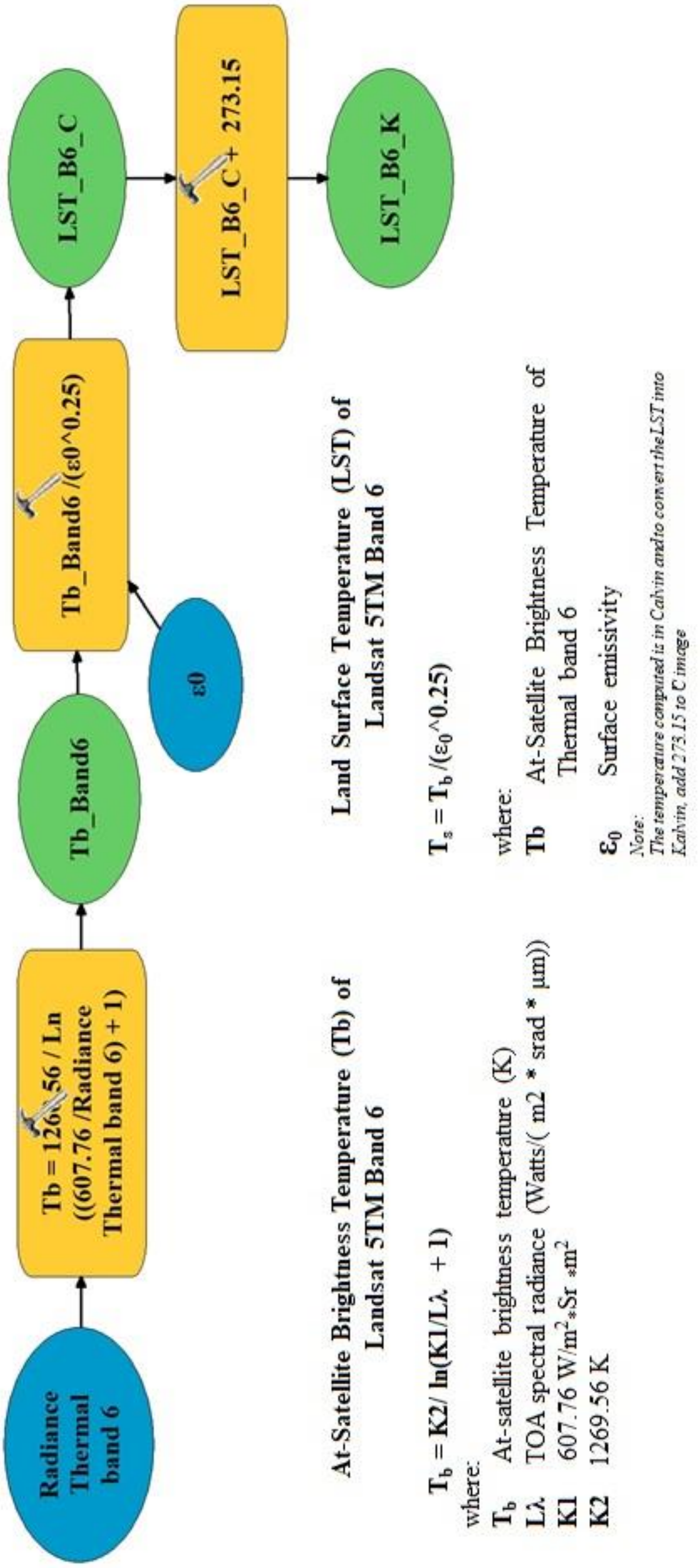

Appendix 18. Model 013 – Land surface temperature using Landsat 8 OLI data.

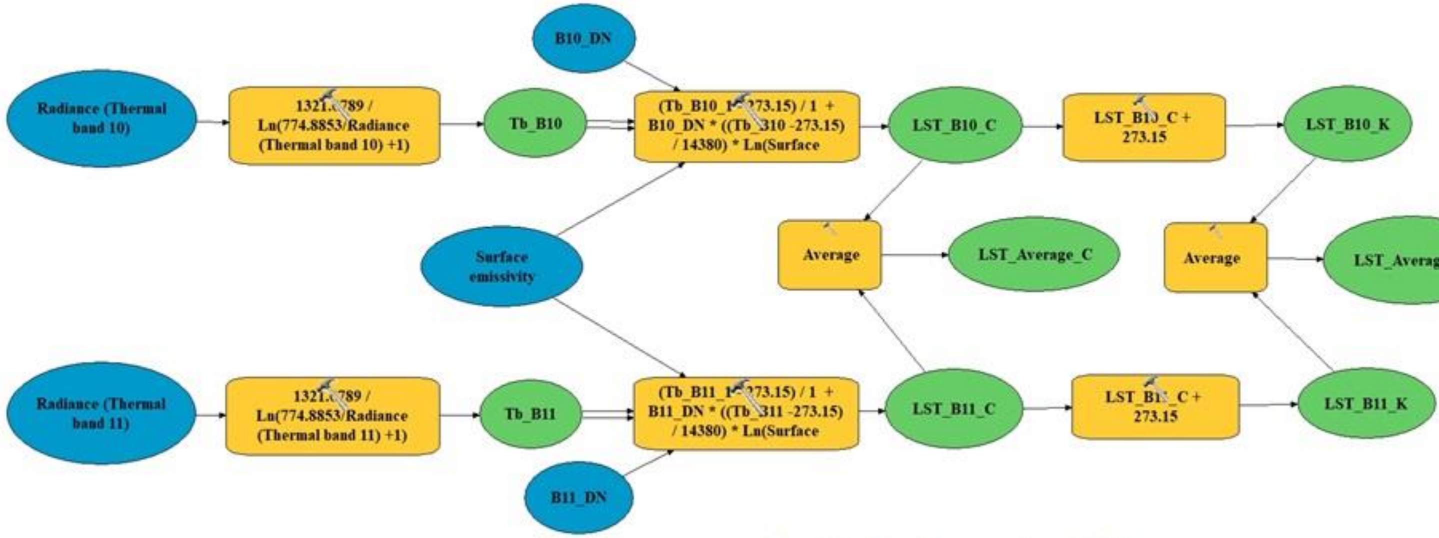

At-Satellite Brightness Temperature (Tb)

$$Tb = K2 / \ln(K1/L\lambda + 1)$$

where:

T_b At-satellite brightness temperature (K)

$L\lambda$ TOA spectral radiance (Watts/(m2 * srad * µm))

K1 Band-specific thermal conversion constant from the metadata (K1_CONSTANT_BAND_x, where x is the band number, 10 or 11)

K2 Band-specific thermal conversion constant from the metadata (K2_CONSTANT_BAND_x, where x is the band number, 10 or 11)

Land Surface Temperature (LST)

$$LST = Tb / 1 + Q_{cal} * (T_b / p) * \ln(\varepsilon_o)$$

where:

Tb At-Satellite Brightness Temperature

Qcal Quantized and calibrated standard product pixel values (DN) of Thermal band B10 or B11

P = h * c/s (1.438 * 10 ^-2 mK)

Where

h plank's constant (6.626 * 10^-34 Js)

s Boltzmann constant (1.38 * 10^-23 J/K)

c velocity of light (2.998 * 108 m/s)

Therefore, **p = 14380**

Note:

1. Normally, wavelength of emitted radiance of 11.5 µm (Thermal Band 10) is used, however, the average of both the thermal band can also be used.

2. The temperature computed is in Calvin and to convert the LST into Kalvin, add 273.15 to ℃ image

Appendix 19. Model 014 - Outgoing longwave radiation.

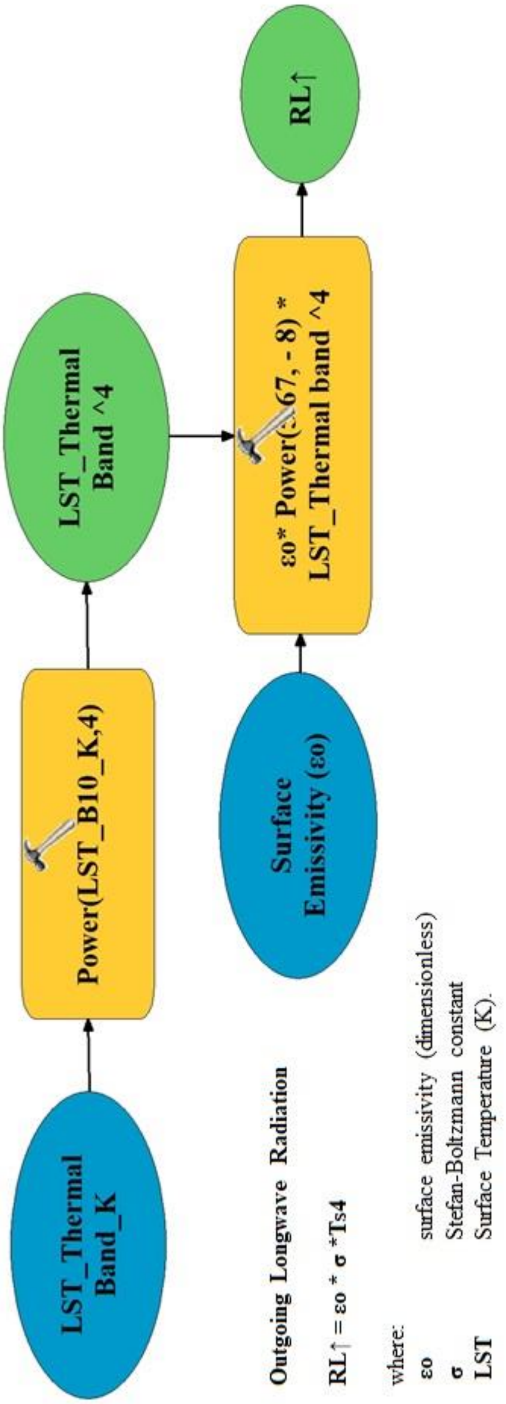

Appendix 20. Model 015 - Net available surface radiation.

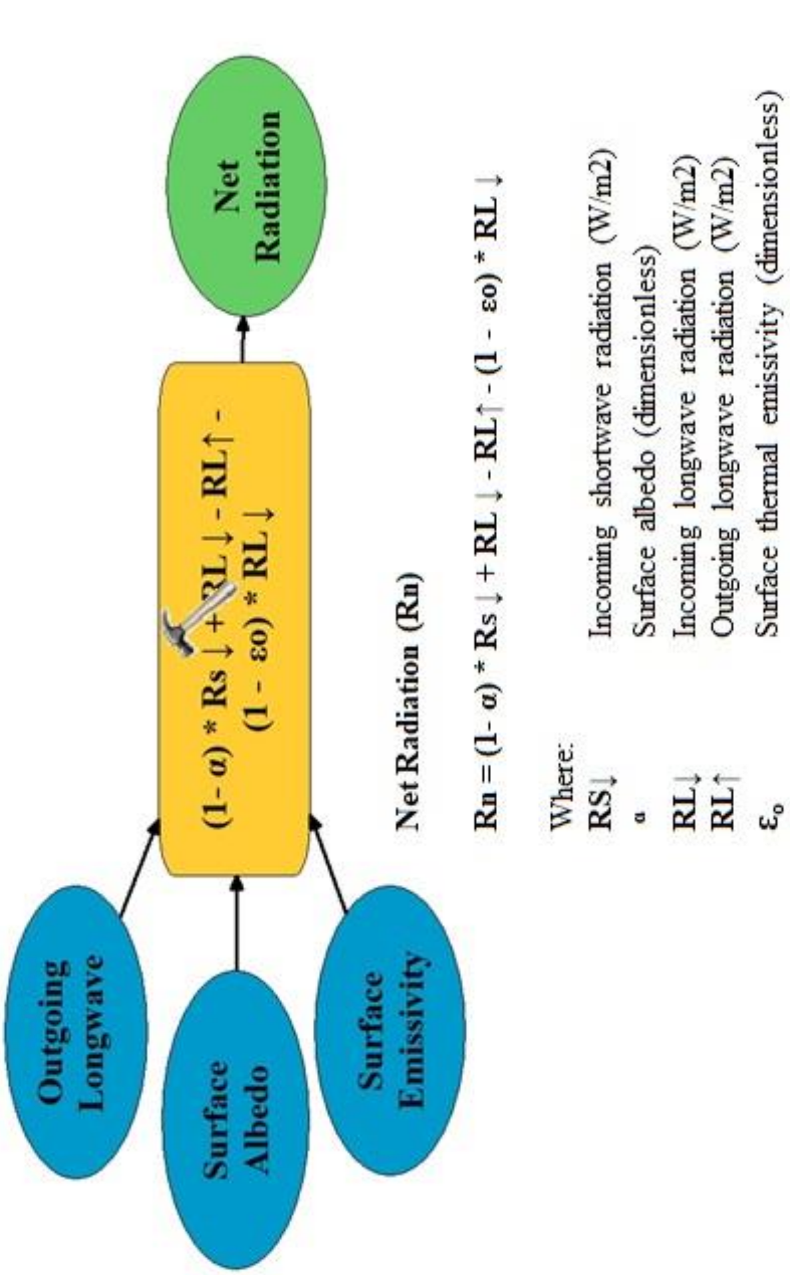

Appendix 21. Model 016 - G/R_n ratio and soil heat flux.

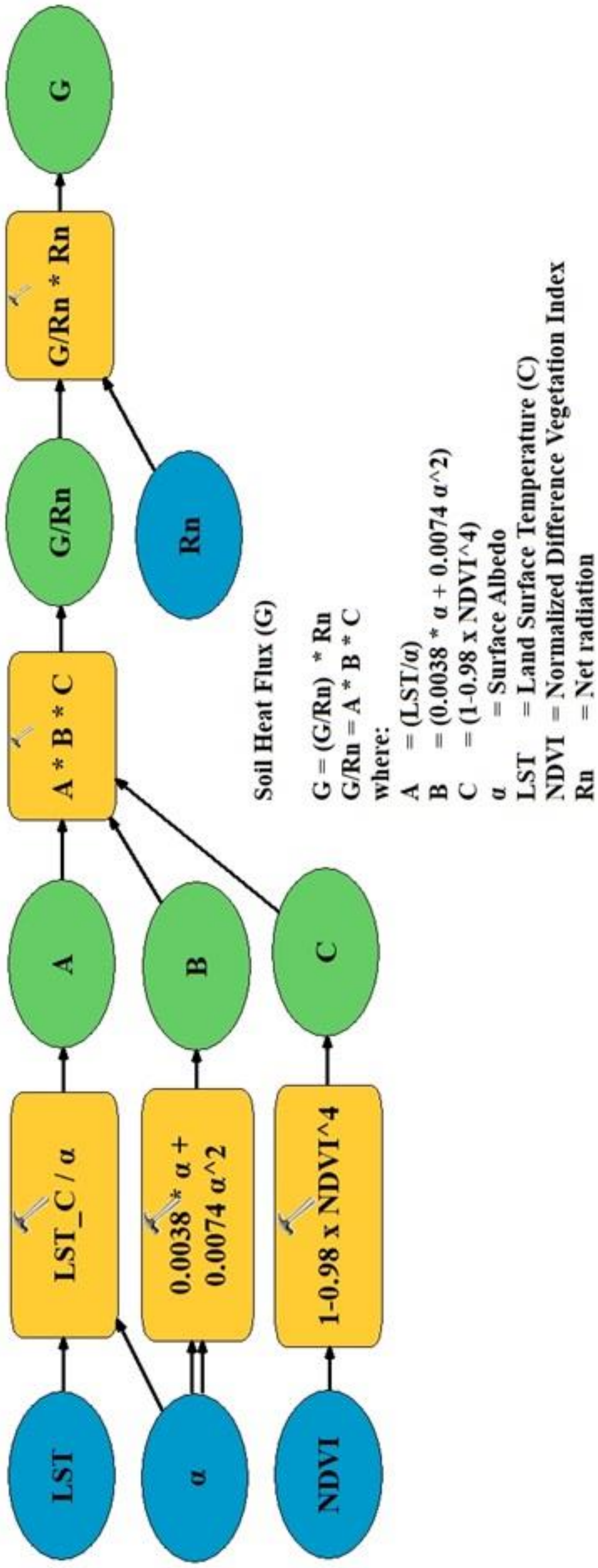

Appendix 22. Model 017 (a- NDVI/Surface albedo ratio; b- Zom_{pix}; and c- Aerodynamic resistance to heat transport (r_{ah}).

Model 017a - NDVI/Surface albedo ratio.

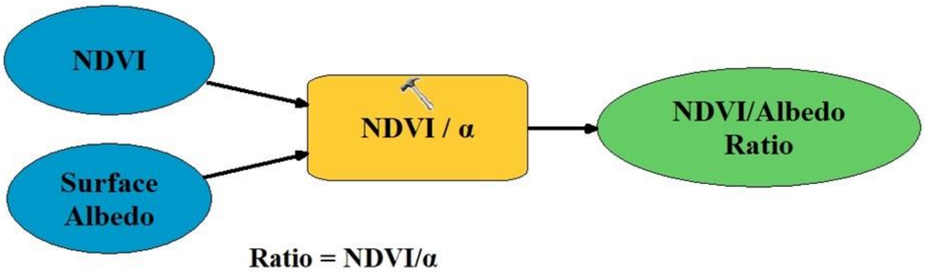

Ratio = NDVI/α

NDVI = Normalised Difference Vegetation Index
α = Surface Albedo

Model 017b - Zom_{pix}.

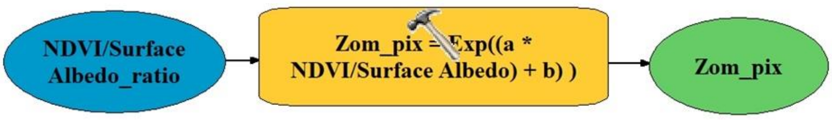

Zompix = exp [(a * NDVI/α) + b]

where:
a & b Correlation constants derived from a plot of ln (Zom) and NDVI/surface Albedo ratio fo0r a cluster of pixels representing specific landcover.

Model 017c - r_{ah} at each pixel.

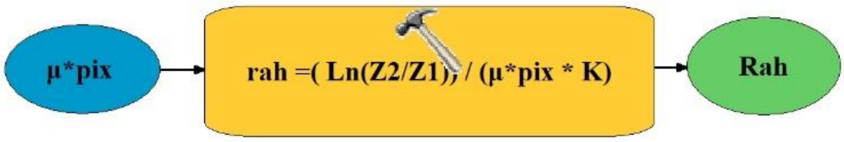

rah =(Ln(Z2/Z1)) / (μ*pix * K)

Where

rah **Aerodynamic resistance to heat transport**

μ*pix **Friction velocity (m/s) of each pixel which quantifies**

Z1 **Height just above the zero plane displacements for the surface or the crop canopy (d ~ 0.67 * vegetation height)**

Z2 **Some distance above the Z1 but less than the surface boundary layer Generally, 0.1m is used for Z1 and 2.0m for Z2**

μ*pix **Friction velocity (m/s) of each pixel which quantifies the turbulent velocity fluctuations in the air. To compute the friction velocity of each pixel, first, the μ* at the weather station and blending height were computed.**

K **von Karman's constant**

Appendix 23. Air density (Kg/m^3) at variable temperature (^{o}C).

Temperature ^{o}C	Air Density kg/m^3
-20	1.395
-10	1.342
0	1.293
10	1.247
20	1.204
30	1.165
40	1.128
50	1.093
60	1.060
70	1.029
80	1.000
90	0.972
100	0.946

Appendix 24. Water vapour and specific heat (C_p - kJ/(kg K)) at variable temperature (^oK).

Specific Heat (cp) kJ/(kg K)							
Temp	c_p	Temp	c_p	Temp	c_p	Temp	c_p
175	**1.850**	600	**2.015**	1250	**2.458**	2400	**2.962**
200	**1.851**	650	**2.047**	1300	**2.490**	2500	**2.987**
225	**1.852**	700	**2.080**	1350	**2.521**	2600	**3.011**
250	**1.855**	750	**2.113**	1400	**2.552**	2700	**3.033**
275	**1.859**	800	**2.147**	1500	**2.609**	2800	**3.053**
300	**1.864**	850	**2.182**	1600	**2.662**	2900	**3.072**
325	**1.871**	900	**2.217**	1700	**2.711**	3000	**3.090**
350	**1.880**	950	**2.252**	1800	**2.756**	3500	**3.163**
375	**1.890**	1000	**2.288**	1900	**2.798**	4000	**3.217**
400	**1.901**	1050	**2.323**	2000	**2.836**	4500	**3.258**
450	**1.926**	1100	**2.358**	2100	**2.872**	5000	**3.292**
500	**1.954**	1150	**2.392**	2200	**2.904**	5500	**3.322**
550	**1.984**	1200	**2.425**	2300	**2.934**	6000	**3.350**

Appendix 25. RefET calculator and data parameter types, units and identification numbers used by RefET to read weather data.

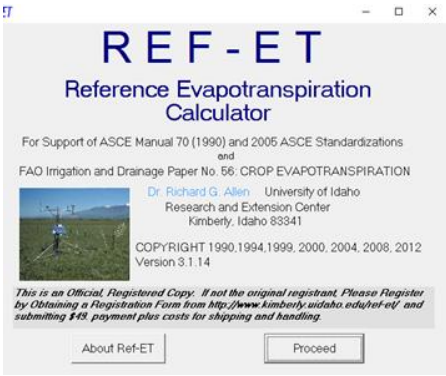

0	Ignore numeric entry (skip)
1	Ignore string (text) entry (skip)
2	Line Feed (go to next line)
3	Max Air Temp, C (daily or hourly)
4	Min Air Temp, C (daily or hourly)
5	Max Air Temp, F (daily or hourly)
6	Min Air Temp, F (daily or hourly)
7	Mean Air Temp, C
8	Mean Air Temp, F
9	Solar Radiation, W/m2
10	Solar Radiation, MJ/m2/d
11	Solar Radiation, cal/cm2/d
111	Solar Radiation, kJ/m2/d
12	Solar Radiation, mm/d
13	Solar Radiation, MJ/m2/hr
14	Solar Radiation, cal/cm2/hr
141	Solar Radiation, kJ/m2/hr
142	Solar Radiation, kJ/m2/min
15	Percent Sunshine, n/N, dec.
16	Percent Sunshine, n/N, %
17	Dewpoint Temperature, C
18	Dewpoint Temperature, F
19	Min. Rel. Humidity, % (daily or hrly)
20	Max. Rel. Humidity, % (daily or hrly)
191	Min. Rel. Humidity, dec. (daily or hrly)
201	Max. Rel. Humidity, dec. (daily or hrly)
21	Ave. Rel. Humidity, %
211	Ave. Rel. Humidity, decimal
22	Ave. Vapor Press., kPa
23	Ave. Vapor Press., mb
231	Ave. Absolute Humidity, kg/m3
232	Ave. Specific Humidity, kg/kg
24	Wet Bulb Temperature, C
25	Dry Bulb Temperature, C
26	Wet Bulb Temperature, F
27	Dry Bulb Temperature, F
28	Ave. Wind Speed, km/day
29	Ave. Wind Speed, m/s
30	Ave. Wind Speed, mi/day
31	Ave. Wind Speed, km/hr
32	Ave. Wind Speed, mi/hr
321	Ave. Wind Speed, knots
33	DayTime (7am-7pm) Wind, km/h
34	DayTime (7am-7pm) Wind, m/s
35	DayTime (7am-7pm) Wind, mi/h
36	Day/Night Wind Ratio, decimal
37	Pan Evaporation, mm/day
38	Pan Evaporation, in/day
39	Soil Heat Flux, MJ/m2/day
40	Soil Heat Flux, cal/cm2/day
41	Soil Heat Flux, W/m2
42	Soil Heat Flux, MJ/m2/hr
43	Soil Heat Flux, cal/cm2/hr
44	Net Radiation, MJ/m2/day
45	Net Radiation, cal/cm2/day
451	Net Radiation, kJ/m2/day
46	Net Radiation, W/m2
47	Net Radiation, mm/day
48	Net Radiation, MJ/m2/hr
49	Net Radiation, cal/cm2/hr
491	Net Radiation, kJ/m2/hr
492	Net Radiation, kJ/m2/min
50	Albedo (if measured), dec.
51	Albedo (if measured), %
52	Lysimeter, mm/day
53	Lysimeter, in/day
54	Lysimeter, mm/period
55	Lysimeter, in/period
56	Precipitation, mm
57	Precipitation, inches
58	Month, 1-12
59	Day, 1-31
60	Hour, 0-24
601	Hour, 0000-2400
602	Hour and Minute, 0000-2359
61	Minute, 0-59
62	Year, 00-99
63	Year, 0000-2099
64	Day of Year, 1-366
65	Measured Grass Ht, m
651	Measured Alfalfa Ht, m
652	Measured Grass Ht, cm
653	Measured Alfalfa Ht, cm
654	Measured Grass Ht, in.
655	Measured Alfalfa Ht, in.
66	Sunshine Hours (daily)
67	Atmospheric Pressure, kPa
68	Atmospheric Pressure, kPa

Appendix 26. Model 018 - Temperature difference between two heights Z_1 and Z_2, (dT) and air temperature (T_a).

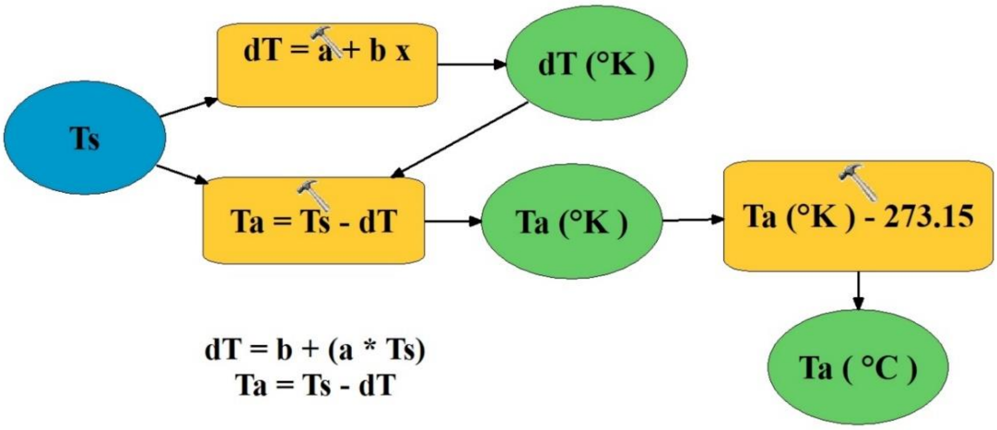

Appendix 27. Model 019 - Sensible Heat Flux (H).

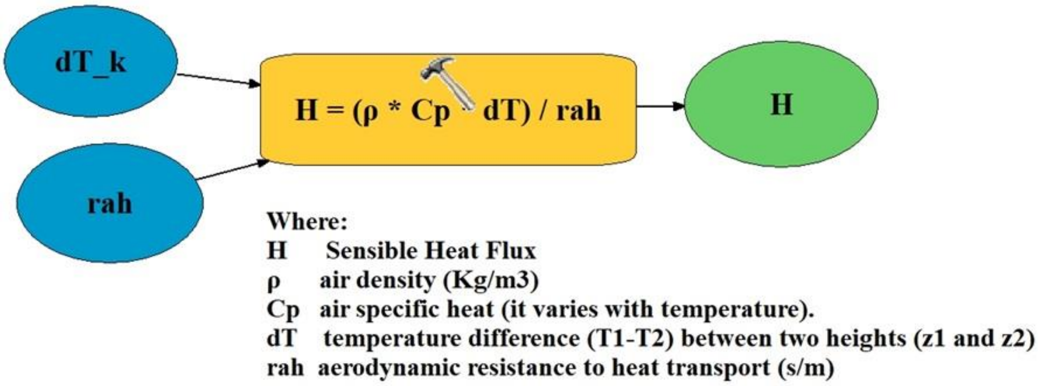

Appendix 28. Model 020 - Monin-Obukhov Length.

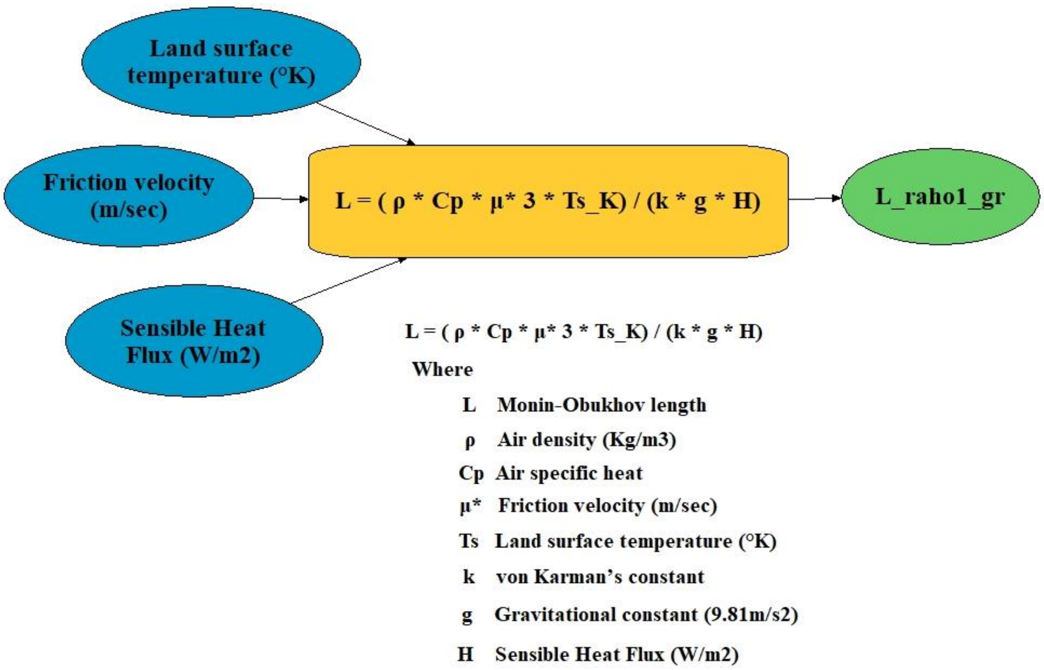

Appendix 29. Model 021 - Stability correction under unstable (29a) or stable (29b) conditions.

(29a) - Stability correction under unstable conditions (L < 0).

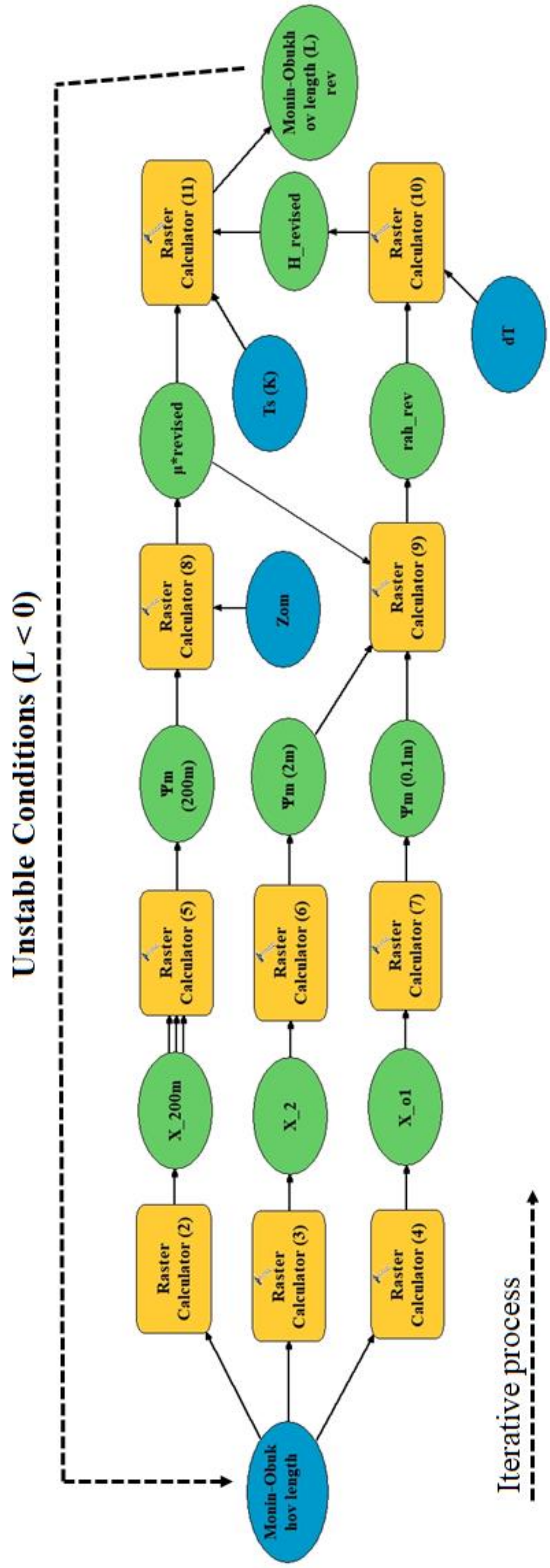

Unstable conditions (L<0)

$$\Psi_{m\,(200m)} = 2\ln\left[\frac{1 + x_{(200m)}}{2}\right] + \ln\left[\frac{1 + x_{(200m)}{}^2}{2}\right] - 2\ \mathrm{ARCTAN}\ [x_{(200m)}] + 0.5\pi$$

$$\Psi_{h\,(2m)} = 2\ln\left[\frac{1 + x_{(2m)}{}^2}{2}\right]$$

$$\Psi_{h\,(0.1m)} = 2\ln\left[\frac{1 + x_{(0.1m)}{}^2}{2}\right]$$

Where:

$$X_{(200m)} = 2\ln\left[\frac{1 - 16\frac{200}{L}}{2}\right]^{0.25}$$

$$X_{(2m)} = 2\ln\left[\frac{1 - 16\frac{2}{L}}{2}\right]^{0.25}$$

$$X_{(0.1m)} = 2\ln\left[\frac{1 - 16\frac{0.1}{L}}{2}\right]^{0.25}$$

$\Psi_{m(200m)}$	Stability correction for momentum transport at 200 meters
Ψ_h	Heat transport between two layers Z1 (0.1m) and Z2 (2m)

$$r_{ah\_revised} = \frac{\mathrm{Ln}\ [Z_2/Z_1] - \Psi_{h\,(Z2)} + \Psi_{h\,(Z1)}}{\mu_{*\_revised} \cdot k}$$

Where:

$r_{ah\_revised}$	Revised aerodynamic resistance to heat transport
Z_2	2.0 m
Z_1	0.1 m
$\Psi_{h\,(Z2)}$ & $\Psi_{h\,(Z1)}$	Stability correction for heat transport at 2m and 0.1 m
$\mu_{*revised}$	Revised friction velocity
K	von Karman's constant (0.41)

$$\mu^{*}_{revised} = \frac{\mu_{200} * k}{\ln\left(\frac{200}{Zom}\right) \Psi_{m\,(200m)}}$$

Where:

μ_{200}	Wind speed at 200m (m/s)
k	von Karman's constant (0.41)
Zom	Roughness length for each pixel (m)
$\Psi_{m\,(200m)}$	Stability correction

(29b) - Stability correction under stable conditions (L > 0).

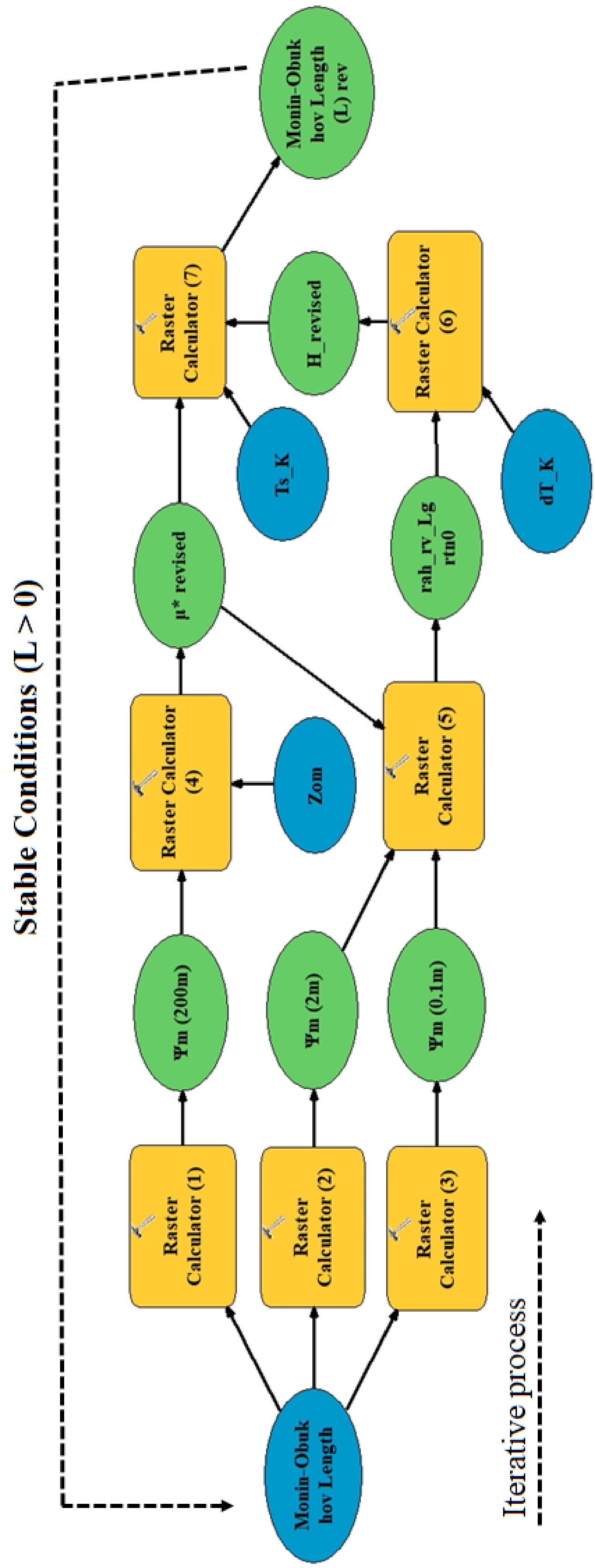

$$\Psi_{m\,(200m)} = \left[-5\ \frac{200}{L}\right]$$

$$\Psi_{h\,(2m)} = \left[-5\ \frac{2}{L}\right]$$

$$\Psi_{h\,(0.1m)} = \left[-5\ \frac{0.1}{L}\right]$$

$$\mu_{*revised} = \frac{\mu_{200} * k}{Ln\left(\frac{200}{Zom}\right) - \Psi_{m\,(200m)}}$$

Where:

μ_{200}	Wind speed at 200m (m/s)
K	von Karman's constant (0.41)
Zom	Roughness length for each pixel (m)
$\Psi_{m\,(200m)}$	Stability correction

$$r_{ah\_revised} = \frac{Ln\,[Z_2/Z_1] - \Psi_{h\,(Z2)} + \Psi_{h\,(Z1)}}{\mu_{*\_revised} * k}$$

Where:

$r_{ah\_revised}$	Revised aerodynamic resistance to heat transport
Z_2	2.0 m
Z_1	0.1 m
$\Psi_{h\,(Z2)}$ & $\Psi_{h\,(Z1)}$	Stability correction for heat transport at 2m and 0.1 m
$\mu_{*revised}$	Revised friction velocity
K	von Karman's constant (0.41)

Appendix 30. Model 022 - ET_{inst}, ET_rf and daily ET

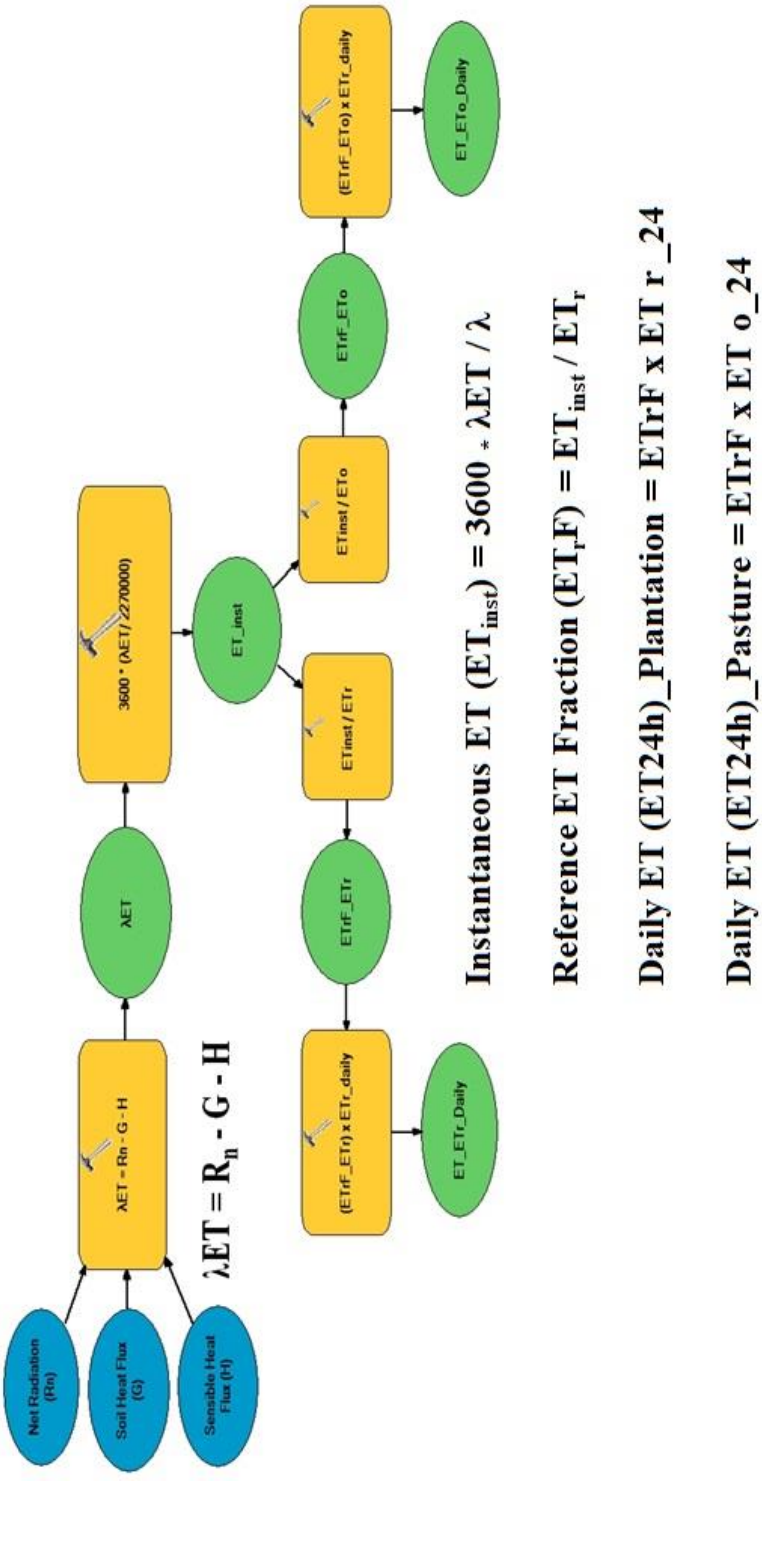

Appendix 31. Correlation between vegetation indices.

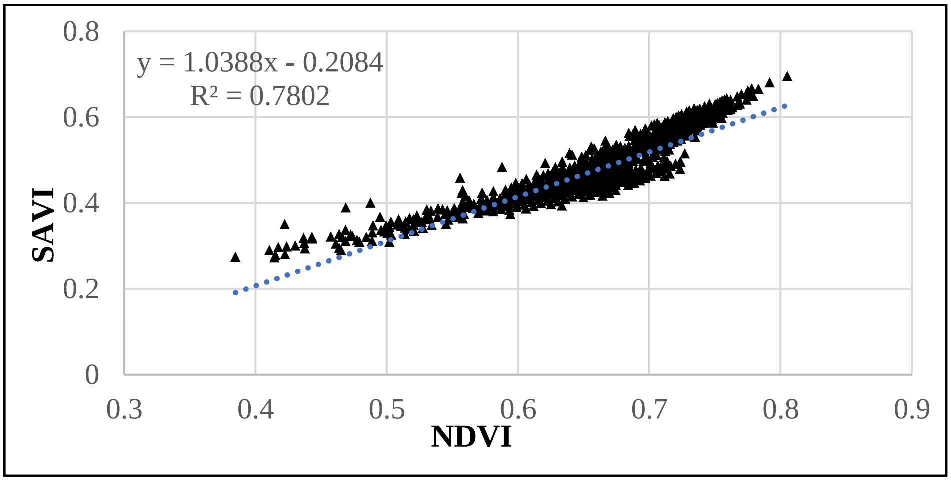

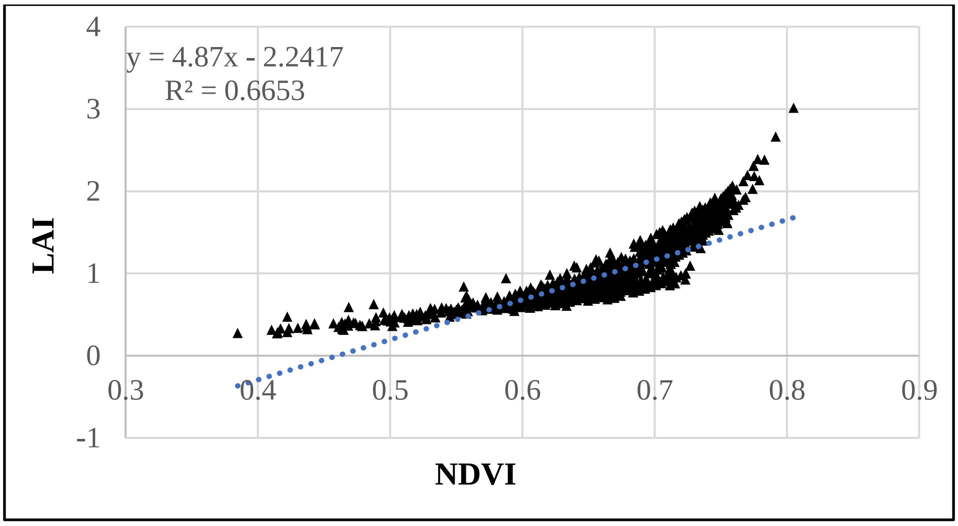

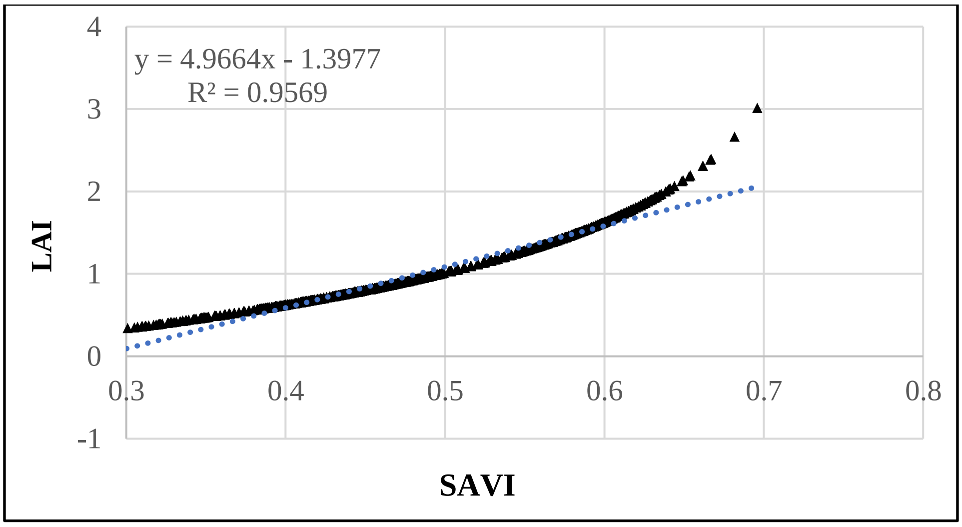

Appendix 32. Correlation of R_n with R_{L_net} and $R_L\uparrow$.

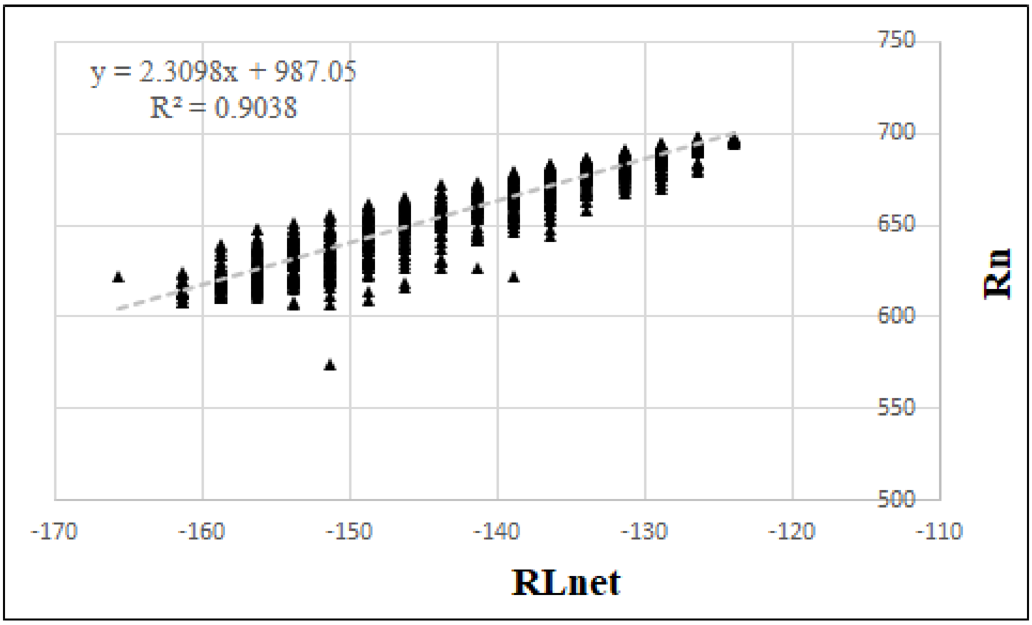

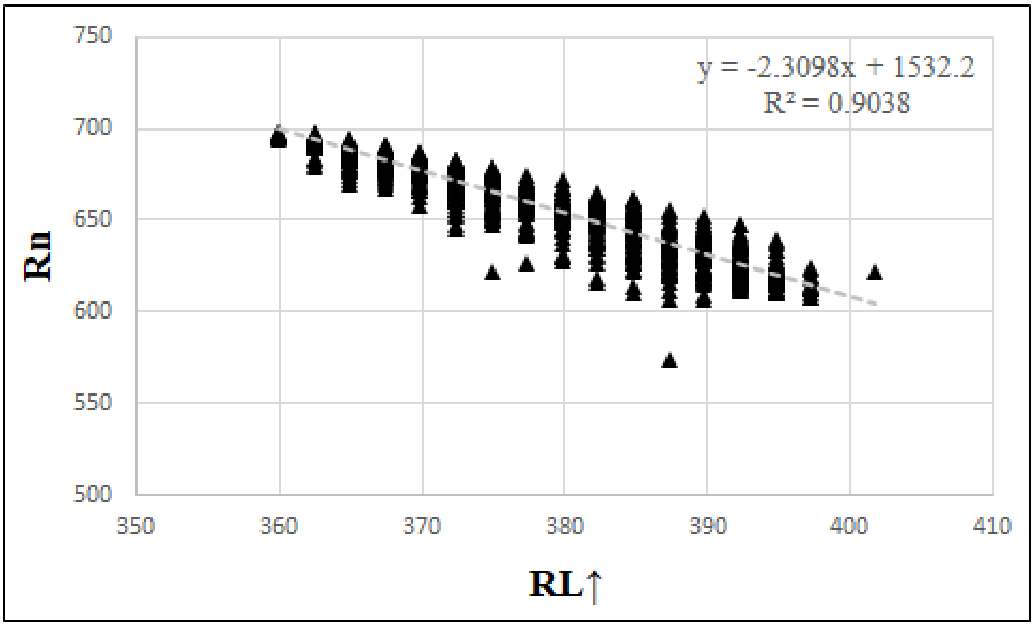

Appendix 33. Correlation of R_n with radiation balance components.

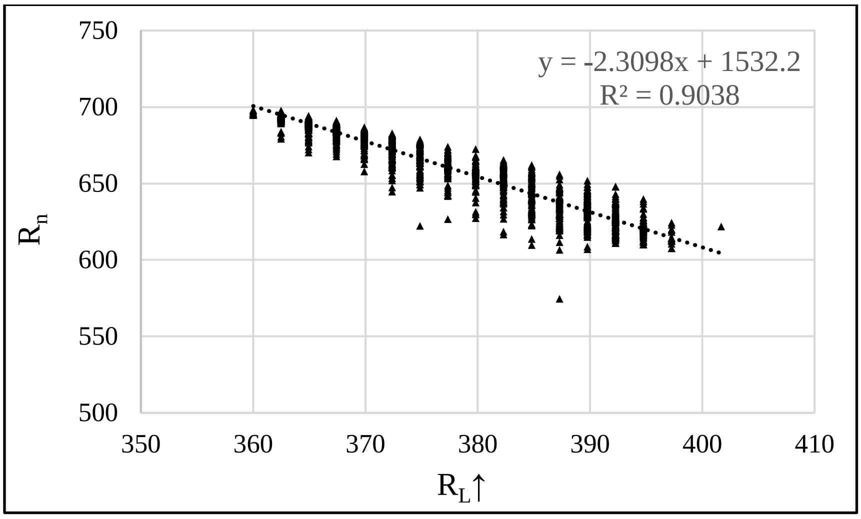

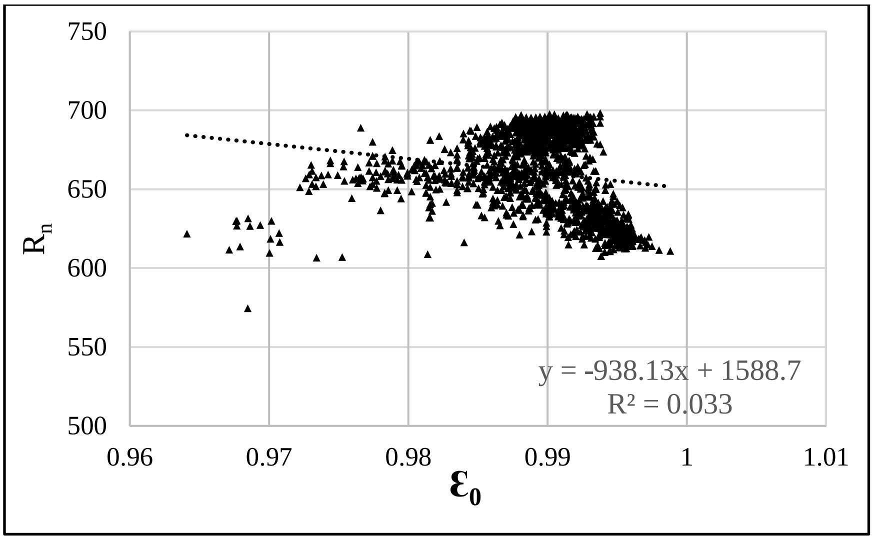

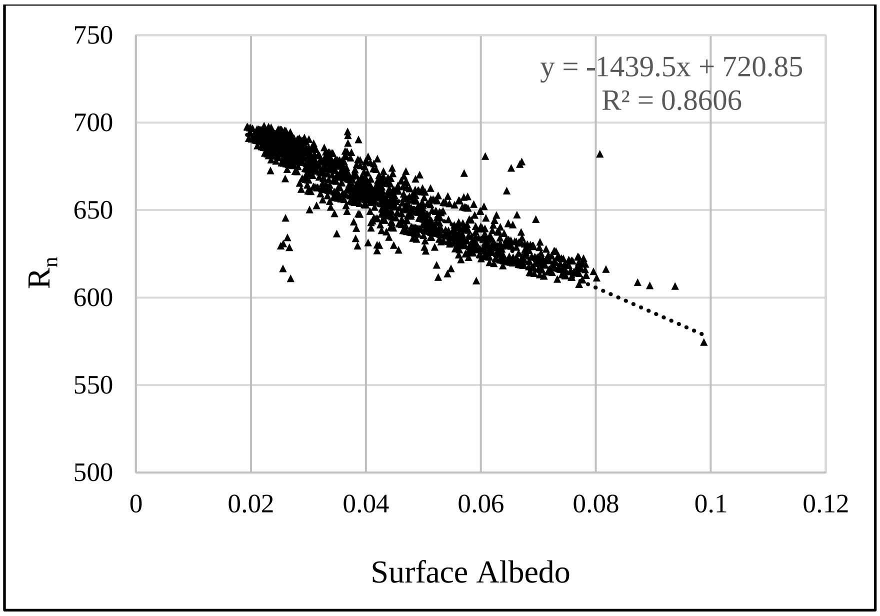

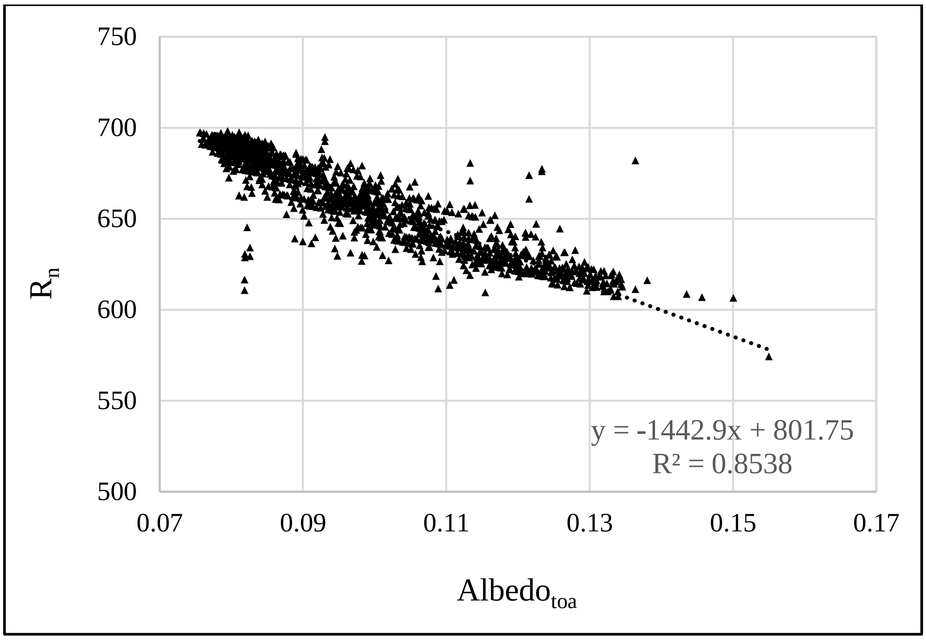
750
700
650
600
550
500
R_n
0.07
0.09
0.11
0.13
0.15
0.17
$Albedo_{toa}$
y = -1442.9x + 801.75
R² = 0.8538

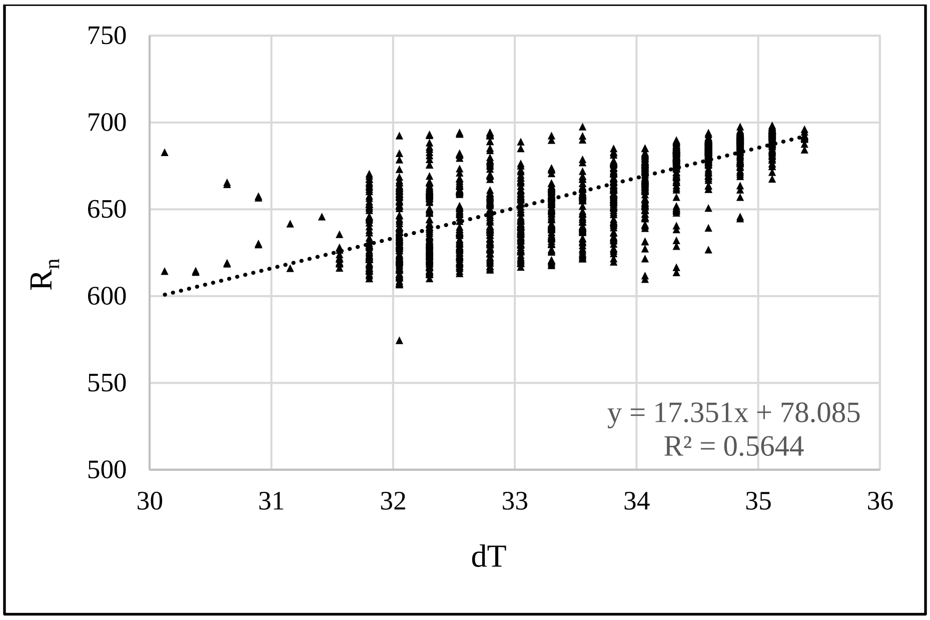
750
700
650
600
550
500
R_n
30
31
32
33
34
35
36
dT
y = 17.351x + 78.085
R² = 0.5644

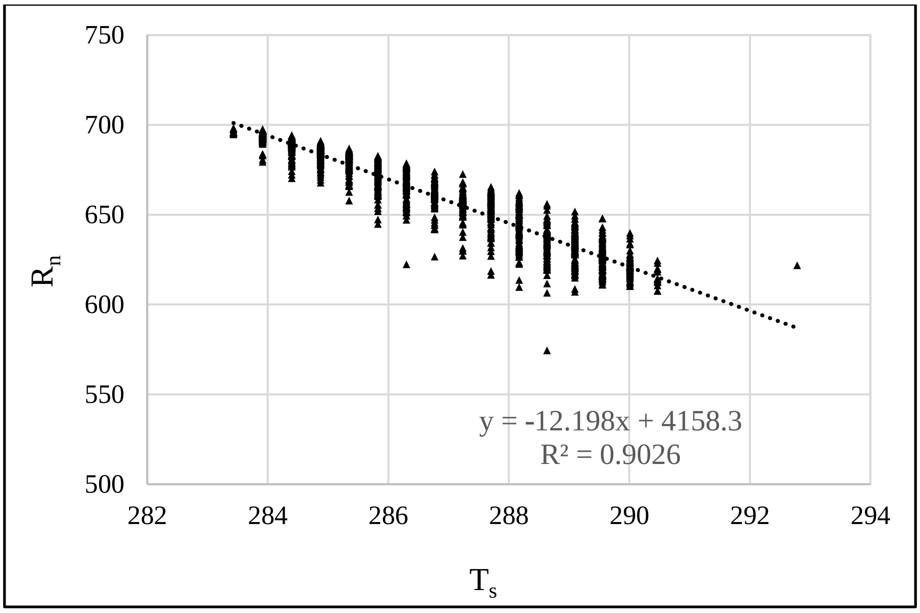
750
700
650
600
550
500
R_n
282
284
286
288
290
292
294
T_s
y = -12.198x + 4158.3
R² = 0.9026

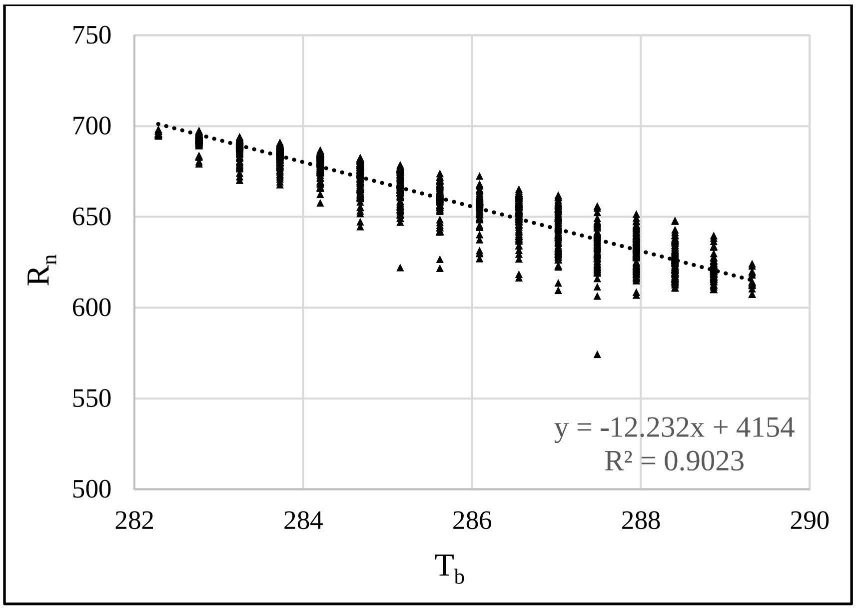
750
700
650
600
550
500
R_n
282
284
286
288
290
T_b
y = -12.232x + 4154
R² = 0.9023

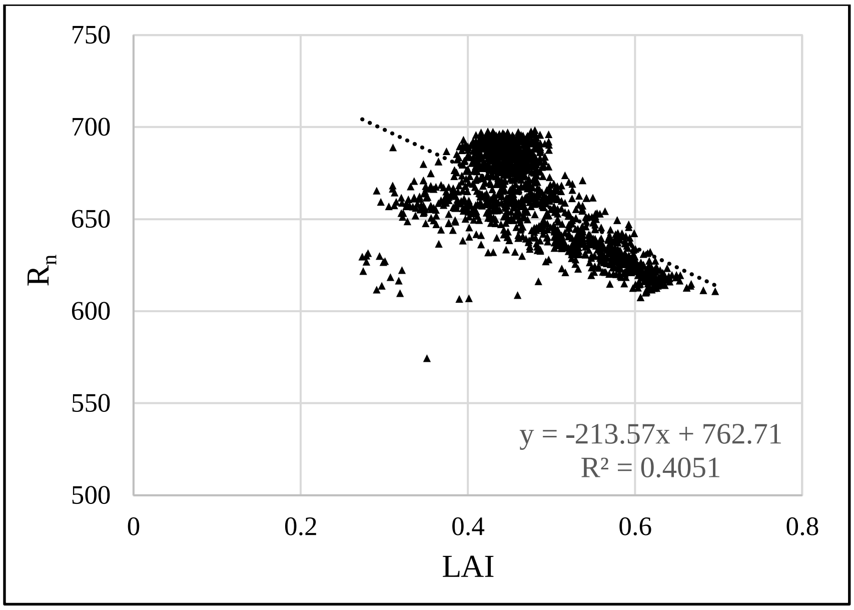
750
700
650
600
550
500
R_n
0
0.2
0.4
0.6
0.8
LAI
y = -213.57x + 762.71
R² = 0.4051

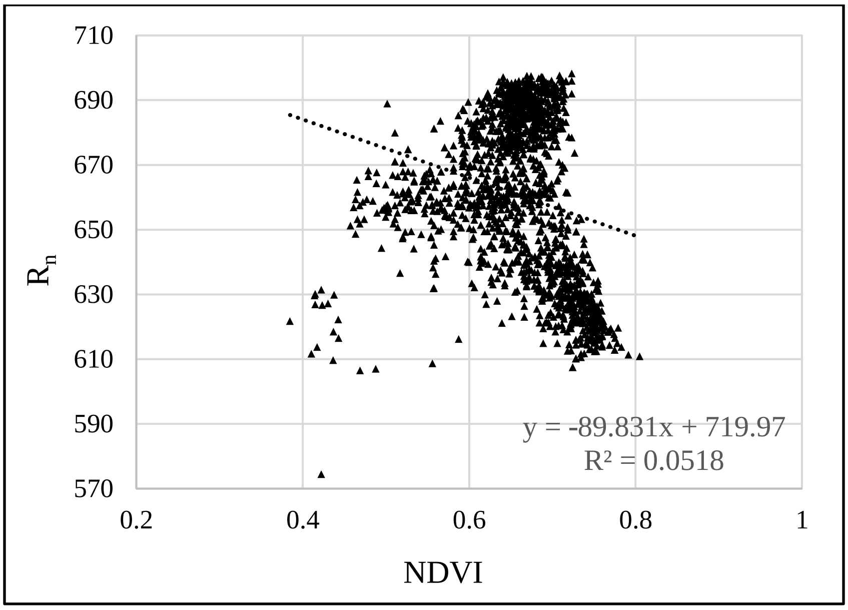
710
690
670
650
630
610
590
570
R_n
0.2
0.4
0.6
0.8
1
NDVI
y = -89.831x + 719.97
R² = 0.0518

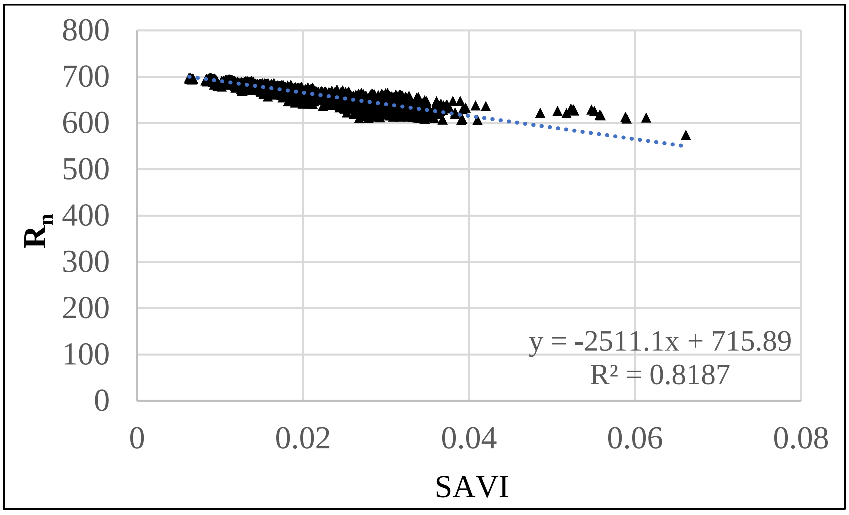
y = -2511.1x + 715.89
R² = 0.8187
Rn
SAVI

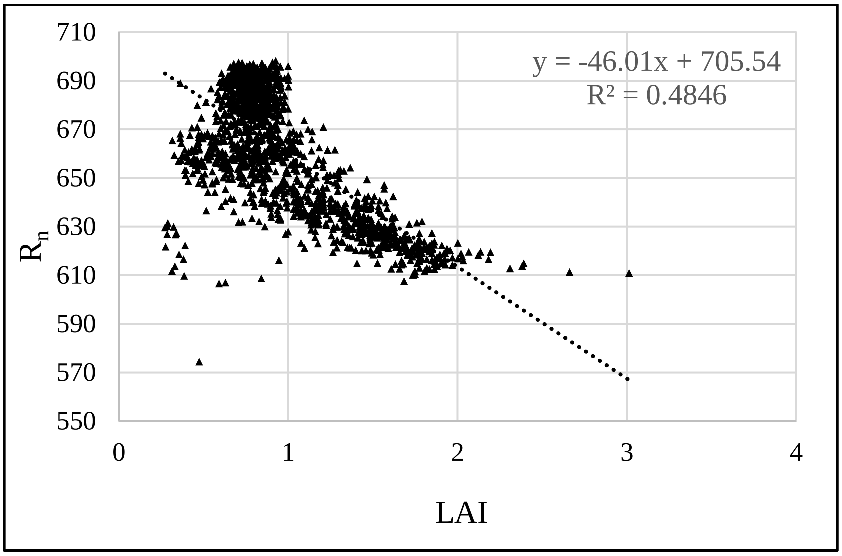
y = -46.01x + 705.54
R² = 0.4846
Rn
LAI

Appendix 34. Correlation of T_s with dT and T_a.

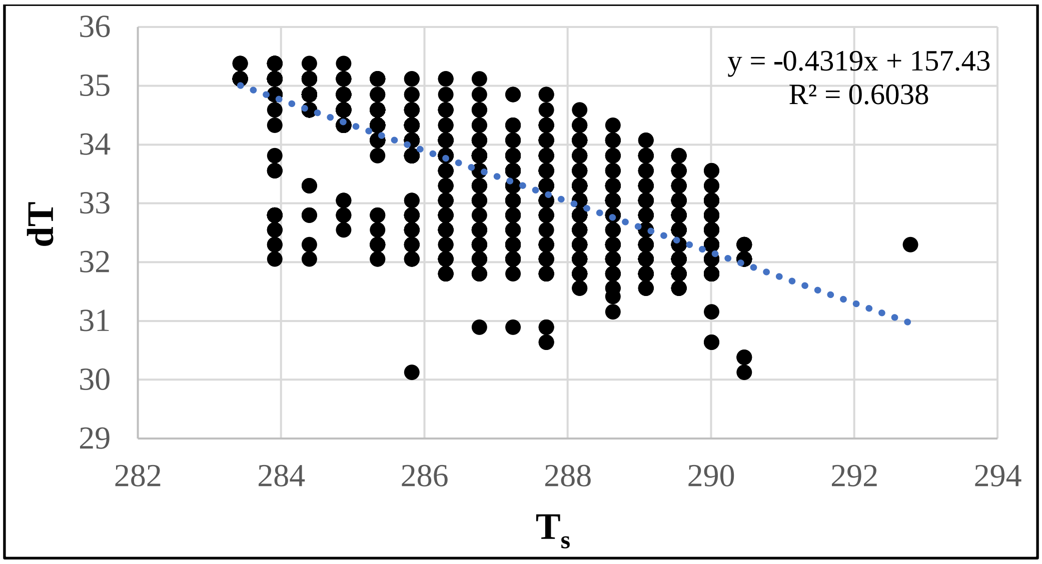

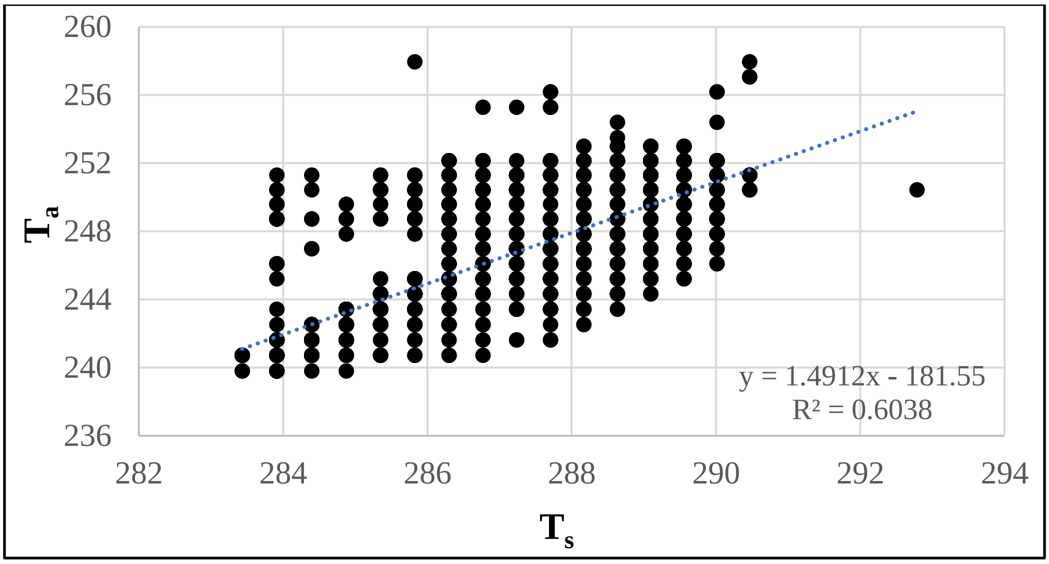

Appendix 35. Correlation between G/R_n ratio with R_L↑ and temperature.

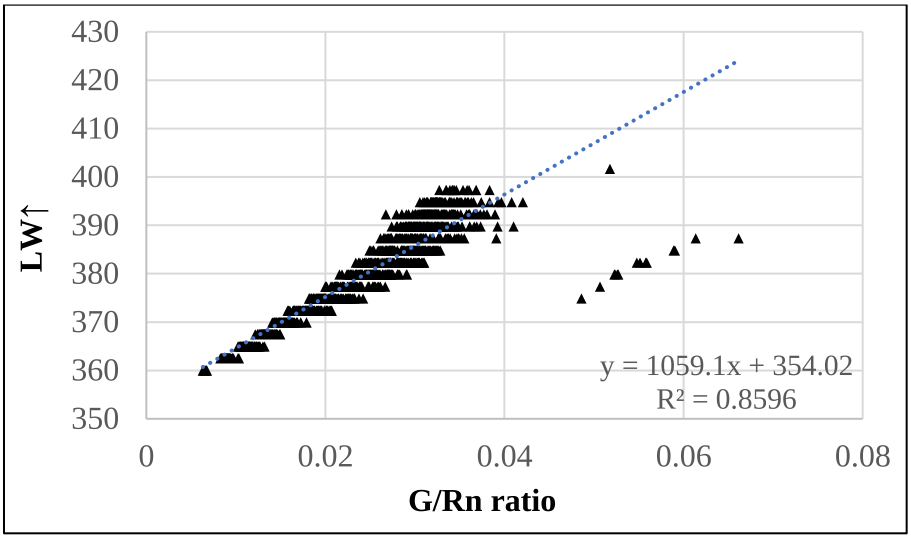

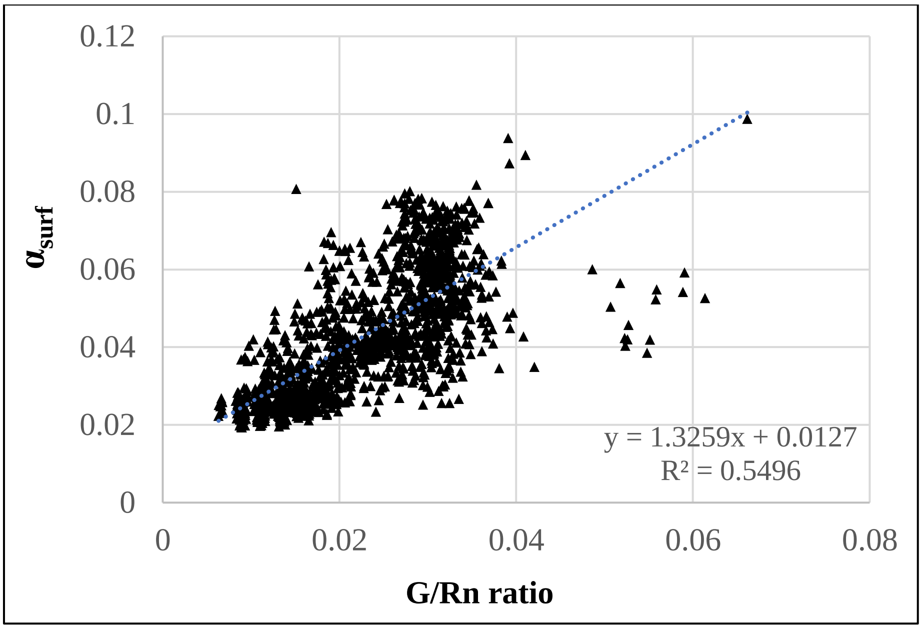

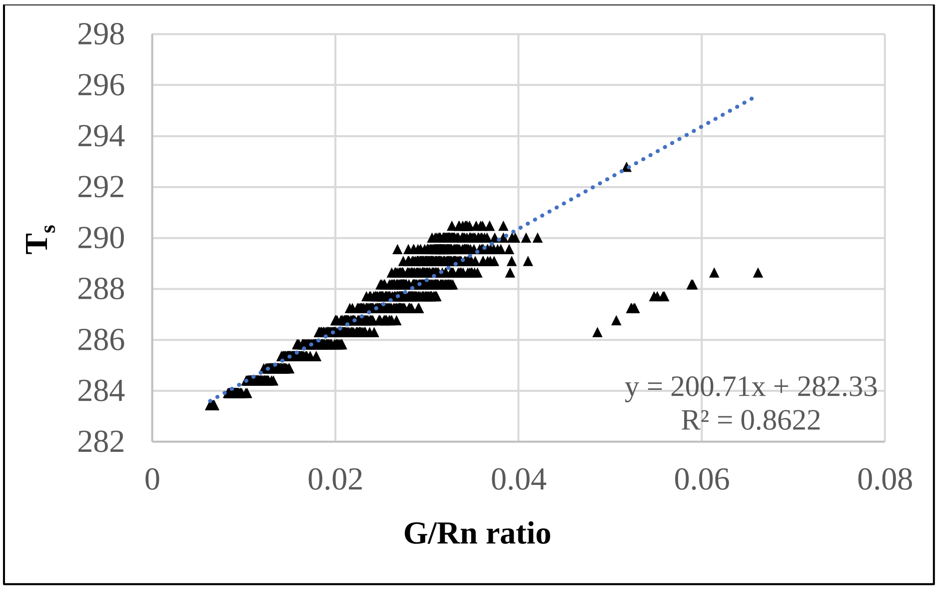

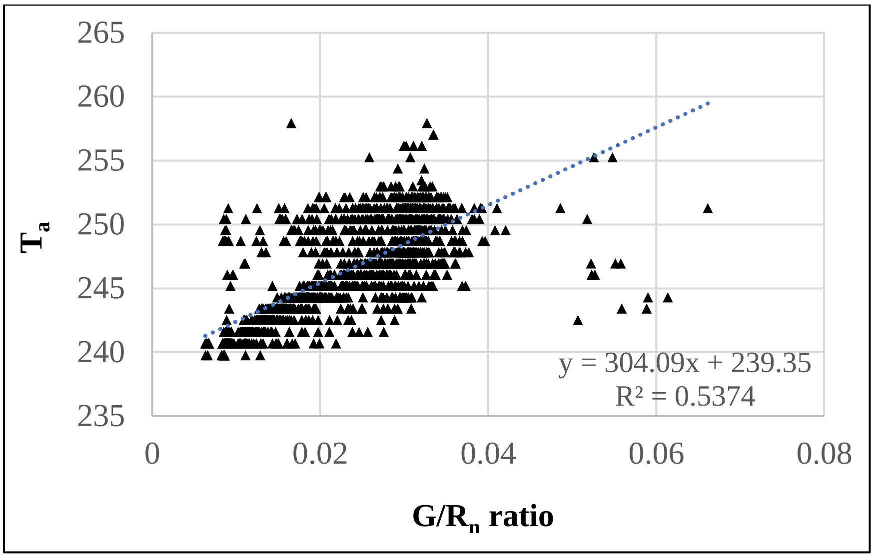
265
260
255
250
245
240
235
T_a
0
0.02
0.04
0.06
0.08
G/R_n ratio
y = 304.09x + 239.35
R² = 0.5374

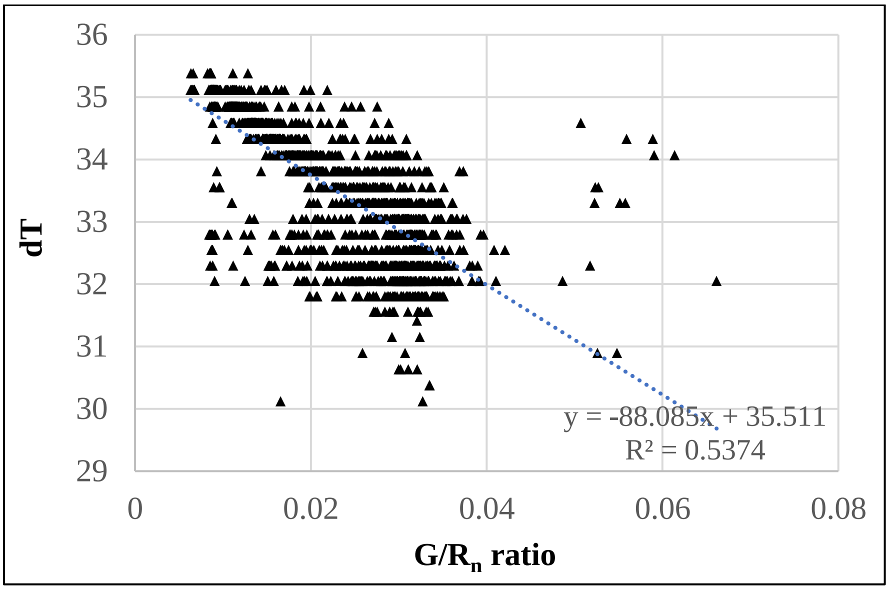
36
35
34
33
32
31
30
29
dT
0
0.02
0.04
0.06
0.08
G/R_n ratio
y = -88.085x + 35.511
R² = 0.5374